Doctoral Dissertation
Doctoral Program in Materials Science and Technology (31st Cycle)

Modelling and Constructing Devices Including Innovative Joining of High Temperature Thermoelectric Modules

Katarzyna Placha
* * * * * *

Supervisors
Prof. Milena Salvo, Supervisor
Dr Richard S. Tuley, Co-Supervisor

Doctoral Examination Committee:
Prof Mike Reece, Referee, Queen Mary University of London, United Kingdom
Dott. Fabrizio Valenza, Referee, CNR-ICMATE National Research Council, Italy

Politecnico di Torino
May 21, 2019

I hereby declare that, the contents and organisation of this dissertation constitute my own original work and does not compromise in any way the rights of third parties, including those relating to the security of personal data.

…….

Katarzyna Placha

Turin, May 21, 2019

Summary

Thermoelectric generators (TEGs) are devices that convert a heat flow into electricity. The efficiency of a thermoelectric generator depends on the thermoelectric properties of the material, the temperature difference across the device, and is often limited by the thermal and electrical losses at contacting interfaces. The vast majority of the thermoelectric research literature focuses on improving the properties of the thermoelectric material. However, the reliability and thermal stability challenges of incorporating thermoelectric materials into high-performance devices still represent a key bottleneck. In this work, fabrication methods for robust, medium-high temperature regime thermoelectric modules are proposed. To achieve this, different metallization layers, their deposition routes and several joining techniques that utilized commercial and novel bonding materials were developed.

Two thermoelectric module assembly approaches were explored. The first one involved testing conventional, high temperature brazing using materials that works in the desirable and narrow brazing window temperature range. Although mechanically strong contacts were formed, extensive growth of the reaction layer at the interconnect – thermoelectric interface and metallization layer delamination were observed that could presumably cause a device failure at higher service temperatures. The second approach involved assembly studies using low-temperature bonding materials and novel

metallization layers that minimized reaction layer formation and resulted in low electrical contact resistance performance. This work also demonstrates an implementation of the Solid-Liquid Interdiffusion (SLID) bonding technique using a novel aluminium-nickel multilayer system and extensive investigation into the electrical, mechanical and microstructural properties of contacting interfaces.

Three module prototypes were fabricated using off-the-shelf $Mm_y(Fe,Co)_4Sb_{12}$ *p-type* (*Mm* - Mischmetal) and $(Ni,Co)Sb_3$ *n-type* thermoelectric materials with average zT ($\overline{zT}$) of 0.12 and 0.27 respectively, measured between 50 °C and 450 °C. The high-temperature thermoelectric performance of device prototypes was fully characterized using in-house developed module test system and related to simulation results from finite element analysis using COMSOL Multiphysics ® software. The highest performing 7-couple thermoelectric module developed in this research was featured with P_{MAX} of 608 mW and power density of 695 mW/cm^2 measured at ΔT = 450 °C in open air.

Acknowledgment

I am extremely grateful to the many people who have helped me in the study for and preparation of this thesis.

First and foremost, I would like to express my sincere gratitude to my advisors Prof Milena Salvo and Dr Richard S. Tuley for their continuous support, motivation and immense knowledge their shared with me.

For their help in testing and providing me with many useful suggestions, I would like to thank many of my colleagues and research staff from Politecnico di Torino, particularly Prof Milena Salvo and Prof Valentina Casalegno who suggested looking into SLID bonding technique and conceptualized mechanical experiments, Sergio Perero , Fabiana D'Isanto, Stefano de la Pierre, Veronica Peretti, Monica Ferraris and Stefano Jamali.

Particular thanks to Prof. Mike Reece and Dr Theo G Saunders from Nanoforce Technology Ltd., Prof Bruno Bureau and Dr Catherine Boussard from University of Rennes, France for support and active collaboration during my secondments.

I want to thank all my colleagues from European Thermodynamics Ltd. for making my time in Leicestershire, England as enjoyable as they were: Kevin

Simpson and Dr Richard S Tuley for giving my an opportunity to work in such an inspirational environment; all passionate engineers and scientist for countless advice and great time exploring countryside and British culture: Mark C Robbins, Lucía Fernández García, Cevriye Koz, Elena Stefanaki, Chris Stuttle, Richard Lydiard, Barry Garner, Rosanna Danza, Itziar Hoces Fernandez, Mark Jones, Tibor Toro, Tim Perry, Guido Francesconi, Cerys Everard, Joseph Burlington, Pawel Rzepecki, Peter Dashwell, Rachel Parry, Aidan Edwards, Helen Gay, Philip Stirley and Nick Porter.

My sincere thanks go to all researchers involved in the CoACH project: Min Yu, Cristian Marro Bellot, Francesco Gucci, Matteo Cavasin, Pablo Lopez Iscoa, Hassan Javed, Francesca Elisa Ciraldo, Nicoletta Toniolo, Bhuvanesh Srinivasan, Acacio Rincon Romero, Alessia Masini, Gianmarco Taveri, Silviu Ivan and Rocío Tejido Rastrilla who made this experience truly enjoyable.

I would like to acknowledge Dott. Fabrizio Valenza and Prof Mike Reece who were my doctoral committee members for reading my dissertation and providing many useful insights.

Finally, I acknowledge the European Union's Horizon 2020 Programme who have provided support and funding through a Marie Skłodowska-Curie Innovative Training Network (CoACH, grant number 642557).

Table of Contents

List of Tables

List of Figures

Definitions and Abbreviations

Symbol	Definition	Unit
$\bar{T}$	Average absolute temperature	K
A	Cross-section area of thermoelements	m^2
$At\%$	Atomic Percent	%
DD	Didymium, i.e. 95 at% Nd, 5 at% Pr	n/a
I	Current	A
I_{SC}	Short circuit current	A
I_{SC}	Short-circuit current	A
k	Constant rate of the reaction	m/s
k_0	Frequency factor	s^{-1}
L	Length of thermoelements	m
Mm	Mischmetal, i.e. 50 at% Ce, 25 at% La	n/a
M_X	Atomic weight of element	g/mol
N	Number of thermocouples	-
P_{MAX}	Maximum power output	W
P_{OUT}	Power output	W
Q	Heat flow	J
Q_A	Activation energy	J/mol
R	Boltzmann constant	JK^{-1}
$R_{(Cold)i}$	Electrical resistance of cold side interconnect	Ω
$R_{(Hot)i}$	Electrical resistance of hot side interconnect	Ω
R_c	Electrical contact resistance	$Ωm^2$

$R_{c,T}$	Thermal contact resistance	m^2KW^{-1}
R_L	Load resistance	Ω
$R_{l,E}$	Electrical contact resistance of thermoelement	$Ωm^2$
$R_{l,T}$	Thermal resistance of thermoelement	m^2KW^{-1}
R_n	Electrical resistance of *n-type TE* leg	Ω
R_p	Electrical resistance of *p-type* TE leg	Ω
$R_{TEG,E}$	Internal Module Resistance	Ω
$R_{TEG,T}$	Thermal resistance per material unit area	m^2KW^{-1}
t	Process time	s
$T_{Braze\ remelt}$	Braze melting temperature	K
$T_{Brazing}$	Brazing temperature	K
T_C	Cold side temperature	K
T_H	Hot side temperature	K
T_M	Material's bulk melting point	K
$T_{M\ HIGH}$	High-temperature melting point material (SLID)	K
$T_{M\ LOW}$	Low-temperature melting point material (SLID)	K
T_{PEAK}	Brazing peak temperature	K
T_S	Sintering temperature	K
$T_{TE\ decomp}$	TE material decomposition temperature	K
t_X	Thickness	m
V	Voltage	V
V_{OC}	Open-circuit voltage	V
$Vol\%$	Volume percent	%
zT	Thermoelectric figure of merit, zT	-
α	Seebeck coefficient	VK^{-1}

α_n	Seebeck coefficient of the *n-type* material	V/K
α_p	Seebeck coefficient of the *p-type* material	V/K
α_S	Sintering factor relative to sample geometry	-
ΔT	Temperature gradient	K
η	Conversion efficiency	%
η_{MAX}	Maximum conversion efficiency	%
κ	Thermal conductivity	W/mK
ρ	Electrical resistivity	Ωm
ρ_x	Elemental density	g/m^3
σ	Electrical conductivity	Sm^{-1}
σ_x	Standard deviation	-
χ_{sc}	Electron affinity	eV
ϕ_m	Electronic work function	eV
$z\bar{T}$	Average thermoelectric figure of merit, zT	-

ASR	Area Specific Resistance
BCC	Body-Centered Cubic
BN	Boron nitride
BOL	Beginning-of-life
BSE	Back-Scattered Electron
CTE	Thermal Expansion Coefficient
DBA	Direct Bonded Aluminium
DBC	Direct Bonded Copper
DIW	Deionized Water
ENIG	Electroless Nickel Immersion Gold
FCC	Face-Centered Cubic Lattice
HEBM	High Energy Ball Milling
HMS	Higher Manganese Silicide
HPT	High-Pressure Torsion
IC	Integrated circuit
IMC	Intermetallic Compound
IPA	Isopropanol
MEMS	Micro-electro-mechanical systems
MMRTG	Multi-mission Radioisotope Thermoelectric Generator
PGEC	Phonon-Glass Electron-Crystal
PV	Photovoltaics
R&D	Research and Development
RT	Room temperature
RTG	Radioisotope Thermoelectric Generator

SEM	Scanning Electron Microscope
SLID	Solid-Liquid Interdiffusion Bonding
SPD	Severe Plastic Deformation
SPS	Spark Plasma Sintering
STU	Segmented Thermoelectric Unicouples
TAGS-85	$Ag_{6.52}Sb_{6.52}Ge_{36.96}Te_{50}$ Alloy
TE	Thermoelectric
TEC	Thermoelectric cooler
TEG	Thermoelectric generator
TEM	Thermoelectric module
TLPB	Transient-Liquid Phase Bonding
TPV	Thermophotovoltaics
XRD	X-Ray Diffraction

Chapter 1

Introduction

The growth in world energy demand which is about to increase 28% by 2040 [1] and the consequences associated with natural resources exploitation such as greenhouse gases emission and global warming, have deepened an interest in advanced, off-grid energy technologies, *e.g.* solar power, including photovoltaics (PV) [2] and thermophotovoltaics (TPV) [3], wind power and fuel cells (FCs) technology [4], just to name a few. Research on new, transformative energy technologies particularly in Europe, driven towards low-carbon economy and sustainable energy systems, is triggered by European legislation to bring environmental and health benefits *i.e.* by reducing air pollution. In October 2014, the European Commission adapted the '2030 climate and energy' framework setting three key targets to be achieved by 2030 [5] such as:

- At least 40% cuts in greenhouse gas emissions (compared to year 1990);
- At least 27% share for renewable energy;
- At least 27% improvement in energy efficiency.

Those goals might be achieved only by intensive work focused on developing energy technologies to enable higher conversion efficiencies and effective

pollution controls. With the current level of knowledge and state-of-the-art technologies, renewable energies cannot utterly replace fossil energy sources but can significantly reduce carbon footprint and improve the energy conversion efficiency of a conventional combustion engines.

Over the past few decades, thermoelectricity has gained much interest as an environmentally sustainable and reliable power generation technology. Thermoelectric energy conversion devices, particularly thermoelectric generators (TEGs), can provide direct conversion of heat flux to electricity and have no moving parts, hence resulting in silent and reliable alternative power system that have the potential for a very long lifetime. Such devices can be used to improve the overall efficiency of various systems where significant amount of energy is wasted as a heat, i.e. exhaust pipes in combustion vehicles [6], jet engines [7] or in oil & gas pipelines [8].

1.1 Motivation

One of the more challenging thermoelectric systems with limited commercially available solutions are those suitable for energy generation application at medium-high temperature range (with T_H = 500 ºC according to LeBlanc [9]). The most commonly studied thermoelectric materials intended to work at these regimes are Skutterudites ($CoSb_3$) [10], Half-Heusler compounds [11], chalcogenides [12] and silicon-based materials including magnesium silicide (Mg_2Si), silicon germanium (SiGe) and higher-manganese silicides (HMS) [13]. Among those materials, Skutterudite compounds with excellent thermoelectric performance and reasonably good mechanical features were proven to be especially useful for the power generation use, including automotive waste heat recovery [6] and deep space energy generation [14]. However, a major limitation

to fully realize the potential of new, promising materials, including the Skutterudites, is the lack of a reliable fabrication and module assembling technology for thermoelectric generators (TEGs) intended to work at temperatures higher than 350 ºC. The state-of-the-art module assembly comprises labour-intensive, pick-and-place methodology including soldering, brazing and adhesive bonding, often limited by low thermal stabilities of joining materials, limited surface wettability and an extensive, interfacial growth of brittle intermetallic compounds (IMCs) reducing their reliability in high-temperature operations. For this reason, commercial, high-temperature thermoelectric modules are not, as yet, available in the market for general use and it is worthwhile to investigate feasibility of new, promising materials in the thermoelectric generator (TEG) system.

To the best of the author's knowledge, no reliable high-temperature module assembly technology has been presented yet that could be transferable to low-cost high-volume, industrial scale manufacturing and meet more demanding service conditions. The majority of the research presented in the literature focuses on the principal investigation of interactions between all components of thermoelectric module and testing of different, sometimes not commercially viable solutions. In the conventional, bulk thermoelectric module fabrication, semiconductor material is synthesized starting from the elemental powders and consolidated into bulk by using well-established technologies. Over past few years, spark plasma sintering technique has been successfully implemented into fabrication of many functional materials, due to the possibility of performing *in-situ* synthesis and consolidation process in one step as well as it's fast speed that reduces the grain growth. Moreover, high pressure and temperature involved in the process (> 50 MPa) opens a possibility of co-sintering of functional material and metallic foils that

would serve as diffusion barrier and top metallization layer necessary for effective wetting of solders/brazes. The next step usually involves cutting of thermoelectric material into the correct shape and joining to metallic electrodes so that unicouples are electrically connected in series and thermally in parallel. Joining of thermoelectric modules is attracting increased research interest as it is being recognized to be an essential step for effective module fabrication and its successful commercialization. Despite learning from the tremendous efforts in the electronics industry, the assembly of TEGs is still particularly challenging, and consequently, thermal-to-electric conversion utilizing these devices has been realized only in niche applications. Similar to MEMS (micro-electro-mechanical systems) and IC (integrated circuit) packaging, structural integration alone results in the most of its fabrication cost and specifically in thermoelectric manufacturing can make up over 43% of the final module price [15]. It is required that thermoelectric module is scalable to high-volume industrial assembly processes, currently limited by 'hand-made' labour due to necessity of machining many dissimilar elements in separate steps. Moreover, the major bottleneck in high-temperature range TEGs manufacturing is the selection of suitable interconnect, joining material and metallization layer with matching thermal and mechanical properties, crucial in medium-high and high temperature operations.

Preliminary experiments and simulations on proposed Skutterudite-based thermoelectric device have shown promising results of achieving high conversion efficiency, comparable with commercial, low-temperature modules based on bismuth telluride (Bi_2Te_3). This is particularly important, as thermoelectric modules that could work at high temperature regime and thus generate more power per module, are not yet available in the market. Additionally, high material cost and extreme rarity of Tellurium in the Earth's crust inevitably influence the

price of the thermoelectric device, questioning the cost-effectiveness of such technology. Hence, a prototype of high-temperature thermoelectric module is to be developed using simple fabrication process that can be implemented into low-cost, industrial manufacturing technology.

1.2 Objective

The main objective of this study is to develop a thermoelectric generator, working at desirable, medium-high temperature range with the module hot-side (T_H) not exceeding 500 ^{o}C. In order to achieve this goal, several bonding techniques and metallization layers must be designed and validated so the effect of the different assembly conditions on the device performance and their stability can be investigated. Moreover, different metallization layers that would be stable over the wide temperature range must be developed using commercially reliable methods and their electrical and mechanical performance must be properly characterized. The prototype thermoelectric generator should be developed using off-the-shelf $Mm_y(Co,Fe)_4Sb_{12}$ *p-type* and $(Ni,Co)_1Sb_3$ *n-type* thermoelectric materials that are easily available for high volume manufacturing.

1.3 Contributions

This thesis brings several contributions to the field of medium-high temperature regime thermoelectric modules fabrication. First of all, commercially available thermoelectric materials were investigated in terms of possibilities in achieving high conversion efficiency thermoelectric modules and their reproducibility. The fabrication of thermoelectric material was performed by *in-situ* synthesis using Spark Plasma Sintering technique. By co-sintering of

metallization material and thermoelectric powders in one step, the manufacturing process would be shortened reducing the overall module fabrication cost. A few diffusion barriers and metallization layers that were presented for the first time were tested along with different joining techniques and their properties were properly characterized. Moreover, innovative low-temperature joining techniques, including nano-Ag sintering and Ag flakes adhesive bonding were presented in the high temperature thermoelectric system for the first time. The Solid-Liquid Interdiffusion (SLID) technique, implementing novel aluminium-nickel inter-layered system was successfully employed to bond interconnect (electrode) and thermoelectric material with resulting contacts characterised with higher than initial re-melting temperatures. The SLID process investigated in this work led to joined patent application (‘Thermoelectric module’, UK provisional patent application no. EP174230753) and can be utilized in other medium-high temperature range thermoelectric systems. Three thermoelectric module prototypes where developed using off-the-shelf thermoelectric material and their high-temperature performance were fully characterized using in-house developed testing rig. The feasibility of low-volume thermoelectric generator assembly process was also demonstrated by realizing all manufacturing steps in-house with available resources. Moreover, numerical modelling was successfully implemented to predict prototype performance and correlated with the experimental results to reveal possible discrepancy of fabrication and module measurement process.

Chapter 2

Fundamentals and the State of the Art

2.1 Thermoelectricity

The thermoelectric effect, observed by Thomas Johann Seebeck in 1823 and initially mistaken for thermomagnetism, constitutes of three different physical effects, namely Seebeck, Peltier and Thomson effect. The former case can be discussed by referring to the schematic of a simple thermocouple junction as shown in Figure 2.1-1. Such a thermocouple consists of two electrically conductive materials (normally metals or semiconductors) depicted as 'A' and 'B' which are electrically connected in series and thermally in parallel. The Seebeck effect is attributed to a voltage generated at the materials' edges ('*a*' and '*b*') when the junction is maintained at a temperature difference to the material edges. The temperature difference denoted as ΔT is a temperature drop between the hot side (T_H) and the cold side (T_C) and $T_C \leq T_H$. The open circuit voltage V_{OC} generated between 'a' and 'b' is proportional to the difference in the temperature (ΔT) between the hot junction and the reference junction and is given by the equation 1:

$$V_{OC} = -\alpha_{AB}(T_H - T_C) = -\alpha_{AB} \cdot \Delta T \qquad 1$$

Where α_{AB} is the Seebeck coefficient of the thermocouple and T_H and T_C are temperatures on the hot and cold sides, respectively.

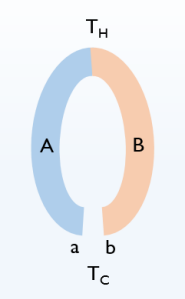

Figure 2.1-1: Schematic diagram of the thermocouple junction.

Later, in 1834, the reverse effect was observed by C. Peltier; when current was passed through two connected dissimilar materials, heat could be either generated or removed at both junctions. The Peltier effect occurs when an external voltage source applied across the junction '*a*' and '*b*', and clockwise current *I* flows through the conductors, resulting in a rate of heating *q* occurs at one junction while a rate of cooling –*q* occurs at the other junction. The ratio of the electric current *I* to the heating rate defines the Peltier coefficient π_{AB} of the thermocouple and is given by the equation 2:

$$\pi_{AB} = {}^{q}/_{I} \qquad 2$$

In the Thomson effect, heat is absorbed or produced at a rate *q* as a result of current *I* flowing through a portion of a single conductor where there is a

temperature difference ΔT. The heating rate q is related to I and ΔT by the equation 3:

$$q = \beta \cdot I \cdot \Delta T \quad (3)$$

Where β is the Thomson coefficient.

In the literature, the thermoelectric effect is usually denoted as the 'Seebeck-Peltier effect' as these physical phenomena have the same fundamental origin. The three thermoelectric effects associated respectively with Seebeck, Peltier and Thomson are gathered together to get a unique description of thermoelectric phenomena by the Kelvin relations. Equation 4 describes the relationship between the Seebeck and Peltier effects, and indicates if the materials suitable for thermoelectric power generation are also suitable for thermoelectric refrigeration.

$$\pi_{AB} = \alpha_{AB} \cdot T \quad (4)$$

Where T is absolute temperature.

$$\frac{d\alpha_{AB}}{dT} = \frac{\beta_A - \beta_B}{T} \quad (5)$$

Where the temperature gradient dT describes at what rate the temperature changes along the length of a material with A and B denoting different positions in each material. Therefore, the Thomson effect is a generalisation of the Peltier effect to include changes in the Seebeck coefficient in one material, for example if the Seebeck coefficient in a material is temperature dependent. While the Seebeck

and Peltier effects are most easily defined and measured for pairs of materials, other methods can be used to calculate an absolute Seebeck coefficient, allowing a Peltier and Seebeck coefficient to be defined separately for each material, so that the properties of any junction can be easily calculated. Therefore, the individual material's Seebeck coefficients, α_A and α_B are defined by:

$$\alpha_{AB} = \alpha_B - \alpha_A \qquad 6$$

2.2 Medium-High Temperature Thermoelectric Materials

Thermoelectric materials are typically classified by the material structure and composition, with chalcogenides, clathrates, silicide, skutterudites and oxides being the most commonly reported in the literature as seen in Figure 2.2-1Figure 2.2-1. In a review by G. J. Snyder *et al* [16], figure of merit data of state-of-the-art commercial materials, particularly for thermoelectric power generation use, can be categorized according to their temperature regimes in which the materials exhibit highest possible $\overline{zT}$ value. Such a classification, as a reasonably practicable approach, allows the prediction of most beneficial material performance at given temperature ranges and might be classified, according to Ref. [17] , such as:

1. Low temperature (T_H = 100 ºC and T_C = 20 ºC);
2. Medium – low temperature (T_H = 250 ºC and T_C = 20 ºC);
3. Medium – high temperature (T_H = 500 ºC and T_C = 50 ºC);
4. High temperature (T_H = 800 ºC and T_C = 50 ºC).

The standard approach to evaluate the performance of thermoelectric material is to calculate the dimensionless thermoelectric material's figure of merit zT, as outlined by equation 7:

$$zT = \frac{\alpha^2 \cdot \sigma}{\kappa} T \qquad 7$$

Where α, σ, and κ are the Seebeck coefficient, electrical and total thermal conductivity, respectively, and T is the absolute temperature. The thermoelectric power factor ($\alpha^2\sigma$) is a relative measure of the power that a thermoelectric generator will provide while the zT is more closely related to the conversion efficiency. Thermoelectric materials must have a high value of Seebeck coefficient, α (see equation 7) in order to generate high electrical potential under a thermal gradient, along with high electrical conductivity, σ, needed to facilitate the movement of electrical carrier. Meanwhile a low thermal conductivity, κ, is desired in order to maintain the temperature drop across the TE element as high as possible. The total thermal conductivity $\kappa = \kappa_{el} + \kappa_{lat}$; where κ_{el} and κ_{lat} are the electronic and lattice contribution to the material conductivity respectively. Since only κ_{lat} is not a function of carrier concentrations and thus independent of the other parameters, it is often a focus of improvement to enhance the material zT. The state-of-the-art materials are characterized with $zT \geq 1$, which is necessary requirement for most technical applications in order to achieve a high conversion efficiency of the thermoelectric device. The value of zT for various thermoelectric materials typically varies considerably as a function of temperature, and for device operation, an average zT ($\overline{zT}$) over the device temperature difference is a better optimization target [18]. This therefore implies that a material is most

effective for an application where the temperature range includes the temperature at which the material *zT* value peaks.

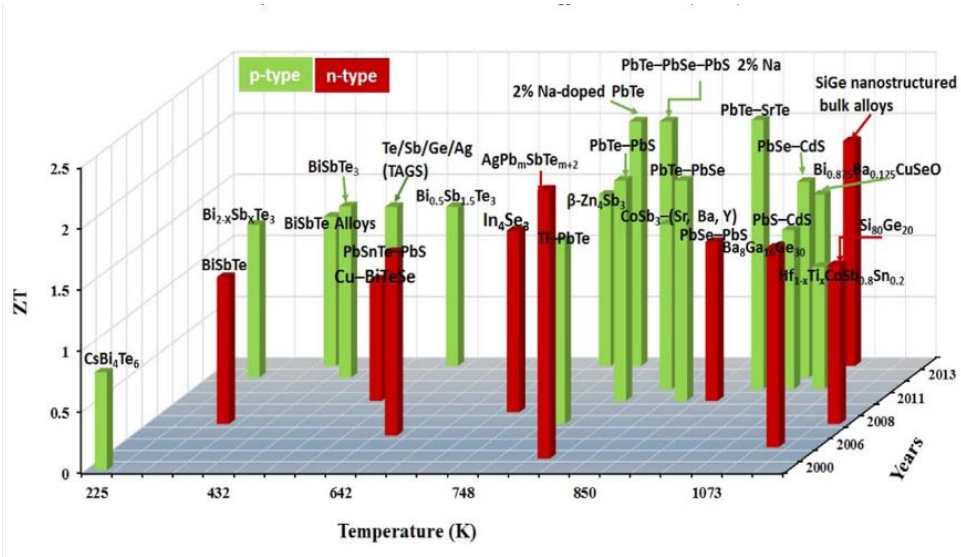

Figure 2.2-1: Peak thermoelectric figure of merit (*zT*) with the temperature at which the peak occurs and year illustrating important milestones, adapted from Ref. [19].

Skutterudites are diamagnetic (Co^{3+}, $3d^6$) narrow band gap (~ 0.2 eV) semiconductors with high carrier mobility and relatively large effective electron mass and have been proven to be highly efficient thermoelectric materials in the medium-high temperature regime [20]. Skutterudites are classified as materials with phonon-glass electron-crystal (PGEC) open crystallographic structure as voids in the crystal structure might be filled with atoms of heavy elements, acting as rattlers and increasing the number of phonon scattering centres, hence reducing the lattice thermal conductivity significantly to levels seen in amorphous structures [21]. This behaviour, in combination with low electrical resistivity and high Seebeck coefficient of doped and/or filled skutterudite makes it a promising alternative for PbTe-based material replacement. High performance, filled skutterudites have a structural-chemical formula of $EP_yT_4X_{12}$, where the filler

atom ‘EP’ being usually an electropositive element enclosed by an icosahedral cage structure formed by tilted pnictogen octahedral (eight per formula unit, made of atoms ‘X’) each centred by a transition metal atom ‘T’ [20] and are the most commonly reported in the literature [22]. In the recent years, different compositions and processing techniques for skutterudite-based materials have been reported leading to development of materials with outstanding high temperature performance. As seen in Figure 2.2-2, the highest reported zT value of 1.3 was achieved for *p-type* $DD_{0.59}Fe_{2.7}Co_{1.3}Sb_{11.8}Sn_{0.2}$ (*DD* stands for didymium, 95 at% Nd and 5 at% Pr) and that of 1.8 for *n-type* $(Sr,Ba,Yb)Co_4Sb_{12}$ + 9.1 wt% $In_{0.4}Co_4Sb_{12}$ materials [23]. These high zT skutterudites have leg efficiencies over 14% and almost 18% in the temperature range of 300 - 800 K respectively and can be achieved by introducing severe plastic deformations (SPD) via high-pressure torsion (HPT) consolidation technique.

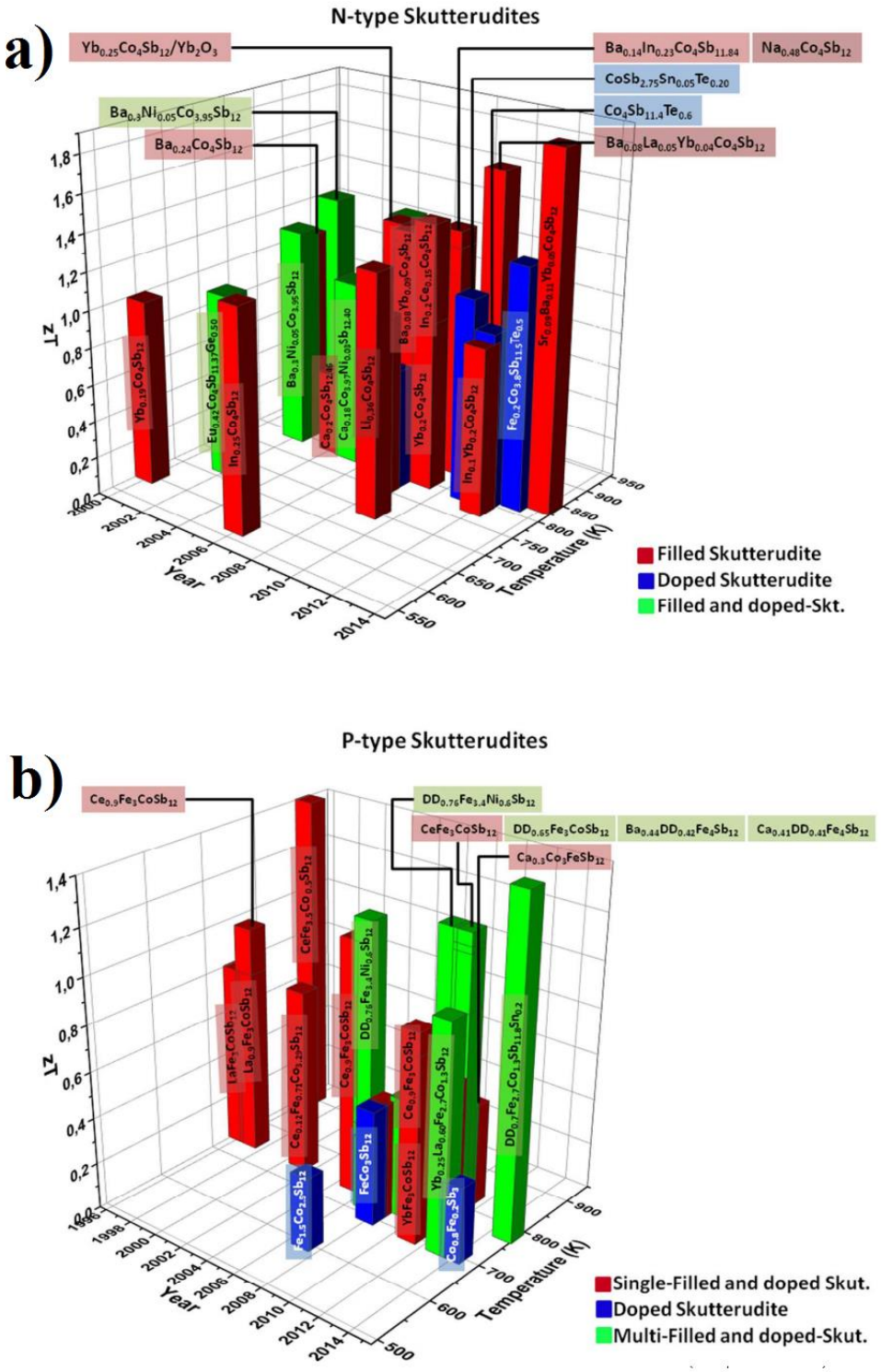

Figure 2.2-2: Summary of *zT* peak values for reported **(a)** *n-type* doped and/or filled Skutterudites and **(b)** *p-type* doped and/or filled Skutterudites depending on the year of publication and operation temperature adapted from Ref. [21].

2.3 Electrical and Thermal Contact Interface

Thermoelectric material–metal interconnect contacts provide an electrical and thermal connection by allowing the passage of electrical current and heat flux across the contacting interfaces. Semiconductor–metal interconnects are at the core of solid-state device performance due to sensitivity to resistance in the electron flow and heat flux, and hence might lead to reduced conversion efficiency of the prototype device (as depicted in Figure 2.3-1a). In the conventional thermoelectric contacts, metal electrodes are joined to the semiconductor elements to provide the permanent interconnection either by the mechanical (i.e. using compression springs [24]) or chemical (i.e. solid-state diffusion bonding [25] or brazing [26]) methods of bonding.

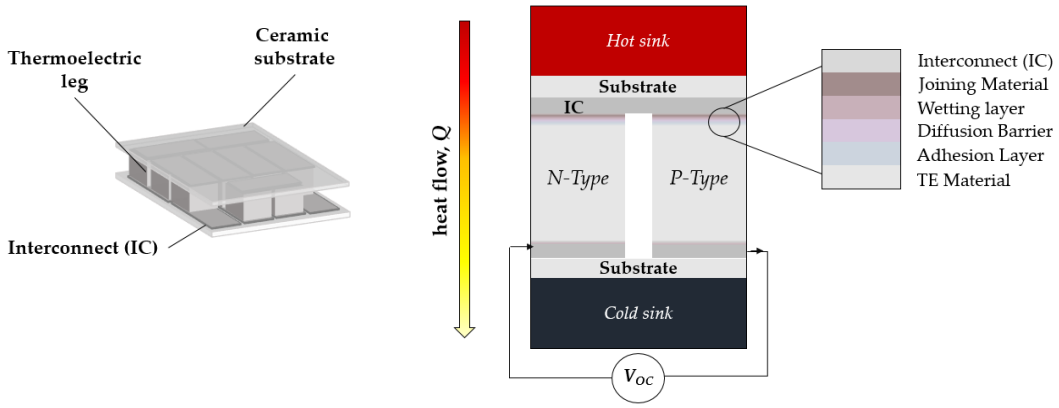

(a) **(b)**

Figure 2.3-1: Schematic illustration of **(a)** 7-coupled thermoelectric prototype module and **(b)** side-view of the module in the generation mode presenting two unicouples made of *p*- and *n-type* thermoelectric material (TE) presenting the heat flow (Q) across the unicouple.

In order to achieve high performance of thermoelectric device, fabrication of robust electrical contacts is needed, especially at the module hot-side as they

usually suffer from more intensive thermal stresses induced during the high temperature service. A ceramic substrate is normally used to provide electrical insulation and is typically made of alumina (Al_2O_3) or aluminium nitride (AlN) to simplify module construction. The metallic interconnect and *n*- and *p-type* thermoelectric that make up the device have a coefficient of thermal expansion (CTE) that differs substantially from the ceramic substrate, so that temperature changes, during the fabrication and service, result in undesirable stresses at contacting interfaces. Moreover, other potential degradation mechanisms, such as thermally-driven interdiffusion at metal/thermoelectric interfaces over time can lead to catastrophic failures in thermoelectric device. Due to enhanced reactivity of all metals at higher temperature, a presumed chemical reaction between thermoelectric and joining material leads to the formation of interfacial reaction layer at the connections, usually consisting of brittle intermetallic compounds (IMCs) which can cause crack propagation and result in high electrical contact resistances. Therefore, additional metallization is often required, to act as a high-temperature diffusion barrier between semiconductor and a braze. The metallization layer can also significantly improve the wettability behaviour of molten joining material over the thermoelectric and may help with relieving residual thermal stresses at the interface induced at high temperature operation. In general, when the properties of the metallization layer, joining material and thermoelectric are considerably different, intermediate sublayers within thermoelectric metallization needs to be introduced. The characteristics of these sublayer materials, particularly in terms of matching their coefficients of thermal expansion, are between those of the substrate and top metallization layer that, in turn, intended performance within required ranges of mechanical loads are achieved. The metallization layer may often act as a stress relieving buffer as

usually ductile material can easily develop plastic deformation at higher temperature and pressure. The proper choice of the sublayer materials is an extremely difficult task and may require multilayer coatings comprising from 3 to 5 layers can provide an optimal performance characteristic. Figure 2.3-1b presents a schematic structure of thermoelectric module with multi-layered metallization typically associated with thermoelectric unicouples intended to work in the medium-high and high temperature regimes. In the multi-layer metallization systems, three different layers are often found to be reported and are divided, depending on the purpose they serve, to 'adhesion layer', 'diffusion layer' and 'wetting layer' accordingly. The first layer to be directly in contact with the substrate, referred as 'adhesion layer', improves the adhesion between the thermoelectric material and 'diffusion barrier'. The high reactivity of the 'adhesion layer' at high temperatures allows two chemically inert interfaces to be joined, due to the chemical reaction that layer undergoes with contacting materials. This solution is a common practice, as the 'diffusion barrier' is not expected to significantly chemically interact with thermoelectric material and a stable intermediate phase (such as intermetallic compound or solid-solution) is normally needed to sustain a continuous mechanical interface. Additionally, chemically inert 'diffusion barrier' which usually comprises one of the refractory metals or amorphous material, often exhibit limited weldability, so that additional top 'wetting layer' is needed. Noble metals such as gold, silver and their alloys are widely used as a top metallization layer due to the excellent surface wettability and high-temperature, anti-oxidation protection.

In summary, the preferred thermoelectric – interconnect junctions, including all metallization stacks, must meet following requirements:

1. The contact electrical resistance (R_c) at the semiconductor–metal interconnect should be at least less than 30 % of the total TE leg resistance (assuming no thermal contact resistances; $R_{c,T} = 0$), in order to maintain > 80 % of the theoretical material efficiency in the working device, according to Ref. [27]. This is determined partly by the thickness and electrical conductivity of the metallization stack, but often more significantly by additional interface effects from the boundaries between the layers, especially the interface to the thermoelectric semiconductor. This is at least partly determined by the electronic work function of the metal (ϕ_m) and the electron affinity (χ_{sc}) of thermoelectric semiconductors and has to be taken in to consideration with the heavily-doped thermoelectric materials [28].

2. The thermal contact resistance ($R_{c,T}$) at the contacting interfaces should be less than 20 % of the thermal resistance of the thermoelectric leg (assuming no electrical contact resistances), in order for the efficiency not to decrease more than 20 % in the working device [27];

3. Contact interfaces must accommodate thermo-mechanical mismatch and residual stresses resulting from differences in coefficients of thermal expansion, Young's modulus and yielding stress of all stacking elements. This is especially crucial requirement at the hot side of thermoelectric module. If the difference in the physical properties between thermoelectric material and metal interconnect is significant, there is a need for multi-layered metallization;

4. High-temperature stability at the module working conditions, including oxidation resistance and lack of extensive chemical interaction or interdiffusion between contacting stack elements;

5. Good adhesion with the interconnect material in needed so that fabricated high quality, mechanically strong bond can withstand moderate shear and compressive stresses (1 MPa) as well as stresses arising from high vertical thermal gradients (approx. 100 - 200 ºC/mm).

2.4 Thermoelectric Generator for Medium—High Temperature Regime Applications

A conventional thermoelectric module consists of highly doped narrow band gap semiconductor thermocouples with two types of materials, one with an excess of *p-type* charge carriers and one with an excess of *n-type* carriers, connected thermally in parallel and electrically in series. Thermoelectric solid-state devices, depending on the target application, can work either in the cooling or generation mode. In the power generation mode, a temperature difference applied across the thermoelectric generator (TEG) module generates a voltage, allowing extraction of electrical power driven by the Seebeck effect (equation 1). In a thermoelectric cooler (TEC) module, as opposed to TEG, heat is pumped by the Peltier effect when electrical power is applied to the thermoelectric module. Figure 2.3-1a,b shows a schematic diagram illustrating conventional, 7-couple thermoelectric module and basic principle of the Seebeck effect in the thermoelectric generator (TEG). Although both types of thermoelectric module can be used in the cooling or power generation mode, this chapter describes in detail features of thermoelectric generator only, as it is a scope of this research.

By assuming no thermal and electrical parasitic losses at the contacting interfaces within the thermoelectric generator, a thermoelectric module acts as a voltage source producing a voltage equal to the open-circuit voltage (V_{OC}) and a

series resistance accounting for the internal electrical resistance of the thermoelectric module ($R_{TEG,E}$), which are given by:

$$V_{OC} = N(\alpha_n - \alpha_p)(T_H - T_C) \quad 8$$

$$R_{TEG,E} = N(R_n + R_p + R_{(Hot)i} + R_{(Cold)i}) \quad 9$$

Where N is the number of series-connected thermocouples, α_n, α_p are the Seebeck coefficient of the *n-type* and *p-type* semiconductors, respectively, and T_H and T_C are temperatures on the hot and cold side of TEG, respectively. R_n and R_p are the electrical resistances of the thermoelectric legs, calculated from $\frac{L}{\sigma A}$, where L, σ and A are length, electrical conductivity and cross-sectional area of thermoelectric element, respectively, and $R_{(Hot)i}$ and $R_{(Cold)i}$ are the electrical resistances of hot and cold interconnections. To simplify further calculations, $R_{(Hot)i}$ and $R_{(Cold)i}$ will not be further considered as Ni(P) plated copper interconnects that are normally used are characterized with significantly higher electrical conductivity than thermoelectric elements are their influence is negligible. The electrical circuit of a TEG is shown in Figure 2.4-1.

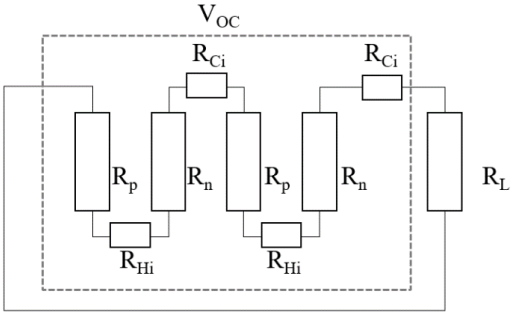

Figure 2.4-1: Electrical resistance network of the thermoelectric generator.

The output power (P_{OUT}) of thermoelectric generator is given by:

$$P_{OUT} = \frac{V_{OC}^2 R_L}{\left(R_{TEG,E} + R_L\right)^2} = \frac{N^2 \alpha^2 (T_H - T_C)^2 R_L}{\left(R_{TEG,E} + R_L\right)^2} \quad 10$$

Where R_L is module load resistance.

If a load resistance R_L attached to the output of the TEG is set equal to the resistance of the thermoelectric module, $R_L = R_{TEG,E}$, the maximum power delivered to the load is:

$$P_{MAX} = \frac{V_{OC}^2}{4R_{TEG,E}} = \frac{N^2 \alpha^2 (T_H - T_C)^2}{4R_{TEG,E}} \quad 11$$

The efficiency of the TEG is the ratio between the energy supplied to the load and the heat energy absorbed at the hot junction. The maximum conversion efficiency (η_{MAX}) of the thermoelectric process, occurring at slightly higher load resistance $R_L = \sqrt{1 + Z\bar{T}}$, is derived to be equal to:

$$\eta_{MAX} = \frac{\Delta T}{T_H} \times \frac{\sqrt{1 + Z\bar{T}} - 1}{\sqrt{1 + Z\bar{T}} + \frac{T_C}{T_H}} \quad 12$$

Where $\bar{T}$ is the average absolute temperature of the hot and cold junctions, i.e. $\bar{T} = \frac{T_C + T_H}{2}$, and Z is the figure of merit of the thermoelectric module defined as:

$$Z = \frac{\alpha^2}{\rho \kappa} \quad 13$$

Where α, κ and ρ are the Seebeck coefficient, thermal conductivity and electrical resistivity of the thermoelectric module, respectively, and $\bar{T}$ is the average absolute temperature given by:

$$\bar{T} = \frac{T_H + T_C}{2} \tag{14}$$

However, a number of secondary effects directly influences the performance of thermoelectric modules. That includes convective and radiative heat losses from the thermoelectric leg to air along with thermal and electrical contact resistances at contacting interfaces and strongly influence the conversion efficiency of the thermoelectric generator. The thermal contact resistance ($R_{c,T}$) and electrical contact resistance (R_C), in particular, are important characteristics of these contacts and are usually taken into account as an integral part of the overall circuit resistance of the thermoelectric device. Moreover, thermal contact resistance at the interfaces, reduces the temperature span across the leg and metal interconnect, leading to module efficiency reduction. According to Ref. [29], with thermal and electrical contact resistances taken into consideration, the conversion efficiency of the thermoelectric generator can be delivered by:

$$\eta = \frac{\Delta T}{T_H} \frac{1}{\left(1 + 2\frac{R_{c,T}}{R_{l,T}}\right)^2 \left(2 - \frac{1}{2}\frac{\Delta T}{T_H} + \frac{4}{zT_H}\frac{1 + 2R_c/R_{l,e}}{1 + 2R_{c,T}/R_{l,T}}\right)} \tag{15}$$

Where R is the resistance given in Ohms, l denotes leg and subscripts e or T denotes the electrical or thermal resistance, respectively.

2.4.1 Bulk Thermoelectric Module Fabrication

Conventional, bulk-based thermoelectric module fabrication is based on many individual steps as presented in Figure 2.4-2. Thermoelectric material is normally synthesized by simple metallurgical route and consolidated into bulk material using i.e. hot-pressing or Spark Plasma Sintering or *in-situ* synthesized by Spark Plasma Sintering technique which can combine the two mechanisms in one processing step. Bulk material is thereafter subjected to coating with a suitable metallization layer normally involving wet or dry deposition methods and machining to rectangular-shaped thermoelectric legs. Good quality cut can be difficult to achieve, as metallization layer can delaminate from the thermoelectric material, owing to the nature of weak mechanical bonding. Joining material, if it is in the paste form, is normally dispersed on the conductive strips, such as copper clads, using dispensing screen or stencil printing process and along with thermoelectric legs assembled into functional structures. The state-of-the-art module joining comprises pick-and-place methodology with soldering [30], brazing [31] and pure metal sintering [32] used for electrical contacts fabrication where the interfacial bonding is triggered by chemical reaction between two materials being in physical contact and depends on the nature of the diffusion of the joining material. As-prepared assembly is thereafter subjected to a high-temperature firing process, i.e. furnace brazing, normally performed in an inert gas, such as argon or nitrogen, to avoid thermoelectric material and braze oxidation.

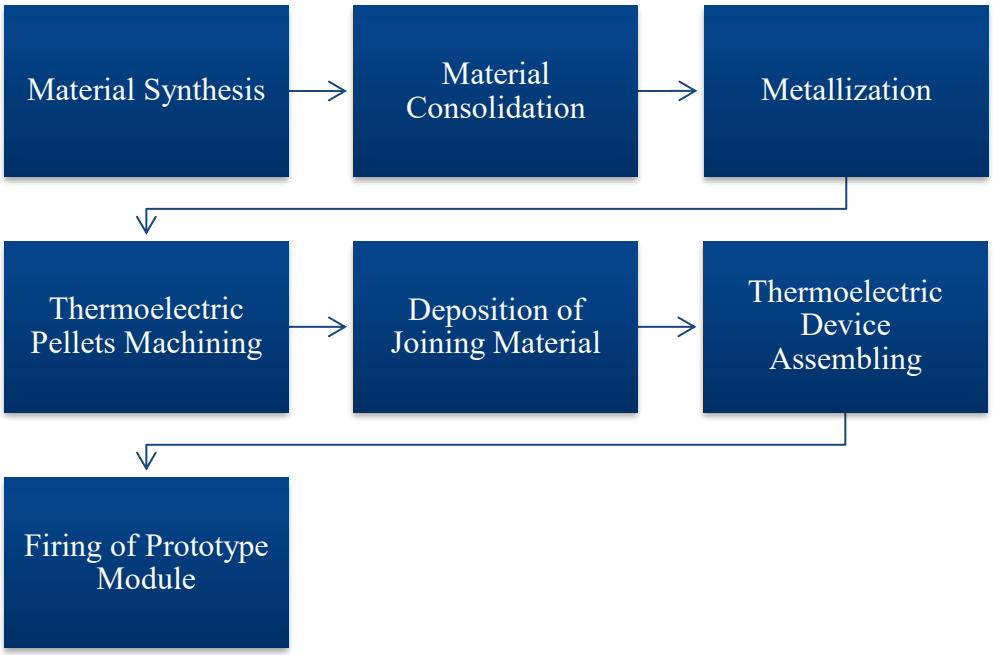

Figure 2.4-2: Sequential steps in the single stage, bulk-based thermoelectric module fabrication process.

2.4.2 Overview of Joining Technologies for Skutterudites Modules

Designing a suitable metallization and bonding technique for $CoSb_3$ - based materials is made difficult by the complex reactivity of its individual components. Antimony (Sb), to a large extent, reacts with most metals to form antimonide intermetallic compounds with a wide range of stoichiometries, with some of these compounds being mechanically brittle at room temperature. Although, a selection of metals forming antimonides of a high melting point could be employed to form a necessary reaction bond, it is difficult to limit the reactivity of antimony such that the metal electrode would not be completely consumed at a nominal operating temperature of up to 500° C through extensive interdiffusion. For that reason, thermoelectric device having improved thermo-mechanical and thermo-chemical properties without compromising the thermoelectric power and efficiency is needed, and a method of making such a device. The suitability of all chosen

thermoelectric composition, metallization layers along with interconnect and joining material are normally tested by meaning of diffusion bonded couples, isothermally aged at desirable service temperature or subjected to thermal cycling over extended period of time. Although this technique provides a useful information about the formation of reaction layer, chemical kinetics and high-temperature stability, in most cases serves only an informational purpose as it cannot be easily transferred to low-cost, industrial module assembly, i.e. due to the difficulties of co-sintering of all module elements in one process step using hot pressing or spark plasma sintering technique. Table 2.4-1 summarizes the metallization layers, contact materials and performance of contacting interfaces for published skutterudite thermoelectric materials. The majority of the implementations use copper as conductive interconnect due to its high electrical conductivity and the fact that they are commercially available as directly bonded copper (DBC) alumina substrates. Elemental copper is proven to easily diffuse and poison the braze at elevated temperatures and to avoid it, it is usually coated with protection layer, normally Ni-P amorphous alloys by simple electroless process [33], providing necessary anti-diffusion protection. Nickel plated copper clad along with brazes from Ag-Cu family are possibly the most commonly reported combination used in the fabrication of medium-high temperature range thermoelectric devices. This is caused by the suitability of Ag-Cu filler metal for lower temperature brazing (eutectic equilibrium at 779 ^{o}C [34]) and its good wettability on Ni surfaces.

Table 2.4-1: Comparison of published advanced of metallization layer for skutterudites including chosen thermoelectric material, R_C and reaction layers formed at the contacting interfaces.

Substrate	Joined materials		Characterisation of contacts		Ref.
	Interconnect, braze	Metallization	R_C ($\mu\Omega \cdot cm^2$)	Identified reaction layers	
Segmented $CoSb_3$-based (*n-type*) Segmented $CeFe_4Sb_{12}$ (*p-type*)	Nb / $Cu_{28}Ag_{72}$	No metallization; Pd and $Pd_{70}Ag_{30}$ alloy in between segments	~ 5	Not specified	[35], [36]
$CoSb_3$ (*p-type*)	Cu / $Ag_{30}Cu_{60}Sn_{10}$	Ni[a]	6.4	Not specified	[37], [38]
	Cu / $Ag_{28}Cu_{72}$	Ni[a]	5.8	-	
	Cu / $Ag_{30}Cu_{60}Sn_{10}$	Mo[a]	14.6	Not specified	
	Cu / $Ag_{30}Cu_{60}Sn_{10}$	$Cr_{80}Si_{20}$[a]	-	Not specified	
$CoSb_3$ (*p-type*)	n/a, $Ag_{60}Cu_{40}$	Co[b]	-	$CoSb_2$, CoSb;	[39]
		Ni[b]	-	Ni_5Sb_2, (Co,Ni)Sb;	
		Ti[a]	-	TiSb, $TiSb_2$, TiCoSb	

[a] Dry deposition method
[b] Wet deposition method

Table 2.4-1 (Continued)

Doped $CoSb_3$ (*n-type*)	Ti	Zr[c]	< 25	B(Zr,Ti), $ZrSb_2$	[40]
$CeFe_{4-x}Co_xSb_{12}$ (*p-type)*			-		
$CoSb_3$ (not specified)	Mo	Ti	Not specified	B(Ti,Mo)	[25]
$In_{0.4}Co_4Sb_{12}$ (*n-type*)	Cu / $Ag_{30}Cu_{60}Sn_{10}$ Cu / $Ag_{30}Cu_{60}Sn_{10}$ $Fe_{82}Cr_{18}$ / Sb	Ni-P Mo -	- - 0.18	-	[41]
$CoSb_3$ (*p-type*)	Diffusion couples	Ni	-	Ni_5Sb_2, (Co,Ni)Sb	[42], [43]
		Ni / Ti	-		
$CoSb_3$ (*p-type*)	Diffusion couples	Ti / Mo - Cu	20	TiSb, TiSb2, TiCoSb	[44], [45], [46]
$CoSb_3$ (*p-type*)	Diffusion couples	Mo / Ti	-	TiSb, TiCoSb	[47]
$CoSb_3$ (*p-type*)	Nb hot-shoe interconnect or Cu – spring loaded	Co/Ti (hot-shoe)	-	-	[48], [49]
		Co/Ti/Ni (cold-shoe)			
Heavily-doped $CoSb_3$ (*n-type*)	Nb hot-shoe interconnect or Cu – spring loaded	Ti (hot-shoe)	-	-	
		Ti/Ni (cold-shoe)			
$Yb_{0.36}Co_4Sb_{12}$ *(n-type)*	Cu / $Zn_{78}Al_{22}$	Pd	477	-	[50]

[c] Hot pressed or Spark Plasma Sintered together with thermoelectric material

Table 2.4-1 (Continued)

$Yb_{0.09}Ba_{0.09}La_{0.05}Co_4Sb_{12}$ *(n-type)*	Al / -	Mo	30	-	[26], [51]
$Mm_{0.28}Fe_{1.52}Co_{2.48}Sb_{12}$ *(p-type)*					
$Co_1Sb_{2.75}Sn_{0.05}Te_{0.2}$ *(n-type)*	Cu / $Pb_{93.5}Sn_5Ag_{1.5}$	Pd/Ni	-	-	[52], [53]
$Ce_{0.5}Yb_{0.5}Fe_{3.25}Co_{0.75}Sb_{12}$ *(p-type)*					
$CoSb_3$ *(p-type)*	-	Au	-	Not specified	[54]
		Pt	-	-	
		Ti	$16 \cdot 10^3$	Not specified	
$Yb_{0.3}Co_4Sb_{12}$ *(n-type)*	$Mo_{50}Cu_{50}$ / CuAgZn	$Ti_{88}Al_{12}$ / Ni	< 10	AlCo Co-Sb-Ti	[55], [56], [57]
$CeFe_{3.85}Mn_{0.15}Sb_{12}$ *(p-type)*		$Ti_{88}Al_{12}$ / Ni			
$CoSb_3$ *(p-type)*	W-Cu diffusion bonded	Ti	< 20	TiSb, $TiSb_2$, TiCoSb	[58]
$Yb_{0.3}Co_4Sb_{12}$ *(p-type)*	Ni diffusion bonded	Mo – Ti / Mo - Cu	< 10	TiCoSb, Ti_3Sb_2, Ti_2Sb	[59]
$Yb_{0.2}Co_4Sb_{12}$ *(n-type)*	Cu / $Ag_{50}Cu_{15.5}Zn_{15.5}Cd_{16}Ni_3$	$Al_{10}Ti_{90}$ / Cu	-	-	[60]
$Nd_{0.45}Ce_{0.45}Fe_{3.5}Co_{0.5}Sb_{12}$ *(p-type)*		$Fe_{60}Ni_{12}Cr_{28}$			

Table 2.4-1 (Continued)

$CoSb_3$ (*n-type*)	-	Ni - / un- doped $CoSi_2$ [c] Co_2Si [c]	< 1[d]	-	[61]
$(Ce_{1-z}Nd_z)_y Fe_{4-x}Co_xSb_{12}$ (*p-type*)	-	Fe–Cr–Ni [c] Fe-Cr-Co [c] Fe-Ni-Co [c]	< 10	-	
$Yb_{0.3}Ca_{0.1}Al_{0.1}Ga_{0.1}In_{0.1}Co_{3.75}Fe_{0.25}Sb_{12}$ (*n-type*) $La_{0.7}Ba_{0.1}Ga_{0.1}Ti_{0.1}Fe_3Co_1Sb_{12}$ *(p-type)*	Co-Fe-Ni alloys	Co-Fe-Ni based alloy	-	Not specified	[62], [63]
(Mm,Sm)$_y$$Co_4Sb_{12}$ (*n-type*) $DD_yFe_3CoSb_{12}$ (*p-type*)	Cu / Incusil ABA[e]	Fe-Ni [c]	~2.3 – 2.5 [d]	(Co, Ni, Fe) Sb IMCs	[64], [65]
Not specified	Al / MGs[f] of Al-Y-Ni, Al-Y-Ni-Co, Al-Y-Ni-Co-La	none	Not specified	Not specified	[66], [67]

[d] Measured at the thermoelectric / metallization interface
[e] Incusil ABA (Ag59Cu27.3Ti1.3In12.5)
[f] Metallic glass

Suitability of pure copper as an interconnect material and Ag-Cu braze for $CoSb_3$ material has been evaluated by Zybala *et al.* [35] - [36]. It was revealed that copper and Ag-Cu braze can easily diffuse into TE material despite use of thin layers of sputtered Ni, Mo and $Cr_{80}Si_{20}$ diffusion barriers, leading to formation of intermediate compounds at contacting interfaces. Additionally, due to significant Ni solubility in Ag-Cu braze alloys at service temperature [68], complete dissolution of the metallization might cause braze poisoning or the formation of undesired reaction layer and finally leads to crack propagation. The need for suitable diffusion barrier on skutterudite-based thermoelectric material was also proved by Chen *et al.* [39]- [43]. Although, $Ag_{60}Cu_{40}$ braze with a liquidus temperature of 779.1 ^{o}C has been proven to exhibit a good wetting on un-coated $CoSb_3$ substrates, lack of additional metallization layer has led to a full copper dissolution into the thermoelectric during the isothermal ageing at 600 ^{o}C, within 3 days only. Among many different metallization and interconnects reported, pure elements including those of transition and refractory metals, are the most commonly explored with variety of TE materials, i.e. Bi_2Te_3 and Sb_2Te_3 [69] and $MgSi_2$ [70] - [71]. Different forms of nickel (such as elemental material or Ni-based amorphous alloys) are being intensively used as a metallization in semiconductors industry as an effective diffusion barrier on copper (due to their high mutual solubility in all concentration range [72]) and are often used as a cold-side metallization of skutterudite-based thermoelectric material [42] due to the close matching of CTE (~13 ppm/K) to the Co-based skutterudites (*p-type* ~ 11 ppm/K and *n-type* ~9 ppm/K) [20]. Nonetheless, high-temperature reactivity makes nickel not desirable for hot-side contacts due to intensive formation of Ni_5Sb_2 and (Co,Ni)Sb reaction layers at minimum temperature of 450 ^{o}C with the reaction rate of approximately 1μm/hour [43]. Such an extensive interfacial

reaction might lead to the reduced temperature stability of any *p-type* hole conducting skutterudite material as nickel easily substitute Co and Fe sites as a doping element, changing semiconductor properties to the *n-type* electron conduction.

Pure nickel and titanium are proven to be not efficient diffusion barrier for skutterudites as they both extensively react with antinomy to form IMCs [42], [43]. W. Chen *et al*. performed a preliminary research on formation kinetics when nickel has been used as a diffusion barrier on $CoSb_3$-based thermoelectric material. According to the experimental findings, elemental nickel is one of the fastest known diffusion elements when contacted with skutterudites with an average growth rate of 1 μm/hour and it is not recommended to use it in direct contact with that material. The reliability of contacts highly depends on compatibility of not only adjusting layers, but also intermetallic compounds formed at interfaces as they are more likely to be the cause of a failure due to their low ductility at room temperature. Moreover, two mechanisms induced by thermal residual stresses, such as volumetric change, associated with the phase transformation at the interface, and CTE mismatch of these intermediate phases can have significant effect on the mechanical stability of such contact. Despite their relatively high electrical resistivity (as compared to that of pure copper) and lack of oxidation resistance, elemental titanium and zirconium have also been intensively investigated as a possible hot-leg metallization on *p-* and *n-type* skutterudite thermoelectrics [40]. Although no visible reaction layer is formed after the joining process, three different intermediate phases can be found at the Ti / $CoSb_3$ interface, i.e. TiSb, $TiSb_2$ and TiCoSb intermediate compounds and are identified as a reason for crack formation at high service temperature (as determined by the isothermal ageing at 625 ºC and presented in Figure 2.4-3) [44–

46,58,73]. Fundamental research on the high-temperature physical properties of MSb_2 (where M = Ti, Zr, Hf) which are intermediate phases formed between $CoSb_3$-based materials and elements of Group 4 (d-block) from the periodic table was conducted by Tavassoli *et al* [74]. They revealed that the CTE of $TiSb_2$ (~ 12.9 ppm/K) is similar to the average value of Co-based *p-type* skutterudites (~ 11 ppm/K), whilst the CTE of $ZrSb_2$ (~ 9.7 ppm/K) and $HfSb_2$ (~ 10.1 ppm/K) are better match to Co-based *n-type* skutterudite materials (~ 9 ppm/K).

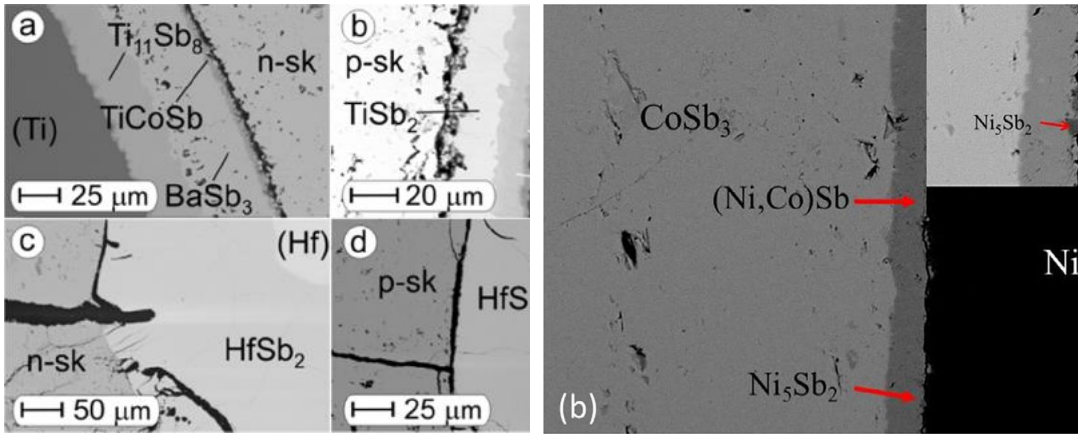

(2.4-3.1) **(2.4-3.2)**

Figure 2.4-3: Interfaces formed using various transition metals at the skutterudite-based thermoelectric material including 2.4-3.1 diffusion zones formed by (a,b) Ti and (c,d) Hf with (a,c) $Ba_{0.3}Co_4Sb_{12}$ *n-type* skutterudite and (b,d) $Mm_{0.75}Fe_3CoSb_{12}$ (*Mm* – mischmetal, La, Ce, Pr, Nd) *p*-type thermoelectric (reprinted from Ref. [74]), 2.4-3.2 Ni – $CoSb_3$ interface isothermally aged at 448 ^oC for 5 hours reprinted from Ref. [43].

Moreover, thermal and electrical performance of intermediate phases at the reaction layer has been proven to be sufficient (such as metallic behaviour with slightly p-type conduction) and will not hamper electric and thermal heat flows in the contact zones. Although, physical and mechanical matching of thermoelectric material, titanium electrode and intermediate intermetallic phase might seem enough to keep the continuous interface at high-temperature service, an extensive

crack formation in the $CoSb_3$ / Ti / Mo-Cu contacts will presumably cause device failure with predicted life-time at the hot-leg temperature of about 500 ^oC is approximately 7 years in the approach presented in the Ref. [44]. Recently, several groups have introduced Fe-Ni low-expansion alloys as a diffusion / metallization layer on skutterudite-based thermoelectric substrates (as seen in Figure 2.4-4). The Ni-Fe family alloys include Fe-Ni-Co alloys of the 'Kovar' type, Fe-Ni alloys of the 'Invar' type and Fe-Ni-Cr. These alloys have low expansion characteristics as a result of a balance between thermal expansion and magnetostrictive changes with the temperature and are often used as effective glass-to-metal seals. Ni-based alloys (including one of Cr-Fe-Co, Fe-Ni-Co and Cr-Fe-Ni alloys) were successfully used as contact materials for $(Ce_{1-z}Nd_z)_y Fe_{4-x}Co_xSb_1$ *p-type* skutterudite thermoelectric [61]. The double-filled skutterudite material has matching thermal expansion coefficient with these alloys and the close matching electronic work function difference of the contact and the thermoelectric material (with 10% - 15% variation) resulting in formation of electrical contact resistance (of ~ 0.4 $\mu\Omega \cdot cm^2$). In that research [61], powder metallurgy process was involved in the contact preparation by ball-milling of pure elemental powders, hot-pressing at 700 ^oC for 5 minutes and hot-pressing with thermoelectric material in the separate consolidation step. Although, metal foils are not recommended for co-sintering with thermoelectric powder as they normally delaminate upon cooling, they are a reasonable substitute for the powder as they face many challenges. As described by Jie *et al.* [61], Ni-based powder alloys when co-pressed with thermoelectric material at a temperature much lower than melting temperature, no more than 85% of their theoretical density can achieved transferring to lower than expected thermal and electrical conductivities. In a similar approach, Fe-Ni alloys were successfully implemented as an effective

diffusion barrier on both $(Mm,Sm)_yCo_4Sb_{12}$ *n-type* and $DD_yFe_3CoSb_{12}$ *p-type* skutterudite materials [64,65]. Despite low $R_{c,E}$ of ~ 2.3-2.5 μΩcm^2 measured on the SKD / Fe-Ni metallization interface, a reaction layer of ~ 14–17 μm-thick IMCs was observed and proven to be thermally stable after isothermal ageing at 500 ºC for 10 h in a vacuum (~10^{-3} Torr) (Figure 2.4-4b).

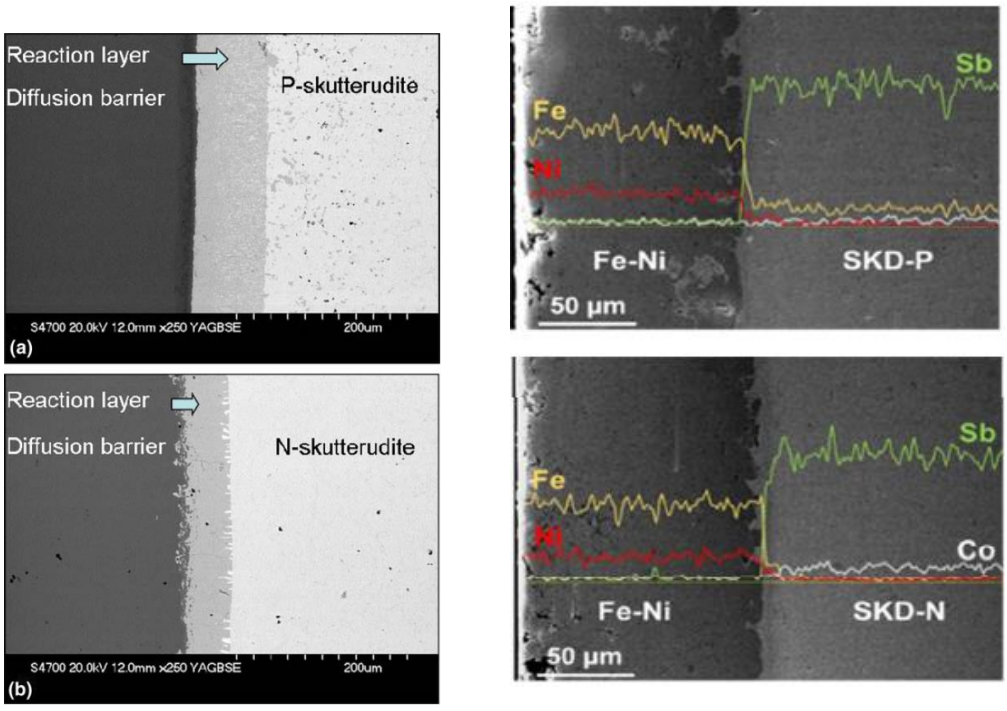

(a) **(b)**

Figure 2.4-4: SEM images of interfaces between *p*- and *n-type* skutterudites along with **(a)** Co-Fe-Ni based diffusion alloys after annealing at 600 ºC for 770 hours in vacuum reprinted from Ref. [62] and **(b)** Fe-Ni metallization layers annealed at 500 ºC for 10 hours in vacuum reprinted from Ref. [64].

Another interesting concept has been also introduced by Jie et al. [61] where transition-metal silicides were successfully implemented as diffusion barriers on *n-type* skutterudite-based thermoelectrics. Due to match of thermal expansion coefficient of *n-type* skutterudite-based thermoelectric material to cobalt silicides – three different configurations have been implemented including $CoSi_2$, Co_2Si and/or doped $CoSi_2$ (preferably Co, Fe, B and Ni).

2.4.3 Overview of Skutterudites Thermoelectric Generators

While many alternative thermoelectric module designs have been proposed in recent years, thus far single-stage and bulk-based thermoelectric module working in the low temperature regime are available on the market. Commonly used low-temperature TE materials, i.e. Bi_2Te_3 and Sb_2Te_3 are utilized in the commercially available thermoelectric devices for both cooling and generation applications since the electrical contacts can be easily fabricated using well-established methods, *i.e.* using lead-free solders (such as SnAgCu – based alloys 'SAC') with a Ni metallization layer [75]. SAC alloys and Pb-based solders have a melting point in the range of 180 ºC – 300 ºC and can also be used as a joining material on the cold-leg of the high-temperature thermoelectric module due to their high reliability and respectable wetting on both metallic and non-metallic interfaces. Nonetheless, the fabrication of stable junction between the electrode and the hot side of medium-high temperature range thermoelectric material (i.e. skutterudites, silicides, or TAGS) is a very challenging task and is the subject of number of ongoing scientific and industrial research. Conventional high-temperature module fabrication is often limited by the relatively large number of processing steps needed for a final prototype development. This has motivated a number of new joining approaches in recent years, including the use of diffusion bonded, brazed or mechanically stabilized contacts.

Over the past decades, little has been reported on development of medium and high temperature thermoelectric modules utilizing skutterudite, half-Heusler or silicide-based materials. Although, skutterudite compounds are characterised with unique, long-term thermoelectric stability [21], their reliability is often limited by the lack of robust contact technology, stable in harsh working environment. Thermoelectric–interconnect contacts are normally formed by furnace brazing of

the entire prototype assembly using metal-alloy braze, which when in the paste form is deposited on the top of conductive substrate. The joining material such as braze, to be compatible with the substrate, must have a liquidus temperature (*Tbrazing*) below the melting point of all the components making the TE module. In the particular case of skutterudite compounds, a relatively low decomposition temperature (T_{TE} *decomp*) of approx. 870 ºC and lack of material stability above the 575 ºC (due to the antimony sublimation [76]) limits the choice of suitable braze flowing at such low temperatures. Moreover, medium-high temperature thermoelectrics require a braze filler metal with solidus temperature above the hot-side device operation temperature (T_H) and below the stability temperature of thermoelectric material (T_{TE} *decomp*). Such a narrow brazing window (T_H « *Tbrazing* « T_{TE} *decomp*) limits the choice of braze to only a few commercially available filler metals which might be used in the fabrication of such thermoelectric modules. The majority of braze combinations reported in the literature include Ag-Cu family such as $Cu_{28}Ag_{72}$ [35,36], $Ag_{30}Cu_{60}Sn_{10}$ [37,38], $Ag_{60}Cu_{40}$ [39], $Zn_{78}Al_{22}$ [50] and $Ag_{59}Cu_{27.3}Ti_{1.3}In_{12}$ (Incusil-ABA) based alloys. Although, brazing is the most common joining technique utilized in the thermoelectric module fabrication, it has many disadvantages due to the need of aggressive flux and reduced creep strength at elevated temperature [77].

The solid-state diffusion bonding has been also utilized in the direct fabrication of electrical contacts without a need for temperature-limited brazing filler metals. During the hot pressing of interconnect material, metallization layer and thermoelectric material (usually alloy powder) at one processing step, atomic interdiffusion across the interface leads to the mixing of constituent elements and creates a strong chemical bonding between them. In essence, the diffusion barrier and metallic interconnects are chosen accordingly to their chemical potential

energy of mixing to promote solid-state diffusion between them as they should be at least partially soluble in each other and remain in the solid state at temperatures above the joining temperature. One of the proposed techniques exploits eutectoid reaction between molybdenum and titanium at 695 ºC [25] as they are completely miscible and do not form brittle intermetallic compounds (IMCs) [78] in all concentration range. Another possible solid-state, diffusion bonding process exploits the eutectoid reaction between titanium – niobium and zirconium – titanium [22]. A list of published skutterudites thermoelectric modules with their performance is given in Table 2.4-2. Additionally, hot-side contacts are suffering in high extend from the thermally induced stresses during the high temperature service. Even when the linear thermal coefficient of all elements in the stack are compatible with each other, ceramics substrate on the hot-side is normally highly mismatched with the rest of the embodiment [79,80]. Options that have been explored and implemented at high temperature thermoelectric include double-sided, direct bonded copper (DBC) ceramics, no rigidly joined ceramics at the hot side, or different types of mechanical clamping [81].

Furthermore, the state-of-the-art skutterudite materials are sensitive to oxidation and might suffer from the moisture and oxygen presence even in the hermetically sealed converter designs. The vast majority of Sb-rich thermoelectric materials suffer from high-temperature instabilities as antimony sublimates near the hot-temperature junctions during the high temperature operations and brazing process. A protective coating was proven to suppress the Sb sublimation and most reported solutions includes metallic coating on the legs near the hot junction [82], aerogel encapsulation [83] and hermetic encapsulation under the argon cover gas.

Table 2.4-2: Summary of various reported BOL (beginning-of-life) data for non-segmented, Skutterudite-based thermoelectric modules operating at medium-high temperature range.

Assembly parameters			**Characterization of TEM**				
TE material	**Design**	**Interconnect, metallization and braze**	P_{OUT} **(at** ΔT**) [W]**	**Module** η **(at** ΔT**) [%]**	**Power density per module (at** ΔT**) [W/cm^2]**	$R_{TEG,E}$ **(at** ΔT**) [mΩ]**	**Ref.**
$(Mm,Sm)_yCo_4Sb_{12}$ (*n-type*) $DD_yFe_3CoSb_{12}$ (*p-type*)	8 couples, 4 x 4 x 4 mm TE legs	Alumina –DBC, Fe-Ni, Incusil	8.1 (297 ºC)	-	2.1 (297 ºC)	42 (RT)	[64]
$Yb_{0.09}Ba_{0.09}La_{0.05}Co_4Sb_{12}$ (*n-type*) $Mm_{0.28}Fe_{1.52}Co_{2.48}Sb_{12}$ (*p-type*)	7 couples, 16 x 16 mm module	Alumina -DBC	1.4 (428 ºC)	8 (480 ºC)	0.74 (530 ºC)	95 (-)	[84], [85]
$Yb_{0.15}Ba_{0.1}Co_4Sb_{12.12}$ (*n-type*) $Mm_{0.9}Fe_{3.5}Co_{0.5}Sb_{12.12}$ (*p-type*)	8 couples, 19 x 39 mm module, no hot-side substrate	Alumina – DBA / - /AlSi	2.13 (352 ºC)	-	0. 57 (352 ºC)	23.2 (352 ºC)	[86]
$CoSb_3$	48 couples, Solid vacuum encapsulation	Si_3N_4 – DBC	7 (461 ºC)	4.1 (461 ºC)	-	-	[87]

Table 2.4-2 (Continued)

$Yb_{0.09}Ba_{0.09}La_{0.05}Co_4Sb_{12}$ (*n-type*) $Mm_{0.28}Fe_{1.52}Co_{2.48}Sb_{12}$ (*p-type*)	32 couples, 50 x 50 mm module, aerogel-encapsulated	Alumina - DBA	8 (470 ºC)	-	0.32 (470 ºC)	180 (420 ºC)	[51]
$Yb_{0.09}Ba_{0.09}La_{0.05}Co_4Sb_{12}$ (*n-type*) $Mm_{0.28}Fe_{1.52}Co_{2.48}Sb_{12}$ (*p-type*)	32 couples, 50 x 50 mm module, aerogel-encapsulated	Alumina – DBA / Mo / -	11.5 (460 ºC)	7.5 (460 ºC)	0.46 (460 ºC)	145 (RT)	[26]
$Yb_{0.3}Ca_{0.1}Al_{0.1}Ga_{0.1}In_{0.1}Co_{3.75}Fe_{0.25}Sb_{12}$ (*n-type*) $La_{0.7}Ba_{0.1}Ga_{0.1}Ti_{0.1}Fe_3CoSb_{12}$ (*p-type*)	32 couples, 50 x 50 mm module	Co-Fe-Ni / Co-Fe-Ni / -	32 (550 ºC)	8 (550 ºC)	1.28 (550 ºC)	-	[62], [63]
$(Yb,Ca,Al,Ga,In)_{0.7}Co_{3.75}Fe_{0.25}Sb_{12}$ (*n-type*) $(La,Ba,Ga,Ti)_{0.9}Fe_3CoSb_{12}$ (*p-type*)	32 couples, 50 x 50 mm module	Copper / not specified / -	25 (550 ºC)	7.2 (550 ºC)	1 (550 ºC)	-	[88]
$Yb_{0.36}Co_4Sb_{12}$ (*n-type*) $Ce_{0.8}Fe_3CoSb_{12}$ (*p-type*)	9 couples, 16 x 13 mm module	Alumina – DBC / Pd / $Zn_{78}Al_{22}$	0.157 (365 ºC)	-	0.075 (365 ºC)	700 (365 ºC)	[50]

Table 2.4-2 (Continued)

$Co_1Sb_{2.75}Sn_{0.05}Te_{0.2}$ (*n-type*) $Ce_{0.5}Yb_{0.5}Fe_{3.25}Co_{0.75}Sb_{12}$ (*p-type*)	9 couples, 16 x 13 mm module	Alumina – DBC / Pd and Ni multi-layer / Pb93.5Sn5Ag1.5 solder	1 (300 ºC)	3 (273 ºC)	0.48 (300 ºC)	~ 85 (300 ºC)	[52], [53]
$Ba_{0.05}Yb_{0.15}Co_4Sb_{12}$ (*n-type*) $Ce_{0.9}Fe_{3.5}Co_{0.5}Sb_{12}$ (*p-type*)	3 couples, 7.45 x 12 mm module	-	0.035 (300 ºC)	7.8 (300 ºC)	0.039 (300 ºC)	500 (-)	[89]
$Yb_{0.27}Co_4Sb_{12}$/0.72 vol% rGo (*n-type*) $Ce_{0.85}Fe_3CoSb_{12}$/1.4 vol% rGo (*p-type*)	8 couples, 20 x 20 mm module	Mo50Cu50 / Ti-Al alloy / CuAgZn braze	3.8 (577 ºC)	8.4 (577 ºC)	0.95 (577 ºC)	-	[90], [57]
$Yb_{0.2}Co_4Sb_{12}$ (*n-type*) $Nd_{0.45}Ce_{0.45}Fe_{3.5}Co_{0.5}Sb_{12}$ (*p-type*)	4 couples, 52 mm^2 module, graphite spray	Alumina – DBC / $Al_{10}Ti_{90}$ / Cu / AgCuZnCdNi Alumina – DBC / $Fe_{60}Ni_{12}Cr_{28}$ / AgCuZnCdNi	1.18 (450 ºC)	-	2.38 (450 ºC)	2.1 (RT)	[60]

Table 2.4-2 (Continued)

$Yb_{0.25}Co_4Sb_{12}$ /Yb_2O_3 (*n-type*) $Ce_{0.45}Co_{2.5}Fe_{1.5}Sb_{12}$ (*p-type*)	2 couples	Mo-Cu (hot-shoe) / Mo / Ag-Cu braze (hot-shoe)	0.14 (490 ºC)	6.4 (490 ºC)	-	23 (490 ºC)	[73]
$CoSb_{2.75}Sn_{0.05}Te_{0.2}$ (*n-type*) $Ce_{0.5}Yb_{0.5}Fe_{3.25}Co_{0.75}Sb_{12}$ (*p-type*)	9 couples, 16 x 13 mm module	Alumina – DBC / Pd / Ni / $Pb_{93.5}Sn_5Ag_{1.5}$	1.85 (448 ºC)	~3 - 4 % (362 ºC)	0.9 (448 ºC)	102 (RT)	[91]

Thermoelectric modules have been in use for more than four decades in the radioisotope thermoelectric generators (RTGs), particularly for the space (i.e. in the Multi-mission Radioisotope Thermoelectric Generator – MMRTG [92]. The silicon germanium (*i.e.* boron doped *p-type* and phosphorous doped *n-type*) segmented unicouples operating at T_H temperatures of 902 – 1000 ºC have been used in the spacecraft powered by RTGs, converting the heat to electricity with efficiencies of < 7% [93]. The first attempt at the use of skutterudite-based thermoelectric module in the power generation application was by the JPL/CalTech team, where a number of segmented thermoelectric unicouples made of $CeFe_4Sb_{12}$ and Bi_2Te_3-based *p-type* legs along with $CoSb_3$ and Bi_2Te_3-based *n-type* legs was designed for high-temperature operation at hot and cold side temperature of 27 ºC and 702 ºC respectively, with predicted thermal to electrical conversion efficiency of up to 15%. Recently, new enhanced MMRTG (eMMRTG) system is expected to replace a PbTe *n-type* and a segmented PbSnTe/TAGS-85 *p-type* with high-performance $Ce_y(Fe,Co)_3Sb_{12}$ *p-type* and $(Yb,Ba)_yCo_3Sb_{12}$ *n-type* skutterudite-based thermoelectric materials in the RTG as a power source in the Mars 2020 rover with conversion efficiency up to ~6.3% at beginning of life (Figure 2.4-5).

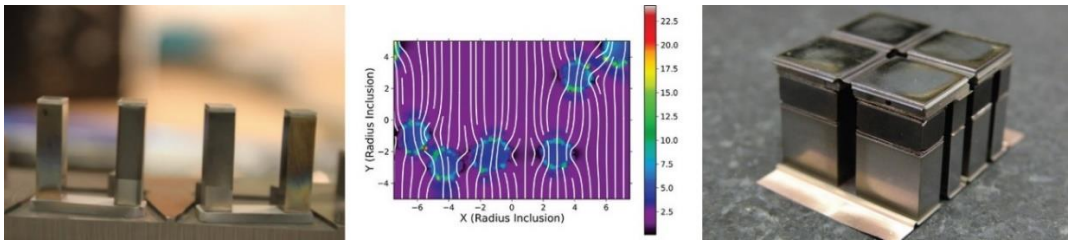

Figure 2.4-5: Left: The skutterudites unicouples used in the eMMRTG. Center: Monte Carlo simulation of heat flow across composite TE material with metal inclusions. Right: High-temperature segmented thermoelectric module. Reprinted from Ref. [94].

Chapter 3

Materials and Methods

In this research, thermoelectric device fabrication involving a number of process steps was developed in collaboration between European Thermodynamics Ltd. (Leicester, UK), Politecnico di Torino (Turin, Italy), University of Rennes 1 (Rennes, France) and Nanoforce Technology Ltd. (London, UK). In Chapter 3.1, a detailed description of the thermoelectric module design, materials synthesis, module fabrication and characterization techniques are presented. In the first step reported in Chapter 3.1, the proposed design of the module is described in detail. In Chapter 3.2, description of material's sintering process is presented as commercially available thermoelectric materials were subjected to an in-situ synthesis using Spark Plasma Sintering (SPS) process performed by Nanoforce Technology Ltd, London, UK. In the electric current assisted sintering, both formation of the Skutterudite phase and bulk consolidation occur during the one-step process. This technique is commercially applicable and cost-effective as it shortens time-consuming synthesis of the thermoelectric material to few minutes only. As-prepared thermoelectric material was fully characterized by testing its high temperature performance including Seebeck coefficient (α), electrical and thermal conductivity (σ and κ) measurements by Nanoforce Technology Ltd,

London, UK. Additionally, pre-alloyed elemental powders and sintered thermoelectric materials were subjected to additional testing including X-Ray Diffraction (XRD) and Scanning Electron Microscope (SEM) microstructural observations performed at the Politecnico di Torino, Turin, Italy. Characterization techniques are described in detail in Chapter 3.2. Afterwards, thermoelectric materials were delivered to European Thermodynamics Ltd. in the form of consolidated, bulk discs and processed further in the thermoelectric prototype fabrication. This included deposition of metallization layer using different techniques namely electroless nickel-phosphorous electroless plating, Physical Vapor Deposition (PVD) and co-sintering of metallic foils with thermoelectric material as described in Chapter 3.3.1, Chapter 3.3.2 and Chapter 3.3.3. The co-sintering technique was performed using Spark Plasma Sintering equipment in Nanoforce Technology Ltd., London, UK and University of Rennes 1, Rennes, France. Thermoelectric legs were cut to desirable size, assembled and joined using three different bonding techniques including conventional brazing, low-temperature Ag-based particles bonding and brazing also called Solid-Liquid Interdiffusion (SLID) bonding. It should be noted that majority of the research is focused on the interfacial investigation at the interconnect–thermoelectric contacts as the comprehensive literature research (presented in Chapter 2) highlighted that these are particularly vulnerable to high-temperature instabilities. Chapter 3.4 presents samples preparation and configuration for the interfacial investigations further characterized in terms of their electrical transport properties and high-temperature chemical stability described in Chapter 3.6. The prototype module preparation is described in the detail in Chapter 3.5. The high-temperature thermoelectric prototype characterization technique is described in Chapter 3.7.

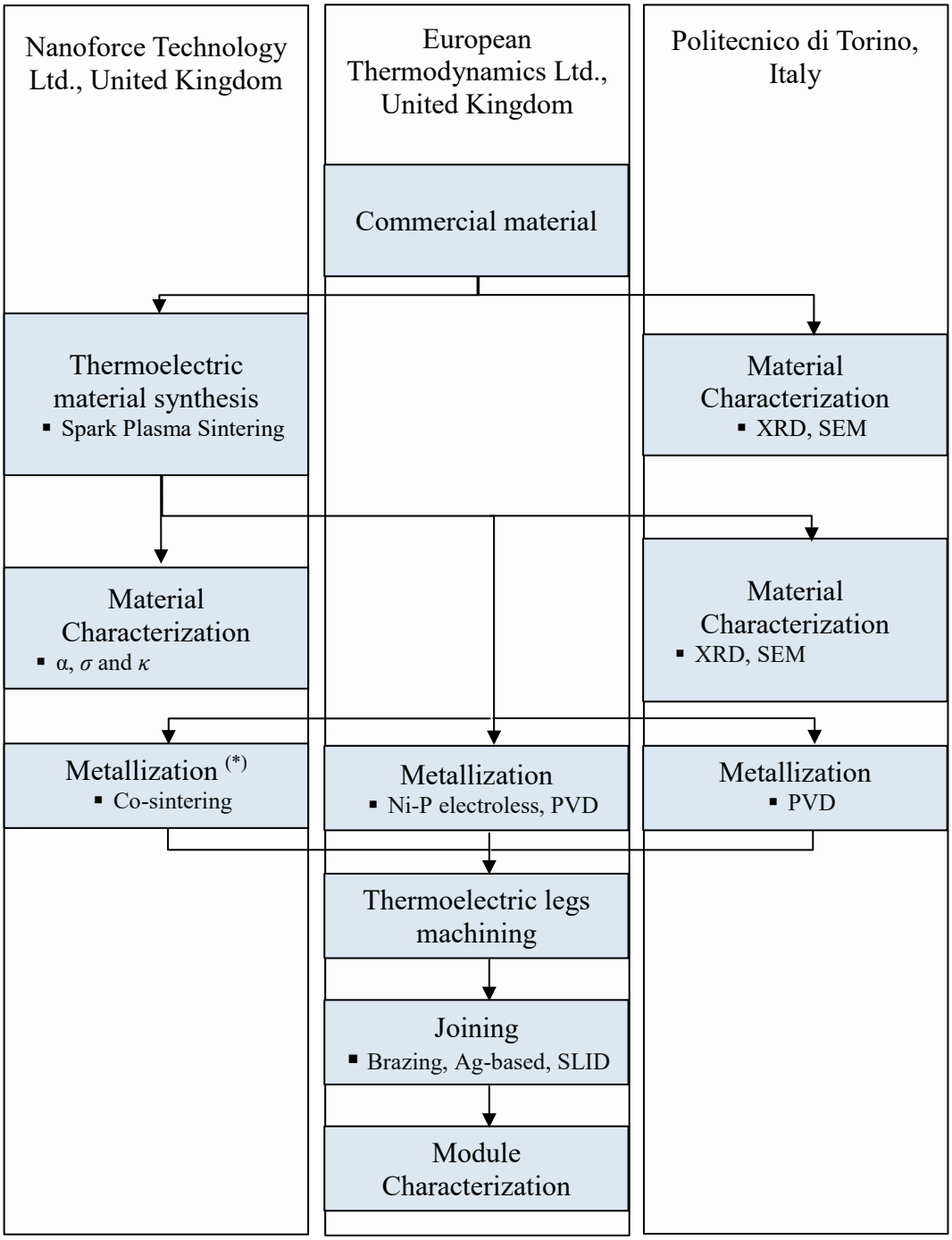

Figure 3: Schematic flowchart with sequential steps used to develop thermoelectric prototype module in this research including partners involved in this research. (*) This part was performed in collaboration with University of Rennes 1 (UR1) in Rennes, France.

3.1 Proposed Thermoelectric Module Design

The conventional, single stage, bulk thermoelectric module design, comprises *n*- and *p-type* semiconductor legs assembled between two partly metallized ceramic plates such that they are electrically connected in series and thermally in parallel. The ceramic plates, forming an electrical insulation between both to the heat source and sink (T_H and T_C) were monolithic alumina plates (Al_2O_3) with direct bonded copper (DBC) interconnects used on the both sides of the thermoelectric module. This design means that CTE mismatches between the copper and ceramic do not result in distortion of the ceramic plate, reducing thermal stresses during the module high temperature service. Schematic drafts of bottom and top DBC alumina substrates used in the prototype fabrication can be seen in Figure 3.1-1. Moreover, ceramic substrates with direct bonded copper (DBC) clads were subjected to Ni-P plating process, by meaning of wet, chemical routes as additional nickel-based diffusion barrier on copper is usually needed in electronic application to reduce joining material poisoning. The resulting Ni-P thickness was normally > 5 μm. Preliminary simulations revealed that by using thermoelectric legs with 2.5 x 2.5 x 3 mm geometries the highest possible power output can be achieved. More information regarding the module optimization can be found in Chapter 5 and Appendix D, Figure D. 1. All elements were implemented in a 7-couple thermoelectric module design sufficiently large for accurate module level measurements. Schematic illustration of the prototype thermoelectric module was presented in Figure 2.3-1a.

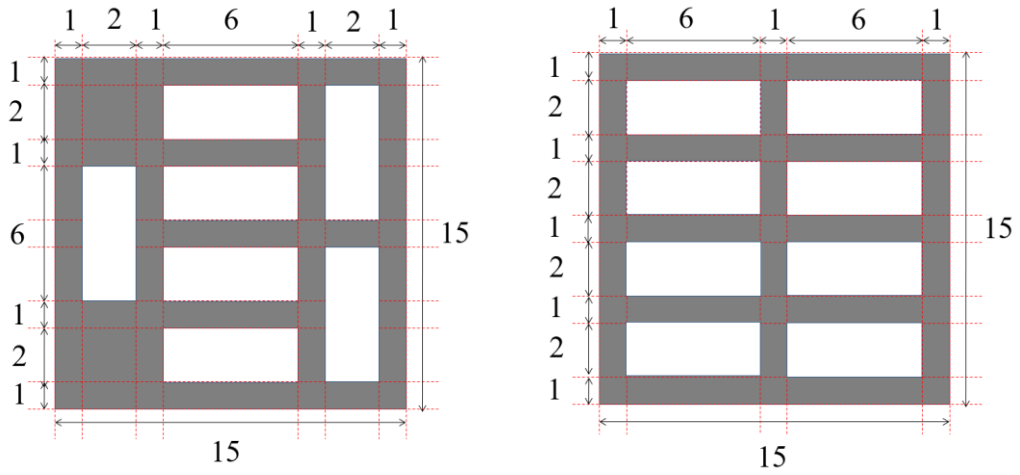

(a) **(b)**

Figure 3.1-1: Schemtic draft of (a) bottom and (b) top direct bonded copper (DBC) alumina (Al_2O_3) sustarates used in the prototype fabrication. Note: white rectangles represent DBC interconnects, grey rectangles represent Al_2O_3 substrate. All given dimensions are in mm. Thickness of DBC interconnect and alumina substrate were 0.03 mm and 0.3 mm, respectively. Courtesy of European Thermodynamics Ltd.

3.2 Thermoelectric Material Fabrication

In this work, polycrystalline materials with nominal composition of $Mm_{0.9}Fe_3Co_1Sb_{12}$ (*Mm* – Mischmetal, i.e. 50 at. % Ce, 25 at. % La) *p-type* and $Ni_{0.15}Co_{0.85}Sb_3$ *n-type* thermoelectrics were synthesized using commercial, pre-alloyed (*via* high energy ball milling (HEBM) process) powders (MATRES s.c.r.l., Italy, 99.995% purity). *In-situ* synthesis was performed by placing 42g of powder inside an Ø40 mm graphite die and sealed with two graphite punches from the top and bottom. To uniformly distribute heat and forces along sintered material, graphite sheet (Erodex, UK) was placed between the punch and thermoelectric material as depicted in Figure 3.2-1a. The *in-situ* synthesis was carried out in the SPS apparatus (FCT HPD25, Rauenstein, Germany) by applying uniaxial pressure of 50 MPa at the peak temperature of 600 ºC and 750 ºC for *p-type* and *n-type* material respectively, and held for 5 min. The material was sintered by Nanoforce Technology Ltd, London, United Kingdom. Figure 3.2-1 presents the temperature and applied pressure distribution during the sintering of $Mm_y(Fe,Co)_4Sb_{12}$ *p-type* and $Ni_xCo_{1-x}Sb_3$ *n-type* thermoelectric materials, respectively. The consolidation process was performed under a vacuum (3 mbar) with heating and cooling rates of 50 ºC/min and as-resulted discs were of > 95 % theoretical density as determined by the Archimedes principle. The Spark Plasma Sintering process is accomplished by applying high amperage pulsed direct current through the metallic electrodes at the top and bottom punches of the graphite die and spacers as depicted in Figure 3.2-1a. The heating process was established by applying the direct current of approx. 2500 A at a voltage of approx. 5 V until the sintering temperature was reached. The die temperature was measured using an optical pyrometer focused on the top of punch through a small

hole inside the graphite die. Afterwards, the thermoelectric material was ground to 3 mm-thick discs using 320-grit diamond wheel and cleaned using IPA in the ultrasonic bath.

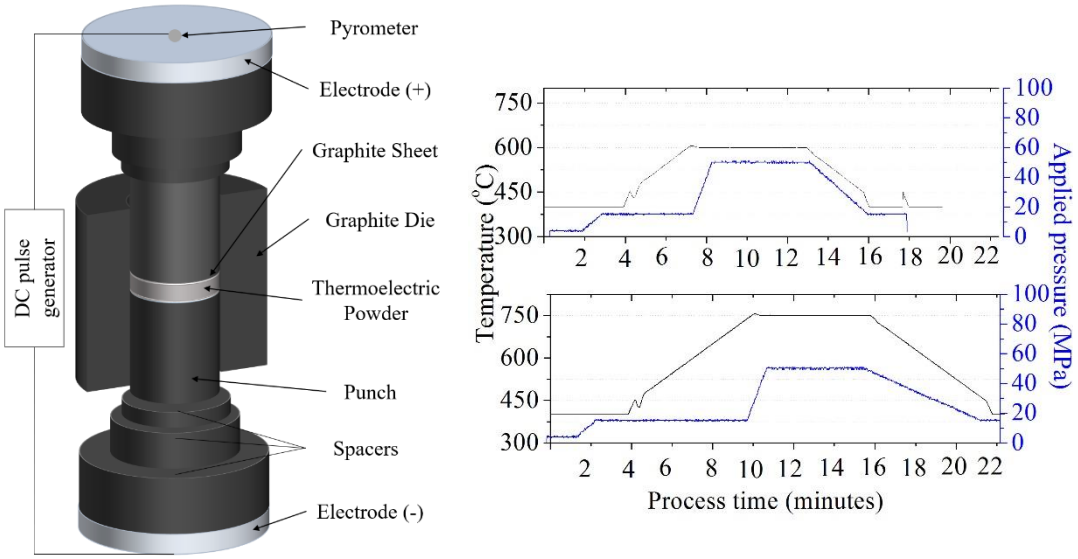

(a) **(b)**

Figure 3.2-1: (a) Cross-sectional schematic of the graphite used in Spark Plasma Sintering (SPS) set-up and **(b)** sintering profiles with temperature and force distribution during the synthesis of $Mm_y(Fe,Co)_4Sb_{12}$ *p-type* (top graph) and $Ni_xCo_{1-x}Sb_3$ *n-type* (bottom graph) thermoelectric material.

3.2.1 X-Ray Analysis

X-ray diffraction (XRD) data for thermoelectric materials were collected using a Bruker D8 Advance Powder X-ray diffractometer, operating with Ge monochromatic Cu $K_{\alpha 1}$ radiation (λ=1.54046 Å) and fitted with a LynxEye detector. Data were collected over the angular range $20 \leq 2\theta/^{o} \leq 80$ for 15 minutes.

3.2.2 SEM-EDS Microstructural Analysis

For the microstructure observation, specimens were mounted in conductive resin, mechanically ground with abrasive papers and polished using 1/4 μm diamond suspension. The high-resolution field emission gun scanning electron microscope (FEGSEM, 1530VP Zeiss GmbH, Germany) with 80 mm^2 energy dispersive X-Ray spectroscopy detector (Oxford Instruments, UK), operating at a voltage of 20 kV under high vacuum was used. Microstructural analysis was performed in secondary electron (SE) and back-scattered electron (BSE) mode while Aztec EDS/EBSD microanalysis software was used to reveal existing phases in at least 5 different regions.

3.2.3 Electrical and Thermal Transport Measurements

The electrical resistivity (ρ) and Seebeck coefficient (α) were measured simultaneously on 3 mm-thick discs (Ø10 mm) using Linseis LSR-3 (ZEM-3, Ulvac, Inc.) equipped with Pt thermocouples and electrode probes. The measurement was performed in the temperature range from 25 ^oC to 550 ^oC in 25 ^oC step under partial pressure of He.

The laser flash method (LFA 457, Netzch Co. Ltd., Selb, Germany) has been used to measure thermal diffusivity (D_T) of sintered materials over the temperature range of 25 ^oC to 550 ^oC under the Ar flow. In order to enhance the heat absorption, graphite was sprayed on the both side of the measured thermoelectric material. The total thermal conductivity (κ) has been calculated using Equation 16:

$$\kappa = D_T \cdot C_p \cdot \rho \qquad 16$$

Where density (ρ) is measured using Archimedes' principle and specific heat capacity (C_p) has been calculated using the Dulong–Petit law.

3.3 Contact Layer Fabrication

As presented in Figure 2.3-1a, conventional thermoelectric unicouple metallization consists of adhesion promoter, diffusion barrier and top metallization layer. To achieve the goal of this thesis, different contact materials and layers configuration were developed and are presented here. Three different deposition / contacting technologies were used for metallization layer fabrication including:

1. Electroless Ni(P) plating described in Chapter 3.3.1;
2. Physical Vapor Deposition (PVD) described in Chapter 3.3.2;
3. Co-sintering with thermoelectric material by Spark Plasma Sintering described in Chapter 3.3.3.

3.3.1 Ni-P Electroless Plating

As-prepared discs of $Mm_y(Fe,Co)_4Sb_{12}$ *p-type* and $Ni_xCo_{1-x}Sb_3$ *n-type* thermoelectric materials were subjected to commercially available plating processes to achieve Ni-based coating on skutterudite material [95,96]. The deposition process consisted of two-step coating by meaning of electrolytical Ni and electroless Ni-P deposition routes. A seed layer of electrolytical Ni was directly deposited on skutterudites as Ni(P) layer was expected to suffer from poor adherence on the un-treated substrate. A Wood's nickel strike solution comprising of $NiSO_4 \cdot 6H_2O$ and 12M HCl electrolyte solution was used in electrolytic Ni plating process to deposit a seed layer on the surface of the thermoelectric material by passing current with a density of 5 A/dm^2 for 2 min. Afterwards, thermoelectric materials were immersed in electroless nickel plating bath comprising 45 wt% $NiSO_4 \cdot 6H_2O$, 25 wt% $NaPO_2H_2 \cdot H_2O$ and 1 wt% $NH_3 \cdot H_2O$

(CASWELL Inc, US) for 45 minutes. The bath temperature was kept at 95 ºC during the deposition process and deionized water was occasionally added to compensate the evaporation losses. The electroless nickel plating process with a phosphorous content of 10 wt% resulted in the nickel – phosphorous Ni(P) amorphous coating layer.

Table 3.3-1: Process sequence of the electroless nickel and electroless nickel immersion gold (ENIG) plating process on copper substrates.

Seq.	Process	Composition	Temperature (ºC)	Time (min)	Notes
1	Soak Cleaning	H_2SO_4, <10 wt% CH_3SO_3H, <10 wt% $C_6H_{14}O_2$	45	5	Rinse with DIW[7] afterwards
2	Chemical Etching	H_2SO_4, <60 wt% $KHSO_5$	30	2	Rinse with DIW afterwards
3	Pre-Dip	5 wt% H_2SO_4	RT	3	No Rinse afterwards
4	Pd Activation	<30 wt% H_2SO_4, n/a	RT	1.5	Rinse with DIW afterwards
5	Electroless Nickel Plating	45 wt% $NiSO_4(H_2O)_6$, 25 wt% $NaPO_2H_2 \cdot H_2O$, 1 wt% $NH_3 \cdot H_2O$	95	45 (Cu), 60 (TE)	Agitation, Rinse with DIW afterwards
6[8]	Immersion Gold Plating	<5 wt% $C_6H_8O_7$, <1 wt% C_2AuKN_2	95	3	Agitation, Rinse with DIW afterwards

[7] DIW – deionized water

[8] Gold finish was used on samples subjected to nano sliver and silver flakes adhesive bonding experiments only

Electroless nickel plated Cu sheets and DBC alumina substrates were needed for Solid-Liquid Interdiffusion Bonding (SLID) subcomponent joining trials and thermoelectric module fabrication, respectively. In order to remove native oxide layer from the copper surface, both copper and DBC alumina substrates were subjected to pre-treatment process including acid cleaning, chemical etching, pre-activation dipping and Pd-activation process. Afterwards, both substrates were immersed in electroless nickel plating bath with the same composition used in the thermoelectric material plating. Process sequence and conditions with solution concentrations used in the process are depicted in Table 3.3-1.

3.3.2 Physical Vapor Deposition (PVD)

The multi-layered metallization was deposited in a form of stacking layers using Physical Vapor Deposition (PVD) technique by Politecnico di Torino, Italy or Teer Coatings Ltd., UK. Thermoelectric discs of $Mm_y(Fe,Co)_4Sb_{12}$ *p-type* and $Ni_xCo_{1-x}Sb_3$ *n-type* materials were placed in the sputtering chamber and plasma ion beam was passed so that the surface contamination and oxide layer were removed from the substrate. The sputtering process was performed under Ar atmosphere in the room temperature and multilayer were simultaneously co-sputtered without a need to break a vacuum. The configuration of chosen metallization layers (with the first one to be in direct contact with thermoelectric and the second one often used as a wetting layer), their thicknesses and CTE values are presented in Table 3.3-2. A standard scotch tape test was performed on as-coated thermoelectric surface to evaluate the adhesion quality according to ASTM D3359 standard [97].

Table 3.3-2: Multi-layered metallization used for $Mm_y(Fe,Co)_4Sb_{12}$ *p-type* and $Ni_xCo_{1-x}Sb_3$ *n-type* thermoelectric materials coating with CTE values measured at room temperature adapted from [98], [105] and [106].

CTE (ppm/K)	Layer	Thickness (nm)	CTE (ppm/K)	Layer	Thickness (nm)	CTE (ppm/K)
Co-based *p-type* skutterudite ~11 ppm/K	**Molybdenum (Mo)**	300	4.8 – 5.1	**Nickel (Ni)**	1200	13.0
	Titanium (Ti)	300	8.4 – 8.6	**Nickel (Ni)**	1200	13.0
Co-based *n-type* skutterudites ~ 9 ppm/K	**Tungsten (W)**	1000	4.5 – 4.6	**Gold (Au)**	50	14.0
	Tungsten silicide (WSi_2)	1000	13.7	**Gold (Au)**	50	14.0

3.3.3 Co-sintering of Metallization Layer and TE Material

The thermoelectric materials in this work were in-situ synthesized by SPS process allowing co-sintering with metallization layers simultaneously at the same process temperature as optimized for the *p-type* and *n-type* pre-alloyed powders. Three different metallization configurations were used including single, bi-layered and tri-layered systems as depicted in Figure 3.3-1a.

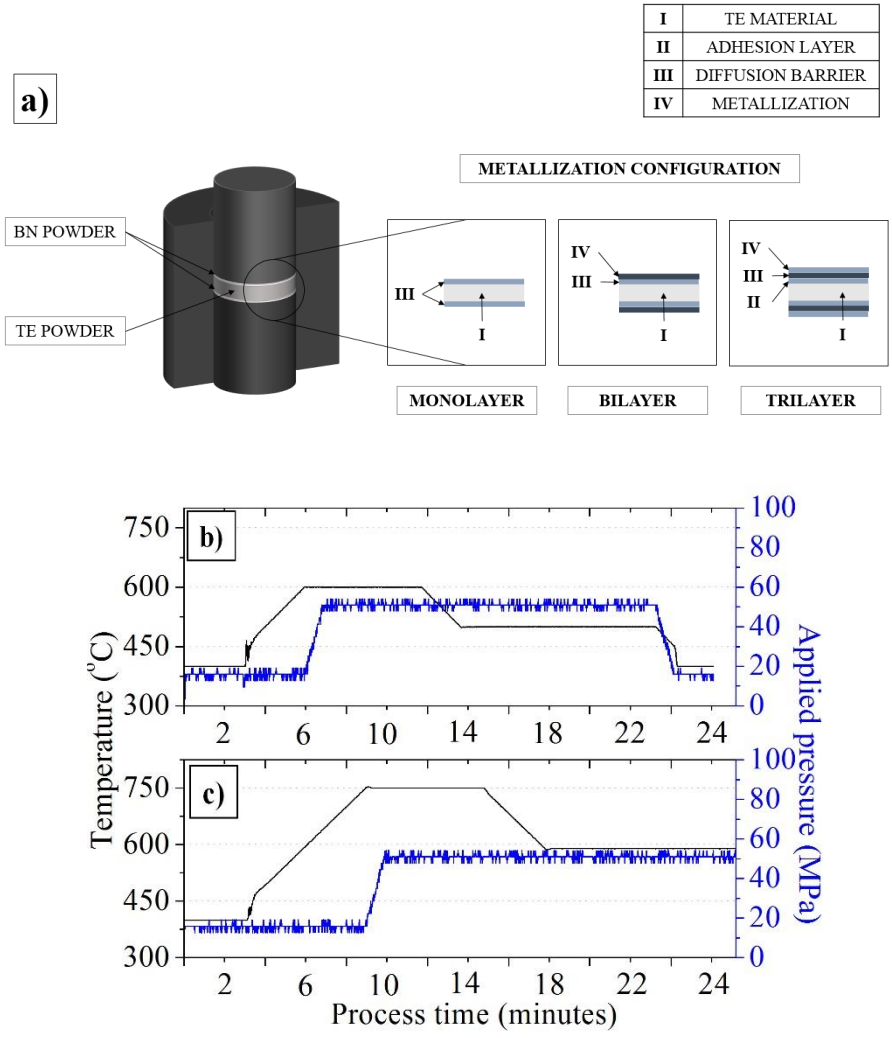

Figure 3.3-1: (a) Schematic illustration of multi-layered samples configuration within graphite die with temperature and applied pressure distribution for **(b)** $Mm_y(Fe,Co)_4Sb_{12}$ *p-* and **(c)** $Ni_xCo_{1-x}Sb_3$ *n-type* thermoelectric material in SPS process. Note: BN is boron nitride and TE is thermoelectric.

In the monolayer metallization, the thermoelectric material was directly co-sintered with a metallic foil being potentially a diffusion barrier and wetting layer simultaneously. To provide single metallization layer, foils of 50 μm-thick Ti (Luoyang Tongrun Info Technology Co., Ltd., 99.7% purity) and 100 μm-thick Zr (Sigma Aldrich, UK, 99.98% purity) were used and are presented in Table 3.3-3.

In order to mitigate the mismatch of the thermal expansion coefficient (CTE) between thermoelectric material and chosen metallization metal, multi-layered design was introduced. Bi-layered design included a combination of 50 μm-thick Zr (Sigma Aldrich, UK, 99.98% purity) diffusion barrier and a 50 μm-thick Ti (Luoyang Tongrun Technology Co., Ltd., 99.7% purity) top layer, a 50 μm-thick Zr (Sigma Aldrich, UK, 99.98% purity) and a 50 μm-thick stainless steel grade 303 (Sigma Aldrich, UK, 99.98% purity) layer, a 25 μm-thick 70 wt% Ti-15 wt% Cu-15 wt% Ni alloy denoted as Ticuni^{TM} (Wesgo Ceramics GmbH) and a 25 μm-thick Mo (Luoyang Aohe Co., Ltd., 99.95% purity) foil. Additionally, a 9 μm-thick Ni (Goodfellow, Cambridge, UK, 99.95% purity) foil was used as both adhesion promoter and top metallization to molybdenum sheet (Luoyang Aohe Co., Ltd., 99.95% purity) in the tri-layered system configuration. Such as unconventional design is expected to provide necessary mechanical bonding of refractory (chemically inert) metal to the thermoelectric material and serve as a diffusion barrier to stop braze poisoning at high working temperatures.

Metallic foils in either single of multi-layered configurations, were cut to circle shaped form using carbon nitride (CN) disc cutters and the hydraulic press. As mentioned above, the same sample configuration within the graphite die was used as optimized for the *p-type* and *n-type* TE material consolidation. Nonetheless, initial tests revealed that at a sintering temperature of 600 ^{o}C and 750 ^{o}C of the *p-type* and *n-type* material respectively, formation of carbides at the

metal and graphite sheet interface cannot be avoided. For that reason, graphite sheet was replaced with a chemically inert boron nitride powder, sprayed at contacting end of the used graphite punch. In order to sinter 3 mm-thick thermoelectric discs, 17.5 g of thermoelectric powder was placed inside the Ø10 mm graphite die on the top of the metallic foil and cold-pressed using hydraulic press. The flat surface of the TE material was interfaced with additional metallic foil and sealed with the graphite punch from the BN-sprayed side. Afterwards, the graphite die was placed inside the SPS vacuum chamber. The co-sintering was carried out in the SPS apparatus (FCT HPD25, Rauenstein, Germany) by applying uniaxial pressure of 50 MPa at the peak temperature of 600 ºC and 750 ºC for *p-type* and *n-type* material respectively, and hold for 5 min. In order to provide necessary contacting time, additional 10 minutes holding at 500 ºC and 590 ºC of *p-type* and *n-type* assemblies respectively, was carried out. Figure 3.3-1a-b presents the temperature and applied pressure distribution during the co-sintering of $Mm_y(Fe,Co)_4Sb_{12}$ *p-type* and $Ni_xCo_{1-x}Sb_3$ *n-type* thermoelectric materials with metallic foils. The consolidation process, as it was in the in-situ synthesis and sintering was performed under a vacuum with heating and cooling rates of 50 ºC/min by Nanoforce Technology Ltd., London, UK.

Table 3.3-3: Metallization layers configuration used for co-sintering experiments using SPS technique with CTE values measured at room temperature adapted from [98], [105] and [106].

CTE (ppm/K)	Layer	Thickness (µm)	CTE (ppm/K)	Layer	Thickness (µm)	CTE (ppm/K)
Co-based *p-type* skutterudite ~11 ppm/K	**Titanium (Ti)**	50	8.4 – 8.6	-		
	Zirconium (Zr)	100	5.7 – 7.0			
	Zirconium (Zr)	50	5.7 – 7.0	**Titanium (Ti)**	50	8.4 – 8.6
Co-based *n-type* skutterudites ~ 9 ppm/K	**Zirconium (Zr)**	50	5.7 – 7.0	**Stainless Steel SS303**	50	17.3 – 18.4
	Ticuni™	25	20.3	**Molybdenum (Mo)**	25	4.8 – 5.1
	Nickel (Ni) / Molybdenum (Mo)	9 / 25	13.0 / 4.8 – 5.1	**Nickel (Ni)**	9	13.0

3.4 Thermoelectric Material Joining

Both coated and un-coated, $Mm_y(Fe,Co)_4Sb_{12}$ *p-type* and $Ni_xCo_{1-x}Sb_3$ *n-type* thermoelectric discs were cut to 2.5 x 2.5 x 3 mm rectangular-shaped pellets (legs) using the diamond cut-off wheel (M1D15, Struers, Denmark) and soaked in acetone to remove any organic residues. As-prepared thermoelectric legs were subjected to thermoelectric-to-interconnect joining tests using material configuration presented in Figure 3.4-1a. In the conventional brazing technique, nickel tab was cut to 2.5 x 2.5 x 0.3 mm size and sandwiched between two thermoelectric (TE) legs with the braze paste screen printed in between.

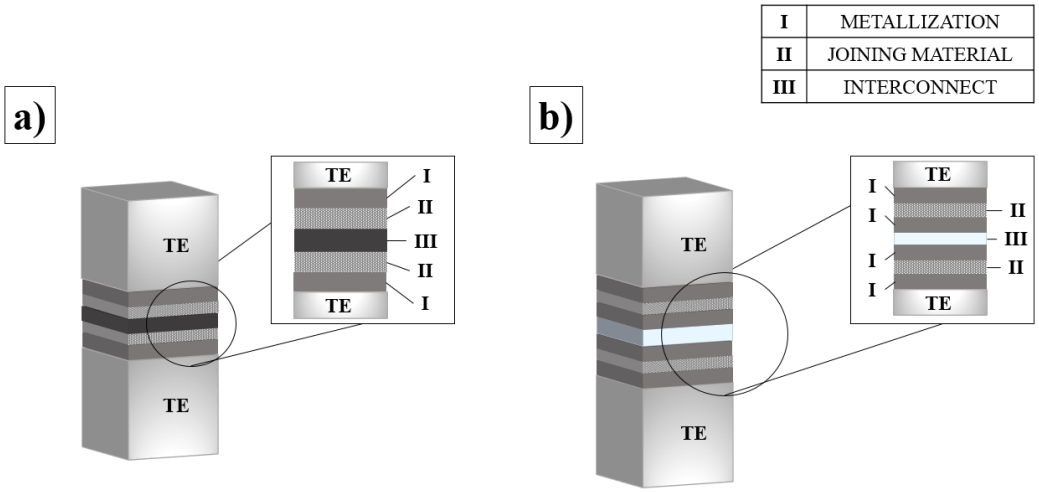

Figure 3.4-1: Schematic illustration of a thermoelectric legs configuration used in **(a)** soldering and/or brazing and **(b)** Solid-Liquid Interdiffusion (SLID) bonding experiments where I. is Ni(P) layer ($T_{M\,HIGH}$) and II. is Al foil ($T_{M\,LOW}$).

In each experiment, ~30 µm-thick layer of a commercial braze was directly screen printed on the top of thermoelectric leg using in-house developed stencil printing fixture (Figure 3.4-2 a-b). Such a design allows to simply control the substrate position inside the fixture and deposit a reproducible amount of paste using fixed screws, stencil and squeegee as depicted in Figure 3.4-2c. In the dispensing process, a cross pattern of about 70% of the top surface of

thermoelectric leg is covered with the paste and the legs are pressed with metallic interconnect until the paste is squeezed around the joining area.

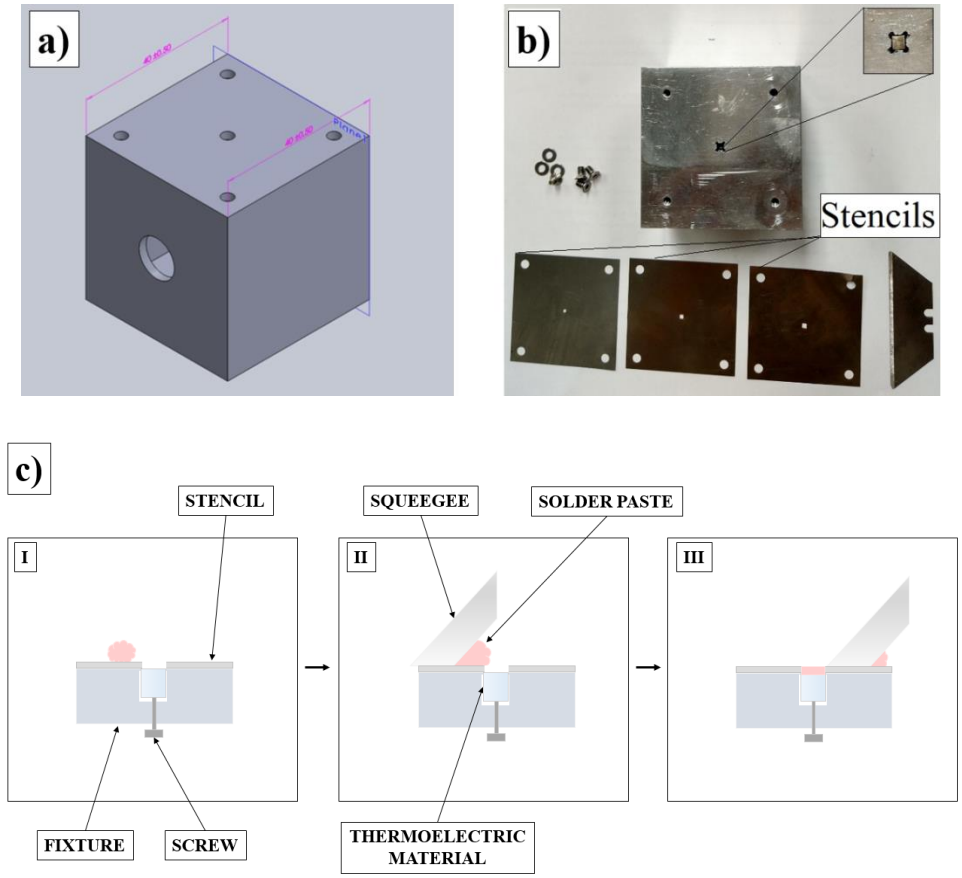

Figure 3.4-2: (a) In-house developed stencil-printing fixture with **(b)** a top-view showing the thermoelectric leg placement and different stencil sizes of the fixture and **(c)** process used to I. Placing the thermoelectric leg inside the fixture; II. Deposit the solder paste on the top of thermoelectric material; III. Removal of excess paste from the assembly.

Different joining materials were used in the brazing experiments including Silver-flo^{TM} 56 commercial alloy (Johnson Matthey, UK), Ag paste (Q-INKS S.r.l, Italy), Ag flake-based conductive adhesive (AREMCO Inc., US) and nano-Ag paste (NBE Technologies, LLC, US) and their properties are presented in Table 3.4-1.

Table 3.4-1: Properties of joining materials used in subcomponent joining and thermoelectric module fabrication experiments.

Braze	Composition	Sheet resist. (μΩcm)	Thermal Conduct. (W/mK)	CTE (ppm/K)	Solidus – Liquidus (°C)
Ag56-CuZnSn	56 at% Ag, 22 at% Cu, 17 at% Zn, 5 at% Sn, Borax and boric acid flux	20.8	14.5	n/a	618 - 655
Ag paste	<68 at% Ag Solvent and glass frit	4.2	n/a	19.6	n/a - 961
Ag flake-based adhesive	Ag and solvent	200	9.1	19.6	n/a - 961
Nano-Ag paste	85 at% Ag and organic binder	2.6	2	19.6	n/a - 961

Joining experiments were performed using in-house developed brazing system equipped with opened tube furnace (Carbolite, UK) and brazing jig designed for both subcomponent and device level bonding tests (Figure 3.4-3). All pastes were fired under different conditions specified by the supplier as presented in Table 3.4-2. Silver braze (Silver-flo^{TM} 56, JM, UK) and Nano-Ag paste (NBE Technologies, LLC) did not need any additional pre-treatment, solvent-based pastes were air dried to reduce viscosity by solvent evaporation. Joining material was screen printed on the top of each thermoelectric element and metal

interconnect was clamped between two thermoelectric pellets and the joining material. The Ag paste (Q-INKS S.r.l.) was pre-dried on the hot plate at 250 ºC for 7 min while conductive Ag flake-based adhesive (AREMCO Inc.) was dried at room temperature for 1 hour. The sintering of specimens using Ag-nano (NBE Technologies, LLC) and Ag flake-based (AREMCO Inc., US) joining materials was performed on the hot plate (MCS77 CTA, Germany) with temperature ramp of 5 ºC / min in air. Specimens with silver braze (Silver-flo^{TM} 56, JM, UK) and pre-dried Ag paste (Q-INKS S.r.l.) joining materials were mounted in the brazing jig and placed inside preheated (up to 710 ºC) tube furnace. This allowed to achieve heating rates of approximately 12 ºC/min. To control joining temperature, thermocouple was placed inside the brazing jig, and its readings were extracted using EasyLog (Lascar USB, UK) software. The brazing jig was removed from the furnace when the peak joining temperature (T_{PEAK}) was reached. All high temperature joining tests were performed in flowing Ar (4 l/min).

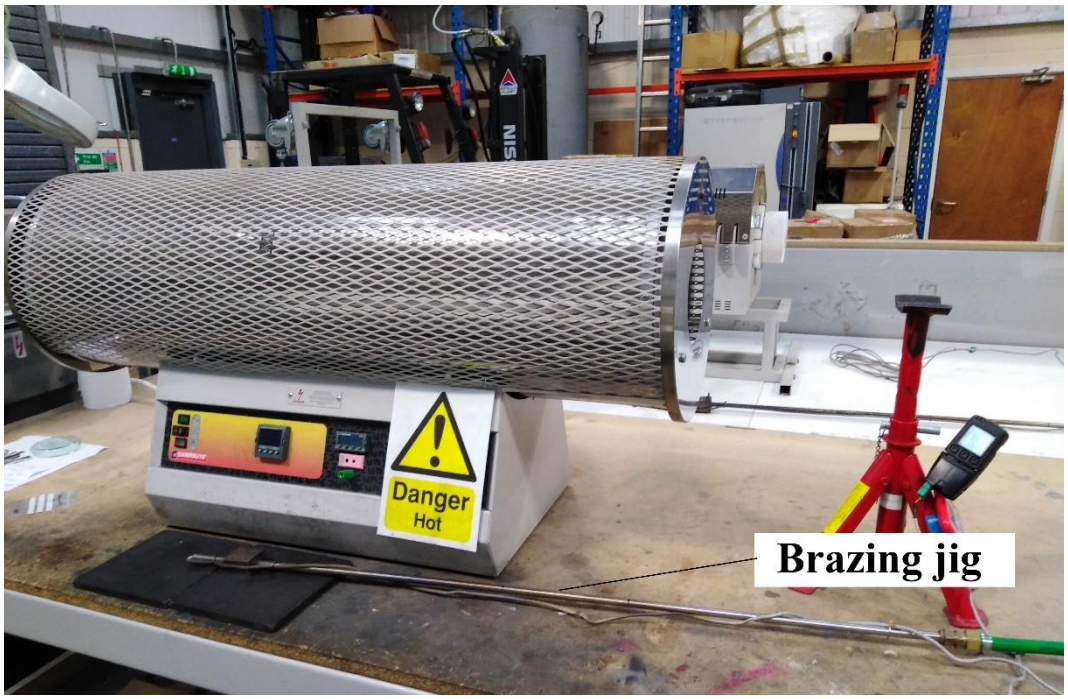

Figure 3.4-3: Furnace brazing setup equipped with brazing jig, thermocouple and argon inlet used for joining trials.

Table 3.4-2: Optimized firing conditions for commercial brazes and solders used in the research.

	Pre-dry			Firing		
Braze	**T_{PEAK} (ºC)**	**Dwelling time (min)**	**Cond.**	**T_{PEAK} (ºC)**	**Dwelling time (min)**	**Cond.**
Ag56-CuZnSn	-	-	-	645	Removed at T_{PEAK}	Ar (4 l/min)
Ag paste	200	7.5	Air	652	Removed at T_{PEAK}	Ar (4 l/min)
Ag flake-based adhesive	25	60	Air	110	60	Air
Ag-nano paste	-	-	-	273	20	Air

Different sample configuration was used in the Solid-Liquid Interdiffusion (SLID) bonding trials. A 17 µm-thick Al foil (Goodfellow, Cambridge, UK, 99.0% purity) ($T_{M\ LOW}$) was incorporated between the Ni(P)-coatings ($T_{M\ HIGH}$) on the thermoelectric pellet and the copper plate and supportive uniaxial pressure of ~0.5 MPa was applied. To provide mechanical stability within brazing jig, two symmetrical joints were fabricated by placing a copper plate between two thermoelectric pellets at the same time, as presented in Figure 3.4-1b. Afterwards, the brazing jig was placed inside a tube furnace (Carbolite, UK) and the assembly was joined at 585 ºC for 15 minutes and 660 ºC for 4.6 minutes in Ar (4 l/min) with a heating rate of 7 ºC/min. The contact assembly was dwelled at the peak temperature for either 15 minutes or 4.6 min, and afterwards, the furnace was switched off and cooled down (at approximately 3 ºC/min cooling rate) until the

samples reached an ambient temperature. The behaviour and microstructural changes in the joining material have been evaluated through isothermal annealing at 450 ºC for 48 h and 96 h in flowing argon to investigate the stability and evolution of the joint.

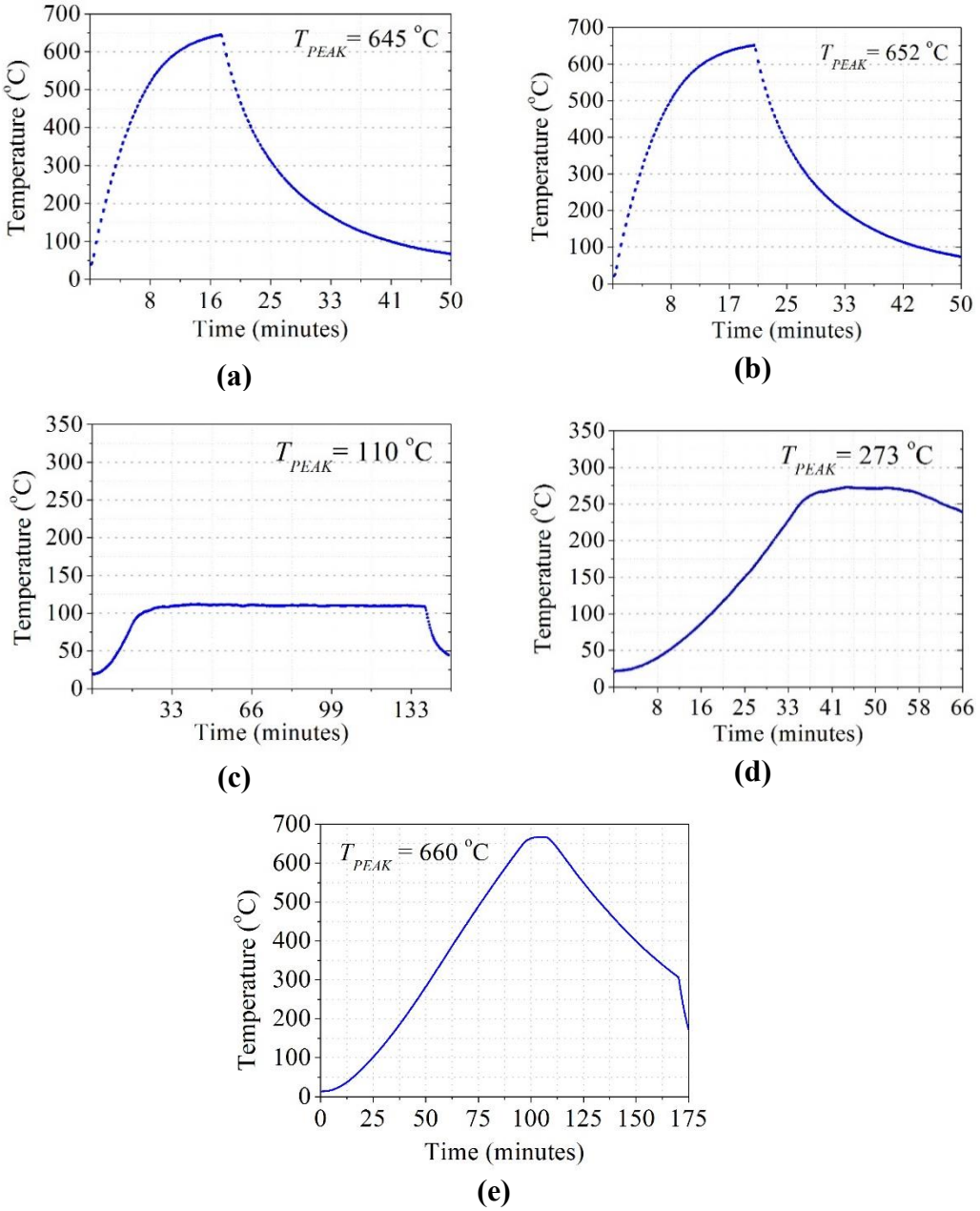

Figure 3.4-4: Temperature profile for **(a)** silver-flo^{TM} 56 braze, **(b)** Ag-based, **(c)** Ag flake-based, **(d)** Ag-nano paste and **(e)** Solid-Liquid Interdiffusion Bonding (SLID) during the thermoelectric-to-interconnect joining experiments and module fabrication.

3.5 Thermoelectric Module Fabrication Process

Thermoelectric module was built using in-house developed brazing system including stainless steel brazing jig with argon inlet and tube furnace shown in Figure 3.4-3. The single stage, bulk thermoelectric module was fabricated by stencil printing of bonding material on the top of metal interconnections and manually placing *n*- and *p-type* thermoelectric legs in turn. Subsequently, top ceramic plate (15 x 15 mm in size) with screen-printed joining materials was placed on top of the prepared assembly and placed inside the brazing jig. Although flowing argon was used during the brazing process, titanium sponge was also placed inside the jig to capture any residual oxygen during the high temperature treatment. As-prepared assembly was afterwards placed inside the preheated (normally up to 710 ^{o}C to provide desired heating rate) tube furnace and annealed at conditions specified in Table 3.4-2. After dwelling, brazing jig was removed from the tube furnace and the assembly was left to cool down until it reached room temperature. Afterwards, module was visually inspected, and if no visible legs displacement was observed, four wires were soldered to the cold side ceramic for further AC resistance and high temperature rig testing.

3.6 Interface Characterization

3.6.1 SEM Microstructural Analysis

For the microstructure observation, specimens were mounted in conductive resin, mechanically ground with abrasive papers and polished using 1/4 μm diamond suspension. The chemical composition of the reaction products was characterized by high-resolution field emission gun scanning electron microscope (FEGSEM, 1530VP Zeiss GmbH, Germany) with 80 mm^2 energy dispersive X-Ray spectroscopy detector (Oxford Instruments, UK) and analysed by Aztec EDS/EBSD microanalysis software.

3.6.2 Electrical Contact Resistance Measurement

The electrical contact resistance of contacting interfaces was periodically measured during the isothermal ageing process using in-house developed four-point probe resistance measurement. The set-up equipped with Keithley 2400 (Keithley Instruments, Inc., US) and DPP205 probe positioner (Cascade Microtech, Inc.) measures the voltage drop across two probes as a function of applied short current pulses (Figure 3.6-1a). The electrical contact resistance (R_C) of contacting interface is given by:

$$R_C = (\mathrm{R}_1 - \mathrm{R}_0) \cdot \mathrm{A} \qquad 17$$

where R_1, R_0 are measured resistance at the metallic electrode and the thermoelectric material and A is a cross-sectional area of this interface.

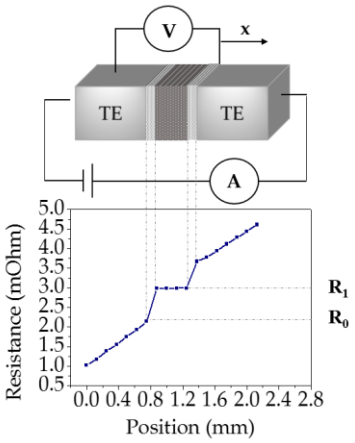

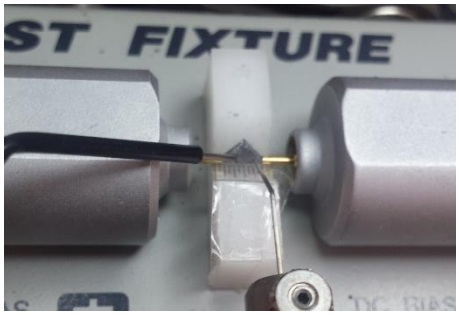

(a) **(b)**

Figure 3.6-1: (a) schematic illustration of four-point probe resistance set-up equipped with scanning probe moving across the surface (x) where the contact resistance (*Rc*) is defined as the ratio of voltage drop across the contact to the current pulse applied to a pair of contacts; graph below shows experimental data with *Rc* measurement of the *p-type* skutterudite specimen bonded using SLID technique at 660 ºC for 4.6 min. Photograph of the sample arrangement in the four-point probe resistance measurement setup is presented in **(b)**. It is worth mentioning that contacting interfaces must have low thermal resistivity, but only electrical performance can be measured using well-established techniques and this research only covered this part.

The standard deviation (σ_x) was calculated from the average values (μ) of at least three measurements (y_i) and plotted as the error bars according to:

$$\sigma_x = \sqrt{\frac{1}{N}\sum_{i=1}^{N}(y_i - \mu)^2} \qquad 18$$

3.6.3 Mechanical Shear Strength

The mechanical strength of joints was assessed using specimens with the cross-sectional size of 2.5 mm × 2.5 mm by measuring apparent shear strength using MTS Criterion 43 (MTS Systems Corporation, US) at room temperature. The shear configuration was adapted according to ASTM D905 standard [99] designed to expose the assembly to direct contact with a shearing blade ≤ 0.3 mm from the thermoelectric/joint interface as depicted in Figure 3.6-2a. A shear load was applied by moving the blade perpendicularly to the longitudinal axis of the assembly with a speed of 0.2 mm/min and preloading of ~5 N. The shear strength was calculated by dividing the maximum force applied by the joining area of at least two specimens of different joining conditions. This measurement does not give precise absolute values, but is a useful relative measure, as quantities of TE materials and requirement over metallisation and joining make it challenging to fabricate required standard sample sizes. The standard deviation (σ_x) was calculated from the average values (μ) of at least three measurements (y_i) and plotted as the error bars according to equation 18.

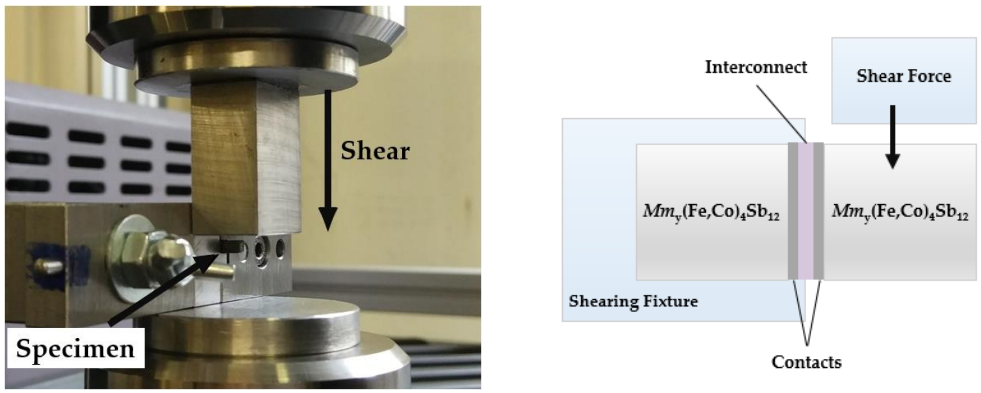

(a) **(b)**

Figure 3.6-2: Configuration used for mechanical strength evaluation showing: **(a)** photograph of sample clamped in the shear test fixture and **(b)** schematic illustration of the specimen and shear test configuration.

3.7 Thermoelectric Module Characterization

In-house developed thermoelectric module test system consists of the stainless steel block heater, the water-cooled heat dissipation plate and is equipped with a power supplier (2400 Keithley Instruments, Inc., US) and desktop PC (seen in Figure 3.7-1a). Thermoelectric device is placed between the cold and hot side heat exchangers with clamping force of 1 MPa kept constant during the measurement. The graphite sheet (Erodex, UK) was used as the thermal interface material and was placed between the module and heat exchangers to provide good thermal contact. The temperature on the cold and hot side of the thermoelectric module was measured using thermocouples located near the heat exchangers which is believed to represent the temperature of both sides of the thermoelectric module by assuming no parasitic thermal losses at contacting interfaces. The setup is capable to sustain a heater temperature up to 500 ºC at the hot side (T_H) while the cold side (T_C) is kept at constant temperature of ~ 30 ºC during the measurement. The set up measures the open circuit voltage (V_{OC}, which is a voltage measured at zero current ($I = 0$)), short circuit current (I_{SC}, which is a measured current at zero voltage ($V = 0$)) and electrical power output (P_{OUT}) at temperature applied at the hot side (T_H) of the thermoelectric module using a variable electrical load. The equivalent electrical circuit of prototype module measurement can be seen in Figure 3.7-1b. The maximum power output (P_{MAX}) was calculated by linear fitting of the voltage-current output and finding the resulting maximum power at given temperature gradient (ΔT). The module internal resistance ($R_{TEG,E}$) was measured directly by using a pseudo-AC test under temperature gradient and was generally close to the load resistance at the maximum power point. All measurements are performed in the open air. The module test rig was designed so that the current

and voltage across a TEG module is measured as the external load sweeps from open circuit to short circuit current conditions. The control program used in the electrical experiment was able to check the temperature difference based on the signals from the thermocouples and control the current in the heater.

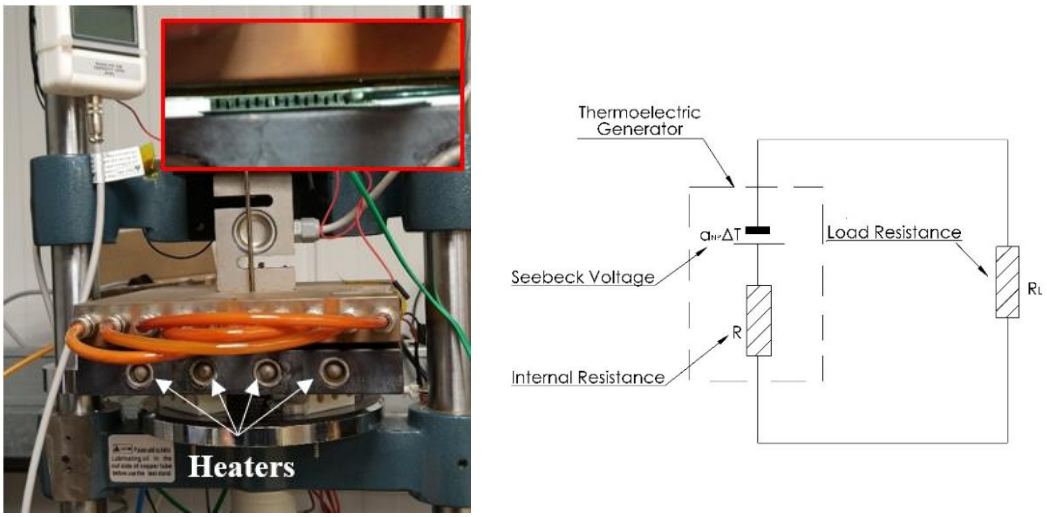

(a) **(b)**

Figure 3.7-1: (a) high temperature module test rig used to evaluate the performance of developed devices with close-up view of the module clamping system with the heater, cooling plate and thermoelectric generator (TEG) clamped between and **(b)** equivalent electrical circuit (Courtesy of European Thermodynamics Ltd.).

Chapter 4

Results and Discussion

4.1 Thermoelectric Material Characterization

This section comprises results from phase and microstructural analysis of $Mm_yFe_{4-x}Co_xSb_{12}$ *p-type* and $Ni_xCo_{1-x}Sb_3$ *n-type* material along with transport properties such as Seebeck coefficient, electrical and thermal conductivity as a function of temperature.

4.1.1 XRD and Microstructural Analysis of *p-type* Thermoelectric

In this research, commercially available multi-element filled (*Mm*-filled) skutterudite material with nominal composition of $Mm_{0.9}Fe_3Co_1Sb_{12}$ was used as *p-type* thermoelectric material. X-Ray diffraction analysis was performed on thermoelectric powders before and after SPS consolidation in order to reveal possible phase change during the *in-situ* reaction synthesis and is presented in Figure 4.1-1. It is clearly visible that starting material is a mixture of elemental powders of cobalt, antimony and iron, with no peaks of dopant element detected due to the XRD detection limit (below 2% for mixed materials). Phase transformation into skutterudite phase that could be indexed to the space group

$Im\bar{3}$ of the parent $CoSb_3$ compound (with a body-centered cubic symmetry space group) can be detected after consolidation at 600 ºC for 5 min using SPS. The typical lattice parameter of $CoSb_3$ compound is around a = 9.0385 Å, has a theoretical density of ρ = 7.631 g·cm^{-3} and comprise a molecular weight of 424.18 g·mol^{-1} with a corresponding volume V = 738.40 Å ^{3} (see JCPDS No. 78-0976). Noticeable quantities of $FeSb_2$ compound and un-reacted Sb impurities were observed as the secondary phase. Although, it has been proven that small amount of $FeSb_2$ and Sb secondary phases do not significantly influence the overall figure-of-merit of $Mm_yFe_{4-x}Co_xSb_{12}$ [100] material, un-reacted antimony is more likely to diminish mechanical stability of the material at elevated temperatures [101]. The excess of antimony comes from starting powders, needed to compensate its possible volatility losses, and normally resides at grain boundaries, thus upon heating above its melting temperature (631 ºC [102]), the microstructure expands to relieve residual stress associated with hot pressing and its vaporization. The influence of excess Sb was proven to slightly enhance thermal conductivity of final material accompanied by the reduction in the electrical resistivity and Seebeck coefficient [103] and yield a porous structure at high temperature treatment due to its evaporation [104].

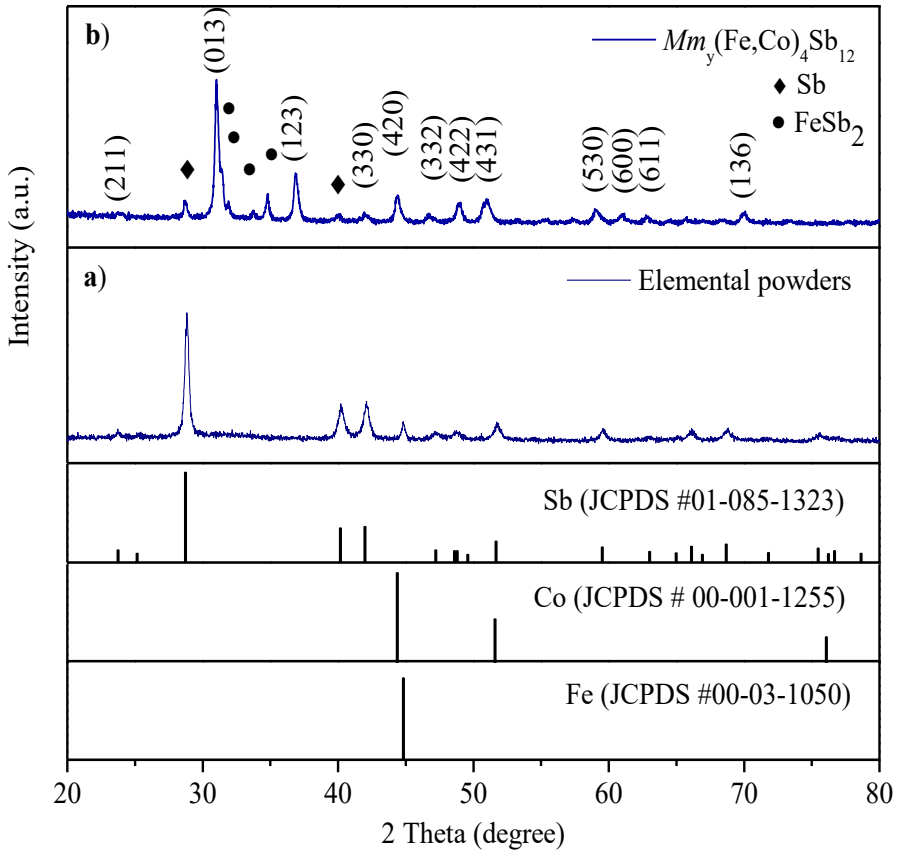

Figure 4.1-1: XRD patterns of **(a)** elemental powders before sintering and **(b)** $Mm_yFe_{4-x}Co_xSb_{12}$ *p-type* thermoelectric material after consolidation at 600 °C for 5 min using SPS with reference patterns of elemental antimony, cobalt and iron. The numbers in brackets denote the *hkl* lattice planes of the skutterudite phase and the symbols show characteristic peaks of impurity phases.

Figure 4.1-2 shows SEM images of sintered $Mm_y(Fe,Co)_4Sb_{12}$ *p-type* thermoelectric material in the back-scattered electron (Figure 4.1-2a) and secondary electron mode (Figure 4.1-2b). The formation of multi-filled skutterudite as a dominant phase with a composition of 3.49 at% Ce – 1.33 at% La - 4 at% Co – 18 at% Fe – 73 at% Sb was confirmed by analysing at least 5 different spots of that material. The *p-type* materials used in this study has both high porosity and compositional inhomogeneity within the material, which was proven to be $FeSb_2$ phase (30 at% Fe – 70 at% Sb), regions of pure iron phase and

residual antimony as presented in Appendix A (Figure A. 1). Although EDS analysis confirmed the formation of $FeSb_2$ second phase inclusions and pure iron regions, no residual antimony at the grain boundaries was detected, due to the similar Z contrast with $Mm_y(Fe,Co)_4Sb_{12}$ compound in back scattered SEM mode. The existence of $FeSb_2$ secondary phase in the $Mm_y(Fe,Co)_4Sb_{12}$ *p-type* thermoelectric material is consistent with the XRD results from Figure 4.1-1 and has been previously reported in the literature when similar processing route and composition were used [105]. The density of as-sintered thermoelectric material was measured using Archimedes principle and for 5 measured samples the average was ~ 96% of the theoretical density.

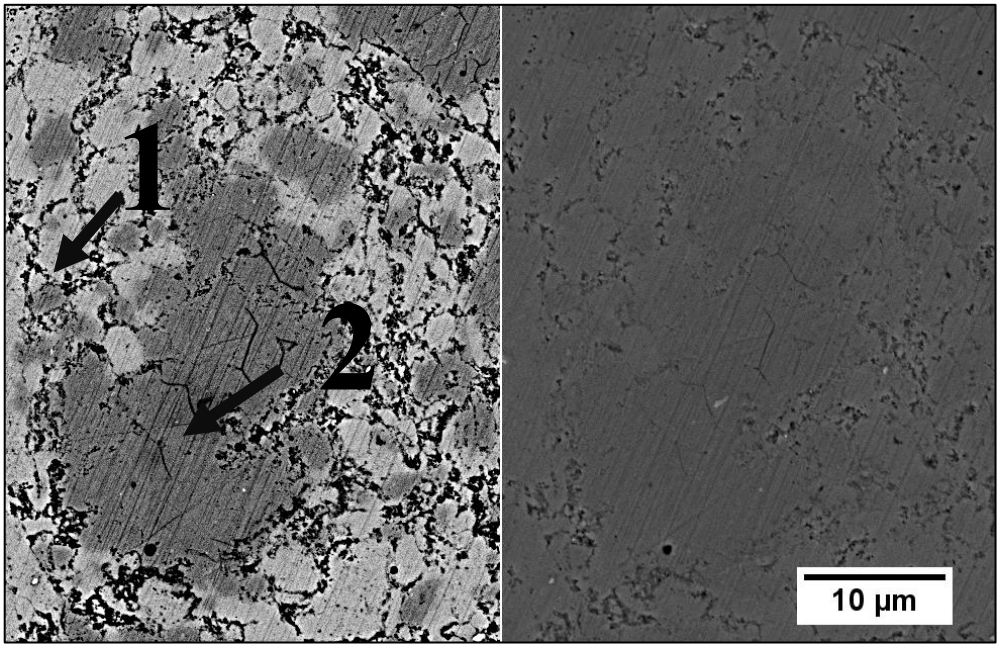

(a) **(b)**

Figure 4.1-2: (a) BSE microscope image revealing the (1) $Mm_y(Fe,Co)_4Sb_{12}$ (3.49 at% Ce – 1.33 at% La - 4 at% Co – 18 at% Fe – 73 at% Sb) and (2) $FeSb_2$ (28 at% Fe – 72 at% Sb) phases with **(b)** corresponding SE image of $Mm_yFe_{4-x}Co_xSb_{12}$ *p-type* thermoelectric material after consolidation at 600 ºC for 5 min using SPS technique.

4.1.2 Transport Properties of *p-type* Thermoelectric

The Seebeck coefficient (α), electrical resistivity (ρ) and total thermal conductivity (κ) of $Mm_y(Fe,Co)_4Sb_{12}$ *p-type* skutterudite was measured as a function of temperature between 25 °C and 550 °C. These values along with calculated figure of merit (zT) are presented in Figure 4.1-3a,b. The electrical resistivity (ρ) along with Seebeck coefficient (α) slightly increase with the temperature, which is a behaviour typically observed in metals or heavily doped semiconductor (degenerated semiconductors). According to the Ref. [106], different performance in the multi-filled skutterudite material can be achieved by replacing Fe with Co atoms and the best achieved so far is possible with the composition used in this study (Fe:Co = 3:1). It is rationalized that Co has one more outer electron than Fe, and is able to fill holes in the relevant valance band, resulting in a semiconductor with a similar band gap to that of $CoSb_3$ (0.5eV) [107].

The temperature-dependent Seebeck coefficient (α) is shown is Figure 4.1-3 (a), and it is significantly lower than results presented in the literature with similar composition [51]. The difference can be attributed to the different preparation technique and porosity which is believed to influence the thermoelectric properties by exacerbate alloy scattering, and thus results in lower carrier mobility and higher values of electrical resistivity (Figure 4.1-2). Although electrical resistivity (ρ) and thermal conductivity (κ) is consistent with reported data [101], relatively lower Seebeck coefficient results in zT of 0.23 measured at 500 °C, and average zT ($\overline{zT}$) of 0.12 measured between 50 °C and 450 °C which is significantly lower than state-of-the-art *Mm*-filled *p-type* skutterudite material (more details can be seen in Figure 2.2-2).

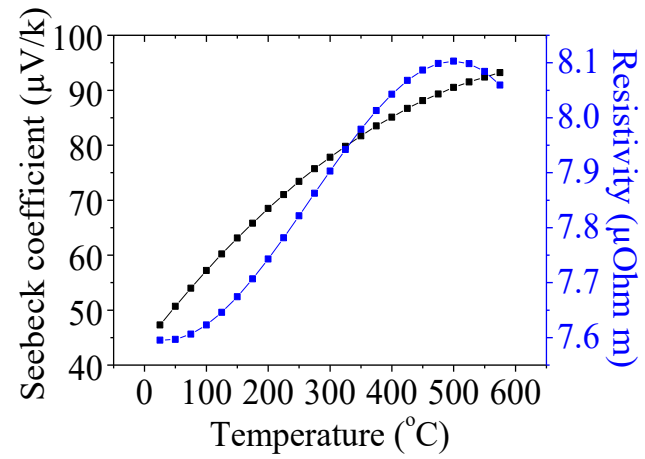

(a)

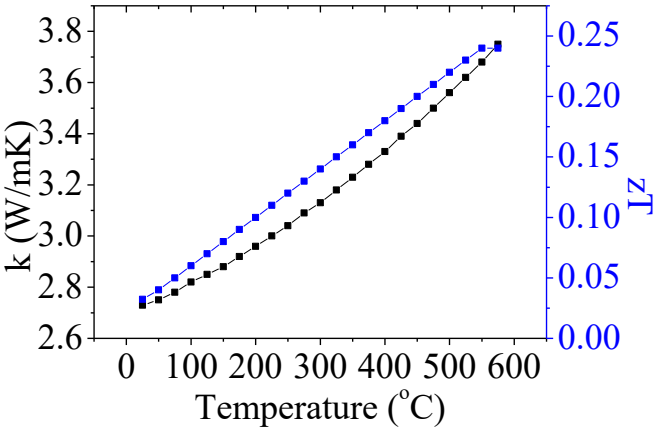

(b)

Figure 4.1-3: Thermoelectric properties including **(a)** the Seebeck coefficient (α) and electrical resistivity (ρ); **(b)** total thermal conductivity (κ) and figure of merit (*zT*) of $Mm_y(Fe,Co)_4Sb_{12}$ *p-type* skutterudite as a function of temperature.

4.1.3 XRD and Microstructural Analysis of *n-type* Thermoelectric

In this research, commercially available Ni-doped skutterudite material with nominal composition of $Ni_{0.15}Co_{0.85}Sb_3$ was used as *n-type* thermoelectric material. X-Ray diffraction analysis was performed on thermoelectric powders before and after SPS consolidation in order to reveal possible phase change during the *in-situ* reaction synthesis and is presented in Figure 4.1-4.

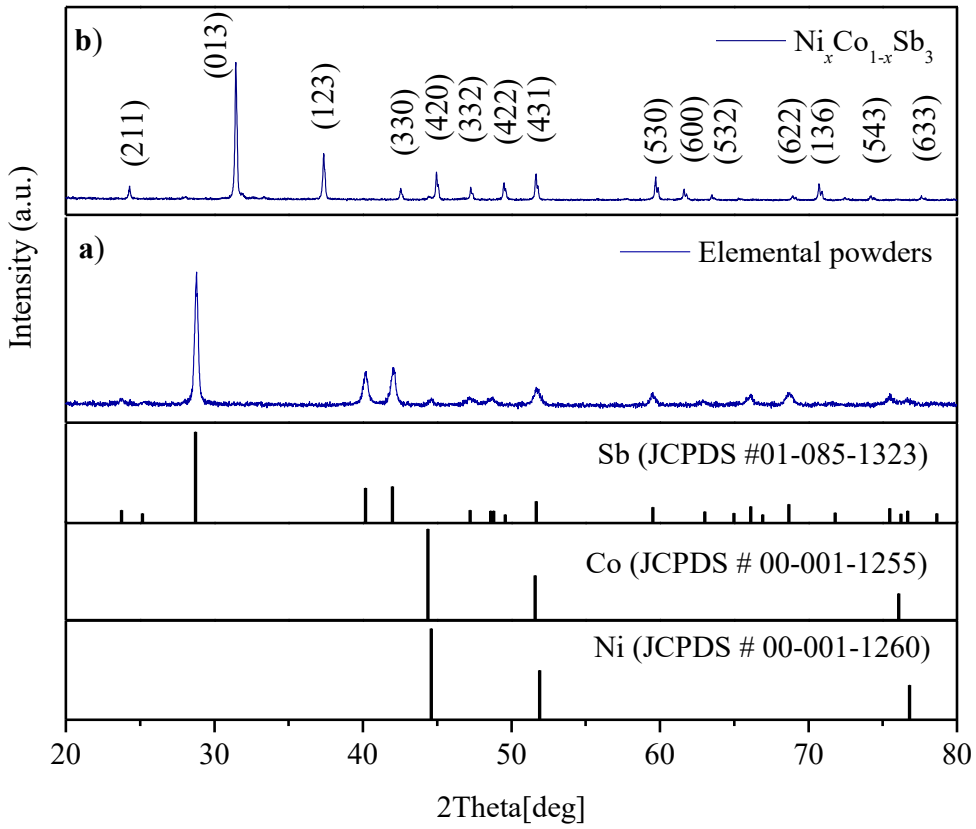

Figure 4.1-4: XRD patterns of **(a)** elemental powders before sintering and **(b)** $(Ni,Co)_1Sb_3$ n-type thermoelectric material after consolidation at 750 °C for 5 min using SPS with reference patterns of elemental antimony, cobalt and nickel. The numbers in brackets denote the hkl lattice planes of the detected skutterudite phase.

It is clearly visible that starting material is a mixture of elemental powders of cobalt and antimony with no detected peaks of nickel due to the XRD detection limit. Phase transformation into skutterudite phase that could be indexed to the space group $Im\bar{3}$ of the parent $CoSb_3$ compound (with a body-centered cubic symmetry space group) can also be detected after consolidation at 750 °C for 5 min using SPS technique. As opposed to *p-type* material (shown in Figure 4.1-1), no second phase (i.e. previously reported CoSb in similar composition [108]) was detected suggesting complete transformation into $CoSb_3$ skutterudite phase.

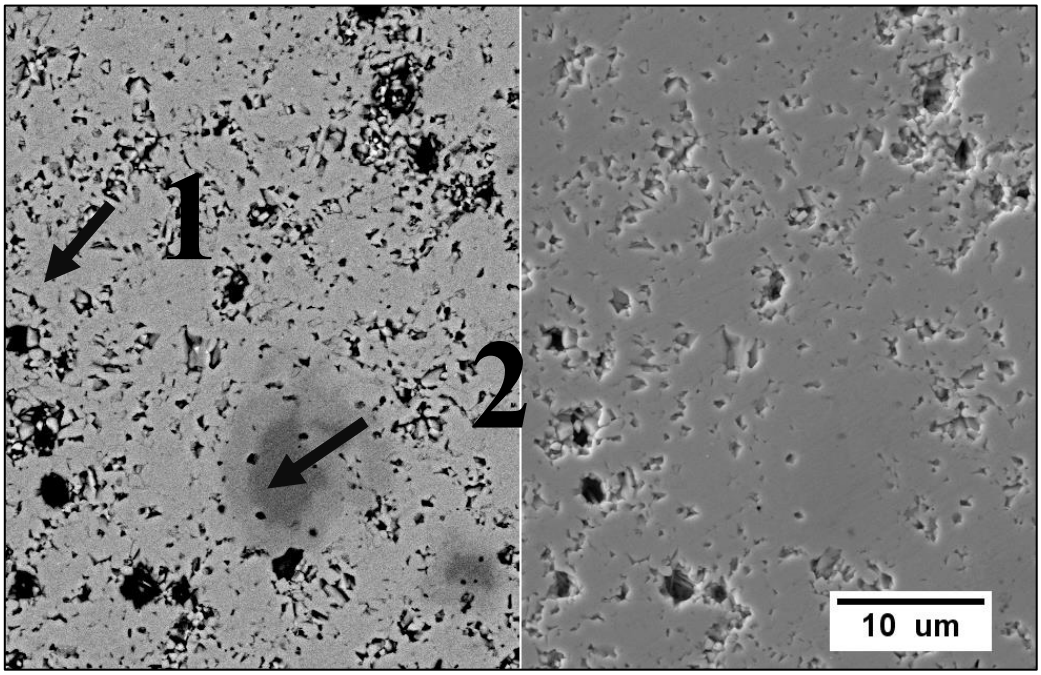

(a) **(b)**

Figure 4.1-5: (a) BSE microscope image revealing the (1) $(Ni,Co)_1Sb_3$ (2.38 at% Ni – 21.81 at% Co – 76 at% Sb), (2) (Co,Ni)Sb (Co — 31 at.% Ni — 54 at.% Sb) with **(b)** corresponding SE image of the same polished surface of microstructure of $Ni_xCo_{1-x}Sb_3$ *n-type* thermoelectric material after consolidation at 750 ºC for 5 min.

Figure 4.1-5 shows SEM images of sintered $(Ni,Co)_1Sb_3$ *n-type* thermoelectric material in the back-scattered electron (Figure 4.1-5a) and secondary electron mode (Figure 4.1-5b). The $Ni_{0.09}Co_{0.8}Sb_3$ (2.38 at% Ni – 21.81 at% Co – 76 at% Sb) skutterudite was identified as a main phase, suggesting that Ni was successfully introduced into the skutterudite matrix. Although no secondary phase was detected by meaning of X-Ray analysis (Figure 4.1-4), regions of inhomogeneous (Co,Ni)Sb phase distribution were found inside the material (Co — 31 at.% Ni — 54 at.% Sb) as seen by EDS analysis presented in Appendix A (Figure A. 2).

4.1.4 Transport Properties of *n-type* Thermoelectric

The temperature dependences of electrical resistivity (ρ), Seebeck coefficient (α) and total thermal conductivity (κ) of $Ni_xCo_{1-x}Sb_3$ *n-type* skutterudite measured between 25 °C and 550 °C along with calculated figure of merit (zT) are presented in Figure 4.1-6. The negative Seebeck coefficient values for the $Co_{1-x}Ni_xSb_3$ thermoelectric material indicate that Ni atoms successfully act as an *n-type* dopants considering that un-doped $CoSb_3$ is proven to be a *p-type* conductor [109].

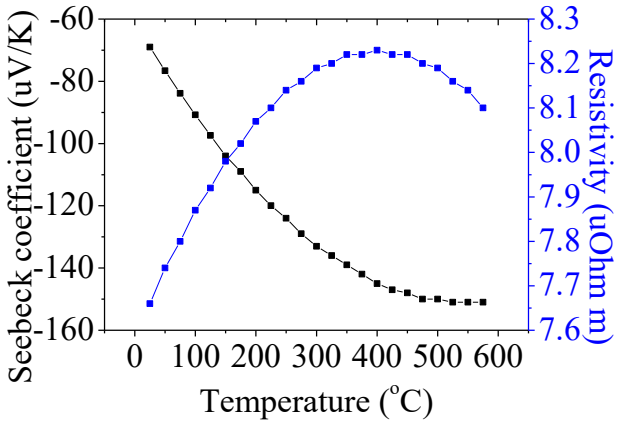

(a)

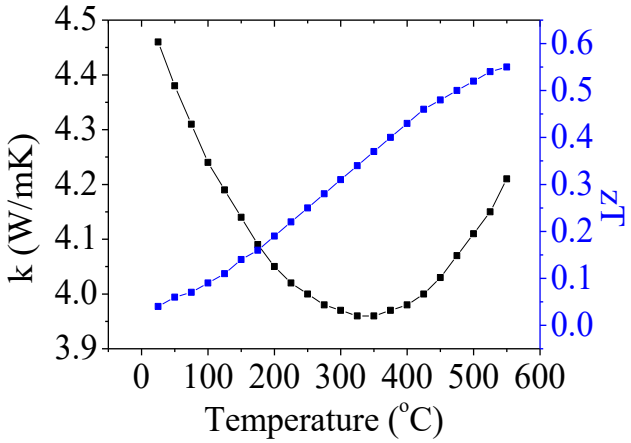

(b)

Figure 4.1-6: Thermoelectric properties including (a) the Seebeck coefficient (α) and electrical resistivity (ρ); (b) total thermal conductivity (κ) and figure of merit (zT) of $(Ni,Co)_1Sb_3$ *n-type* skutterudite as a function of temperature.

The Seebeck coefficient and electrical resistivity (ρ) of Ni-doped $CoSb_3$ semiconductor are comparable to values reported with similar composition and consistent with the Ref. [109]. The peak zT value measured at 500 ºC was 0.52 and average zT ($\overline{zT}$) of 0.27 measured between 50 ºC and 450 ºC. consistent with Ref. [108].

4.2 Thermoelectric Contacts Characterization

Many potentially suitable processes and joining materials were initially tested on non-metallized and metallized skutterudites according to the ASTM F44-95 [110] standard but due to the insufficient performance of these contacts, only successful candidates will be presented here. In this respect, it is worth mentioning joining materials that were used for initial joining trials, but lack of mechanical or electrical performance resulted in lack of in-depth analysis of these specimens. The Al-Si joining material with standard $KAlF_4$ flux normally used for brazing of Al-based alloys was tested on Ni(P) coated thermoelectrics. This alloy requires a low-temperature curing conditions as it undergo eutectic transformation at 577 ºC (at 11.7 wt% Si) which could be suitable for skutterudite-based materials, but limited wetting resulted in poor mechanical performance and fracture of as-joined specimens. Another commonly used for aluminium-to-aluminium bonding is Zn-22Al braze (with T_M = 482 ºC) which was also tested on Ni(P) coated thermoelectrics but similar effect to Al-12Si braze was achieved. Moreover, Ni conductive paste (PELCO®, Ted Pella, Inc.) was tested on Ni(P) coated skutterudites at 250 ºC but electrical contact resistance (R_C) of as-joined specimens was much higher than the acceptable limit (> 10^{-3} Ωcm^2). The fabrication techniques that were able to form sufficiently robust contacts for further testing included furnace brazing using Ag56Cu22Zn17Sn5 braze, Ag paste, low-temperature joining using nano-Ag paste and Ag flake-based conductive adhesive, and innovative Solid-Liquid Interdiffusion (SLID) bonding technique based on Al-Ni interlayers.

4.2.1 Ag56-CuZnSn Filler Braze

Brazing alloys from the Ag-Cu family are preferred joining materials used in the hot-side contact fabrication in the medium-high temperature range skutterudite-based modules as they can operate at the suitable brazing window (T_H « $T_{brazing}$ « $T_{TE\ decomp}$). As polycrystalline $Mm_y(Fe,Co)_4Sb_{12}$ *p-type* and $(Ni,Co)_1Sb_3$ *n-type* thermoelectrics were consolidated at 600 ºC and 750 ºC respectively, it is important for their stability that the brazing process is ideally performed at slightly lower temperatures. The most promising braze alloy with a composition of 56 at % Ag - 22 at % Cu - 17 at % Zn - 5 at % Sn (Silver-flo^{TM} 56, Johnson Matthey, UK) has a suitable brazing range with liquidus temperature of 655 ºC and tensile strength of 48 kg/mm^2 (measured at room temperature) and was used in this research. As can be seen in Appendix A (Figure A. 3), resulting braze microstructure after firing at 655 ºC for 5 minutes (in flowing argon) consists of two ductile phases: α(Ag) -solid solution of copper, zinc, tin in silver and α(Cu) - solid solution of silver, zinc and tin in copper matrix. The braze was fired at the lowest required temperature, due to the very low consolidation and TE decomposition temperatures. The braze practicality highly depends on the wettability on both joined material's and the chosen flux that is able to remove oxides formed during the high-temperature brazing. In this research commonly used flux of borax and boric acid was used. The Silver-flo^{TM} 56 braze can easily wet and dissolve nickel interconnect and region of high nickel concentration in the α(Cu) phase can be found near the nickel substrate as both copper and nickel are completely miscible in all concentration ranges [68]. Although solubility of nickel in the α(Cu) solid solution helps with a formation of a strong mechanical bond between nickel interconnect and braze, high temperature operation might

presumably lead to a complete consumption of nickel interconnect by the braze and failure of thermoelectric device.

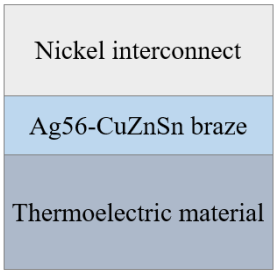

(a)

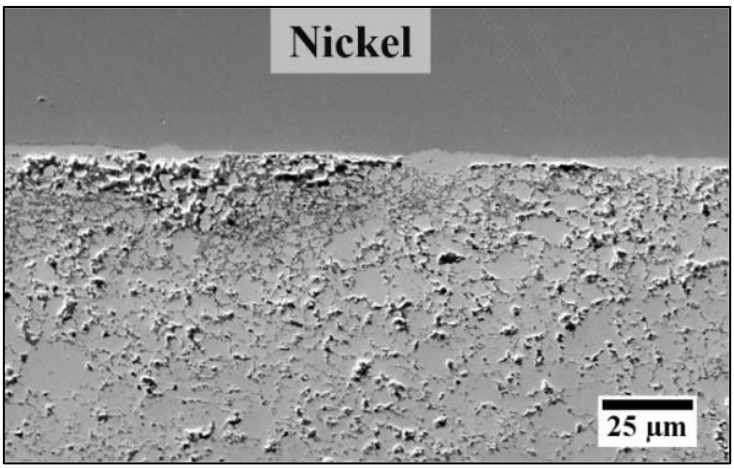

(b)

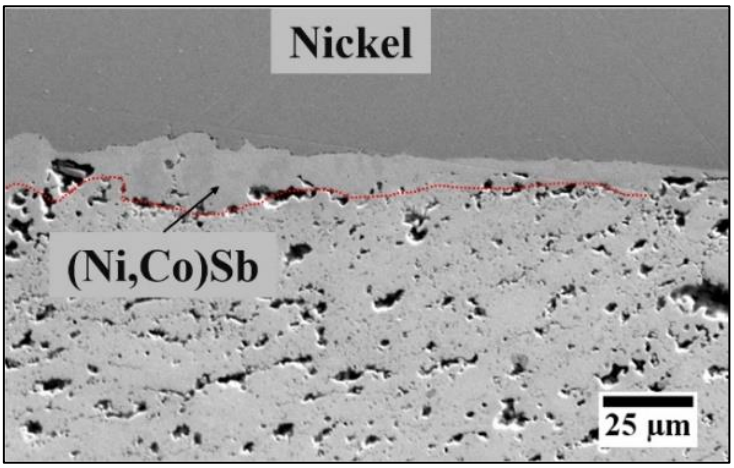

(c)

Figure 4.2-1: (a) Schematic illustration and interfacial microstructure of **(b)** $Mm_y(Fe,Co)_4Sb_{12}$ *p-type* and **(c)** $(Ni,Co)Sb_3$ *n-type* non-metallized skutterudites joined with nickel interconnect using Ag56-CuZnSn braze at 655 ºC 5 minutes in

flowing Ar. Regions highlighted in red highlight reaction layer of formed (Ni,Co)Sb secondary phase.

Figure 4.2-1a present a schematic illustration of the materials' configuration before high-temperature brazing using Ag56-CuZnSn braze and non-metallized thermoelectric materials. The SEM images of non-metallized $Mm_y(Fe,Co)_4Sb_{12}$ *p-type* and $(Ni,Co)_1Sb_3$ *n-type* thermoelectrics bonded with nickel interconnect using Silver-flo™ 56 braze at 655 ºC (5 min dwell and flowing argon) are presented in Figure 4.2-1b,c. A continuous interface was only found in the *n-type* contact (Figure 4.2-1c) with a reaction layer of (Ni,Co)Sb compound formed on the thermoelectric side. A high porous interface can be observed in the *p-type* contacts (Figure 4.2-1b) and minor reaction layer (Ni-Sb intermetallic compound) was found at the nickel–skutterudite interface. Moreover, lack of braze at the contacting interface and elemental copper and nickel residues that were found inside skutterudite matrix are presumably caused by the filler metal complete dissolution into the thermoelectric material and suggests that additional diffusion barrier is needed.

Encouraged by the recent findings on effectiveness of titanium as a diffusion barrier and adhesion layer for medium-high range skutterudites [46], multi-layered titanium (0.3 μm-thick) and nickel (1.2 μm-thick) coating was further investigated as potential metallization. Top metallization layer of nickel is usually needed due to the lack of braze wettability on titanium substrates caused by the stable TiOx oxide formations at the surface at higher temperatures. Figure 4.2-2 presents schematic illustration and interfacial microstructure of $Mm_y(Fe,Co)_4Sb_{12}$ *p-type* and $(Ni,Co)_1Sb_3$ *n-type* skutterudite substrates coated with 0.3 μm-thick titanium and 1.2 μm-thick nickel joined to nickel interconnect at 655 ºC using Silver-flo™ 56 braze (5 min dwell and flowing argon). Titanium and nickel layers

were not found at the joined interface, as their reactivity at high temperature results in a complete dissolution into thermoelectric material, and is consistent with Ref. [54].

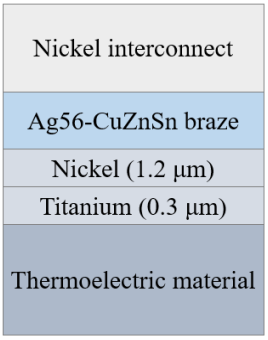

(a)

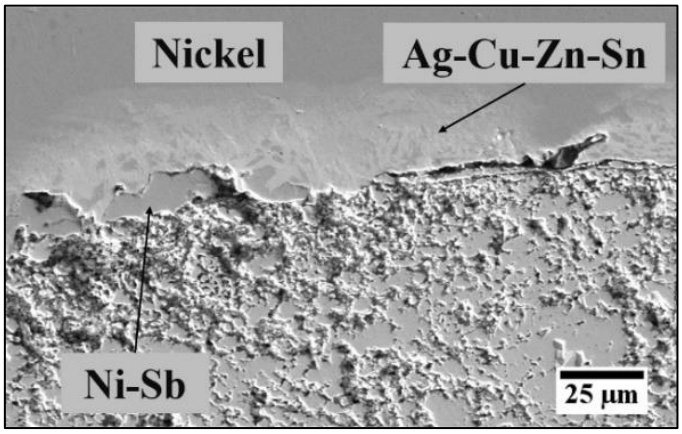

(b)

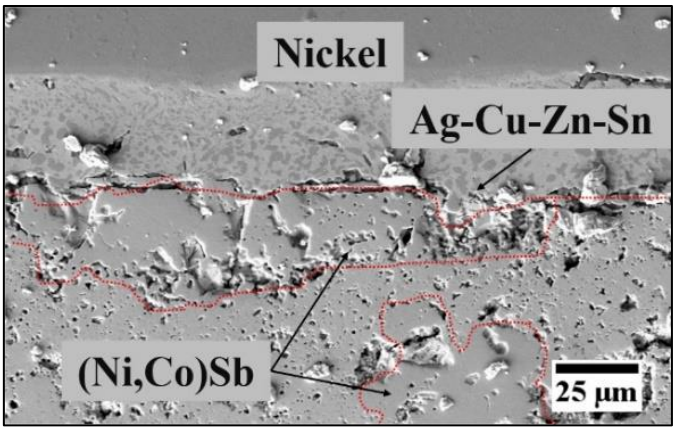

(c)

Figure 4.2-2: (a) Schematic illustration and interfacial microstructure of **(b)** $Mm_y(Fe,Co)_4Sb_{12}$ *p-type* and **(c)** $(Ni,Co)Sb_3$ *n-type* skutterudites coated with Ti (0.3 μm-thick) / Ni (1.2 μm-thick) joined with Ni using Ag56–CuZnSn braze at

655 ºC for 5 min in flowing Ar. Red lines highlight formed layer of (Ni,Co)Sb.

The metallization layers of 0.3 µm-thick titanium and 1.2 µm-thick nickel are dissolved into skutterudite matrix, leading to the thermoelectric material exposure to Ag56-CuZnSn braze. In such case, antimony can easily react with both braze and nickel interconnect (see Appendix A, Figure A. 4 and Figure A. 5) resulting in nickel-antimony reaction and intermetallic phases precipitation at the interface. Similar effects observed in non-metallized interfaces seen in Figure 4.2-1b,c such as complete braze dissolution in the *p-type* and formation of reaction layer at the *n-type* skutterudite interface suggest that 0.3 µm-thick titanium and 1.2 µm-thick nickel layers are not effective diffusion barrier / metallization as they are not stable at high joining temperature.

One of the most reported diffusion barrier for skutterudite material is molybdenum as it is proven to suppress antimony diffusion and formation of the interfacial reaction layer, i.e. observed in the $Yb_{0.3}Co_4Sb_{12}$ *n-type* skutterudite and Ti/Mo multi-layered system [111]. Figure 4.2-3 presents $Mm_y(Fe,Co)_4Sb_{12}$ *p-type* and $(Ni,Co)_1Sb_3$ *n-type* skutterudite substrate with 0.3 µm-thick molybdenum and 1.2 µm-thick nickel multilayer metallization joined to nickel substrate at 655 ºC using Silver-flo^{TM} 56 braze (5 min dwell and flowing Ar). It is worth mentioning that 0.3 µm-thick molybdenum layer is significantly thinner than previously reported by other research groups as PVD coating approach was used. Discontinuous layer of molybdenum was found to be partially delaminated from the skutterudite surface with visible cracking, presumably caused by the thermal stresses induced by the deposition process or differences of thermal expansion coefficient (CTE) of skutterudites and molybdenum. Elemental copper and nickel were found inside the porous structure, near the joining area, proving that braze and nickel coating were not effective barrier layers.

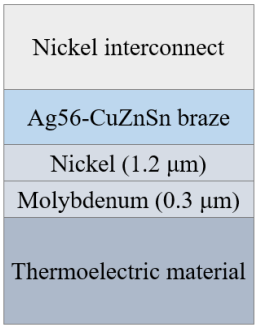

(a)

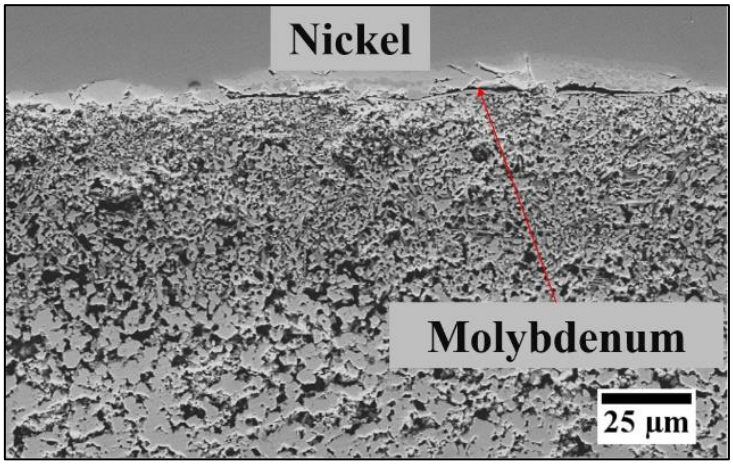

(b)

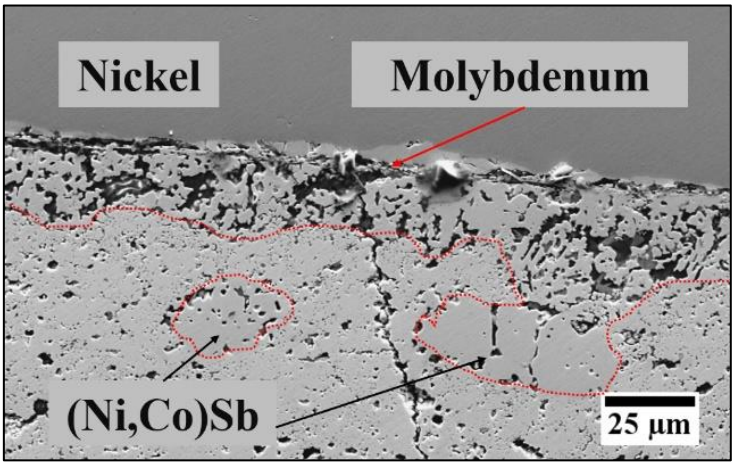

(c)

Figure 4.2-3: (a) Schematic illustration and interfacial microstructure of **(b)** $Mm_y(Fe,Co)_4Sb_{12}$ *p-type* and **(c)** $(Ni,Co)Sb_3$ *n-type* skutterudites coated with Mo (0.3 µm-thick) / Ni (1.2 µm-thick) and joined with nickel interconnect using Ag56–CuZnSn braze at 655 ºC for 5 minutes in flowing Ar. Red lines highlight formed reaction layer of (Ni,Co)Sb.

Moreover, 35 μm-thick porous microstructure of the thermoelectric – nickel interface, was observed in all brazed *p-type* thermoelectric samples and was confirmed by the EDS analysis to be antimony deficient region (Appendix A, Figure A. 6). Un-reacted antimony, which was found to precipitate at grain boundaries of skutterudite phase during the consolidation process and its presence was later confirmed by the XRD analysis (seen in Figure 4.1-1) is more likely to volatilize and evaporate at bonding conditions as the brazing temperature (655 ºC) exceeds both material consolidation (600 ºC) and elemental antimony melting point (~ 630 ºC [102]). It is also possible that the flux (combination of boric acid and borax) found in the commercial Silver-flo^{TM} 56 braze was too aggressive and the reason behind unreacted antimony dissolution during brazing. Although molybdenum was found at the *n-type* skutterudite – nickel interface after the high temperature brazing process, (Ni,Co)Sb reaction layer with similar compositions to the one found in non-metallized surfaces was observed.

Figure 4.2-4 presents the interfacial microstructure of the $Mm_y(Fe,Co)_4Sb_{12}$ *p-type* and $(Ni,Co)_1Sb_3$ *n-type* skutterudite substrate with coatings of chemically deposited Ni and Ni(P) layers, brazed to Ni(P) plated copper substrate at 655 ºC using Silver-flo^{TM} 56 braze. Similar to Ti/Ni coated samples (Figure 4.2-2), complete nickel dissolution in the skutterudite matrix can be observed, leading to formation of reaction layer at both *n-* and *p-type* skutterudites. As revealed by EDS analysis shown in Appendix 7 (Figure A. 7), the formation of two reaction layers at the *p-type* skutterudite and Ag-Cu-based braze interface can be observed including continuous layer of Ni-Sb (47 at% Ni – 53 at% Sb) and precipitates of Fe-P or Ni-P intermetallic compound. Intensive growth of (Ni,Co)Sb reaction layer is observed at the *n-type* skutterudite- braze interface (Figure 4.2-4c) as nickel from the Ni(P) layer was completely consumed by the antimony diffusing

from the skutterudite substrate and its diffusion from the metallic interconnect. EDS analysis of the *n-type* contacts can be found in Appendix A (Figure A. 8).

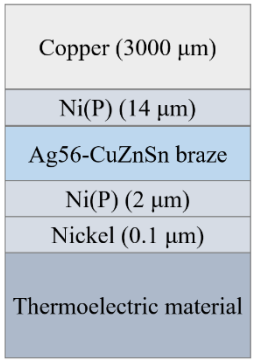

(a)

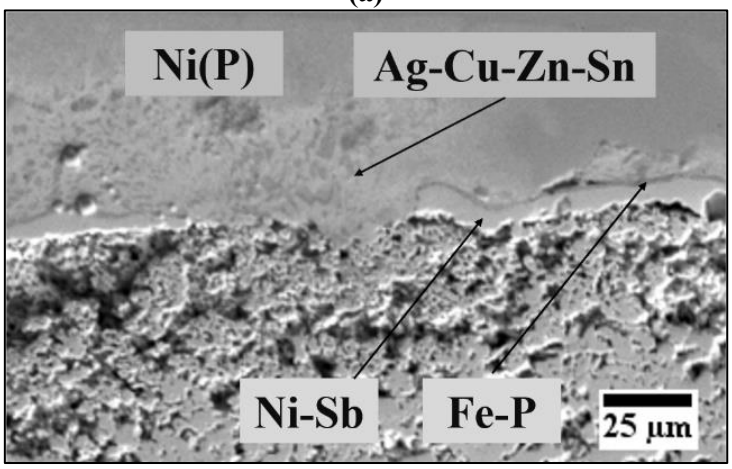

(b)

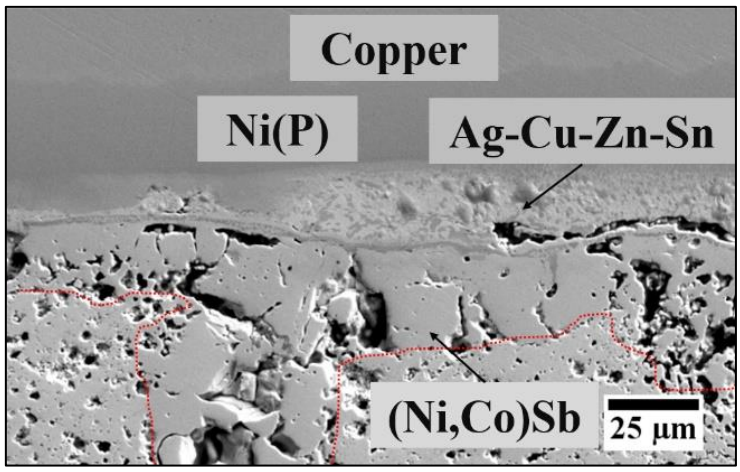

(c)

Figure 4.2-4: (a) Schematic illustration and interfacial microstructure of Ni (0.1 µm-thick) /Ni(P) (2 µm-thick) plated **(b)** $Mm_y(Fe,Co)_4Sb_{12}$ *p-type* and **(c)** $(Ni,Co)Sb_3$ *n-type* skutterudites joined with Cu/Ni(P) interconnect using Ag56–CuZnSn at 655 ºC (5 min in Ar). Regions highlighted in red shows (Ni,Co)Sb phase.

In order to summarize microstructural analysis of *p-* and *n-type* thermoelectric material joined to nickel interconnect using Ag56-CuZnSn braze at 655 ^{o}C in argon, interface was evaluated in terms of materials' interfacial porosity, cracks or voids within contact and secondary phase formation (Table 4.2-1). As mentioned above, all brazed *p-type* materials were characterized with porous microstructure and voids at the contact interface. Moreover, titanium/nickel and Ni/Ni(P) metallization along with Ag56-CuZnSn braze were dissolved in the *p-* and *n-type* thermoelectric material, as only constituent elements of the braze were found within thermoelectric substrate. Secondary phases of Ni-Sb intermetallic compounds and (Ni,Co)Sb layers were found in the $Mm_y(Fe,Co)_4Sb_{12}$ *p-type* and $(Ni,Co)_1Sb_3$ *n-type* contacts respectively. Brittle intermetallic phase of crystalline Ni-P was found in the Ni/Ni(P) coated *n-type* skutterudite contacts along with Fe-P phase in the *p-type* material.

Table 4.2-1: Summary of the microstructural analysis of skutterudites joined with nickel interconnect using Ag56–CuZnSn braze at 655 ^{o}C (5 min in Ar).

	Mm*$_y$(Fe,Co)$_4$Sb$_{12}$ *p-type			**(Ni,Co)Sb$_3$ *n-type***		
	Porosity	**Cracks / voids**	**Second phases**	**Porosity**	**Cracks / voids**	**Second phases**
Non-metallized	Yes	Yes	Ni-Sb IMCs	No	No	(Ni,Co)Sb
Ti/Ni (0.3/1.2 µm)	Yes	Yes	Ni-Sb IMCs	No	Yes	(Ni,Co)Sb
Mo/Ni (0.3/1.2 µm)	Yes	Yes	minimal	No	Yes	(Ni,Co)Sb
Ni/Ni(P) (0.1/2 µm)	Yes	Yes	Ni-Sb and Ni-P, Fe-P IMCs	No	Yes	(Ni,Co)Sb and Ni-P IMCs

4.2.2 Ag Paste

As seen in Chapter 4.2.1, lack of high temperature stability of thermoelectric material and partial dissolution of nickel interconnect in the α(Cu) phase, suggests Cu-based joining materials might be not suitable in high temperature operations.

Despite Ag and Ni have the same crystal structure and small difference in atom radii (within 15%), the solubilities of Ag in ffc (Ni) phase and Ni in fcc (Ag) phase are very limited [111]. Nickel and silver are both thermodynamically stable and not soluble in each other at any concentration range and combination of these two is believed to be a good choice for high temperature operations, suitable in the skutterudite-based thermoelectric system. In the current module design, copper with Ni(P) plated layer is in contact with the joining material, so that no reaction layer between Ni-based interconnect and Ag-based joining material is expected. The skutterudite materials have a high Sb content which undergo eutectic reaction with Ag at 483 ºC [112] so that additional diffusion barrier is normally needed to avoid formation of undesirable phases at the thermoelectric-braze interface. Figure 4.2-5 presents interfacial microstructure of non-metallized $Mm_y(Fe,Co)_4Sb_{12}$ *p-type* and $(Ni,Co)Sb_3$ *n-type* skutterudite materials joined to nickel interconnect using Ag paste (Q-INKS S.r.l, Italy) at 652 ºC in Ar. Although no interaction between silver and nickel was observed, two reaction layers with a composition of Co - 40 at% Ni – 46 at% Sb and Co – 68 at% Ni - 27 at% Sb were observed in the $(Ni,Co)Sb_3$ *n-type* contacts. Similar to Ref. [43], layers identified by EDS were (Ni,Co)Sb and Ni_5Sb_2 IMC phase with 5 at% Co solubility. Although silver is proven not to react with thermoelectric material and nickel interconnect, formation of Ni-Sb-Co intermediate compound at the contacting interface suggest excessive nickel diffusion through silver joining material.

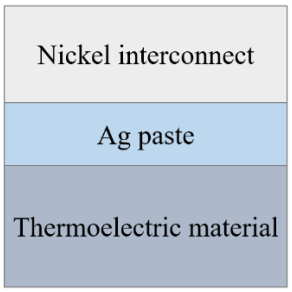

(a)

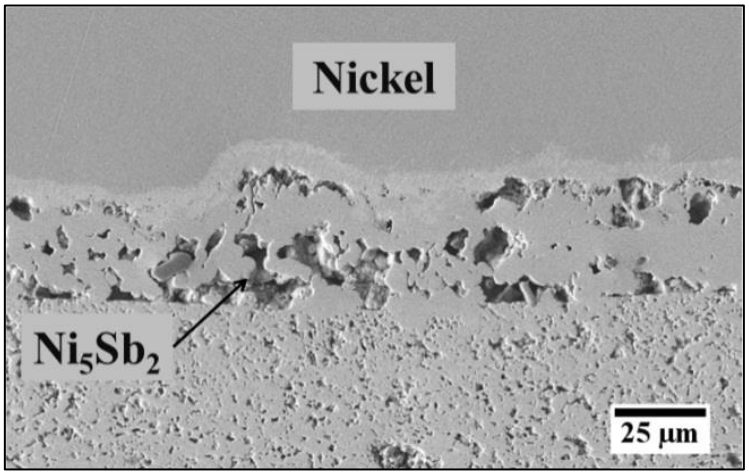

(b)

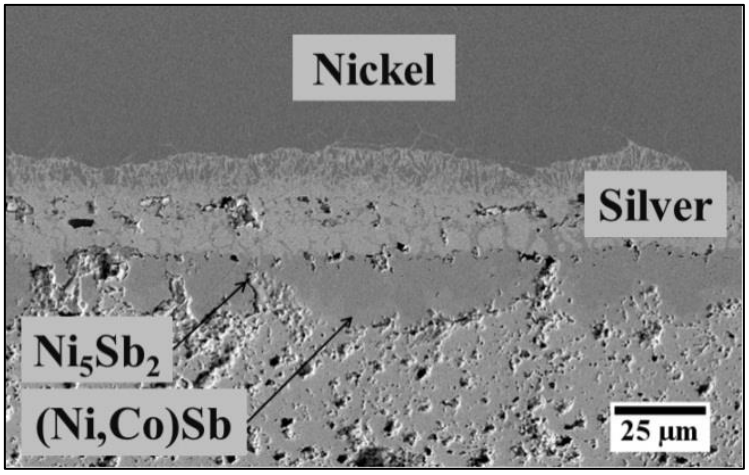

(c)

Figure 4.2-5: (a) Schematic illustration of contact configuration before heat treatment and interfacial microstructure of **(b)** $Mm_y(Fe,Co)_4Sb_{12}$ *p-type* and **(c)** $(Ni,Co)Sb_3$ *n-type* non-metallized skutterudites joined with nickel interconnect using Ag paste at 652 ºC in Ar.

Figure 4.2-6 presents interfacial microstructure of $Mm_y(Fe,Co)_4Sb_{12}$ *p-type* and $(Ni,Co)Sb_3$ *n-type* skutterudites with 0.3 μm-thick titanium and 1.2 μm-thick nickel metallization joined to nickel interconnect using Ag paste (Q-INKS S.r.l, Italy) at 652 °C in Ar. Similar to Ag56-CuZnSn brazed contacts (Figure 4.2-2), complete dissolution of titanium and nickel into skutterudite matrix led to exposure of bulk thermoelectric to the joining agent and thicker than applied metallization layers need to be deposited. Similar to non-metallized material, formation of two different reaction layers at the silver/skutterudite interface as identified by EDS analysis (Appendix A, Figure A. 9) with a composition of Co – 49.18 at% Sb – 41.42 at% Ni attributed to the (Co,Ni)Sb phase and Co – 30.34 at% Sb – 66.55 at% Ni attributed to Ni_5Sb_2 phase with 3.1 at% Co solubility [43].

One of the attributes of high-temperature Ag-based joining process is an extensive growth of the reaction layer at the skutterudite–silver interface as a result of interactions between constituents of the base thermoelectric substrate and nickel interconnect material. Although silver is in contact with the thermoelectric material, only nickel was presumed to diffuse through silver's thick layer and silver itself did not react with any of the element of the skutterudite. The formation of layered intermediate compounds is normally attributed to the formation of mechanically strong bonds between two joined components, but their high-temperature stability might suffer due to extensive growth of these layers during the high temperature service. Moreover, when a thick layer of brittle intermetallic compounds is formed at the interfaces, room temperature joint strength is drastically reduced.

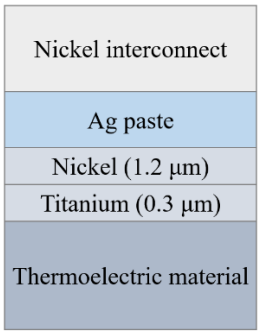

(a)

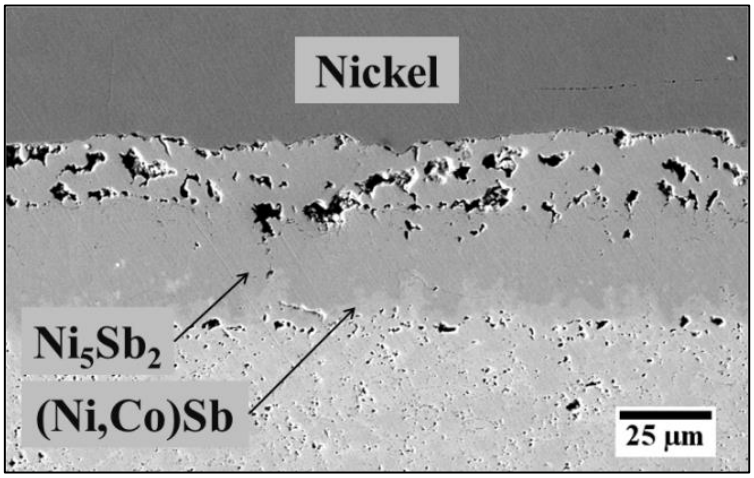

(b)

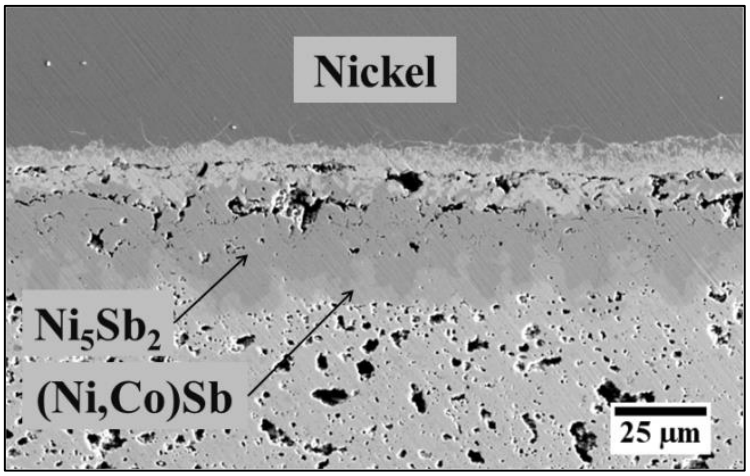

(c)

Figure 4.2-6: (a) Schematic illustration of contacts configuration before heat treatment and interfacial microstructure of **(b)** $Mm_y(Fe,Co)_4Sb_{12}$ *p-type* and **(c)** $(Ni,Co)Sb_3$ *n-type* skutterudites with Ti (0.3 μm-thick) / Ni (1.2 μm-thick) metallization joined with nickel interconnect using Ag paste at 652 ºC in Ar.

One of the challenges in the formation of robust contacts is formation of chemically stable intermediate phases that could not intensively grow over prolonged period. To achieve this, 0.3 μm-thick molybdenum diffusion barrier and 1.2 μm-thick top nickel layers were effectively deposited on the top of $Mm_y(Fe,Co)_4Sb_{12}$ *p-type* and $(Ni,Co)Sb_3$ *n-type* skutterudites and joined with nickel interconnect using Ag paste (Q-INKS S.r.l, Italy) at 652 ºC in Ar. As seen in Figure 4.2-7 there is no formation of continuous Ni-Sb reaction layer at joined interface, as molybdenum successfully acts as diffusion barrier and successfully reduce nickel and antinomy interdiffusion. Nonetheless, significant mismatch of thermal expansion coefficients (CTE) between Co-based *p-type* skutterudites (~ 11 ppm/K), Co-based *n-type* skutterudite materials (~ 9 ppm/K) and molybdenum (~ 4.8 – 5.1 ppm/K) leads to the visible delamination of molybdenum layer that might disintegrate at high-temperature operations. Although molybdenum effectively reduces nickel and antimony interdiffusion, thin Ni-Sb phase precipitates still can be observed inside silver joining material.

Encouraged by the excellent high-temperature stability of the nickel–silver interface, Ni / Ni(P) metallized $Mm_y(Fe,Co)_4Sb_{12}$ *p-type* and $(Ni,Co)Sb_3$ *n-type* thermoelectrics were joined with nickel tabs using the high-temperature Ag paste (Q-INKS S.r.l, Italy) at 652 ºC in Ar. As expected, Ni(P) – skutterudites interface instabilities caused by the nickel depletion from Ni(P) coating and its dissolution in the skutterudite matrix as well as Ni interconnect diffusion through Ag layer led to the formation of Ni-Sb reaction layer, and are consistent with other studies on Ni–skutterudite interfaces [42,43].

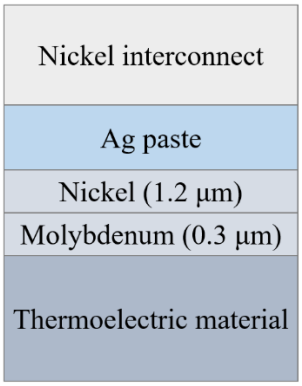

(a)

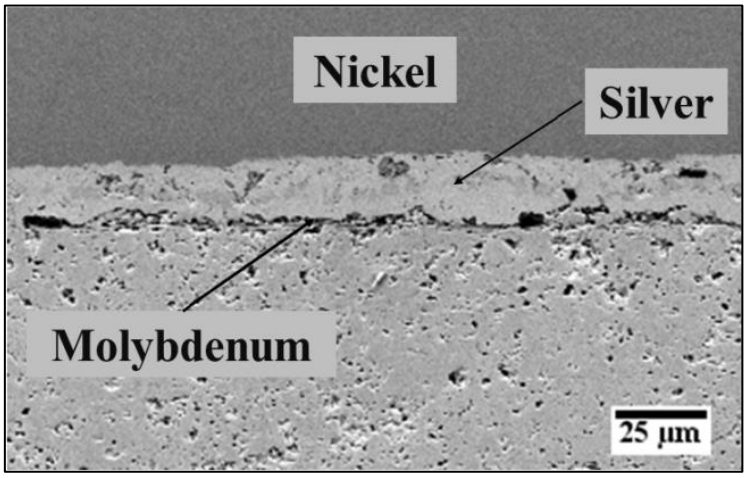

(b)

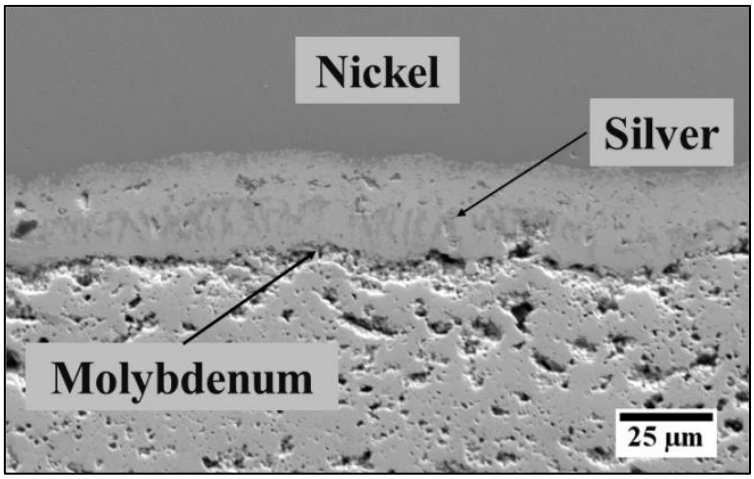

(c)

Figure 4.2-7: (a) Schematic illustration of contacts configuration before heat treatment and interfacial microstructure of **(b)** $Mm_y(Fe,Co)_4Sb_{12}$ *p-type* and **(c)** $(Ni,Co)Sb_3$ *n-type* skutterudites with Mo (0.3 µm-thick) and Ni (1.2 µm-thick) metallization joined with nickel interconnect using Ag paste at 652 ºC in Ar.

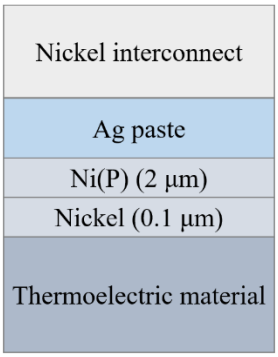

(a)

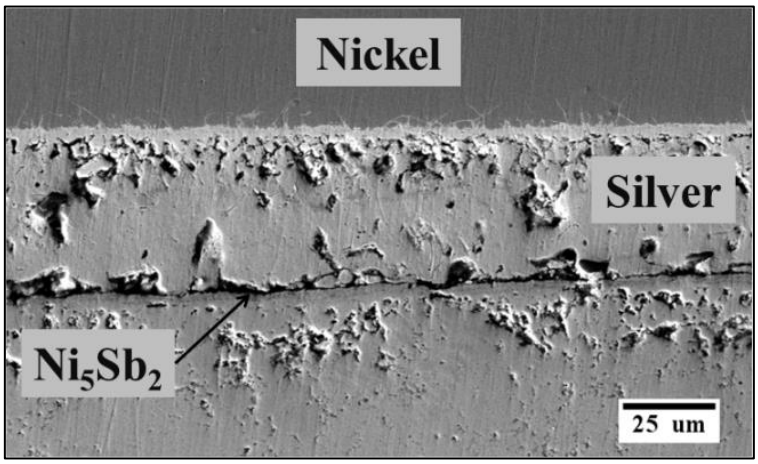

(b)

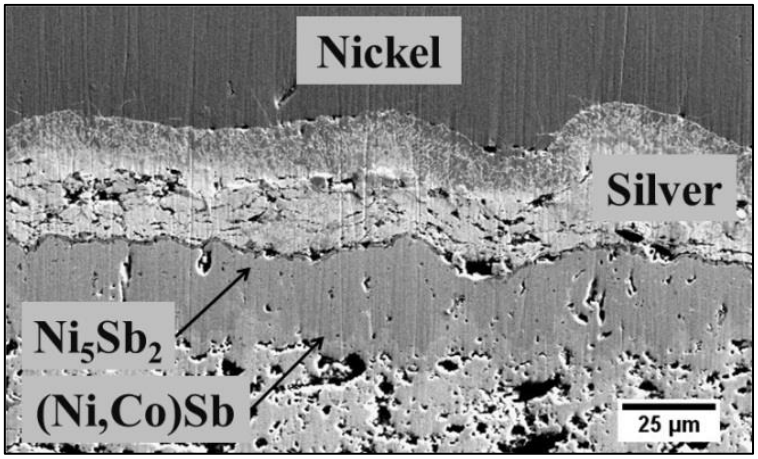

(c)

Figure 4.2-8: (a) Schematic illustration of contacts configuration before heat treatment and interfacial microstructure of **(b)** $Mm_y(Fe,Co)_4Sb_{12}$ *p-type* and **(c)** $(Ni,Co)Sb_3$ *n-type* skutterudites with Ni (0.1 µm-thick) / Ni(P) (2 µm-thick) metallization joined with nickel interconnect using Ag paste at 652 °C in Ar.

Similarly to non-metallized (Figure 4.2-5) and Ti / Ni coated (Figure 4.2-6) skutterudites, formation of two different reaction layers at the silver/skutterudite was observed with a composition of Co – 49.18 at% Sb – 41.42 at% Ni which can be attributed to the (Co,Ni)Sb phase and Co – 30.34 at% Sb – 66.55 at% Ni which is Ni_5Sb_2 phase with minimal Co solubility. Interestingly, $Mm_y(Fe,Co)_4Sb_{12}$ *p-type* thermoelectric material joined using Ag paste did not exhibit porous microstructure, as observed in material joined using silver-flo^{TM} 56 braze (Figure 4.2-4) .

In order to summarize microstructural analysis of *p*- and *n-type* thermoelectric material joined to nickel interconnect using Ag paste at 652 ^{o}C in Ar, interface was evaluated in terms of materials' porosity, cracks or voids formed within contact interface and secondary phase formation (Table 4.2-2). As opposed to Ag56-CuZnSn - *p-type* contacts brazed at similar temperature, no material porosity was observed near the contact interface, neither Ag dissolution by the thermoelectric material. Although Ag joining material did not react with thermoelectrics, extensive nickel diffusion from interconnect through silver layer led to formation of two different reaction layers of Ni_5Sb_2 IMCs and (Ni,Co)Sb phase. Molybdenum (0.3 μm-thick) diffusion layer was able to effectively inhibit nickel diffusion through Ag joining material but small precipitation of Ni-Sb phase was still observed in contacting interfaces.

Table 4.2-2: Summary of the microstructural analysis of skutterudites joined with nickel interconnect using Ag paste at 652 ºC in Ar.

	$Mm_y(Fe,Co)_4Sb_{12}$ *p-type*			$(Ni,Co)Sb_3$ *n-type*		
	Porosity	**Cracks / voids**	**Second phases**	**Porosity**	**Cracks / voids**	**Second phases**
Non-metallized	No	Yes	Ni_5Sb_2	No	No	Ni_5Sb_2 and (Ni,Co)Sb
Ti/Ni (0.3/1.2 μm)	No	Yes	Ni_5Sb_2 and (Ni,Co)Sb	No	Yes	Ni_5Sb_2 and (Ni,Co)Sb
Mo/Ni (0.3/1.2 μm)	No	Yes	Ni-Sb precipitates	No	Yes	Ni-Sb precipitates
Ni/Ni(P) (0.1/2 μm)	No	Yes	Ni_5Sb_2	No	No	Ni_5Sb_2, (Ni,Co)Sb and Ni-P IMCs

4.2.3 Electrical Performance Evaluation of Ag56-CuZnSn Braze and Ag Paste Contacts

Figure 4.2-9a presents *Rc* measurements performed on non-metallized and metallized skutterudites joined with Ni interconnect using 56 at% Ag - 22 at% Cu – 17 at% Zn – 5 at% Sn braze (Johnson Matthey, UK) at 655 ºC (5 minutes dwell with flowing Ar). It can be seen that *Rc* for all $(Ni,Co)Sb_3$ *n-type* contacts is in the acceptable range below < $7.28 \cdot 10^{-5}$ Ω·cm^2 [27]. The lowest value of $(3.12 \pm 0.77) \cdot 10^{-5}$ Ω·cm^2 was obtained for the *n-type* contact formed without metallization and using Silver-flo^{TM} 56 braze, presumably enhanced by the formation of thin, continuous (Ni,Co)Sb reaction layer without visible cracks or voids inside as shown in Figure 4.2-1b. Slightly higher *Rc* values of $(6.69 \pm 1.14) \cdot 10^{-5}$ and $(7.34 \pm 0.77) \cdot 10^{-5}$ Ω·cm^2 were measured at nickel interconnect - $(Ni,Co)Sb_3$ *n-type* contacting interfaces with Ti (0.3 μm) / Ni (1.2 μm) and Ni (0.1 μm) / Ni(P) (2

μm) metallization respectively. Both contacts as proven by SEM analysis, showed dissolution of the metallization layer and interface degradation by the extensive formation of (Ni,Co)Sb reaction layer with many crack and voids inside (Figure 4.2-2b and Figure 4.2-4b). The Mo (0.3 μm) / Ni (1.2 μm) metallization layers were not dissolved in the skutterudite matrix, and despite diffusion barrier penetration and reaction layer formation in the *n-type* contacts, *Rc* was measured to be $(4.91 \pm 1.04) \cdot 10^{-5}$ Ω·cm^2.

High-temperature Silver-flo^{TM} 56 braze was proven to be partially destructive to $Mm_y(Fe,Co)_4Sb_{12}$ *p-type* thermoelectric material as the microstructure of near-the-contact surfaces showed intensive porosity, presumably caused by the braze dissolution in the skutterudite matrix (Figure 4.2-1a) or aggressive flux (boric acid and borax). As expected, *Rc* of $Mm_y(Fe,Co)_4Sb_{12}$ *p-type* – nickel interconnects did not fall below acceptable range and were as high as $(1.41 \pm 0.46) \cdot 10^{-4}$ Ω·cm^2 in non-metallized specimens. The *Rc* values of $(8.29 \pm 2.04) \cdot 10^{-5}$ Ω·cm^2, $(8.78 \pm 7.63) \cdot 10^{-5}$ Ω·cm^2 and $(1.08 \pm 0.1) \cdot 10^{-4}$ Ω·cm^2 were measured at nickel - ($Mm_y(Fe,Co)_4Sb_{12}$ *p-type* contacts with Ti (0.3 μm) / Ni (1.2 μm), Mo (0.3 μm) / Ni (1.2 μm) and Ni (0.1 μm) / Ni(P) (2 μm) metallization respectively. It is believed, that the high degradation rate of $Mm_y(Fe,Co)_4Sb_{12}$ *p-type* thermoelectric material is caused by presence of un-reacted antinomy residing at the grain boundaries which at high brazing temperature (higher than sublimation of antimony ~ 630 ^oC [102]) is either partially vaporized and along with Ag-Cu based braze dissolved in the skutterudite matrix. The porosity, also observed in SEM analysis (Figure 4.2-1a), inhibits continuous electron flow through the grain boundaries and thermoelectric material, by effectively reducing the contact area.

The electrical contact resistance (*Rc*) of joints formed between $Mm_y(Fe,Co)_4Sb_{12}$ *p-type* and $(Ni,Co)Sb_3$ *n-type* thermoelectric material and nickel

interconnect using Ag-paste along with various thermoelectric metallization are presented in Figure 4.2-9b. The (Ni,Co)Sb_3 *n-type* connections have acceptable values, below the required range of < 7.28 $\cdot 10^{-5}$ $\Omega \cdot cm^2$. It is consistent with microstructural analysis shown in Figure 4.2-5b, due to the formation of voids-free contacts and despite the formation of two distinguish IMCs at the interface such as (Co,Ni)Sb and Ni_5Sb_2 phase. Interestingly, $Mm_y(Fe,Co)_4Sb_{12}$ *p-type* material joined to nickel interconnect reach low value of $(3.43 \pm 0.67) \cdot 10^{-5}$ $\Omega \cdot cm^2$ when Ti (0.3 μm) / Ni (1.2 μm) metallization were employed. It is consistent with the results on Ag56-CuZnSn brazed samples as Ti/Ni metallization was dissolved and the reaction layers of (Co,Ni)Sb and Ni_5Sb_2 phase were formed at the interface (Figure 4.2-6a). At the same time, Ag paste does not completely wet non-metallized $Mm_y(Fe,Co)_4Sb_{12}$ *p-type* material as seen in Figure 4.2-5a, which transferred to *Rc* values > 6.8 $\cdot 10^{-5}$ $\Omega \cdot cm^2$ which is higher than acceptable limit [27].

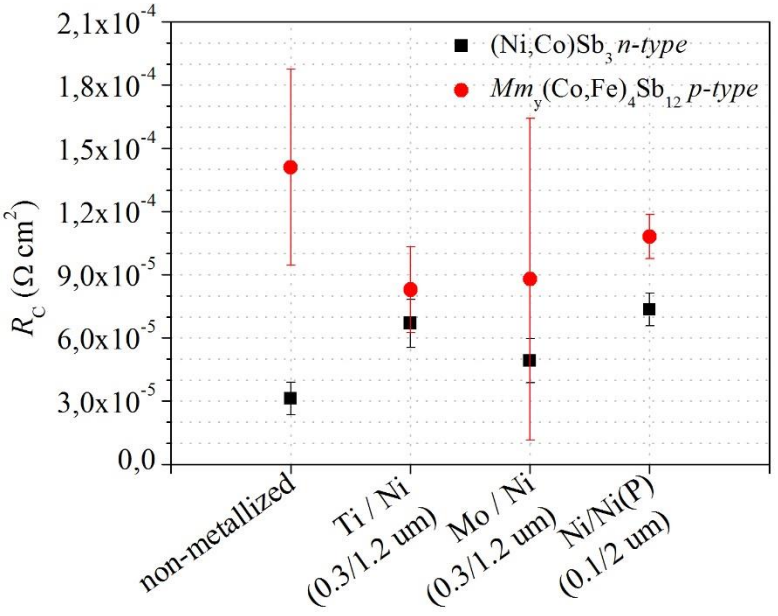

(a)

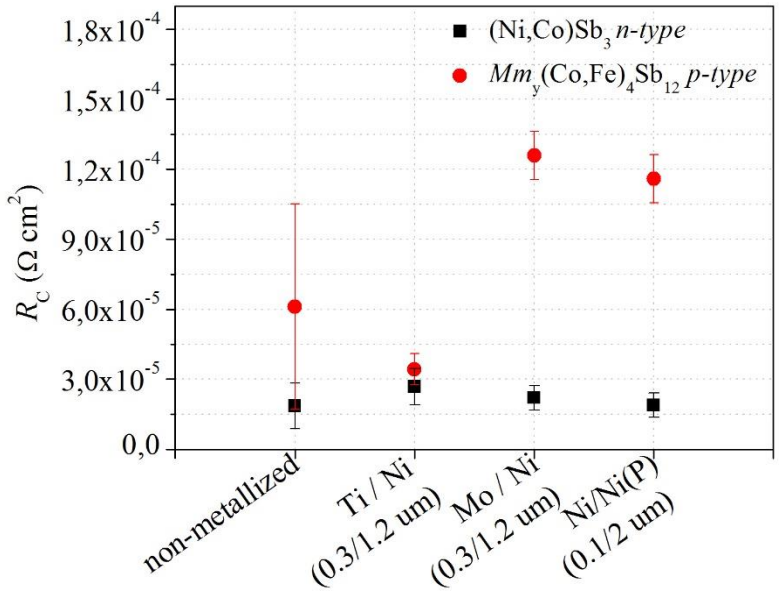

(b)

Figure 4.2-9: Graphs representing the electrical contact resistance (*Rc*) of $Mm_y(Fe,Co)_4Sb_{12}$ *p-* and $(Ni,Co)Sb_3$ *n-type* skutterudites with various metallization joined with nickel using **(a)** Ag56-CuZnSn braze (Johnson Matthey, UK) at 655 ºC (5 minutes in Ar) and **(b)** Ag paste (Q-INKS S.r.l, Italy) at 652 ºC in Ar.

4.2.4 Ag flake – based Conductive Adhesive

Since silver and nickel are not soluble in each other in any concentration range, lack of interaction between joining material and interconnect works in benefit for the contact chemical stability at higher temperatures. As proven in Chapter 4.2.1 and 4.2.2, instabilities at the nickel interconnect – Ag-based braze - skutterudite interface were the main cause of extensive intermediate phase formation that could possibly lead to joint embrittlement and TE device failure. The initial joining trials showed that antimony is the most diffusive element (along with cobalt being second the fastest) in the *p*- and *n-type* skutterudite material and tends to form brittle intermetallic phases with most of the transition elements in various stoichiometries. In order to inhibit Sb and Co diffusion, an effective diffusion barrier that could be chemically inert with both skutterudite and joining material and a reliable joining technology are needed. As already reported in [61], $CoSi_2$- and Co_2Si-based silicides were successfully implemented as diffusion barriers on *n-type* skutterudite materials [61]. Moreover, refractory metals such as tungsten or molybdenum, which are chemically inert with most of the elements (including antimony and cobalt) might be a possible choice for stable diffusion barrier that inhibit intermediate layer formation at contacting interfaces but might delaminate from TE due to the CTE mismatch.

As an addition to diffusion barrier improvements, a significantly lower temperature bonding process was investigated. The Ag flake-based conductive adhesive (AREMCO Inc, US) was used as joining material for skutterudites and metal interconnect cured at 110 ^{o}C for 60 minutes in the air. One of the advantages of low-temperature bonding process is the possibility to form robust joints without the need to subject skutterudite materials to higher-than-sintering temperature, as necessary in high-temperature joining experiments using Ag-Cu-

based and Ag pastes. Additionally, silver flakes that constitute Ag flake-based joining material, as advised by the supplier, are stable at temperatures higher than initial joining temperature, up to 960 ºC (Ag melting point). In the joined contacts, both contacting interfaces and joining material itself are responsible for the final performance of the joint. In the case of low-temperature silver based joining materials (Ag flake-based conductive adhesive and sintered Ag-nano, as further presented in Chapter 4.2.5), top Au or ENIG metallization layer was implemented on both skutterudite and nickel interconnect substrates as noble metal is usually required for satisfactory adhesion. Although any additional metallization layer may potentially influence the electrical performance of the joint, Au layer was essential, as initial tests performed on uncoated skutterudites and nickel interconnects joined with low-temperature, Ag-based joining materials resulted in high contact resistance values in the range between 10^{-3} and 10^{-4} Ωcm^2, below initial expectations.

~0.5 µm-thick tungsten and 0.05 µm-thick top gold layers were investigated as potential diffusion barrier and top metallization layer on both $Mm_y(Fe,Co)_4Sb_{12}$ *p-type* and $(Ni,Co)Sb_3$ *n-type* skutterudite materials. Pure tungsten is hard and brittle material, which makes it difficult to deposit using PVD technique and the resulting layer often embrittles during the machining of thermoelectric legs. As seen in Figure 4.2-10, thin and continuous layer of tungsten (< 0.5 µm) was found at the skutterudite – silver flake interface and no delamination or crack were observed. Moreover, as joining process was performed at low temperatures (T_{PEAK} = 110 ºC for 1 hour in air), no damage was caused to thermoelectric material's properties and its microstructure.

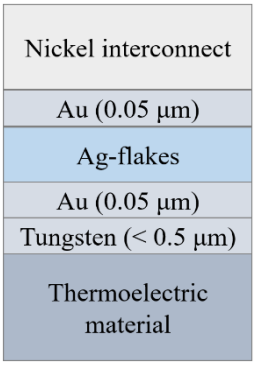

(a)

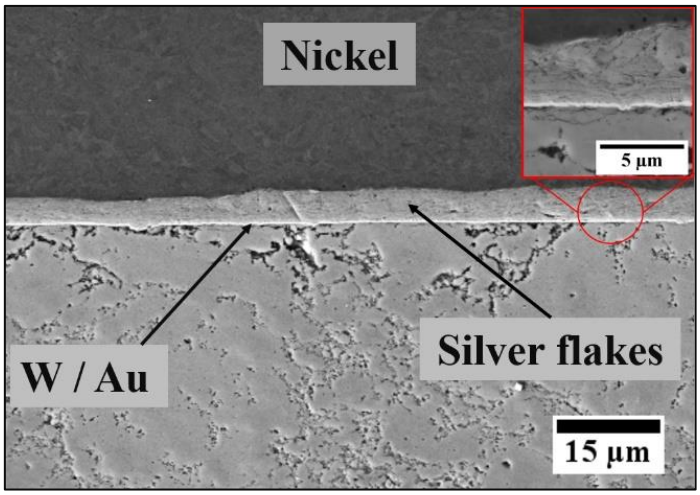

(b)

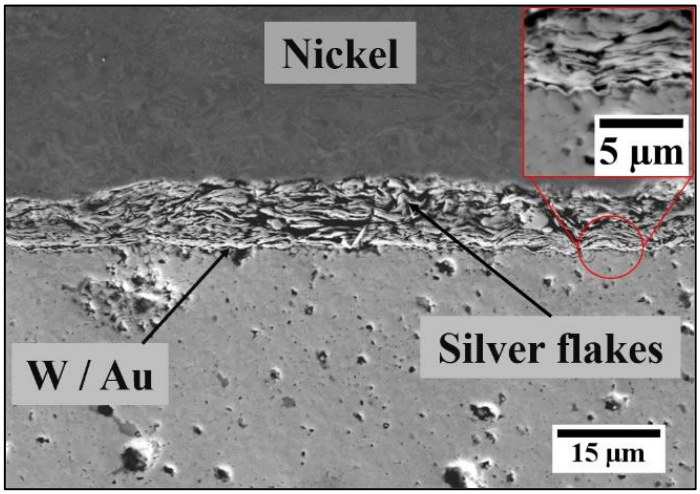

(c)

Figure 4.2-10: (a) Schematic illustration of contacts configuration and interfacial microstructure of **(b)** $Mm_y(Fe,Co)_4Sb_{12}$ *p-type* and **(c)** $(Ni,Co)Sb_3$ *n-type* skutterudites with W (<0.5 µm-thick) / Au (0.05 µm-thick) metallization joined with Au coated Ni interconnect using Ag flakes (AREMCO Inc.) at 110 ºC in the air.

Encouraged by the recent findings on silicide-based metallization for Si semiconductors, including $CoSi_2$ and Co_2Si [61], titanium silicides [113] and nickel silicides [114], 2 μm-thick tungsten silicide (WSi_2) and 0.05 μm-thick top Au layers were investigated as potential metallization on both $Mm_y(Fe,Co)_4Sb_{12}$ *p-type* and $(Ni,Co)Sb_3$ *n-type* skutterudite materials. It is believed that amorphous WSi_2 layer will stay stable during the high temperature operations (up to 650 ºC) as this material has high crystallization temperature [115] and both tungsten (W) and silicon (Si) are chemically inert with antimony (Sb). As shown in Figure 4.2-11, a continuous layer of WSi_2 can be found at the interfaces and good adhesion between sintered Ag flake-based conductive adhesive and WSi_2 (> 1 μm)/Au (0.05 μm) coated $Mm_y(Fe,Co)_4Sb_{12}$ *p-* and $(Ni,Co)Sb_3$ *n-type* skutterudite materials. It is worth highlighting that the ~ 0.05 μm-thick Au layer was not observed in the EDS mapping due to equipment detection limits and initial XRD tests on WSi_2/Au coated skutterudites showed wide amorphous peak of WSi_2 layer (EDS mapping showed in Appendix 14). Moreover, the formation of (Co,Ni)Sb and Ni_5Sb_2 intermetallic reaction layers was successfully inhibit and no reaction between WSi_2/Au coating and both $Mm_y(Fe,Co)_4Sb_{12}$ *p-type* and $(Ni,Co)Sb_3$ *n-type* was observed. The interfacial reaction layer was not found in any low-temperature, Ag flake-based contacts, including W/Au sputtered (Figure 4.2-10) and Ni / Ni(P) / Au plated (Figure 4.2-12) skutterudites, as opposed to high temperature contacts of 56 at% Ag – 22 at% Cu – 17 at% Zn – 5 at% Sn braze (Figure 4.2-1) and Ag paste (Figure 4.2-5).

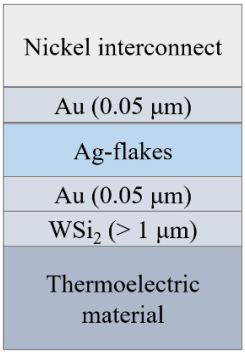

(a)

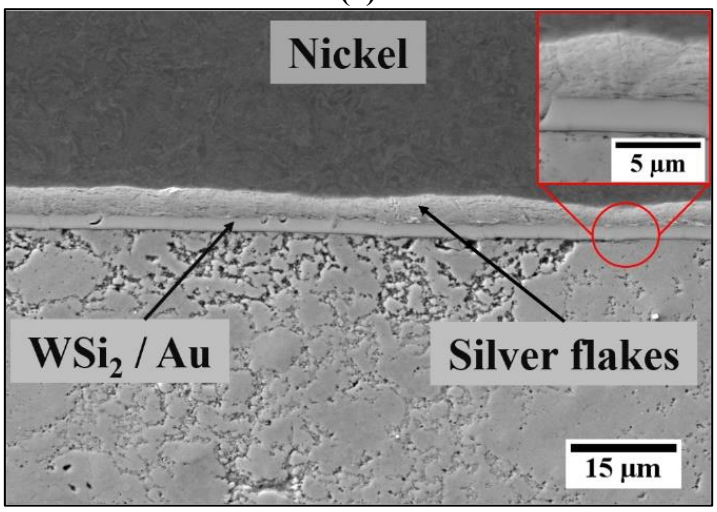

(b)

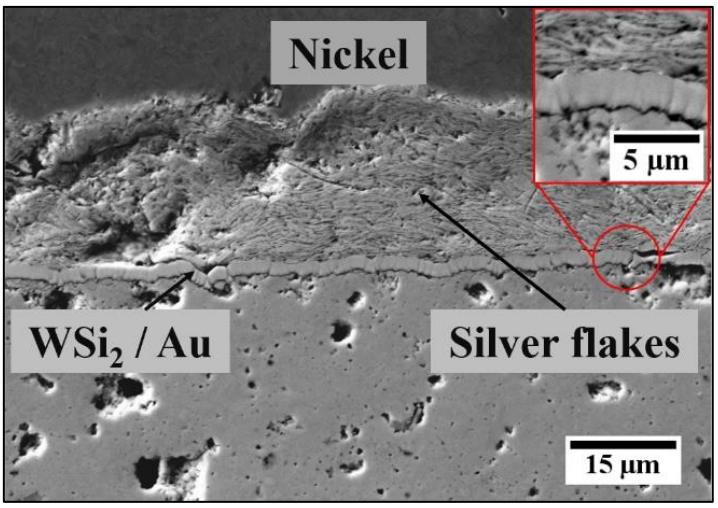

(c)

Figure 4.2-11: (a) Schematic illustration of contacts configuration and interfacial microstructure of **(b)** $Mm_y(Fe,Co)_4Sb_{12}$ *p-type* and **(c)** $(Ni,Co)Sb_3$ *n-type* skutterudites with WSi_2 (>1 µm-thick) / Au (0.05 µm-thick) metallization joined with Au/Ni interconnect using Ag flakes (AREMCO Inc.) at 110 °C in air.

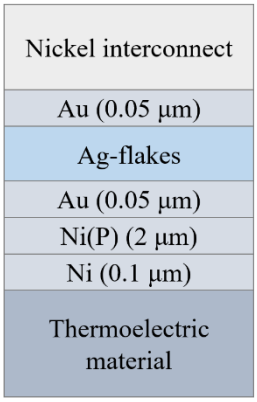

(a)

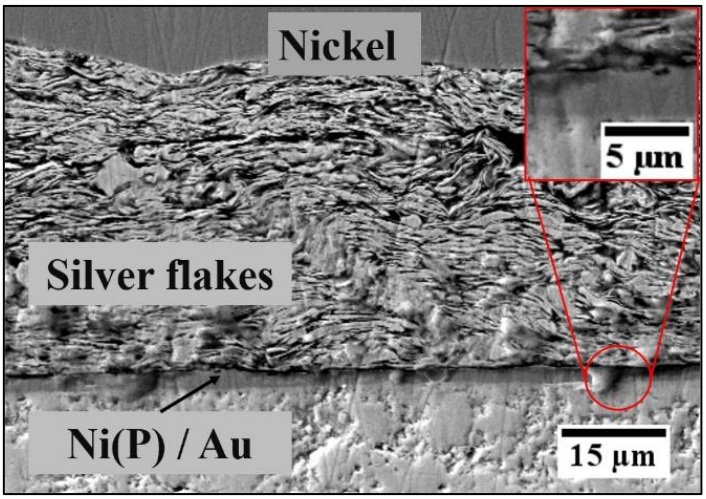

(b)

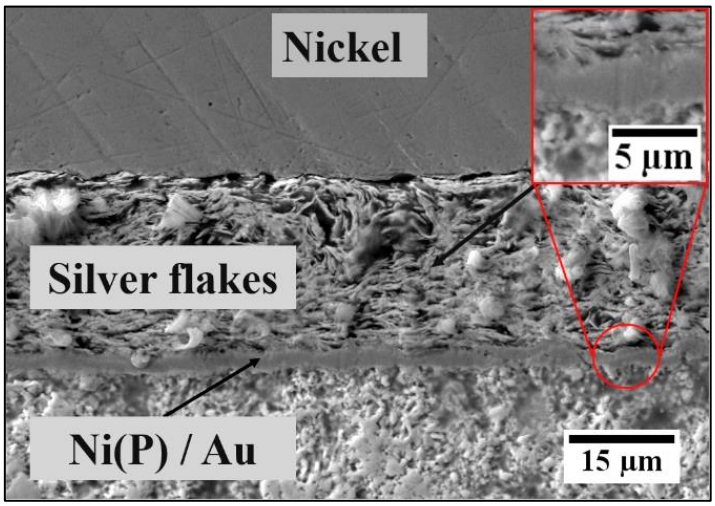

(c)

Figure 4.2-12: (a) Schematic illustration of contacts configuration and interfacial microstructure of **(b)** $Mm_y(Fe,Co)_4Sb_{12}$ *p-type* and **(c)** $(Ni,Co)Sb_3$ *n-type* skutterudites with Ni/Ni(P)/Au metallization joined with Au coated Ni interconnect using Ag flakes (AREMCO Inc.) at 110 ºC in the air.

4.2.5 Ag-nano Paste Sintering

Nanoparticle sintering is recently being considering as best joining alternative for typical SAC solders used in microelectronics assembly. The exceptional properties of Ag-nano particles have been recently tested in high-temperature systems as the material's remelting temperature is higher than initial curing temperature. Encouraged by the results of low temperature Ag flake-based joining technique, Ag-nano paste (NBE Technologies, LLC, US) was used in the same metallization configuration. Although Ag is the main constituent of both joining material, Ag-nano paste is based on nano spheres while the Ag based conductive adhesive contains flake-shaped silver particles but mechanism behind bonding is very similar. Thermal sintering is the main mechanism involved in forming nanoparticles silver contacts for low temperature diffusion bonding and it is controlled by sintering temperature and time. The sintering temperature of common materials are given by the equation:

$$T_S = \alpha_S T_M \qquad 19$$

Where Ts is the sintering temperature, T_M is a material's bulk melting temperature and α_S is factor relative to material geometries. Values for α_S of 0.1 – 0.3 are normally reported for nanoparticle sized materials [116]. Considering the silver melting point of 961 ºC (its theoretical value) and α factor of 0.3, sintering temperature (Ts) > 270 ºC should be enough to achieve completely dense contact and was used in these experiments. The pre-heating at 50 - 100 ºC is often needed to remove the organic binder from Ag paste because rapid volatilization of solvent during the sintering tends to separate the bonding interfaces and produces voids within the joint.

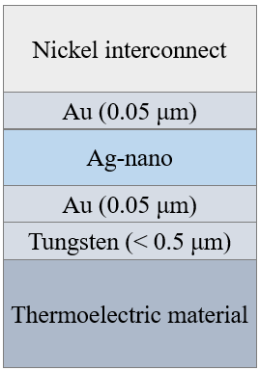

(a)

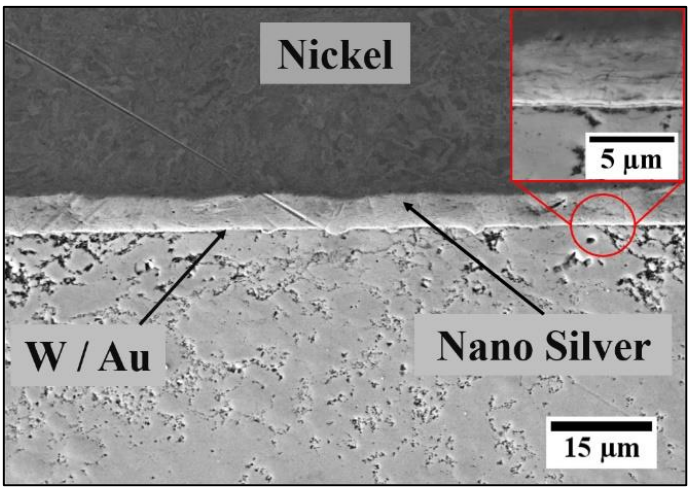

(b)

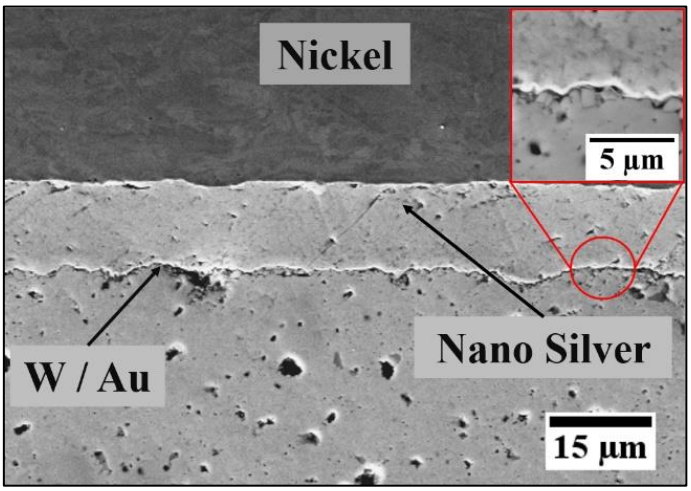

(c)

Figure 4.2-13: (a) Schematic illustration of contacts configuration and interfacial microstructure of **(b)** $Mm_y(Fe,Co)_4Sb_{12}$ *p-type* and **(c)** $(Ni,Co)Sb_3$ *n-type* skutterudites with W (< 0.5 µm-thick) / Au (0.05 µm-thick) metallization joined with Au coated Ni interconnect using Ag-nano (NBE Technologies, LLC, US) at 273 ^oC in the air.

As specified by the supplier of Ag-nano paste (NBE Technologies, LLC), an effective removal of organic binder can be done by simply controlling the sintering heating rate below 5 ºC / min, which was used in this experiment. Figure 4.2-13, Figure 4.2-14 and Figure 4.2-15 present microstructural analysis of Ni/Au interfaces bonded to W/Au, WSi_2/Au and Ni(P)/Au coated skutterudite respectively, using Ag-nano paste at 273 ºC (in the air) by thermo-compression technique. A satisfactory interface without visible cracks can be formed and joining material was dense and adhered well to gold and ENIG-finished surfaces. Moreover, as seen in Figure 4.2-15, inside the sintered Ag-nano contacts, the pores visible at the Ni/Au – Ag interface are often precursors of microcracks and might presumably grow into large cracks propagating across the whole joint interface. Upon thermal cycling or isothermal ageing, the pore size is proven to grow and merge into larger cracks which dominates the performance of nano-sintered contacts [32]. Semiconductor-metallization interface quality also plays vital role in the reliability and performance of the high-medium temperature thermoelectric modules. As the Ag-nano sintering bonding was performed at low temperatures, no material's damage and Ni/Ni(P)/Au metallization layers delamination was observed at the as-joined specimens. Moreover, the W/Au and WSi_2/Au sputtered layers were visible at the contacting interfaces, but they seemed slightly delaminated from the surface of skutterudite material. As mentioned before, the adhesion on all the PVD sputtered coatings was evaluated by a scotch tape test according to ASTM D3359 standard [97] with an excellent 4B-level performance, so that delamination effect was more likely induced during the samples machining to rectangular shape pellet. Moreover, no secondary phase formation was observed at the thermoelectric-metallization interface in all as-joined specimens.

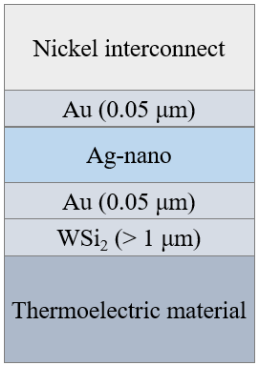

(a)

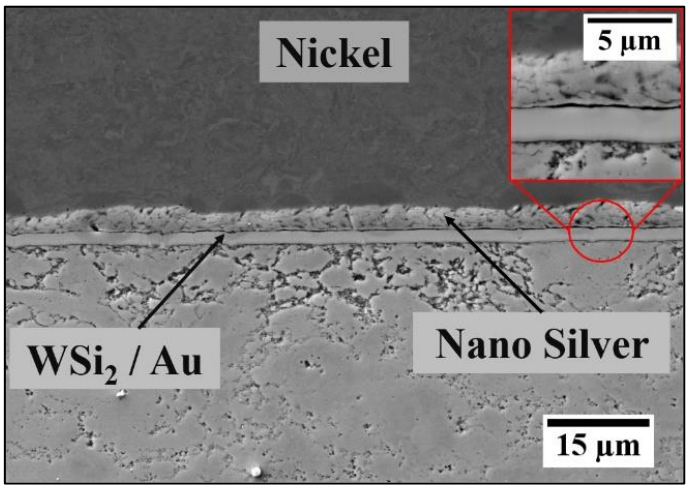

(b)

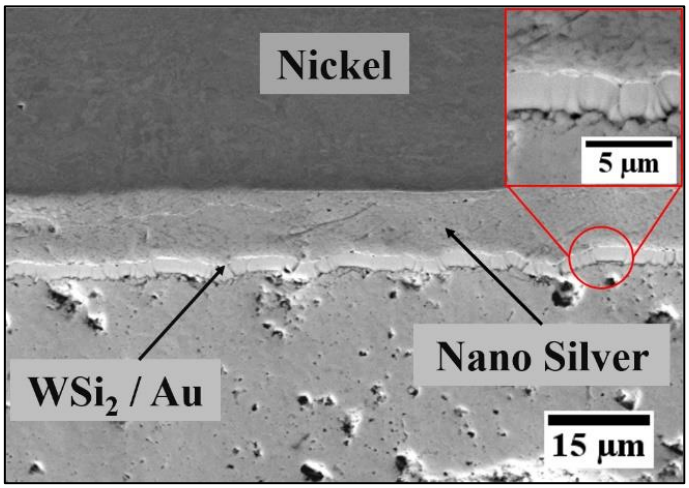

(c)

Figure 4.2-14: (a) Schematic illustration of contacts configuration and interfacial microstructure of **(b)** $Mm_y(Fe,Co)_4Sb_{12}$ *p-type* and **(c)** $(Ni,Co)Sb_3$ *n-type* skutterudites with WSi_2 (>1 μm-thick) / Au (0.05 μm-thick) metallization joined with Au coated Ni interconnect using Ag-nano (NBE Technologies, LLC, US) at 273 ^oC in the air.

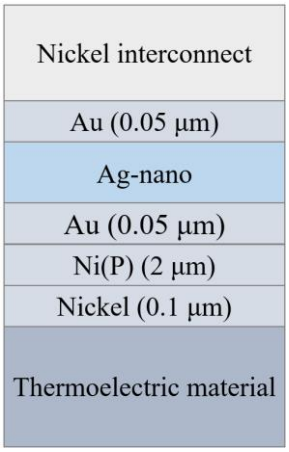

(a)

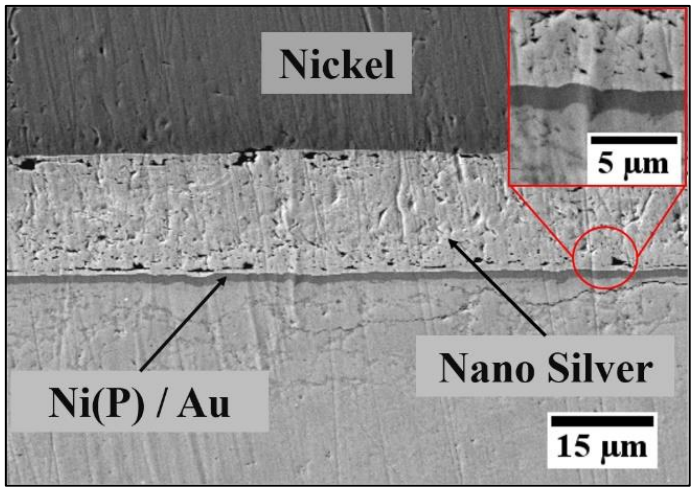

(b)

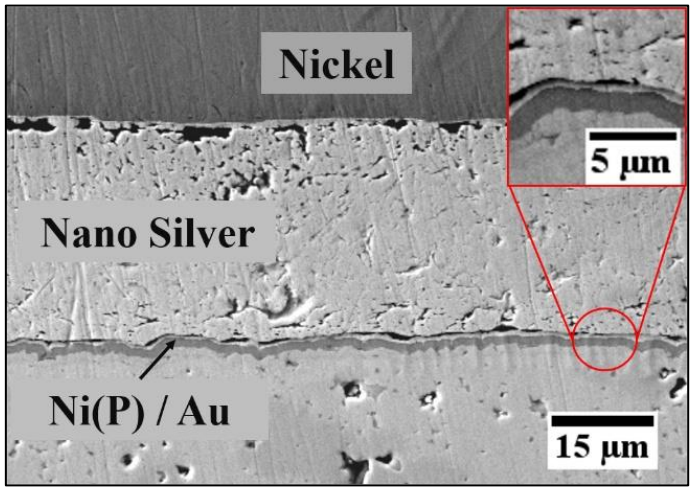

(c)

Figure 4.2-15: (a) Schematic illustration of contacts configuration and interfacial microstructure of **(b)** $Mm_y(Fe,Co)_4Sb_{12}$ *p-type* and **(c)** $(Ni,Co)Sb_3$ *n-type* skutterudites with Ni/Ni(P)/Au metallization joined with Au coated Ni interconnect using Ag-nano (NBE Technologies, LLC, US) at 273 ºC in the air.

Initial isothermal ageing tests were performed on specimens bonded using low temperature, Ag-based joining materials. All contacting samples were isothermally aged at 450 ºC for 48 hours in flowing Ar but only these of Ni (0.1 μm) / Ni(P) (2 μm) / Au (0.05 μm) metallized sample survived testing and their microstructural properties were further analysed. Figure 4.2-16a presents interfacial macrostructure of $(Ni,Co)Sb_3$ *n-type* skutterudite with Ni (0.1 μm-thick) / Ni(P) (2 μm-thick) / Au (0.05 μm-thick) metallization joined with Au coated Ni interconnect using Ag flakes (AREMCO Inc.) at 110 ºC in open air and isothermally aged at 450 ºC for 48 hours in flowing Ar. It can be seen that metallization layer dissolved in the skutterudite material and < 2 μm-thick Ni-Sb-Co reaction layer was formed at the interface. Based on EDS analysis, the reaction layer is composed of Co—38 at.% Ni—52 at.% Sb and is defined as Ni_5Sb_2 IMCs with 10 at% Fe and 0.5 at% Ce solubilities. EDS analysis can be found in Appendix A (Figure A. 16). Moreover, silver flakes kept their continuity and as expected, based on previous results reported in Chapter 4.2.2, did not react with either nickel or skutterudite material.

The interfacial microstructure of $(Ni,Co)Sb_3$ *n-type* skutterudite with Ni (0.1 μm-thick) / Ni(P) (2 μm-thick) / Au (0.05 μm-thick) metallization joined with Au coated Ni interconnect using Ag-nano paste (NBE Technologies, LLC, US) at 273 ºC in the air and isothermally aged at 450 ºC for 48 hours in Ar can be seen in Figure 4.2-16b. As opposed to Ag flake-based contacts, nano Ag contact along with Ni/Ni(P)/Au metallization were completely dissolved presumably in the *n-type* skutterudite material. Interestingly, ~ 20 μm-thick reaction layer was formed and is a result of continuous nickel diffusion into thermoelectric material. Based on EDS analysis, the reaction layer is composed of Co—34 at.% Ni—51 at.% Sb and can be attributed to the (Co,Ni)Sb phase, which is consistent with results

presented in Chapter 4.2.2. EDS analysis can be found in Appendix A (Figure A. 17). It is evident that flake-shaped particles work in contact stability benefits as they keep their integrity at high temperature and inhibit nickel continuous diffusion and formation of reaction layer.

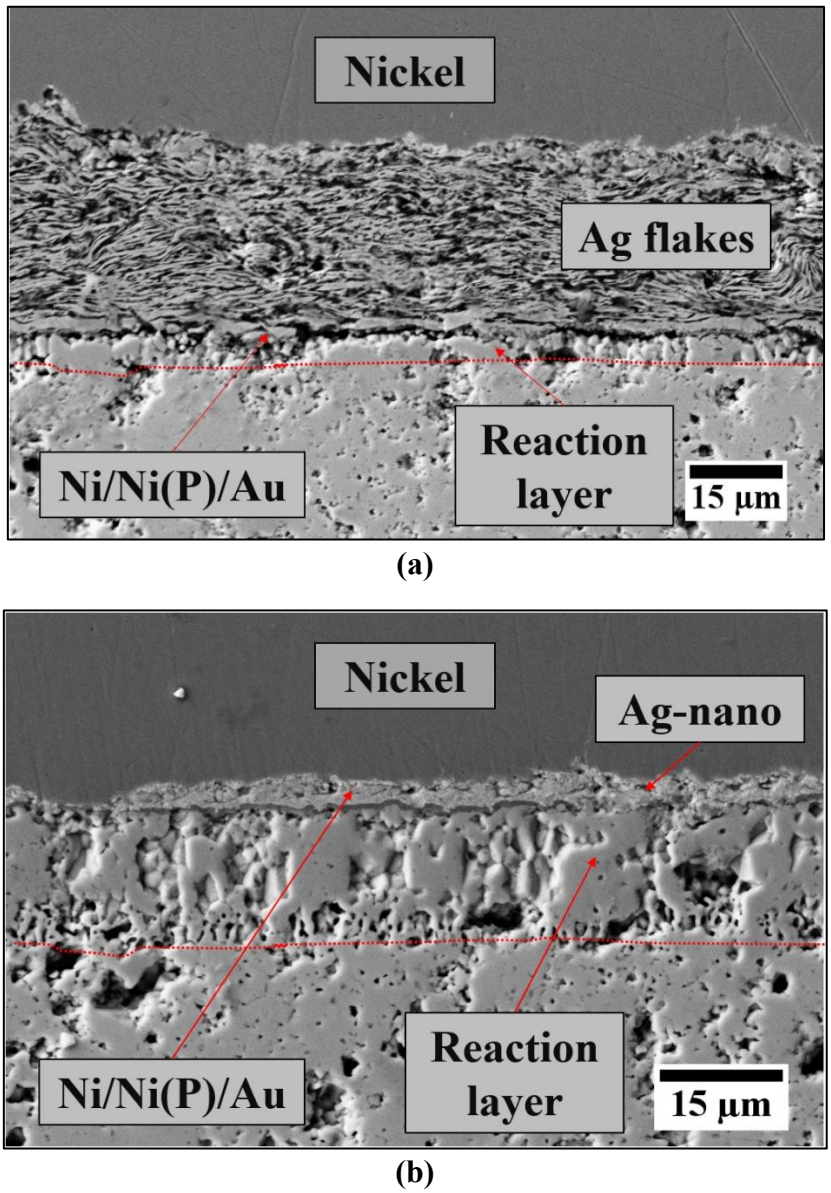

Figure 4.2-16: Interfacial microstructure of (Ni,Co)Sb_3 *n-type* skutterudite with Ni (0.1 µm-thick) / Ni(P) (2 µm-thick) / Au (0.05 µm-thick) metallization joined with Au coated Ni interconnect using **(a)** Ag flakes (AREMCO Inc.) at 110 ^{o}C in open air and **(b)** Ag-nano paste (NBE Technologies, LLC, US) at 273 ^{o}C in open air that were isothermally aged at 450 ^{o}C for 48 hours in flowing Ar.

4.2.6 Electrical Performance Evaluation of Ag Flake and Ag-nano Contacts

Two low-temperature joining techniques (< 300 ºC) including sintering of Ag-nano particles and Ag flake-based adhesive were used because high brazing temperatures were proven to be damaging for thermoelectric material and thin metallization layer. Moreover, it was assumed that bonding at temperatures lower than initial consolidation temperatures (*in-situ* synthesis by Spark Plasma Sintering) might have a positive impact on electrical conductivity of thermoelectric – interconnect joints. Both low-temperature, Ag-based joining materials normally do not contain corrosive flux (such as borax and boric acid found in Silver-flo^{TM} 56 braze) so that degradation of *p-type* material could be avoided. Additionally, bonding at lower temperatures can help with stability of relatively reactive metallization layers (such as Ti (0.3 µm) / Ni (1.2 µm) and Ni (0.1 µm) / Ni(P) (2 µm) presented in Chapter 4.2.1 and Chapter 4.2.2) so that reaction layer of various intermediate compounds with different electrical performance (such as (Ni,Co)Sb and Ni_5Sb_2 IMCs) can be inhibited. As seen in Figure 4.2-17a, the lowest *Rc* values of (1.49 ± 0.23) $\cdot 10^{-5}$ Ω·cm^2 and (1.40 ± 3.94) $\cdot 10^{-5}$ Ω·cm^2 were measured at the Ni/Au-coated - Ni (0.1 µm) / Ni(P) (2 µm) /Au (0.05 µm) coated $Mm_y(Fe,Co)_4Sb_{12}$ *p-type* and $(Ni,Co)Sb_3$ *n-type* interfaces respectively, when Ag-nano paste was used. Similar, low values of (2.27 ± 5.44) $\cdot 10^{-5}$ Ω·cm^2 and (2.0· ± 0.08) $\cdot 10^{-5}$ Ω·cm^2 were measured for $Mm_y(Fe,Co)_4Sb_{12}$ *p-type* and $(Ni,Co)Sb_3$ *n-type* skutterudites respectively, when joined to Ni/Au-coated interconnect using Ag flake conductive adhesive (Figure 4.2-17b). The low electrical contact resistance of Ni (0.1 µm) / Ni(P) (2 µm) / Au (0.05 µm) coated skutterudites is consistent with SEM microstructural analysis (Figure 4.2-12 and Figure 4.2-15) as crack-free interfaces without interfacial reaction layer of brittle

IMCs were observed. Moreover, metallization layers of Ni, Ni(P) and Au are normally characterized with relatively high-electrical conductivity [117] so that the passage of electrical current across the contacting interfaces was allowed.

The electrical contact resistance (*Rc*) of joints formed between W (< 0.5 μm) / Au (0.05 μm) metallized $Mm_y(Fe,Co)_4Sb_{12}$ *p-type* and $(Ni,Co)Sb_3$ *n-type* thermoelectric material and Ni/Au-coated interconnect using Ag-nano and Ag flake-based joining materials are presented in Figure 4.2-17. Relatively high *Rc* values of $(3.54 \pm 0.34) \cdot 10^{-4}$ Ω·cm^2 and $(1.98 \cdot \pm 0.25) \cdot 10^{-3}$ Ω·cm^2 were measured for W/Au coated $(Ni,Co)Sb_3$ *n-* and $Mm_y(Fe,Co)_4Sb_{12}$ *p-type* contacts respectively, when Ag-nano paste was used. Moreover, *Rc* of $(6.79 \pm 3) \cdot 10^{-4}$ Ω·cm^2 and $(1.3 \cdot \pm 0.31) \cdot 10^{-3}$ Ω·cm^2 were measured for W/Au coated $(Ni,Co)Sb_3$ *n-* and $Mm_y(Fe,Co)_4Sb_{12}$ *p-type* contacts respectively, when Ag flake-based joining material was used. As tungsten and gold have high room temperature electrical conductivity [118], low electrical performance of W/Au metallized contacts can be attributed to insufficient tungsten – skutterudite contact observed in SEM analysis (Figure 4.2-10 and Figure 4.2-13)

Relatively high electrical contact resistance was measured for joints formed between WSi_2 (> 1 μm) / Au (0.05 μm) metallized $Mm_y(Fe,Co)_4Sb_{12}$ *p-type* and $(Ni,Co)Sb_3$ *n-type* thermoelectric material and Ni/Au-coated interconnect using Ag-nano and Ag flake-based joining materials are presented in Figure 4.2-17. The poor electrical performance of WSi_2 / Au metallization is presumably caused by the low electrical conductivity of amorphous WSi_2 layer which is expected to crystallize during the high temperature operations or reduced conductivity at the WSi_2 - skutterudite interface.

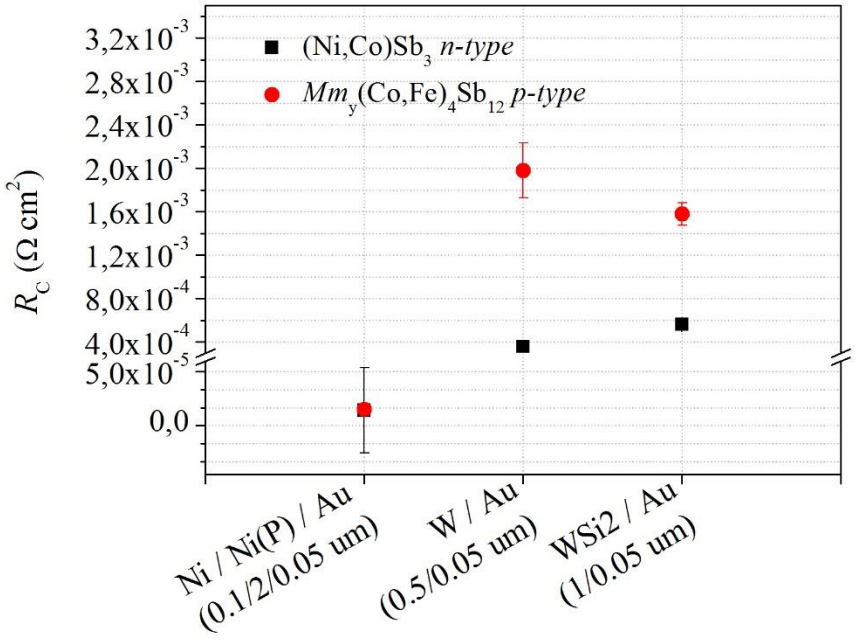

(a)

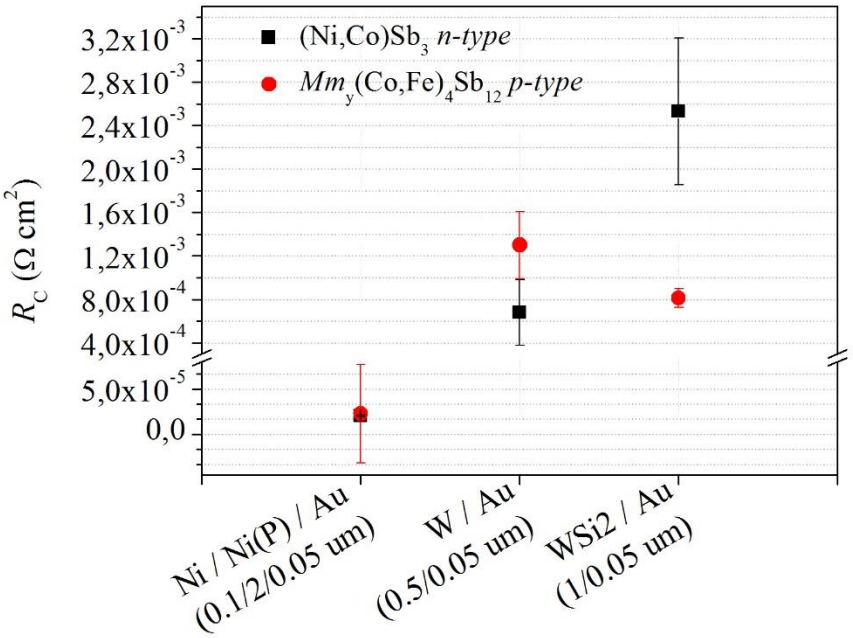

(b)

Figure 4.2-17: Graphs representing the electrical contact resistance (R_C) of (Ni,Co)Sb_3 *n-* and $Mm_y(Fe,Co)_4Sb_{12}$ *p-type* thermoelectric material and different metallization layers joined with Au-coated Ni interconnect using **(a)** Ag-nano paste and **(b)** Ag flake-based conductive adhesive.

Isothermal ageing test were performed on specimens bonded using low temperature, Ag-based joining materials and involved thermal treatment at 450 ^{o}C for 48 hours in flowing Ar. Figure 4.2-18 presents electrical contact resistance for thermally aged Ni (0.1 μm) / Ni(P) (2 μm) / Au (0.05 μm) metallized *n*- and *p-type* skutterudites joined with Au plated nickel interconnect using Ag-nano paste and Ag flake-based joining materials. (Ni,Co)Sb_3 *n-type* contact that was joined using Ag-nano joining material showed the highest thermal stability as *Rc* of 7.6 ± 6.2 $\cdot 10^{-5}$ Ωcm^2 was measured which represents an increase by 441.9% compared to as-joined specimens. At the same time, *Rc* of the *n-type* contacts joined using Ag flake-based joining material was measured of 1.9 ± 0.9 $\cdot 10^{-4}$ Ωcm^2 which represents an increase by 870.4% with as-joined specimens. This can be explained by microstructural analysis presented in Figure 4.2-16b, as nano-Ag based contacts formed reasonably continuous interface and formation of (Co,Ni)Sb reaction layer. In the *n-type* contacts that were joined using Ag flake-based joining material, voids at the thermoelectric-joining material are clearly visible, which are presumably responsible for the high electrical contacts resistance (Figure 4.2-16a).

The Mm_y(Fe,Co)$_4Sb_{12}$ *p-type* contacts were previously proven to suffer in the highest extend from thermal instabilities (Chapter 4.2.1 and Chapter 4.2.2). The isothermal ageing of Ni (0.1 μm) / Ni(P) (2 μm) / Au (0.05 μm) metallized *p-type* skutterudites was proven to be destructive for the samples joined with Au plated nickel interconnect using Ag flake-based. The *Rc* of Ni (0.1 μm) / Ni(P) (2 μm) / Au (0.05 μm) metallized *p-type* skutterudites joined with Ni/Au interconnect using Ag-nano paste was measured of 2.84 ± 0.3 $\cdot 10^{-4}$ Ωcm^2. This represents 1798% increase compared to specimens at the beginning-of-life conditions.

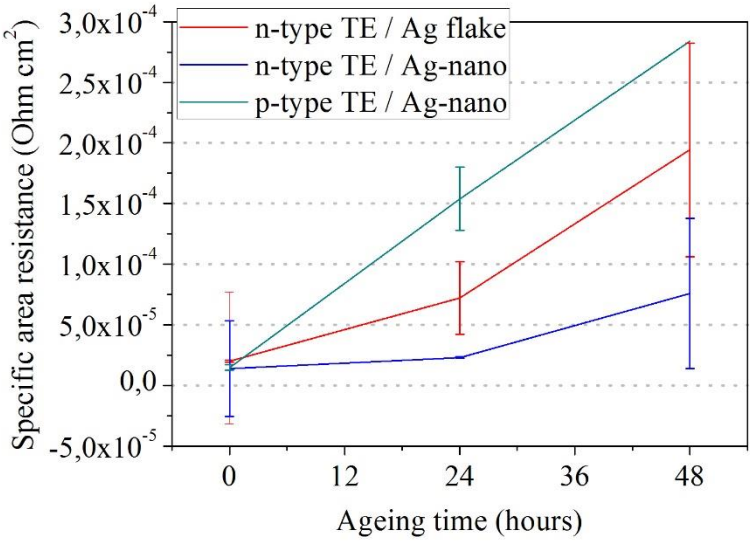

Figure 4.2-18: Summary of the electrical contact resistance (*Rc*) obtained for Ni (0.1 μm) / Ni(P) (2 μm) / Au (0.05 μm) metallized *n*- and *p-type* contacts joined with Au plated nickel interconnect using Ag-nano paste and Ag flake-based material including the evolution upon the isothermal ageing at 450 °C in flowing argon. Note: '0 hours' specimens are contacts at the BOL conditions.

4.2.7 Solid-Liquid Interdiffusion (SLID) Bonding [9]

One promising interconnect technology for high-temperature microelectronic packaging is solid-liquid interdiffusion (SLID) bonding [119], also called transient liquid-phase bonding (TLPB) [119], and diffusion brazing [34]. The SLID bonding technique is based on binary interlayer systems comprising a high-melting-point material - $T_{M\ HIGH}$ and a low-melting-point material - $T_{M\ LOW}$ which is heated to its molten state resulting in the formation of intermetallic compounds (IMCs) through a diffusion-reaction mechanism. SLID bonding has been

[9] Part of this chapter has been published as Placha K., Tuley R. S., Salvo M., Casalegno V., Simpson K., Solid-Liquid Interdiffusion (SLID) Bonding of p-Type Skutterudite Thermoelectric Material Using Al-Ni Interlayers, *Materials* **2018**, *11*(12), 2483; https://doi.org/10.3390/ma11122483

commonly explored using Sn and In as $T_{M\ LOW}$ filler systems [120–124] with several advantages over standard solder interconnections such as outstanding thermal stability due to increased re-melting temperature and power handling capability with current densities exceeding the capability of solders [125]. In the present work, we assess Al-Ni diffusion couples as a potential joining material for high-temperature thermoelectric modules assembly application. Among various intermetallic compounds, Al-Ni IMCs are associated with unique properties, such as high thermal stability, tremendous oxidation and corrosion resistance along with excellent performance in creep strength [126]. The aluminium-nickel bi-layered system has already been classified as a particularly suitable structural energetic material used in a reactive, multilayer brazing foils due to its exceptional exothermic properties [127,128]. Encouraged by the remarkable properties of Al-Ni IMCs and recent findings on flux-less solid-liquid interdiffusion (SLID) bonding technique in thermoelectric manufacturing [129,130], a new joining technique utilizing the aluminium - nickel system has been developed and is reported here.

In order to test the feasibility of Al-Ni solid–liquid interdiffusion bonding in the current design, electroless Ni(P) coating on Cu interconnect, *p*- and *n-type* skutterudites was introduced. Although previous bonding experiments utilized Ni interconnect, SLID bonding needed Ni(P) plated Cu, as excess Ni could influence final microstructure. Moreover, seed layer (< 0.5 μm-thick) of electrolytic Ni was deposited prior to electroless plating to ensure good Ni(P) adhesion to skutterudite surface but only Ni(P) coating was believed to be a source of Ni needed for Al – Ni reaction to occur. Phosphorous content in the top Ni(P) coating was 18 at.% which, as reported in the literature [117], results in the mixture of amorphous and microcrystalline microstructure and is expected to partially crystallize upon

heating to Ni_3P phase [131]. As seen in Figure 4.2-19, as-deposited 14 µm-thick Ni(P) coating and < 0.5 µm Ni layer show good adherence to the thermoelectric materials (4B-level according to ASTM D3359 standard [97]) and Cu substrate.

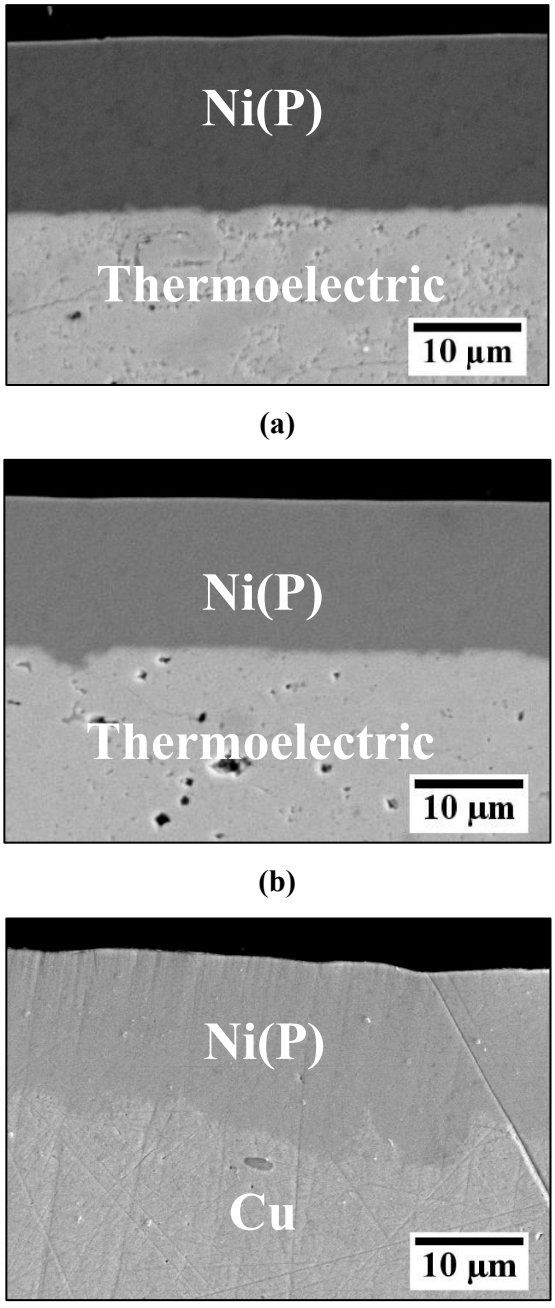

Figure 4.2-19: SEM cross-sectional analysis of **(a)** $Mm_y(Fe,Co)_4Sb_{12}$ *p-type* and **(b)** $(Ni,Co)Sb_3$ *n-type* material with Ni Wood's and Ni(P) layers along with **(c)** Cu with Ni(P) layer.

It has been reported, that due to the lack of high-temperature thermal stability of skutterudites and metal interconnects, implementing an additional diffusion barrier is needed [46,58]. Fundamental research on high-temperature stability between $CoSb_3$-based thermoelectric material and Ni interconnect conducted by Chen, *et al*. [43], revealed extensive growth of reaction layers, i.e., (Co,Ni)Sb and Ni_5Sb_2 phases at the skutterudite–nickel interface at high temperatures. Although contact interface is expected to suffer from the Ni/$CoSb_3$ high-temperature instabilities, no diffusion barrier was implemented as SLID technique was aimed to *in-situ* form Al-Ni IMCs that could serve as a bonding material and an effective diffusion barrier between the thermoelectric material and interconnect simultaneously.

In this research, the bonding process is designed so that layers of Ni(P)-Al-Ni(P) at the temperature of molten aluminium ($T_{M\ LOW}$) undergo solid–liquid interdiffusion reaction leading to the formation of intermetallic compounds (IMCs) through a diffusion-reaction mechanism. Moreover, lower temperatures ($\leq T_{M\ LOW}$) were also tested so that solid-solid interdiffusion was a mechanism behind the Ni(P)-Al-Ni(P) multilayer transition into Al-Ni intermediate compounds. As thermoelectric module assembly is expected to be performed in a one single step, for the practical reasons, both *n*- and *p-type* thermoelectric materials were subjected to the same joining procedure. Based on the phase diagram [132], there are five thermodynamically stable intermetallic compounds existing in the Al-Ni binary system but Al_3Ni and Al_3Ni_2 phases are the only two expected to be found in the reactive diffusion zone in both solid–solid and solid–liquid, nickel-aluminium interfaces [120, 121]. To achieve the subject of this study for maintaining a single Al_3Ni_2 phase between two Ni layers ($T_{M\ HIGH}$), it was

calculated, based on the following equation, the initial thickness of Ni needed for 17 µm-thick Al foil ($T_{M\,LOW}$):

$$\frac{t_{Ni}}{t_{Al}} = \frac{2M_{Ni}/\rho_{Ni}}{3M_{Al}/\rho_{Al}} \qquad 20$$

where t are the thicknesses of both nickel and aluminium layers, M are the atomic weights and ρ are elemental densities, i.e., 8.9 g/cm^3 and 2.7 g/cm^3 of Ni and Al, respectively. However, deviations from the theoretical model were expected as Ni(P) instead of pure Ni was used in this study. According to Equation 20, a symmetrical joint consisting of two 3.75 µm-thick Ni(P) layers and 17 µm-thick Al foil (Figure 3.4-1b) should be enough to maintain a single Al_3Ni_2 phase. While it would be advantageous to completely consume the nickel layer to avoid any subsequent reaction with the skutterudite material, initial experiments indicated that thicker Ni(P) layers are required, as any excess aluminium can react with the thermoelectric to form the wider band gap [135] aluminium antimonide, increasing the contact resistance (R_C). Moreover, elemental nickel is also consumed by the formation of intermetallic compounds (IMCs) at the skutterudite–Ni(P) interface and its depletion at the interconnection side caused by the Ni and Cu miscibility [136] at all concentration ranges. Therefore, thicker than calculated Ni(P) layers were deposited, i.e. ~14 µm-thick on both *n*- and *p-type* skutterudites and copper as seen in Figure 4.2-19.

The joining process was performed at two different temperatures, i.e., 585 °C ($\leq T_{M\,LOW}$) for 15 minutes and 660 °C ($= T_{M\,LOW}$) for 4.6 minutes (as calculated in Equation 22 and 23) and the resulting joints' microstructure are presented in Figure 4.2-20 and Figure 4.2-21 respectively. It is clear that joining at 585 °C for 15 minutes is not sufficient for complete phase transformation, as some residual aluminium at the joined interface can be found, and the only formed IMC is Al_3Ni_2 (40 at. % Ni and 60 at. % Al) as identified by EDS analysis. EDS mapping of *p*- and *n-type* contacts bonded with Ni(P) plated copper interconnects at 585 °C for 15 minutes can be found in Appendix A (Figure A. 10 and Figure A. 11). It is believed, that during the heating of the assembly, connected metallic interfaces form a solid solution until its saturation and, as expected, the formation of IMCs through the solid-state diffusion process occurs slower compared to that of the solid–liquid kinetic. A complete transformation of aluminium filler is observed at a joining temperature of 660 °C as two distinct IMCs, i.e., Al_3Ni2 (38 at.% Ni and 62 at.% Al) near the Ni(P) coating and Al_3Ni (24 at.% Ni and 76 at.% Al) in the centre line can be found (Figure 4.2-21). EDS mapping of *p*- and *n-type* contacts bonded with Ni(P) plated copper interconnects at 660 °C for 4.6 minutes can be found in Appendix A (Figure A. 12 and Figure A. 13). This is consistent with other studies performed on non-thermoelectric, aluminium–nickel diffusion couples [133,137].

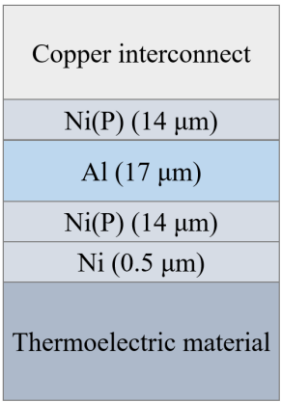

(a)

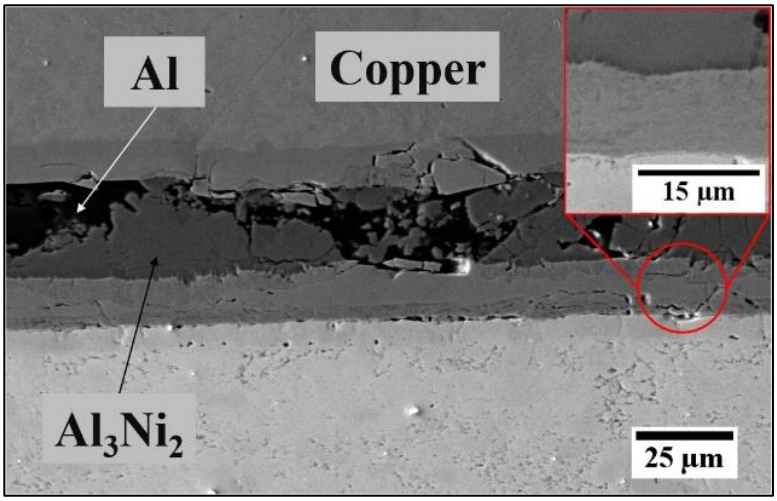

(b)

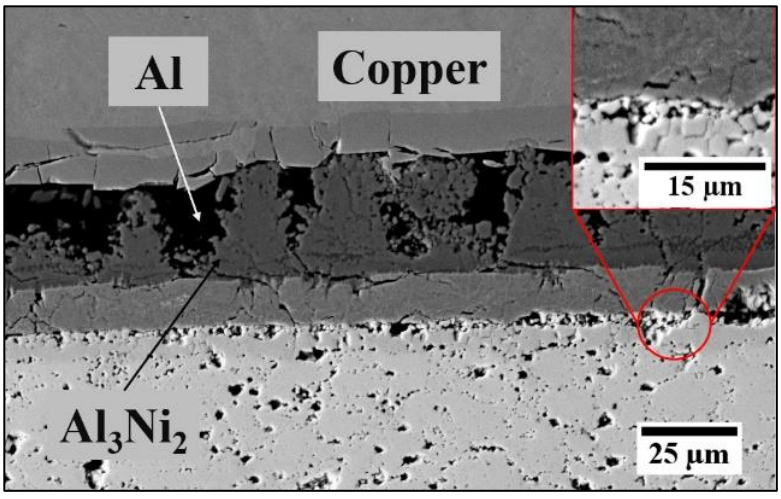

(c)

Figure 4.2-20: (a) Schematic illustration of sample configuration before heat treatment and SEM cross-sectional microstructure of **(b)** $Mm_y(Fe,Co)_4Sb_{12}$ *p-type* and **(c)** $(Ni,Co)Sb_3$ *n-type* interfaces bonded to Ni(P) coated Cu interconnect using Al-Ni SLID technique at 585 ºC for 15 minutes in Ar.

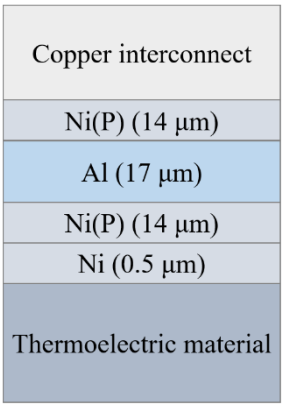

(a)

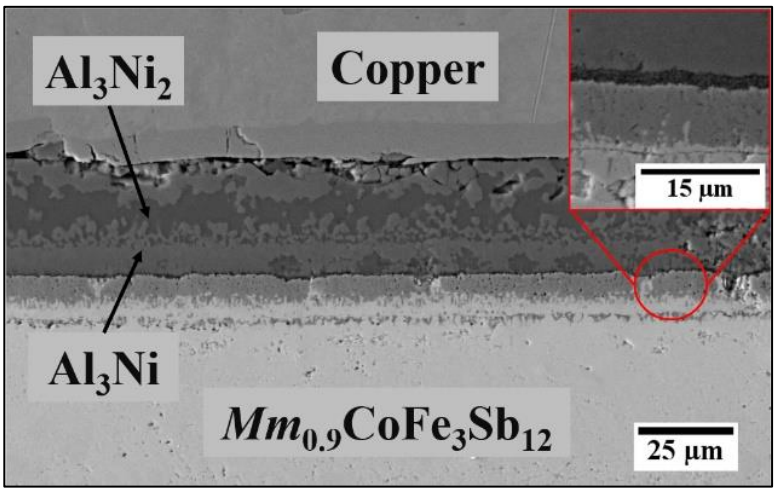

(b)

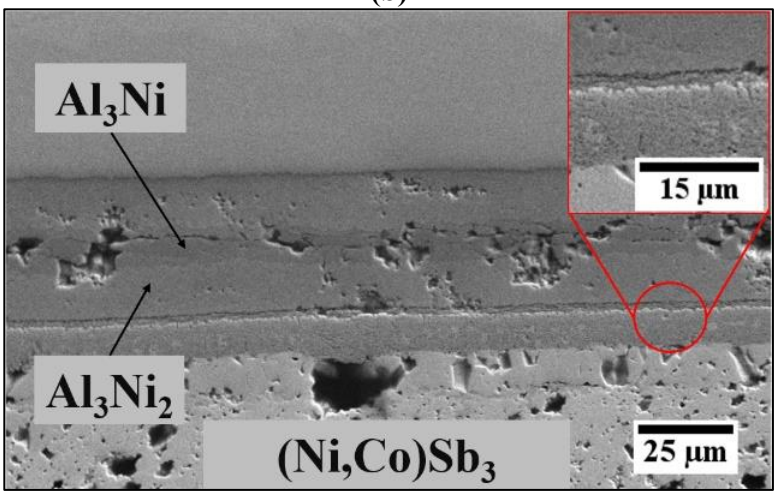

(c)

Figure 4.2-21: (a) Schematic illustration of sample configuration before heat treatment and SEM cross-sectional microstructure of **(b)** $Mm_y(Fe,Co)_4Sb_{12}$ *p-type* and **(c)** $(Ni,Co)Sb_3$ *n-type* interfaces bonded to Ni(P) coated Cu interconnect using Al-Ni SLID technique at 660 ^oC for 4.6 minutes in Ar.

A kinetic model was used to explain Al_3Ni_2 IMCs growth behaviour and to determine the process heating profile. Considering the joint design based on two nickel-based layers to be contacted with 17 µm-thick aluminium foil, the transition time was calculated based on the formation of Al_3Ni_2 at the expense of 7.5 µm of Ni(P) deposit. The thickness of the resulting bonding layer was calculated from the following equation:

$$t_{Al_3Ni_2} = \frac{M_{Al_3Ni_2}}{\rho_{Al_3Ni_2}} \times \frac{t_{Al}\rho_{Al}}{3M_{Al}} \qquad 21$$

where t are the thicknesses of both aluminium and the resulting Al_3Ni_2 IMCs layer, M are the atomic weights and ρ are the elemental densities, i.e., 4.7 g/cm^3 Al_3Ni_2 phase. According to equations 20 and 21, from the consumption of 7.5 µm Ni from both Ni(P) layers and 17 µm-thick Al foil, a final joint with a 24 µm-thick Al_3Ni_2 layer is expected. As shown in Figure 4.2-21 the 28.6 µm-thick contacts are thicker than its theoretical estimation which might be induced by the formation of a two-phase bonding region (Al_3Ni + Al_3Ni_2). The parabolic equation based on Fick's diffusion law was used to determine the bonding conditions as follows:

$$X(t,T) = k \times t^n \qquad 22$$

where X is the average thickness of the intermetallic compound, t is the joining process time, T is the bonding temperature, k is the constant rate, and n is a time

exponent. In addition, the temperature dependence of reaction rate k can be expressed by the following Arrhenius relationship:

$$k = k_0 exp\left(-\frac{Q_A}{RT}\right) \quad 23$$

where k_0 is the frequency factor, R is the Boltzmann constant, and Q_A is the activation energy for the growth of the designed Al_3Ni_2 phase. According to Tumminello, *et al* [138], the two empirical parameters attributed to Al_3Ni_2 phase growth, k and n are 8.5×10^{-8} m/s and 0.844, respectively. Based on equations 22 and 23, complete transition to the Al_3Ni_2 phase can be achieved within 4.6 min, which was used in the experiment. Additionally, longer bonding process including treatment for 15 minutes and 60 minutes at 660 ºC, but formation of Kirkendal void within bonding line and Al-Sb IMCs were observed. One of the attributes of the SLID bonding process is that both solid–liquid and solid–solid diffusion mechanism play the key roles in isothermal solidification, which makes a process more time consuming than standard soldering [139]. However, due to the high diffusivity of solid nickel in molten aluminium [140], a combination of Al-Ni diffusion couple is a good choice, making the joining process as fast as 4.6 min. Additionally, the resulting IMCs, Al_3Ni and Al_3Ni_2 are characterized with higher than initial re-melting temperature with theoretical values of 854 °C and 1133 °C, respectively [132]. In order to investigate the microstructural evolution of the fully transformed contact, isothermal ageing on the assemblies joined at 585 °C for 15 minutes and 660 °C for 4.6 minutes was performed and the cross-sectional view of these microstructures can be seen in Figure 4.2-22 and Figure 4.2-23 respectively.

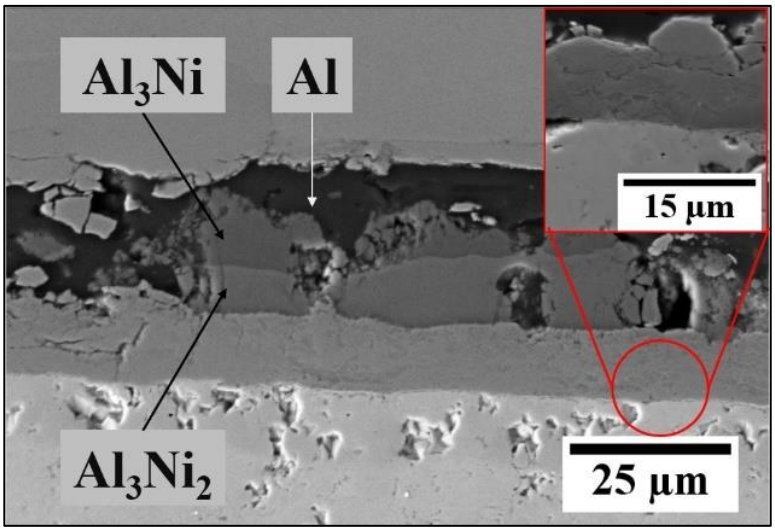

(a)

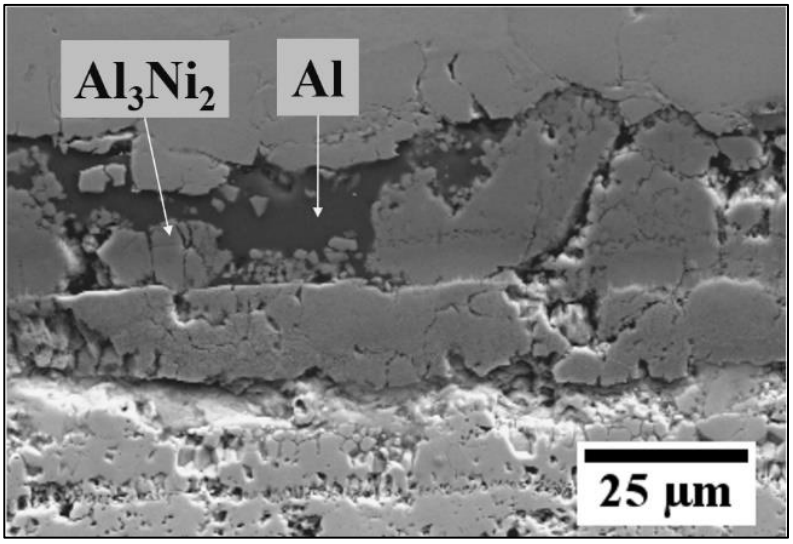

(b)

Figure 4.2-22: SEM cross-sectional microstructure of **(a)** $Mm_y(Fe,Co)_4Sb_{12}$ *p-type* and **(b)** $(Ni,Co)Sb_3$ *n-type* interfaces bonded to Ni(P) coated Cu interconnect using Al-Ni SLID technique at 585 ºC for 15 minutes in Ar and isothermally aged at 450 ºC for 96 hours under Ar.

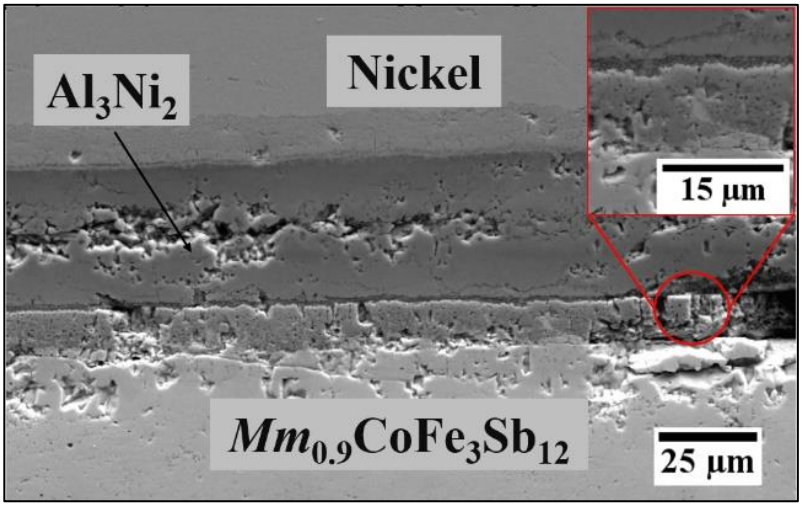

(a)

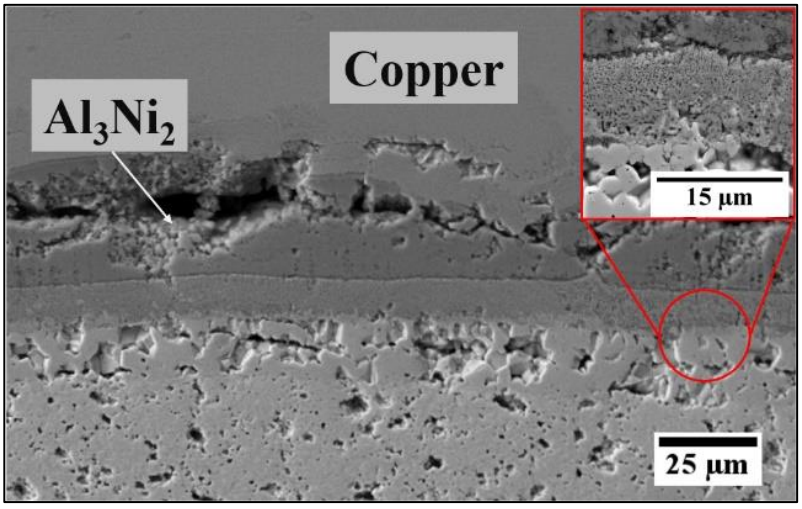

(b)

Figure 4.2-23: SEM cross-sectional microstructure of **(a)** $Mm_y(Fe,Co)_4Sb_{12}$ *p-type* and **(b)** $(Ni,Co)Sb_3$ *n-type* interfaces bonded to Ni(P) coated Cu interconnect using Al-Ni SLID technique at 660 ºC for 4.6 minutes in Ar and isothermally aged at 450 ºC for 96 hours under Ar.

Isothermal ageing was proven to promote homogenisation within the bond line as a reduction of the Al_3Ni phase in favour of growing Al_3Ni_2 was observed. It is believed that during the homogenisation process, excess nickel from Ni(P) is causing unstable Al_3Ni phase continual conversion into Al_3Ni_2 IMCs through grain boundary diffusion, which may influence the joint's thermal stability, as the Al_3Ni_2 phase has a higher melting point than Al_3Ni phase. The residual phosphorous was accumulated at the Al_3Ni_2 / Ni(P) interface as a result of Ni depletion from the Ni-P coating due to the formation of desirable Al_3Ni_2 IMCs. The high magnification image of the Ni(P)–Al_3Ni_2 interface are highlighted in the red squares in Figure 4.2-22 and Figure 4.2-23. Additionally, Kirkendall voids are found within the two-phase region (Al_3Ni + Al_3Ni_2) in specimens joined at 660 ºC for 4.6 minutes, representing a surface fraction of 4.4%, although some of these are believed to be induced by pulling out the brittle intermetallic grains during the polishing process and might not be an effect of the joining process itself.

Based on the cross-sections of the joints, a 6 and 10 µm-thick Co-Ni-Sb reaction layer at the Ni(P) – *p*- and *n-type* skutterudite interfaces respectively, can be observed at specimens bonded at 660 °C for 4.6 minutes (Figure 4.2-21) and stays unchanged after isothermal ageing at 450 °C for 96 h (Figure 4.2-23). As opposed to samples joined at 660 ºC, isothermal ageing at the same conditions influences the reaction layer thickness formed at contacts bonded at 585 ºC for 15 minutes. As seen in Figure 4.2-20 and Figure 4.2-22, reaction layer thickness increases from 5 µm to 12 µm and from 8 µm to 15 µm for *p*- and *n-type* specimens bonded at 585 ºC for 15 minutes and isothermally aged at 450 ºC for 96h in flowing Ar. It is believed that unreacted Ni from the Ni(P) layer diffuses through skutterudite interface and selectively bonds with skutterudite material (Co and Sb elements, exclusively) leading to a growth of interfacial reaction layer.

Moreover, when the amorphous nickel was fully consumed due to formation of Al-Ni intermediate compound and partial crystallization of Ni-P layer, the Ni-Sb-Co layer stayed unchanged, as no free nickel was left at the interface. A reaction layer with similar composition was also observed in the brazed contacts when Ni(P)/Au coating was implemented as a metallization layer presented in Chapter 4.2.1. Based on EDS analysis, the reaction layer is composed of Co—44 at.% Ni—52 at.% Sb which is consistent with results of Ref. [43]. Beside the formation of (Ni,Co)Sb reaction layer at the skutterudite-Ni(P) interface and presumable Ni-P layer crystallization, Fe-P intermetallic precipitates were found in the p-type contacts joined at minimal temperature of 660 ºC for 4.6 minutes.

4.2.8 Electrical Performance Evaluation of Al-Ni Solid-Liquid Interdiffusion (SLID) Bonded Contacts

Figure 4.2-24 presents *Rc* of $Mm_y(Fe,Co)_4Sb_{12}$ *p-type* and $(Ni,Co)Sb_3$ *n-type* skutterudites joined with metal interconnect using Al-Ni Solid-Liquid Interdiffusion (SLID) bonding at 585 ºC for 15 minutes and 660 ºC for 4.6 minutes in Ar. The contact resistance (*Rc*) of $Mm_y(Fe,Co)_4Sb_{12}$ *p-type* assemblies joined at 585 ºC and 660 ºC was measured to be $(2.8 \pm 0.4) \cdot 10^{-5}$ Ω·cm^2 and $(4.8 \pm 0.3) \cdot 10^{-5}$ Ω·cm^2 respectively, which contribute by approx. 12 % and 21 % to the total thermoelectric pellet resistivity. At the same time, the contact resistance (*Rc*) of $(Ni,Co)Sb_3$ *n-type* material assemblies joined at 585 ºC and 660 ºC was measured to be $(5.14 \pm 0.76) \cdot 10^{-5}$ Ω·cm^2 and $(2.87 \pm 0.64) \cdot 10^{-5}$ Ω·cm^2 respectively.

The evolution of the electrical performance of $Mm_y(Fe,Co)_4Sb_{12}$ *p-type* contacts during isothermal ageing at 450 ºC in flowing Ar (Figure 4.2-24), showed that high-temperature contact degradation led to the *Rc* increase by 370 %

and 68% within 96 hours for assemblies joined at 585 ºC and 660 ºC respectively. Subsequently, electrical contact resistance (*Rc*) of (Ni,Co)Sb_3 *n-type* contacts (Figure 4.2-24) increased by 149 % and 69 % within 96 hours of isothermal ageing at 450 ºC in flowing Ar. The degradation of electrical performance is presumably caused by the Al_3Ni phase transformation into Al_3Ni_2 phase and a partial Ni(P) delamination from the skutterudite material as observed in Figure 4.2-22 and Figure 4.2-23. It is worth to add that the electrical resistivity of $Mm_y(Fe,Co)_4Sb_{12}$ *p-type* and (Ni,Co)Sb_3 *n-type* skutterudite pellets measured at room temperature using four-point probe technique showed negligible changes in the materials electrical performance after SLID bonding process.

Table 4.2-3: Summary of the electrical contact resistance (Rc) obtained for *n-* and *p-type* contacts using Al-Ni Solid-Liquid Interdiffusion (SLID) bonding performed at different joining conditions including the evolution over the isothermal ageing at 450 ºC in flowing argon. Note: '0 hours' specimens are contacts at the beginning-of-life conditions.

Thermoelectric element	**Conditions**	**0 hours**	**48 hours**	**96 hours**
		Rc ($\Omega \cdot cm^2$)		
(Ni,Co)Sb_3 *n-type*	585 ºC, 15 min, Ar	$5.14 \cdot 10^{-5}$ $\pm 7.6 \cdot 10^{-6}$	$8.75 \cdot 10^{-5}$ $\pm 2.3 \cdot 10^{-5}$	$1.28 \cdot 10^{-4}$ $\pm 1.8 \cdot 10^{-5}$
	660 ºC, 5 min, Ar	$2.87 \cdot 10^{-5}$ $\pm 6.4 \cdot 10^{-6}$	$3.15 \cdot 10^{-5}$ $\pm 3.5 \cdot 10^{-6}$	$4.86 \cdot 10^{-5}$ $\pm 1.35 \cdot 10^{-5}$
$Mm_y(Fe,Co)_4Sb_{12}$ *p-type*	585 ºC, 15 min, Ar	$2.84 \cdot 10^{-5}$ $\pm 3.6 \cdot 10^{-6}$	$9.85 \cdot 10^{-5}$ $\pm 3.54 \cdot 10^{-5}$	$1.34 \cdot 10^{-4}$ $\pm 7.5 \cdot 10^{-6}$
	660 ºC, 5 min, Ar	$4.85 \cdot 10^{-5}$ $\pm 3.2 \cdot 10^{-6}$	$6.4 \cdot 10^{-5}$ $\pm 3.7 \cdot 10^{-6}$	$8.16 \cdot 10^{-5}$ $\pm 9.2 \cdot 10^{-6}$

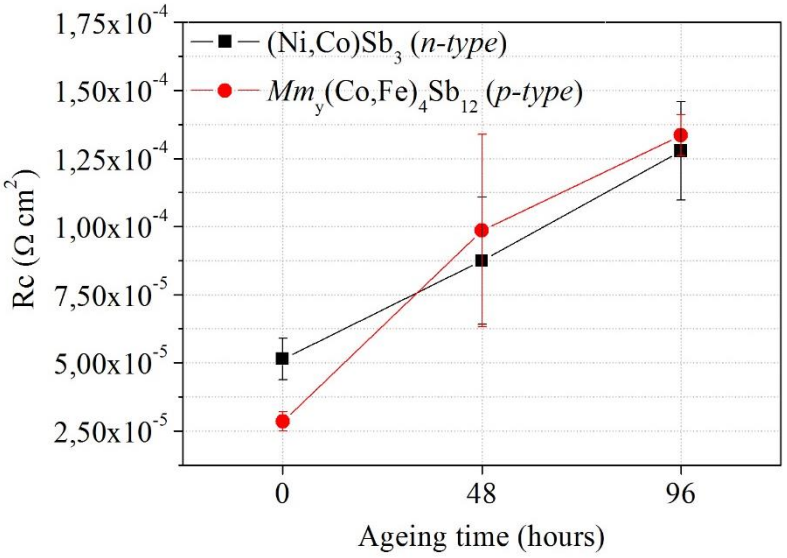

(a)

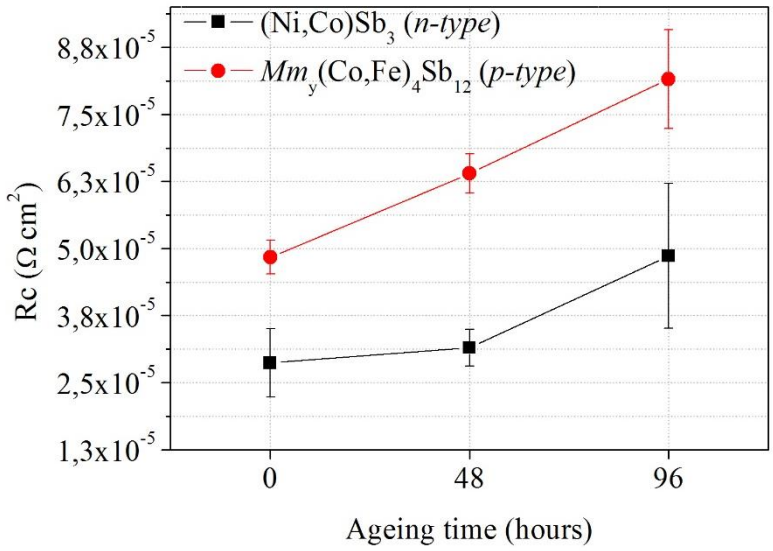

(b)

Figure 4.2-24: Graphs representing the electrical contact resistance (R_C) of $(Ni,Co)Sb_3$ *n-* and $Mm_y(Fe,Co)_4Sb_{12}$ *p-type* materials joined with Ni(P)-coated copper interconnect at **(a)** 585 ºC for 15 minutes and **(b)** 660 ºC for 4.6 minutes and isothermally aged at 450 ºC in Ar. Note: '0 hours' specimens are contacts at the beginning-of-life conditions.

4.2.9 Mechanical Strength Evaluation

The mechanical strength of bonded specimens was evaluated by measuring apparent shear strength at room temperature adapted from ASTM D905 standard [99]. As shown in Chapter 4.2.1 and Chapter 4.2.2, contacts brazed at higher temperatures (those of Ag56-CuZnSn and Ag paste contacts) were proven to form reaction layer of relatively brittle IMCs at the thermoelectric – metal/metallization interface. This is presumed a reason for specimens' fracture at pre-loads of ~ 5 N during the shear testing (which in the given specimen's geometry corresponds to 0.8 MPa). These specimens will be further listed as contacts with mechanical shear strength < 0.8 MPa. The low-temperature contacts (those of nano-Ag and Ag-flake based adhesives) did not exhibit any interfacial changes but due to presumable insufficient surface pre-cleaning and possible presence of nanometres-thick oxide layer at the surface before metallization sputtering, low mechanical shear strength was expected. In this chapter, successful specimens with apparent shear strength measured for $Mm_y(Fe,Co)_4Sb_{12}$ *p-* and $(Ni,Co)Sb_3$ *n-type* thermoelectric-interconnect contacts are presented in Table 4.2-4.

Non-metallized skutterudites were joined with nickel interconnect using 56 at% Ag - 22 at % Cu - 17 at % Zn - 5 at % Sn braze (silver-flo^{TM} 56) at 655 ºC in argon. Despite the reaction layer of brittle IMCs seen at the contacting interfaces, the apparent shear strength of 5.27 ± 0.01 MPa and 14.22 ± 4.84 MPa was measured for $(Ni,Co)Sb_3$ *n-type* and $Mm_y(Fe,Co)_4Sb_{12}$ *p-type* specimens respectively. Similar mechanical performance was expected in the Ni / Ni(P) plated specimens as the metallization layer that was dissolved in the skutterudite matrix and Ag-Cu based braze led to complete material exposure and possible degradation. Nonetheless, apparent shear strength of 3.71 ± 1.26 MPa and 6.16 ± 1.41 MPa was measured for Ni/Ni(P) plated $(Ni,Co)Sb_3$ *n-type* and

$Mm_y(Fe,Co)_4Sb_{12}$ *p-type* specimens respectively. This is significantly lower than non-metallized skutterudites, presumably due to the precipitation of brittle phosphides IMCs (Ni-P in *n*- and both Fe-P and Ni-P in *p-type* contacts) at the joining interface. Moreover, Mo (0.3 μm) / Ni (1.2 μm) coating that was proven to be stable with skutterudite materials (as no chemical reaction between two was observed), showed low apparent shear strength of 2.94 ± 1.79 MPa and 4.69 ± 1.02 MPa on for $(Ni,Co)Sb_3$ *n-type* and $Mm_y(Fe,Co)_4Sb_{12}$ *p-type* respectively, presumably caused by the coating partial delamination from the materials'.

The mechanical testing was performed on specimens joined using Ag paste, but they did not withstand 5 N mechanical pre-loading during the shear testing. In order to investigate the failure that occurs at such low loads, the fractured surface of the Ni / Ni(P) plated $Mm_y(Fe,Co)_4Sb_{12}$ *p-type* specimens joined to nickel were analysed by scanning electron microscope and EDS and is presented in Appendix A (Figure A. 14). The fracture seems to propagate along or very close to the Ni interconnect – Ag paste interface and partially at the Ni(P) from the thermoelectric side – Ag paste as regions of partially exposed Ni(P) and dense Ag layers were detected by the EDS elemental mapping images. The reason behind weak bonding between sintered Ag layer and Ni interconnect or Ni(P) coating on skutterudites (as observed in Figure 4.2-8) is the lack of chemical reaction between Ag and Ni as they are immiscible at all concentration ranges [141].

The apparent shear strength was tested for three different materials' metallization and nano-Ag paste used as a joining material including W/Au (1 μm / 0.05 μm), WSi_2 / Au (1 μm / 0.05 μm) and Ni / Ni(P) / Au (0.1 μm / 2 μm / 0.05 μm). The apparent shear strength of $(Ni,Co)Sb_3$ *n-type* – interconnect bonded with nano-Ag paste was as low as 1.36 ± 0.08 MPa while *p-type* contacts failed during specimen pre-loading. Robust interface between WSi_2 / Au (1 μm / 0.05 μm-

thick) coating on $(Ni,Co)Sb_3$ *n-type* and $Mm_y(Fe,Co)_4Sb_{12}$ *p-type* specimens resulted in high measured apparent shear strength of 7.69 ± 0.01 and 6.12 ± 0.87 MPa respectively. Slightly higher values were measured for Ni / Ni(P) / Au (0.1 µm / 2 µm / 0.05 µm) coated $(Ni,Co)Sb_3$ *n-type* and $Mm_y(Fe,Co)_4Sb_{12}$ *p-type* skutterudites with apparent shear strength of 9.65 ± 0.28 MPa and 11.42 ± 0.96 MPa respectively. These relatively high values were caused by the lack on reaction layer that is usually found at the contacts formed at higher temperatures and no visible changes in skutterudites microstructure near the bonding interface. Moreover, top Au metallization layer helped with adhesion between the silver and the metallisation. Lower values were obtained for the WSi_2 / Au (1 / 0.05 µm-thick) coated $(Ni,Co)Sb_3$ *n-type* and $Mm_y(Fe,Co)_4Sb_{12}$ *p-type* specimens joined using Ag flake-based adhesive and equal 1.92 ± 0.34 MPa and 5.248 ± 0.02 MPa respectively. Moreover, apparent shear strength of Ni / Ni(P) / Au (0.1/2/0.05 µm-thick) coated $(Ni,Co)Sb_3$ *n-type* and $Mm_y(Fe,Co)_4Sb_{12}$ *p-type* skutterudites bonded using Ag flake-based adhesive was 0.99 ± 0.08 and 3.31 ± 0.01 MPa respectively.

Table 4.2-4: Summary of the apparent shear strength measured for $(Ni,Co)Sb_3$ *n*- and $Mm_y(Fe,Co)_4Sb_{12}$ *p-type* thermoelectrics joined to metal interconnect using different joining techniques and metallization layers at the BOL conditions. Specimens that fractured during the pre-loading are listed as < 0.8 MPa. * Specimens joined at 660 ºC for 4.6 minutes in Ar using Solid-Liquid Interdiffussion (SLID) technique.

Thermoelectric element	**Metallization**	**Silver-flo™ 56**	**Ag paste**	**Ag-nano**	**Ag flakes**	**Al-Ni SLID***
		Apparent Shear Strength (MPa)				
$(Ni,Co)Sb_3$ *n-type*	**Non-metallized**	5.27 ± 0.01	< 0.8	n/a	n/a	n/a
	Ti/Ni (0.3/1.2 µm)	< 0.8	< 0.8	n/a	n/a	n/a
	Mo/Ni (0.3/1.2 µm)	2.94 ± 1.79	< 0.8	n/a	n/a	n/a
	W/Au (1/0.05 µm)	n/a	n/a	1.36 ± 0.08	< 0.8	n/a
	WSi_2/Au (1/0.05 µm)	n/a	n/a	7.69 ± 0.01	1.92 ± 0.34	n/a
	Ni/Ni(P) (0.1/2 µm)	3.71 ± 1.26	< 0.8	n/a	n/a	n/a
	Ni/Ni(P)/Au (0.1/2/0.05 µm)	n/a	n/a	9.65 ± 0.28	0.99 ± 0.08	n/a
	Ni/Ni(P) (0.1/14 µm)	n/a	n/a	n/a	n/a	2.4 ± 0.08

Table 4.2-4 (Continued)

Thermoelectric element	Metallization	Silver-flo™ 56	Ag paste	Ag-nano	Ag flakes	Al-Ni SLID*
		Apparent Shear Strength (MPa)				
$Mm_y(Fe,Co)_4Sb_{12}$ *p-type*	**Non-metallized**	14.22 ± 4.84	< 0.8	n/a	n/a	n/a
	Ti/Ni (0.3/1.2 μm**)**	< 0.8	< 0.8	n/a	n/a	n/a
	Mo/Ni (0.3/1.2 μm**)**	4.69 ± 1.02	< 0.8	n/a	n/a	n/a
	W/Au (1/0.05 μm)	n/a	n/a	< 0.8	< 0.8	n/a
	WSi_2/Au (1/0.05 μm)	n/a	n/a	6.12 ± 0.87	5.248 ± 0.02	n/a
	Ni/Ni(P) (0.1/2 μm)	6.16 ± 1.41	< 0.8	n/a	n/a	n/a
	Ni/Ni(P)/Au (0.1/2/0.05 μm)	n/a	n/a	11.42 ± 0.96	3.31 ± 0.01	n/a
	Ni/Ni(P) (0.1/14 μm)	n/a	n/a	n/a	n/a	4.49 ± 0.58

Mechanical testing was performed on Al-Ni SLID bonded contacts at the BOL conditions and the shear strength is presented in Table 4.2-5. The apparent shear strength of 2.4 ± 0.08 MPa and 4.49 ± 0.57 MPa was measured for $(Ni,Co)Sb_3$ *n-type* and $Mm_y(Fe,Co)_4Sb_{12}$ *p-type* material respectively, at the contact samples joined at 660 ºC for 4.6 min in Ar. Slightly higher apparent shear strength of 3.12 ± 0.78 MPa and 5.14 ± 0.51 MPa was measured for $(Ni,Co)Sb_3$ *n-type* and $Mm_y(Fe,Co)_4Sb_{12}$ *p-type* samples respectively, joined at 585 ºC for 15 minutes. It is evident, Solid-Liquid Interdiffusion (SLID) joining technique that was developed in this research is limited by the relatively low mechanical performance of such contacts as higher shear strength can be achieved by using Ag56-CuZnSn braze, Ag-based paste or low-temperature Ag sintering.

Scanning electron microscope along with EDS analysis was performed to observe the fractured interface and understand possible failure mode occurring at the BOL conditions within $Mm_y(Fe,Co)_4Sb_{12}$ *p-type* contacts joined at 660 ºC for 4.6 min and is presented in Appendix A (Figure A. 15). The fracture seems to propagate in the mixed mode – along or very close to the Ni(P) - Al_3Ni_2 intermetallic interface and within the joining area (as schematically shown in Figure 4.2-25) as the three distinct regions of Ni(P), Al_3Ni_2 and Al_3Ni can be detected by the EDS elemental mapping images. The top view image of sheared contact (Appendix A, Figure A. 15) suggests that the fracture occurring at the Ni(P) – intermetallic interface was not caused as initially expected within Al_3Ni_2 and Al_3Ni IMCs but presumably Ni(P) coating crystallisation at elevated temperature. This is consistent with SEM analysis (seen in Figure 4.2-21) and formation of P-rich and crystalline Ni-P IMCs within Ni(P) coating which are recognised as brittle phases and are often responsible for the mechanical failure of electroless Ni(P) coating while high-temperature welding of stainless steel

elements [131]. Moreover, specimens that were subjected to isothermal ageing were characterized by poor mechanical performance, as they failed during the pre-loading (~ 5 N) in the shear strength measurement.

Table 4.2-5: Summary of the apparent shear strength measured for $(Ni,Co)Sb_3$ *n*- and $Mm_y(Fe,Co)_4Sb_{12}$ *p-type* thermoelectric material joined to metal interconnect using Al-Ni Solid-Liquid Interdiffusion (SLID) bonding techniques at different process conditions.

Conditions	**585 ºC for 15 min**	**660 ºC for 4.6 min**
Thermoelectric element	Apparent Shear Strength (MPa)	
$(Ni,Co)Sb_3$ *n-type*	3.12 ± 0.78	2.4 ± 0.08
Mm_y*(Fe,Co)$_4$Sb$_{12}$ *p-type	5.14 ± 0.51	4.49 ± 0.57

Considering that the mechanical properties of skutterudite – metallic interconnects are rarely reported in the literature, and the mechanical strength depends on several variables, i.e. measurement set-up configuration, it is challenging to quantitatively compare to other high-temperature thermoelectric junctions previously reported. Nonetheless, according to Ref. [142], the maximum bonding strength of 13.2 MPa was achieved in low-temperature (Pb,Sn)Te/Cu layers bonded by solid-liquid interdiffusion (SLID) using In-Ag system, suggesting that low mechanical reliability of IMCs-based joints might cause failure in long-term operations, thus requires further improvement.

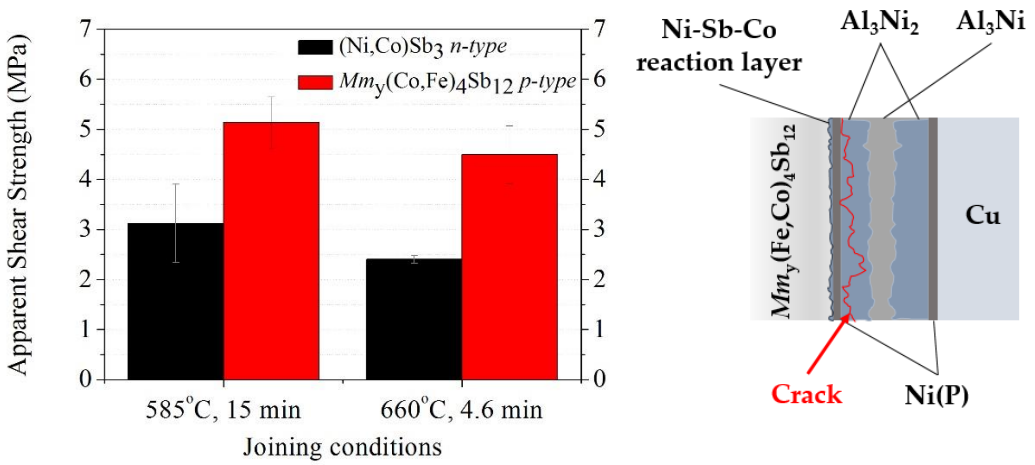

(a) **(b)**

Figure 4.2-25: Mechanical performance of bonded specimens: **(a)** apparent shear strength of *p-type* and *n-type* contacts formed using Al-Ni Solid-Liquid Interdiffusion (SLID) bonding at different joining conditions and **(b)** schematic illustration of $Mm_y(Fe,Co)_4Sb_{12}$ *p-type* specimen bonded at 660 °C for 4.6 min with fracture mode of sheared assembly marked in red.

4.2.10 Conclusions

A great effort in this thesis is put towards characterizing the electrical contact resistance and microstructure of metal interconnect–semiconductor interfaces developed using various joining techniques. The results presented in Chapter 4.2 were achieved by high temperature brazing using 56 at% Ag - 22 at% Cu – 17 at% Zn – 5 at% Sn filler metal and Ag paste, low temperature metal sintering using Ag-nano and Ag flake-based paste as well as novel, aluminium – nickel Solid-Liquid Interdiffusion (SLID) bonding technique.

Semiconductor – metal interconnects are at the core of solid-state device performance due to sensitivity to resistance in the electron flow and heat flux, and

hence might lead to reduced conversion efficiency of the prototype device. In order to achieve high performance of thermoelectric device, fabrication of high-performance and robust contacts is needed. The room temperature electrical performance was evaluated by measuring the electrical contact resistance (R_C) at contacting interfaces using four-point probe measurements. According to Ref. [27], in order to maintain > 80 % theoretical material efficiency in the working device, the electrical contact resistance (R_C) at the thermoelectric – metal contacts needs to be at least less than 30% of the total TE leg resistance (assuming no thermal contact resistances). By considering one thermoelectric pellet dimension of 2.5 × 2.5 × 3 mm and the electrical resistivity of $Mm_y(Fe,Co)_4Sb_{12}$ *p-type* thermoelectric material of 7.59 μΩ·m (measured by four-point probe resistivity at room temperature), the electrical contact resistance measured at the given sample geometries (schematically shown in Figure 3.6-1) should be < $6.8 \cdot 10^{-5}$ Ω·cm^2 in order to achieve high module performance promised from material measurements. Simultaneously, the electrical contact resistance for $(Ni,Co)Sb_3$ *n-type* contacts should be < $7.28 \cdot 10^{-5}$ Ω·cm^2, as the electrical resistivity of TE material of 8.09 μΩ·m was measured by four-point probe resistivity at room temperature. The results on *Rc* measurements of thermoelectric-interconnect contacts developed in this research are presented in Table 4.2-6.

High temperature bonding techniques, including Ag56-CuZnSn braze, Ag paste and Al-Ni Solid-Liquid Interdiffusion (SLID) bonding helped with formation of satisfactory *n-type* contacts in terms of their electrical performance as measured *Rc* was in the acceptable range below < $7.28 \cdot 10^{-5}$ Ω·cm^2 in all metallization configurations (see Table 4.2-6). This can be explained by the microstructural analysis of contacting interfaces as formation of reaction layers between two joined components that was observed, normally works in joint's

electrical benefit. These layers were identified as Ni_5Sb_2 and (Ni,Co)Sb compounds and were observed in both Ag56-CuZnSn and high-temperature Ag contacts when pure nickel was used as interconnect material. It is believed that the formation of reaction layers occurs due to the constant nickel diffusion through joining material and will lead to nickel complete dissolution into the thermoelectric material and interfacial phase change upon time. The Ag56-CuZnSn based and high-temperature sintered Ag contacts did not retain mechanical integrity after isothermal ageing at 450 ºC and excessive formation of Ni-Co-Sb reaction layers along with consumption on nickel interconnect was believed to be a mechanism behind joints failure. Al-Ni Solid-Liquid Interdiffusion (SLID) bonding was proven to successfully hinder reaction layer growth as Cu - Ni(P) plated interconnect with limited nickel accessibility was used. 10 μm-thick (Ni,Co)Sb interfacial reaction layer observed in the *n-type* contacts joined by SLID technique (at 660 ºC for 4.6 minutes in Ar) and stayed unchanged upon ageing (at 450 ºC for 96 hours in Ar) due to the complete nickel transformation into Al-Ni and Ni-P IMCs phase (Figure 4.2-21c and Figure 4.2-23b). Moreover, no copper diffusion through Al-Ni IMCs bonding material was observed upon ageing but Kirkendall void and P-rich phase formation were presumably a reason behind samples failure during pre-loading (of ~ 5 N) in the mechanical shear testing. The high content of phosphorous in the Ni(P) layer was responsible for coating crystallization and precipitation of brittle Ni-P intermetallic compounds along with Fe-P phases in the *p-type* contacts. Initial joining tests were performed with pure nickel used instead of Ni(P) coating and promising results were achieved but requires additional quantifying.

The *p-type* contacts suffer the most in terms of their electrical and microstructural performance as a result of high-temperature brazing treatment

with Ag56-CuZnSn braze (655 ºC for 5 minutes in flowing Ar). Un-reacted antimony, which was found to precipitate at grain boundaries of skutterudite phase during the consolidation process is presumed to volatilize at bonding temperature or react with Ag56-CuZnSn braze leaving a porous microstructure near the contacting interface. The electrical performance of the $Mm_y(Fe,Co)_4Sb_{12}$ *p-type* contacts as presented in Table 4.2-6, shows higher than acceptable (< 6.8 $\cdot 10^{-5}$ $\Omega \cdot cm^2$) *Rc* measured in all specimens joined with nickel interconnect using Ag56-CuZnSn braze and high temperature Ag paste. The electrical contact resistance of 4.86 $\cdot 10^{-5}$ $\Omega \cdot cm^2$ was measured for *p-type* specimens formed using Al-Ni SLID bonding technique and is consistent with microstructural analysis as continuous interfaces with no visible cracks within bonding material were formed (Figure 4.2-21b).

Low temperature Ag-nano and Ag flake-based joining materials were proven to be effective in forming high-performance electrical contacts in both *n-* and *p-type* specimens. The low values of electrical contact resistances (< $2 \cdot 10^{-5}$ $\Omega \cdot cm^2$) were measured on Ni/Ni(P)/Au coated samples as reduced joining temperature inhibit the formation of interfacial reaction layer. Moreover, lack of corrosive flux (such as borax and borax acid found in commercial silver-flo^{TM} 56 braze) helped with a stability of unreacted antimony with *p-type* skutterudite material and no porous microstructure was found at the contacting interfaces. Two other metallization layers of W/Au (1/0.05 μm-thick) and WSi_2/Au (1/0.05 μm-thick) materials were tested along with low-temperature joining materials with relatively poor electrical performance as a result of tungsten delamination and low electrical conductivity of amorphous WSi_2 phase.

Table 4.2-6: Summary of the electrical contact resistance (Rc) obtained for *n*- and *p-type* thermoelectrics using different joining techniques and metallization layers at the BOL conditions. * Specimens joined at 660 ºC for 4.6 minutes in Ar using Solid-Liquid Interdiffussion (SLID) technique.

Thermoelectric element	Metallization	Silver-flo™ 56	Ag paste	Ag-nano	Ag flakes	Al-Ni SLID*
		Rc ($\Omega \cdot cm^2$)				
(Ni,Co)Sb_3 ***n-type***	**Non-metallized**	$3.12 \cdot 10^{-5} \pm 7.7 \cdot 10^{-6}$	$1.85 \cdot 10^{-5} \pm 9.79 \cdot 10^{-6}$	n/a	n/a	n/a
	Ti/Ni (0.3/1.2 µm)	$6.69 \cdot 10^{-5} \pm 1.14 \cdot 10^{-5}$	$2.68 \cdot 10^{-5} \pm 7.84 \cdot 10^{-6}$	n/a	n/a	n/a
	Mo/Ni (0.3/1.2 µm)	$4.91 \cdot 10^{-5} \pm 1.04 \cdot 10^{-5}$	$2.2 \cdot 10^{-5} \pm 5.23 \cdot 10^{-6}$	n/a	n/a	n/a
	W/Au (1/0.05 µm)	n/a	n/a	$3.54 \cdot 10^{-4} \pm 3.4 \cdot 10^{-5}$	$6.79 \cdot 10^{-4} \pm 3 \cdot 10^{-4}$	n/a
	WSi_2/Au (1/0.05 µm)	n/a	n/a	$5.6 \cdot 10^{-4} \pm 5.35 \cdot 10^{-5}$	$2.53 \cdot 10^{-3} \pm 6.75 \cdot 10^{-4}$	n/a
	Ni/Ni(P) (0.1/2 µm)	$7.34 \cdot 10^{-5} \pm 7.7 \cdot 10^{-6}$	$1.88 \cdot 10^{-5} \pm 5.23 \cdot 10^{-6}$	n/a	n/a	n/a
	Ni/Ni(P)/Au (0.1/2/0.05 µm)	n/a	n/a	$1.40 \cdot 10^{-5} \pm 3.94 \cdot 10^{-5}$	$2.0 \cdot 10^{-5} \pm 8.92 \cdot 10^{-7}$	n/a
	Ni/Ni(P) (0.1/14 µm)	n/a	n/a	n/a	n/a	$2.87 \cdot 10^{-5} \pm 6.4 \cdot 10^{-6}$

Table 4.2-6 (Continued)

Thermoelectric element	Metallization	Silver-flo™ 56	Ag paste	Ag-nano	Ag flakes	Al-Ni SLID*
				Rc ($\Omega \cdot cm^2$)		
Mm*$_y$(Fe,Co)$_4$Sb$_{12}$ *p-type	**Non-metallized**	$1.41 \cdot 10^{-4}$ $\pm 4.66 \cdot 10^{-5}$	$6.12 \cdot 10^{-5}$ $\pm 4.39 \cdot 10^{-5}$	n/a	n/a	n/a
	Ti/Ni (0.3/1.2 μm)	$8.29 \cdot 10^{-5}$ $\pm 2.04 \cdot 10^{-5}$	$3.43 \cdot 10^{-5}$ $\pm 6.7 \cdot 10^{-6}$	n/a	n/a	n/a
	Mo/Ni (0.3/1.2 μm)	$8.78 \cdot 10^{-5}$ $\pm 7.63 \cdot 10^{-5}$	$1.26 \cdot 10^{-4}$ $\pm 1.03 \cdot 10^{-5}$	n/a	n/a	n/a
	W/Au (1/0.05 μm)	n/a	n/a	$1.98 \cdot 10^{-3}$ $\pm 2.54 \cdot 10^{-4}$	$1.3 \cdot 10^{-3}$ $\pm 3.09 \cdot 10^{-4}$	n/a
	WSi$_2$/Au (1/0.05 μm)	n/a	n/a	$1.58 \cdot 10^{-3}$ $\pm 1.03 \cdot 10^{-4}$	$8.13 \cdot 10^{-4}$ $\pm 8.42 \cdot 10^{-5}$	n/a
	Ni/Ni(P) (0.1/2 μm)	$1.08 \cdot 10^{-4}$ $\pm 1.04 \cdot 10^{-5}$	$1.16 \cdot 10^{-4}$ $\pm 1.7 \cdot 10^{-5}$	n/a	n/a	n/a
	Ni/Ni(P)/Au (0.1/2/0.05 μm)	n/a	n/a	$1.49 \cdot 10^{-5}$ $\pm 2.3 \cdot 10^{-6}$	$2.27 \cdot 10^{-5}$ $\pm 5.44 \cdot 10^{-5}$	-
	Ni/Ni(P) (0.1/14 μm)	n/a	n/a	n/a	n/a	$4.84 \cdot 10^{-5}$ $\pm 3.16 \cdot 10^{-6}$

Many bonding techniques in terms of their microstructural, electrical and mechanical performance were investigated and reported in Chapter 4 and only the most promising candidates were used for the fabrication of module prototype. In order to evaluate reliability of each joining technique along with metallization and possibility of implementing into industrial manufacturing of high-performance thermoelectric module, overall performance was compared and listed in Table 4.2-7. To clearly summarize suitability of each technique, electrical (E), mechanical (M) and more subjective microstructural (R) performance of $Mm_y(Fe,Co)_4Sb_{12}$ *p-type* (+) and $(Ni,Co)Sb_3$ *n-type* (+) contacts were analysed in terms of their acceptability level. As seen in Table 4.2-7, each cell contains three letters in three distinguish colours, depending on the measured performance. In the case of electrical suitability (E), green colour indicates measured electrical contact resistance < $6.8 \cdot 10^{-5}$ $\Omega \cdot cm^2$, yellow colour indicates contact resistance between $6.8 \cdot 10^{-5}$ $\Omega \cdot cm^2$ and $1.4 \cdot 10^{-4}$ $\Omega \cdot cm^2$ and red colour is for $R_C > 1.4 \cdot 10^{-4}$ $\Omega \cdot cm^2$. The mechanical performance (M) was evaluated by measuring apparent shear strength with minimum acceptable strength of > 5 MPa highlighted in green, yellow colour indicated apparent shear strength between 5 MPa and 0.8 MPa and red when specimens failed during the pro-loading with approximately value of < 0.8 MPa. Moreover, based on the SEM microstructural analysis, formed contacts were evaluated in terms of the joint quality, cracks and reaction layer formation that would have significant impact on the performance of thermoelectric module. Although the quality of these characteristics is very subjective, green, yellow and red colours were used for the good, acceptable and poor performance of contacting interfaces (R).

Table 4.2-7: Comparison of electrical (E), mechanical (M) and microstructural (R) performance of chosen joning technique and metallization design in the *n*- (-) and *p-type* (+) contacts in terms of suitability for prototype module fabrication. * Specimens joined at 660 ºC for 4.6 minutes in Ar using Solid-Liquid Interdiffussion (SLID) technique.

Metallization	**Silver-flo™ 56**	**Ag paste**	**Ag-nano**	**Ag flakes**	**Al-Ni SLID***
	Suitable solution				
Non-metallized	(-) E M R (+) E M R	(-) E M R (+) E M R	n/a	n/a	n/a
Ti/Ni (0.3/1.2 µm)	(-) E M R (+) E M R	(-) E M R (+) E M R	n/a	n/a	n/a
Mo/Ni (0.3/1.2 µm)	(-) E M R (+) E M R	(-) E M R (+) E M R	n/a	n/a	n/a
W/Au (1/0.05 µm)	n/a	n/a	(-) E M R (+) E M R	(-) E M R (+) E M R	n/a
WSi_2/Au (1/0.05 µm)	n/a	n/a	(-) E M R (+) E M R	(-) E M R (+) E M R	n/a
Ni/Ni(P)/Au[j] (various thicknesses)	(-) E M R (+) E M R	(-) E M R (+) E M R	(-) E M R (+) E M R	(-) E M R (+) E M R	(-) E M R (+) E M R

According to results depicted in Table 4.2-7, two low-temperature bonding techniques using nano-Ag and Ag flake-based joining materials and higher temperature Solid-Liquid Interdiffusion (SLID) bonding technique were characterized with the highest overall performance at the beginning-of-life conditions. Moreover, two metallization layers that were combined with these joining techniques resulted in the optimal performance needed for high performance, medium-high regime thermoelectric generator. Based on the given results, five combinations of bonding techniques and metallization were

[j] Au top layer was introduced in the Ag-nano and Ag flakes bonding only

shortlisted for the module prototype fabrication and included WSi_2/Au (1/0.05 μm) and Ni/Ni(P)/Au (0.1/2/0.05 μm) metallized skutterudites with Ag-nano and Ag flake-based adhesive along with SLID technique. These combinations are highlighted with squares in Table 4.2-7. The WSi_2/Au (1/0.05 μm) metallization has relatively poor electrical performance due to the high resistivity but it was assumed that WSi_2 amorphous layer will partially crystallize during the high-temperature measurement (or the service) which was further confirmed. Moreover, module with WSi_2/Au (1/0.05 μm) layer was only assembled using Ag flake-based bonding material as initial reliability test revealed that Ag-nano paste based modules are more likely to be mechanically unstable at temperatures higher than 350 ^{o}C. Additionally, initial tests revealed difficulties with performing module-level assembly using Al foils in the SLID technique and resulting prototype module was characterized with an electrical shunt and very high module resistivity.

4.3 Thermoelectric Material–Metallization Co-sintering

One of the challenges in the development of robust high-temperature thermoelectric device is fabrication of stable diffusion barrier and metallization stack that includes adhesion layer diffusion barrier and wetting top layer. Contacts in the skutterudite-based modules, in the high extend, suffer from the intensive thermal stresses induced during the high-temperature service. These stresses include a volumetric change, associated with the phase transformation at the skutterudite–metallization interface and thermal expansion coefficient (CTE) mismatch of the components. Nonetheless, a lack of chemical interaction and CTE mismatch, i.e. between molybdenum and skutterudite thermoelectric material, as shown in Chapters 4.2.1 and 4.2.2, results in metallization stack delamination and presumable device failure at elevated temperature. Thermoelectric material in this research was *in-situ* synthesized using spark plasma sintering technique and involved high temperature consolidation and applied high uniaxial pressure (> 50 MPa). Such conditions could be beneficial for formation of strong mechanical bond between thermoelectric material and metallization stack and were previously reported for nickel-chalcogenide thermoelectric systems [143]. In this chapter, initial tests on co-sintering of thermoelectric material with various metallic foils in single and multi-metallization design are presented. Although resulting materials did not survive further processing due to cutting process limits, and so were not characterized further, initial microstructural analysis of most successful candidates will be presented here. Moreover, for the sake of brevity, complete EDS analyses of contacting interfaces will be not presented in the following Chapter 4.3.

Co-sintering of thermoelectric material and metallization foils was performed at the conditions optimized for *in-situ* synthesis of $Mm_y(Fe,Co)_4Sb_{12}$ *p-type* and $(Ni,Co)Sb_3$ *n-type* skutterudite materials. In order to promote formation of interfacial reactions, an additional holding at temperatures of at least 78% of the initial in-situ synthesis temperature was carried out. That included dwelling with uniaxial pressure of 50 MPa applied for 10 minutes at 500 ºC and 590 ºC for *p-type* and *n-type* assemblies respectively. In the single metallization design, 50 µm-thick titanium and 100 µm-thick zirconium foils were bonded with thermoelectric material at one-step sintering step. As can be seen in Figure 4.3-1a, there is no formation of reaction layer at the *p-type* $Mm_y(Fe,Co)_4Sb_{12}$ – titanium interface, due to the insufficient processing temperature (600 ºC). Although no presumable chemical reaction occurred at the contact, a continuous interface between the two materials with no visible cracks was observed.

At the same time, $(Ni,Co)Sb_3$ *n-type* thermoelectric material was co-sintered with Ti foil (99.7% purity) at 750 ºC and < 5 µm-thick Ti- rich intermediate layer was observed at the interface. A visible crack between reaction layer and thermoelectric (seen in Figure 4.3-1b) was presumably caused by the thermal stresses induced during the cooling and volumetric change of the newly formed phase. As determined by EDS analysis, the phase consisted of 34 at% Ti, 20 at% Co, 10.5 at% Ni and 35.5 at% Sb which is consistent with results of Ref. [46]. Although, high-pressure involved in the SPS process works beneficially to the interfacial integration due to the formation of mechanically strong bonds, high temperature normally enhances formation of interfacial secondary phases, such as brittle intermetallic compounds (IMCs). The chemical phenomena occurring at interfaces determine it structure and properties. The chemical reaction between the ceramic and the metal may easily initiate bond formation; however, thick

brittle reaction layers or intermetallic compounds formed at the interface often cause premature failure at very low stresses. Crack formed at the titanium – skutterudite interface are induced by thermal stresses induced in the contact during cooling due to the CTE mismatch and differing mechanical responses of metal and skutterudite.

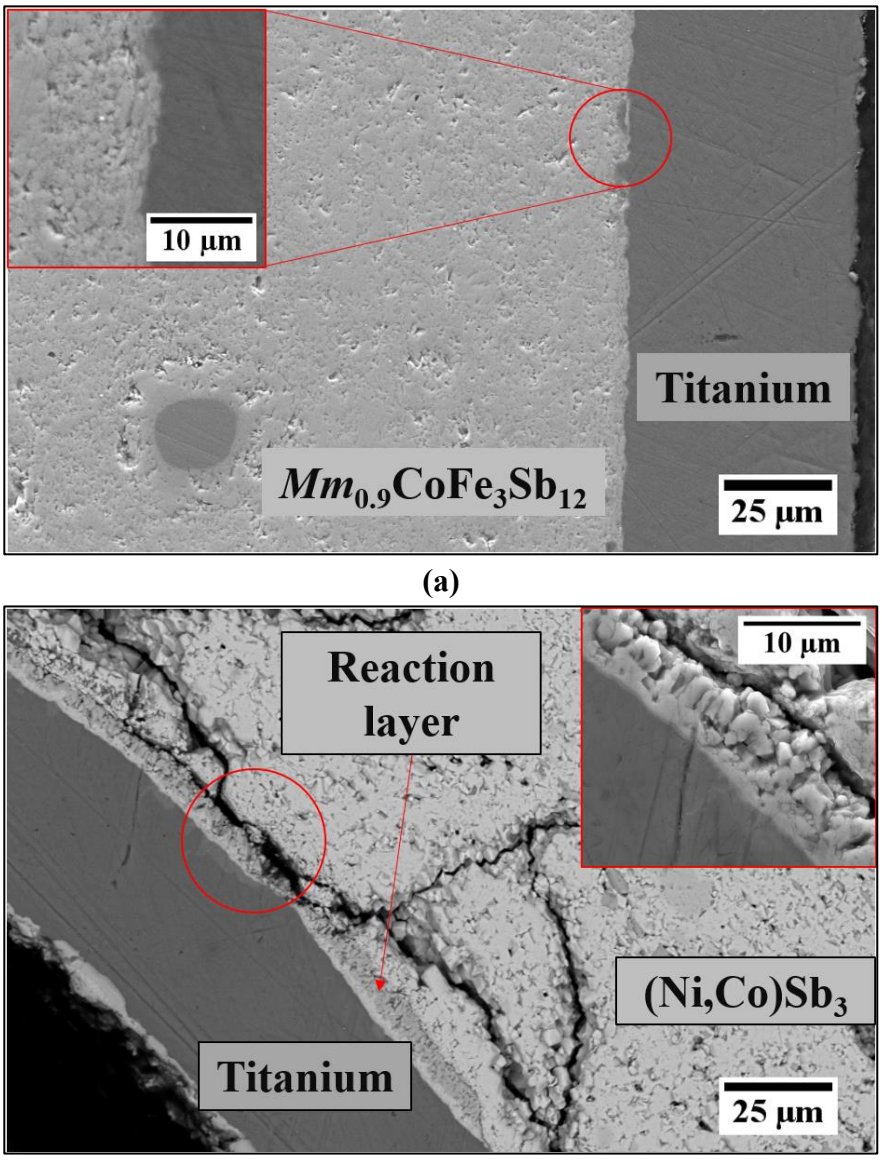

Figure 4.3-1: Interfacial microstructure of the **(a)** $Mm_y(Fe,Co)_4Sb_{12}$ *p-type* and **(b)** $(Ni,Co)Sb_3$ *n- type* skutterudite–interconnect interfaces co-sintered during the *in-situ* synthesis by SPS with 50 µm-thick Ti foil (99.7% purity). Red circle shows higher magnification images of contacting interfaces.

A 100 µm-thick Zr layer (99.98% purity) was introduced as potential metallization for $Mm_y(Fe,Co)_4Sb_{12}$ *p-type* and $(Ni,Co)Sb_3$ *n-type* skutterudites. As seen in Figure 4.3-2, 3.5 µm-thick and 12.5 µm-thick reaction layers were formed at the zirconium and *p*- and *n-type* contacts respectively, and were determined by EDS (not shown here) as $ZrSb_2$ phase (33 at% Zr and 67 at% Sb).

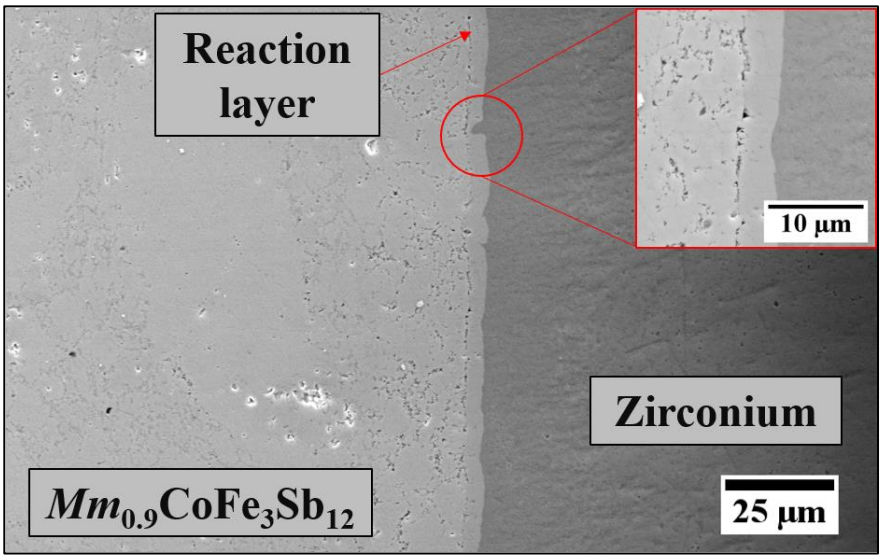

(a)

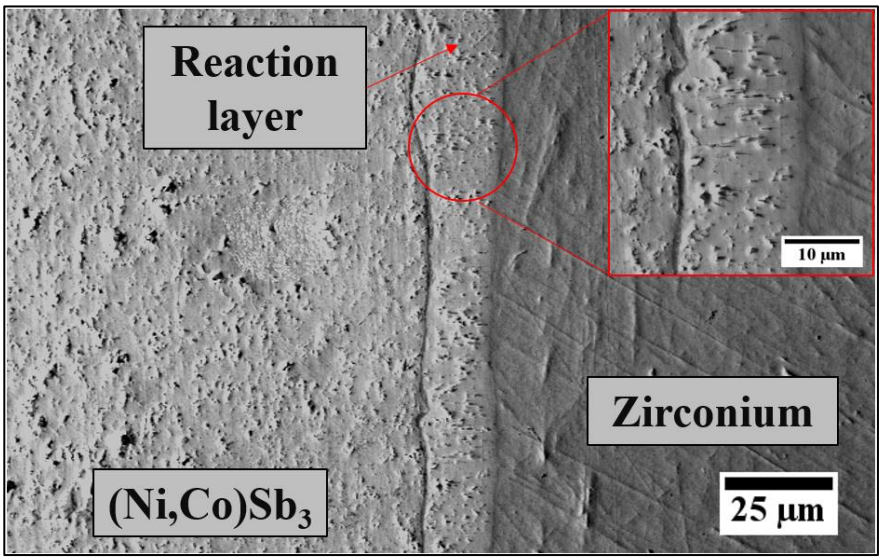

(b)

Figure 4.3-2: Interfacial microstructure of the **(a)** $Mm_y(Fe,Co)_4Sb_{12}$ *p-type* and **(b)** $(Ni,Co)Sb_3$ *n- type* skutterudite–interconnect interfaces co-sintered during the *in-situ* synthesis by SPS with 100 µm-thick Zr foil (99.98% purity). Red circle shows higher magnification images of contacting interfaces.

In the bi-layered design, thermoelectric powders (elemental mixture) were co-sintered with 50 μm-thick Zr and 50 μm-thick Ti foils using conditions optimized for pre-alloyed powders in one sintering step. Such a design shortens the consolidation process, by allowing thermoelectric material *in-situ* synthesis and its full consolidation to nearly 98% of its theoretical density and formation of diffusion (zirconium) and top metallization (titanium) layer in only one process step. First layer to be in contact with thermoelectric material is used to create a strong (and chemically stable) bond between top metallization layer, that is usually in contact with joining material. As seen in Figure 4.3-2, thermoelectric material when contacted with zirconium, formed a thin $ZrSb_2$ IMC layer in $Mm_y(Fe,Co)_4Sb_{12}$ *p-type* and $(Ni,Co)Sb_3$ *n-type* materials. The zirconium foil could be possibly utilized as adhesion layer, since titanium, stainless steel and molybdenum that are designed to serve as top wetting layers at the initial joining test delaminated from the skutterudite interface. Figure 4.3-3a presents $Mm_y(Fe,Co)_4Sb_{12}$ *p-type* thermoelectric material co-sintered with 50 μm-thick zirconium and 50 μm-thick titanium foil. Although $ZrSb_2$ IMC was observed at the thermoelectric – zirconium interface, no intermediate phase at the zirconium – titanium interface was observed. Successful solid-state diffusion bonding between zirconium and titanium layer was achieved at conditions optimized for $(Ni,Co)Sb_3$ *n-type* skutterudite (Figure 4.3-3b) with β(Zr,Ti) solid solution formed at the interface due to the joining temperature (750 ^{o}C) the minimum temperature of the α(Zr,Ti) – β(Zr,Ti) phase transformation. This is consistent with results of Ref. [144].

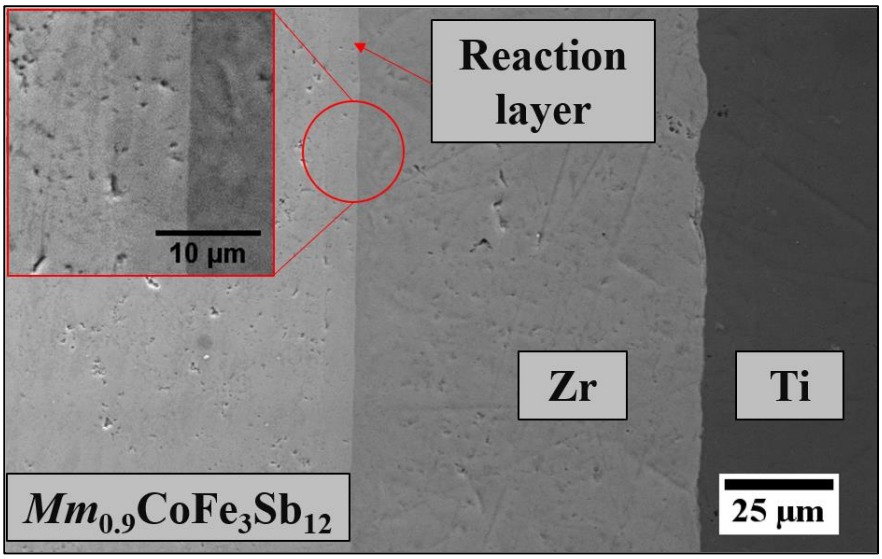

(a)

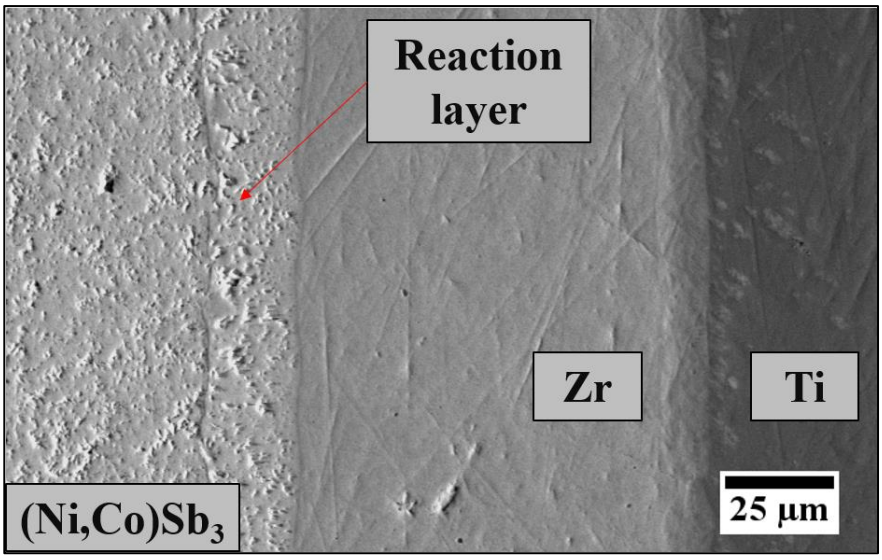

(b)

Figure 4.3-3: Interfacial microstructure of the **(a)** $Mm_y(Fe,Co)_4Sb_{12}$ *p-type* and **(b)** $(Ni,Co)Sb_3$ *n- type* skutterudite–interconnect interfaces co-sintered during the *in-situ* synthesis by SPS with 50 µm-thick Zr and 50 µm-thick Ti foil. Red circle shows higher magnification images of contacting interfaces.

Figure 4.3-4 shows $Mm_y(Fe,Co)_4Sb_{12}$ *p-type* and $(Ni,Co)Sb_3$ *n-type* skutterudite materials co-sintered with 50 µm-thick zirconium and 50 µm-thick stainless steel (SS303 series) foils. Similar to Zr-Ti bi-layered metallization, the formation of $ZrSb_2$ IMC at the skutterudite – zirconium interface is observed in both $Mm_y(Fe,Co)_4Sb_{12}$ *p-type* and $(Ni,Co)Sb_3$ *n-type* contacts, with no chemical

reaction observed between Zr and SS303 material. Lack of intermediate layer formation between zirconium and SS303 stainless steel is presumably a result of low bonding temperature and no chemical interaction between elements constituting both materials. It is believed that pre-sintering of Zr-SS303 foils at minimum temperature of 800 ºC could induce intermediate phase formation (such as $FeZr_3$ intermetallic compound) and form strong chemical bond between these materials.

Figure 4.3-5 presents $Mm_y(Fe,Co)_4Sb_{12}$ *p-type* and $(Ni,Co)Sb_3$ *n-type* thermoelectric materials co-sintered with 25 µm-thick 70 at% Ti – 15 at% Cu – 15 at% Ni (Ticuni™) adhesion layer and 25 µm-thick Mo foil. Ticuni™ foil is used for 'active brazing' process and often commercially available foils are in form of tri-layered material (core is made of CuNi and external layer is Ti) that has a liquidus temperature of 960 ºC. The reason for using Ticuni™ layer was to join Molybdenum foil to skutterudite-based materials by diffusion bonding process. It can be seen that 1 µm-thick $TiSb_2$ IMC layer with minimal Fe, Co, Ni and Cu solubility (33 at% Ti, 65.5 at% Sb, 0.6 at% Fe, 0.2 at% Co, 0.4 at% Ni and 0. 3 at% Cu as determined by EDS analysis) formed at the $Mm_y(Fe,Co)_4Sb_{12}$ *p-type* - Ticuni™ interface. At the same time, lack of reaction between molybdenum and Ticuni™ led to the delamination of top molybdenum layer. Titanium and molybdenum are completely miscible above 882 ºC and below that temperature, the solubility of Mo and Ti is restricted as the maximum solubility of Mo in α-Ti is less than 0.5% at 600 ºC. Joining of $(Ni,Co)Sb_3$ *n-type* material was performed at higher than *p-type* temperatures thus thicker interfacial reaction layer (~ 15 µm-thick) was formed at that interface and no reaction layer at the Ticuni™ – molybdenum interface (Figure 4.3-5b). As determined by EDS analysis, reaction layer consists of 31 at% Ti, 22 at% Co, 10 at% Ni and 36 at% Sb. It is consistent

with results for specimens co-sintered with pure Ti foils presented in Figure 4.3-1b.

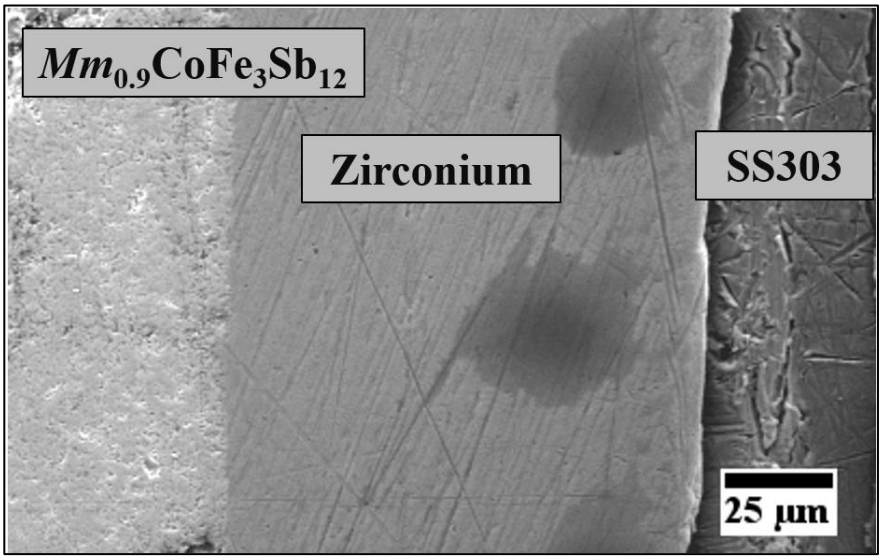

(a)

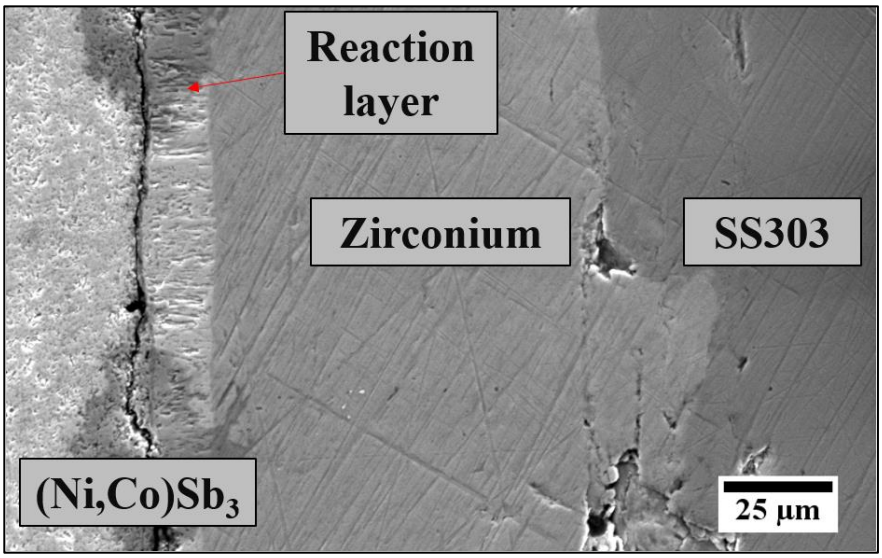

(b)

Figure 4.3-4: Interfacial microstructure of the **(a)** $Mm_y(Fe,Co)_4Sb_{12}$ *p-type* and **(b)** $(Ni,Co)Sb_3$ *n- type* skutterudite–interconnect interfaces co-sintered during the *in-situ* synthesis by SPS 50 µm-thick Zr and 50 µm-thick SS303 (stainless steel) foil. Red circle shows higher magnification images of contacting interfaces.

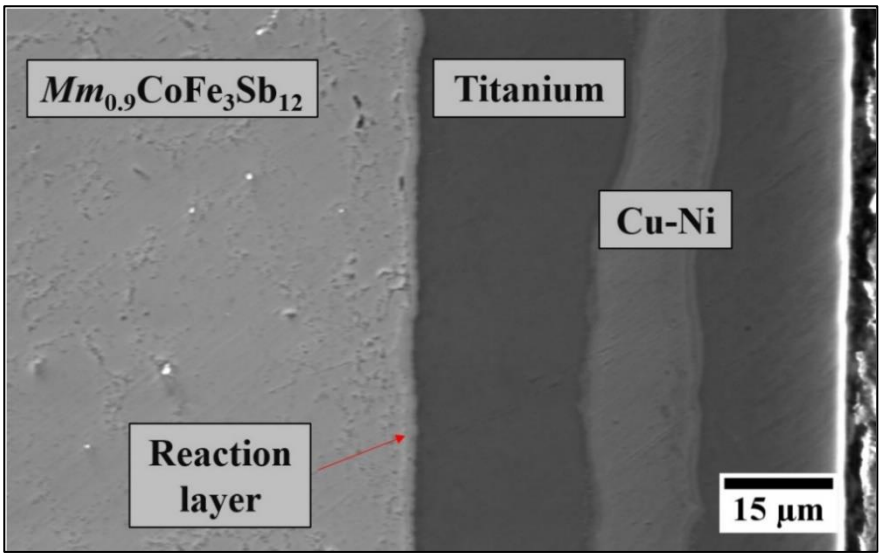

(a)

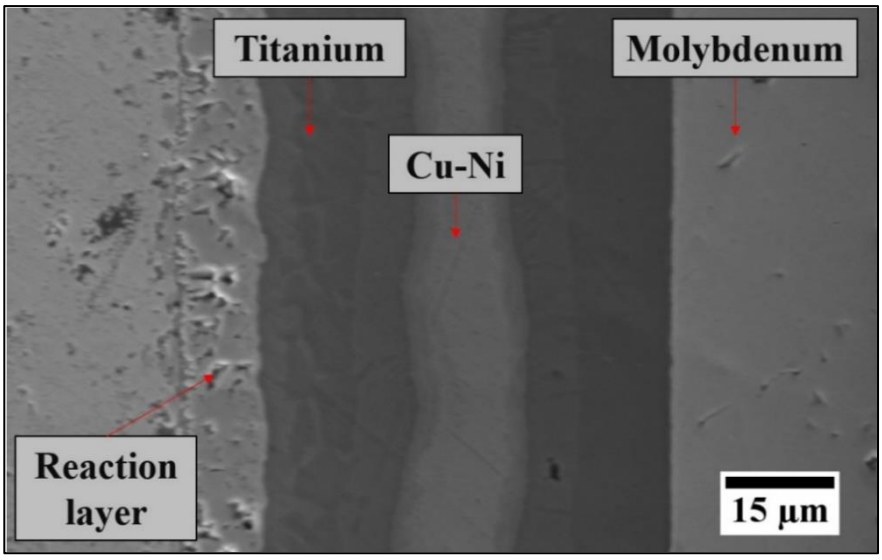

(b)

Figure 4.3-5: Interfacial microstructure of the **(a)** $Mm_y(Fe,Co)_4Sb_{12}$ *p-type* and **(b)** $(Ni,Co)Sb_3$ *n- type* skutterudite–interconnect interfaces co-sintered during the *in-situ* synthesis by SPS with 50 µm-thick 70 at% Ti – 15 at% Cu – 15 at% Ni (Ticuni^{TM}) and 25 µm-thick Mo foils foil. Red circle shows higher magnification images of contacting interfaces.

In the tri-layered design, thermoelectric powders (elemental mixture) were joined with pre-sintered 9 µm-thick nickel, 25 µm-thick molybdenum and 9 µm-thick nickel discs using conditions optimized for pre-alloyed powders in one sintering step. The sintering of 9 µm-thick Ni - 25 µm-thick Mo - 9 µm-thick Ni

interlayers was carried using Spark Plasma Sintering technique by applying uniaxial pressure of 50 MPa for 10 minutes so that nickel-molybdenum, solid-state reaction could occur. Pre-sintering of metallization stack was necessary as initial tests performed in a conventional way resulted in molybdenum layer delamination. Although Ni-Mo intermetallic compound was not found at contacting interfaces, as expected from the phase diagram [145], minor reaction was expected, as layers within stack did not delaminated. Thin nickel layer was implemented as both adhesion and top, wetting layer, as molybdenum was found to relatively easily delaminate at higher service temperatures and experiences limited wettability by molten brazes [34]. As seen in Figure 4.3-6, two distinguish layers of Ni_5Sb_2 IMCs (Ni-rich being in contact with molybdenum) can be found at the Ni (9 μm-thick) / Mo (25 μm-thick) / Ni (9 μm-thick) and both *n-* and *p-type* contacts. Although two layers of relatively brittle Ni_5Sb_2 IMCs were formed at the skutterudite-molybdenum interface, chemical bond between two elements in stack will presumably work in materials' mechanical benefit.

The configurations of different metallization and resulting interfacial reaction layers are summarized in Table 4.3-1. The *n-type* contacts were found to form thicker reaction layers at the contacting interfaces, as compared to *p-type* contacts, presumably due to the higher processing temperature (750 ^{o}C). Moreover, high temperature was also found beneficial for the formation of β(Zr,Ti) solid solution between zirconium and titanium metallization stacks as α(Zr,Ti) – β(Zr,Ti) phase transformation could occur [146]. The *p-type* contacts were found to form significantly thinner interfacial reaction layers of intermetallic compounds (such as Ti-rich (Co,Ni)Sb, $ZrSb_2$ or Ni_5Sb_2). The pre-sintering of metallization stack was proven to succesfully intergate various metal foils that can be further co-sintered with thermoelectric material using in-situ synthesis. Nonetheless, in order

to avoid foil delamination, less aggressive cutting technique or sintering to thermoelements' required shape is necessary.

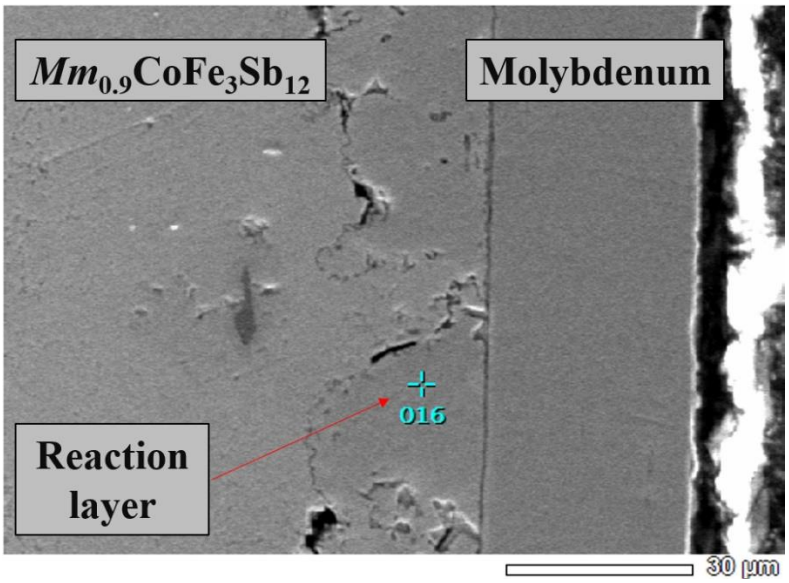

(a)

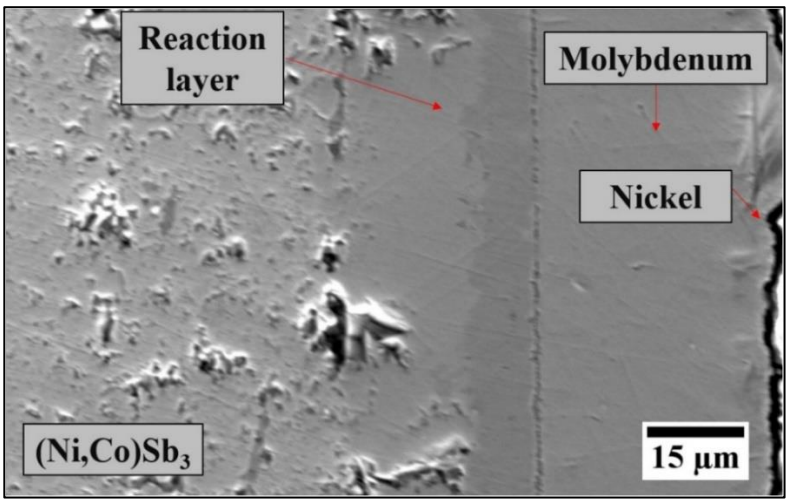

(b)

Figure 4.3-6: Interfacial microstructure of the **(a)** $Mm_y(Fe,Co)_4Sb_{12}$ *p-type* and **(b)** $(Ni,Co)Sb_3$ *n- type* skutterudite–interconnect interfaces co-sintered during the *in-situ* synthesis by SPS with 9 µm-thick Ni, 25 µm-thick Mo and 9 µm-thick Ni foil. Red circle shows higher magnification images of contacting interfaces.

Table 4.3-1: Summary of the microstructural analysis of $Mm_y(Fe,Co)_4Sb_{12}$ *p-type* and $(Ni,Co)Sb_3$ *n- type* skutterudites co-sintered with metallization layers.

		Mm*$_y$(Fe,Co)$_4$Sb$_{12}$ *p-type		**(Ni,Co)Sb$_3$ *n-type***	
		Second phases		**Second phases**	
		Thickness (µm)	**Composition**	**Thickness (µm)**	**Composition**
Ti (50 µm)		Not observed		< 5	Ti-rich (Co,Ni)Sb
Zr (100 µm)		3.5	$ZrSb_2$	12.5	$ZrSb_2$
Zr (100 µm) / Ti (50 µm)	**SKD-Zr**	3.5	$ZrSb_2$	12.5	$ZrSb_2$
	Zr-Ti		-	7	β(Zr,Ti)
Zr (100 µm) / SS303 (50µm)	**SKD-Zr**	3.5	$ZrSb_2$	12.5	$ZrSb_2$
	Zr-SS303	-	-	-	-
Ticuni™ (25 µm) / Mo (25 µm)	**SKD-Ticuni™**	1	$TiSb_2$	15	Ti-rich (Co,Ni)Sb
	Ticuni™ - Mo	-	-	-	-
Ni (9 µm) / Mo (25 µm) / Ni (9 µm)	**Ni-Mo**	-	presumably	-	presumably
	Ni-SKD	25	Ni-rich Ni_5Sb_2 and Ni_5Sb_2	25	Ni-rich Ni_5Sb_2 and Ni_5Sb_2

Chapter 5

TEG Simulation and Modelling

The finite element modelling was used to simulate the thermoelectric generator performance using COMSOL Multiphysics® software. The model template was developed by Dr Richard Tuley from European Thermodynamics Ltd. In simple calculations of module performance, the variation of thermoelectric materials parameters as a function of temperature along the thermoelectric leg are neglected. COMSOL Multiphysics® modelling allows the full temperature dependence to be included. The Seebeck coefficient (α), electrical (σ) and thermal (κ) conductivities are dependent on the temperature and the thermoelectric properties used are those obtained from the high-temperature measurements (Figure 4.1-3 and Figure 4.1-6). These are used in a performance simulation of single *p-n* unicouple in the generation mode, with the additional parameters used given in Table 5.1-1. Moreover, electrical contact resistance (*Rc*) delivered from leg-to-leg joining experiments were used in simulations. The electrical domain was modelled as a *n-* and *p-type* elements arranged in unicouples connected in series while thermally combined in parallel.

Table 5.1-1: Thermal and electrical properties of elements used in the modelling.

Component	Material	Dimensions (mm)	ρ (kg/m^3)	Cp (J/kgK)	κ (W/mK) [kl]	σ (S/m) [ml]	α (V/K) [ml]
Ceramic substrates	Al_2O_3	6×2.5×1	3900	900	27	0	0
Interconnects	Cu	6×2.5×0.3	8700	385	400	$5.9\cdot10^{7}$	$6.5\cdot10^{-6}$
***n-type* TE leg**	$(Ni,Co)Sb_3$	2.5×2.5×3	7640[m]	235	$5\cdot10^{-6}T^2-6.4\cdot10^{-3}T+5.89$	$6.31\cdot10^{-2}T^2-84.86T+150039$	$3\cdot10^{-10}T^2-5\cdot10^{-7}T+5\cdot10^{-5}$
***p-type* TE leg**	$Mm_y(Fe,Co)_4Sb_{12}$	2.5×2.5×3	7940[m]	232	$1\cdot10^{-6}T^2+0.3\cdot10^{-3}T+2.52$	$1.78\cdot10^{-2}T^2-38.34T+142688$	$-1\cdot10^{-10}T^2+2\cdot10^{-7}T-5\cdot10^{-6}$

[k] Temperature (T) in kelvin (K)
[l] Assumed value in the ideal case scenario
[m] Assumption in the ideal conditions of the thermoelectric material being 100% dense

The numerical modelling was performed with segregated parametric solvers of the 3D - Finite Element Analysis (FEA) tool by combining thermoelectric effect (the Seebeck, Peltier and Thomson effect), temperature coupling and electromagnetic heat source in the steady state conditions. With this approach, multidimensional effects caused by the heat transfer can be illustrated using the equation for the steady-state multidimensional temperature and electrical distribution in the thermoelectric material. The symmetry element of a single thermoelectric unicouple was simulated and the performance was then multiplied by the number of unicouples used in the experiments to allow comparison and validation of experimental results. The unicouple design and meshing used in the simulation is presented in Figure 5.1-1a. In the boundary conditions it was assumed that the voltage in the positive lead to the *n-type* thermoelectric leg is 0V and the load resistance swept to find the best power output. The Multiphysics equations were solved for different T_H temperatures ranging from 55 ºC to 530 ºC while cold side temperature T_C was kept constant at 30 ºC. Two models were developed with different *Rc* parameters including 'model 1' for the prototypes with Ni (0.1 µm-thick) / Ni(P) (2 µm-thick) / Au (0.05 µm-thick) thermoelectrics' metallization and nano-Ag paste and Ag flakes bonding materials, and 'model 2' for the prototype with WSi_2 (1 µm-thick) / Au (0.05 µm-thick) metallization and Ag flakes-based bonding material.

Table 5.1-2: Assumed values used in the simulations.

	***Rc n-type* TE – interconnect (Ωcm^2)**	***Rc p-type* TE – interconnect (Ωcm^2)**	***Rc,T* Al_2O_3 – hot/cold sink (Km^2/W)**	**T_C and T_H (^oC)**
Model 1	$2.5 \cdot 10^{-5}$	$2.5 \cdot 10^{-5}$	$1.5 \cdot 10^{-4}$	30/55 to 530
Model 2	$5.0 \cdot 10^{-4}$	$8.0 \cdot 10^{-4}$	$1.5 \cdot 10^{-4}$	30/55 to 530

A simulated power output and thermoelectric device efficiency was calculated according to the equations 24 and 25:

$$P_{OUT} = V \cdot I \tag{24}$$

$$\eta = \frac{V \cdot I}{Q} \cdot 100\% \tag{25}$$

where Q is heat flux supplied by the heater.

The temperature (Figure 5.1-2) and electrical potential (Figure 5.1-3) distribution in the thermoelectric unicouple can be generated by combining these equations and variable material properties at the temperature gradient applied across the material. The performance of thermoelectric devices with Ni (0.1 µm-thick) / Ni(P) (2 µm-thick) / Au (0.05 µm-thick) metallization ('module 1' and 'module 2') and WSi_2 (1 µm-thick) / Au (0.05 µm-thick) metallization ('module 3') that was optimized to 7-couple module is presented in Appendix B (Table B. 1).

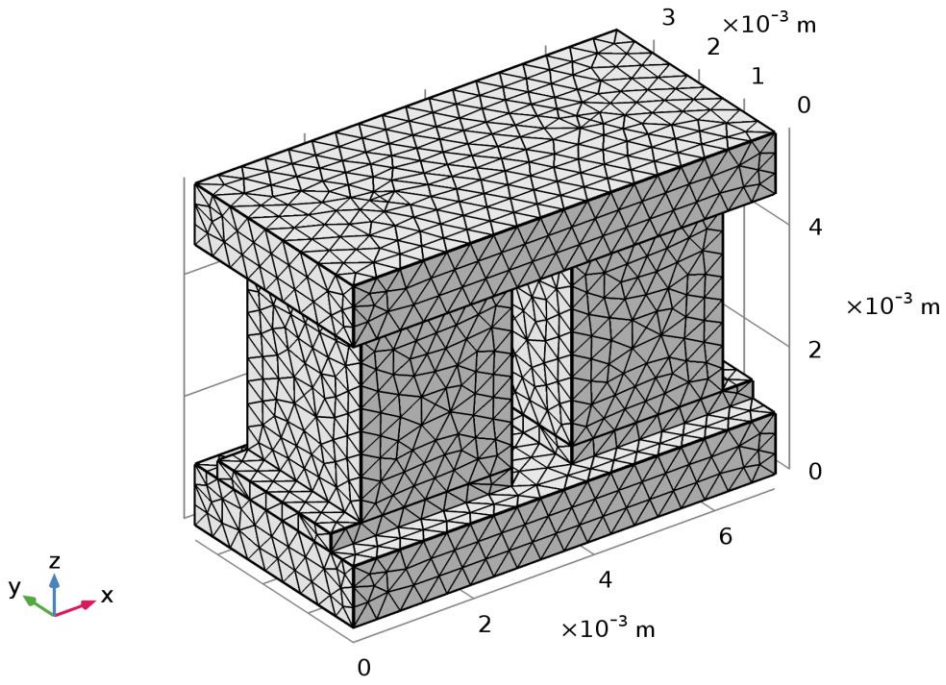

(a)

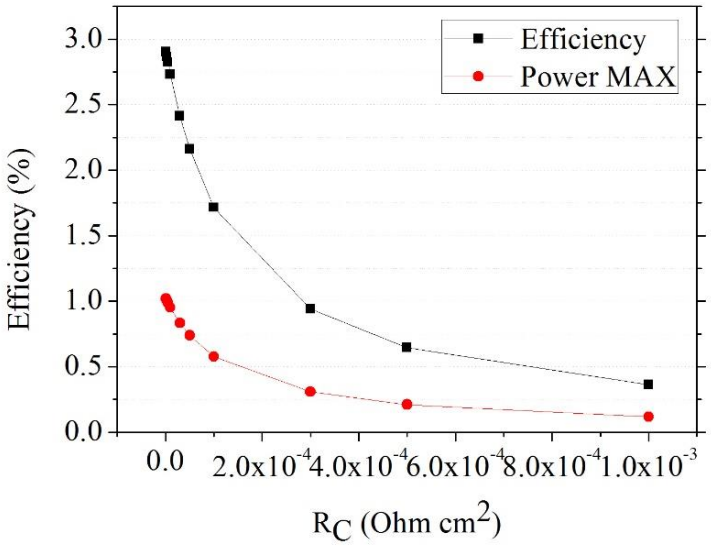

(b)

Figure 5.1-1: (a) Mesh used in the finite element analysis for single unicouple and **(b)** graph presenting the influence of the electrical contact resistance on the efficiency and power output of 7-couple skutterudite module optimized to hot-side module's temperature (T_H).

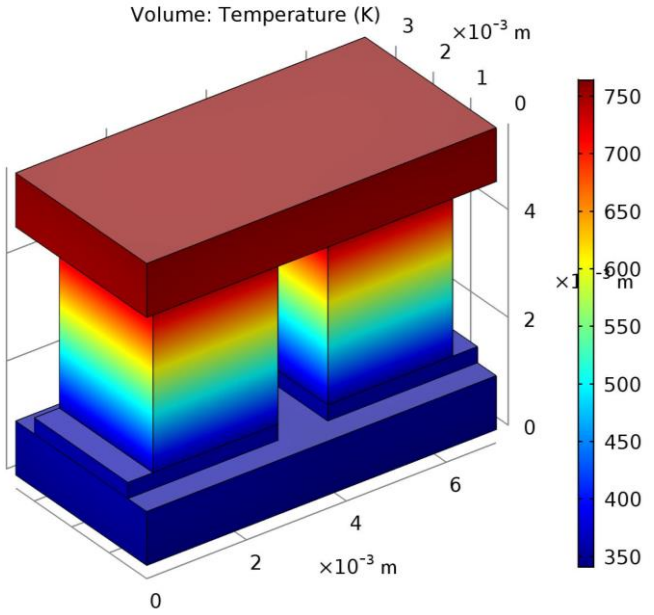

(a)

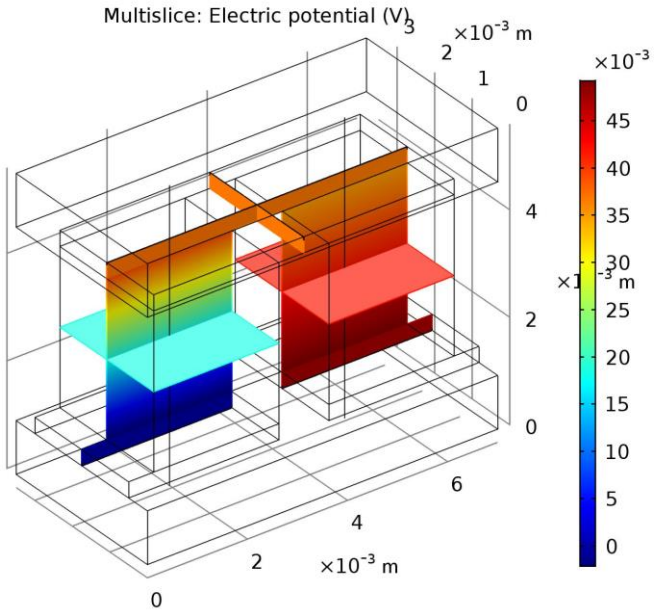

(b)

Figure 5.1-2: Simulated thermoelectric unicouple performance presenting **(a)** temperature and **(b)** electric potential distribution using 'model 1' (prototypes with Ni (0.1 µm-thick) / Ni(P) (2 µm-thick) / Au (0.05 µm-thick) thermoelectrics' metallization and nano-Ag paste and Ag flakes bonding materials) at ΔT = 500 °C.

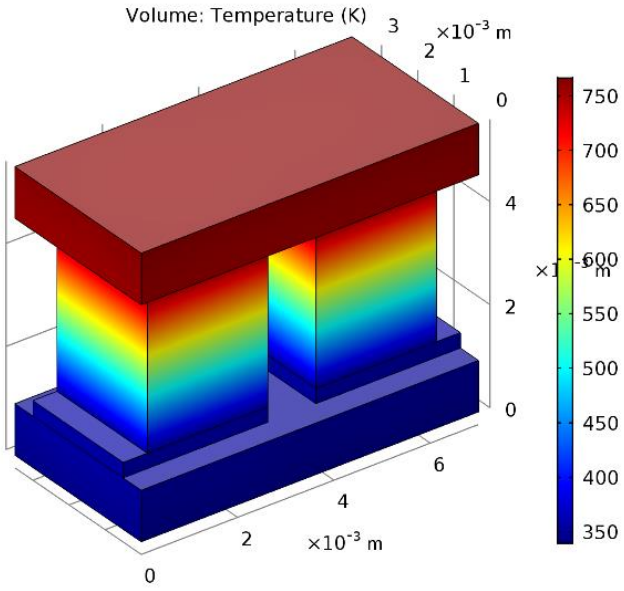

(a)

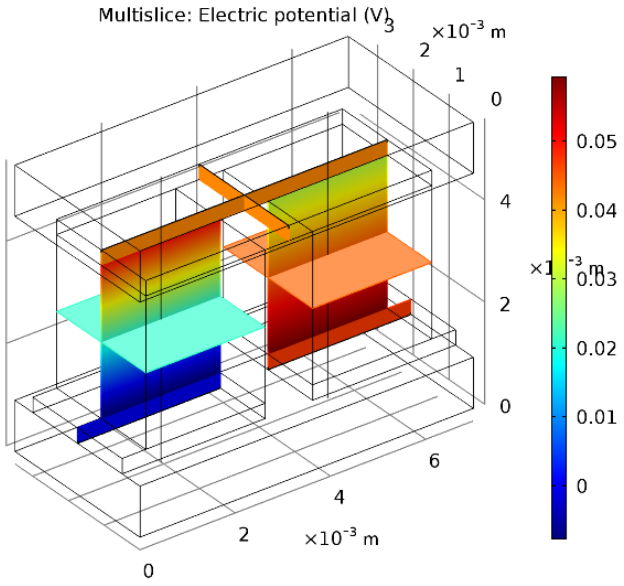

(b)

Figure 5.1-3: Simulated thermoelectric unicouple performance presenting **(a)** temperature and **(b)** electric potential distribution using 'model 2' (prototype with WSi_2 (1 µm-thick) / Au (0.05 µm-thick) metallization and Ag flakes-based bonding material) at ΔT = 500 ºC.

The simulated performance of skutterudite-based thermoelectric device, delivered in 'model 1' (Figure 5.1-4a) and 'model 2' (Figure 5.1-4) was optimized for 7-couple prototype and included maximum power output (P_{MAX}) and efficiency at a range of temperature gradients. The maximum power output rapidly rises along with increasing efficiency at higher module's hot-side (T_H) temperature, proving that higher module's power output can be achieved by raising the nominal hot-side temperature. High-temperature performance of thermoelectric module prototypes with emphasis on the influence of electrical contact resistance was analysed in this thesis. Two key characteristics were under the consideration: heat-to-electric conversion efficiency (η) and maximum power output (P_{MAX}) at given temperature gradient as described by the equation 15. The overall degradation of these characteristics with increase of the R_C is analysed for the prototype modules that were optimized to achieve the temperature difference of 450 ºC as seen in Figure 5.1-1b. The quality of electrical contacts is a crucial factor that greatly affects the performance of the skutterudite-based thermoelectric modules. To maintain modules' conversion efficiency at an acceptable level, an electrical contact resistance (R_C) in the range from 10^{-6} Ωcm^2 to $3 \cdot 10^{-5}$ Ωcm^2 should be provided, whereas with greater resistance, the performance decreases dramatically. Moreover, the impact of electrical contact resistances on the module high temperature performance can also be clearly seen, as 'model 2' assumed *Rc* values significantly lower than 'model 1' (Table 5.1-2).

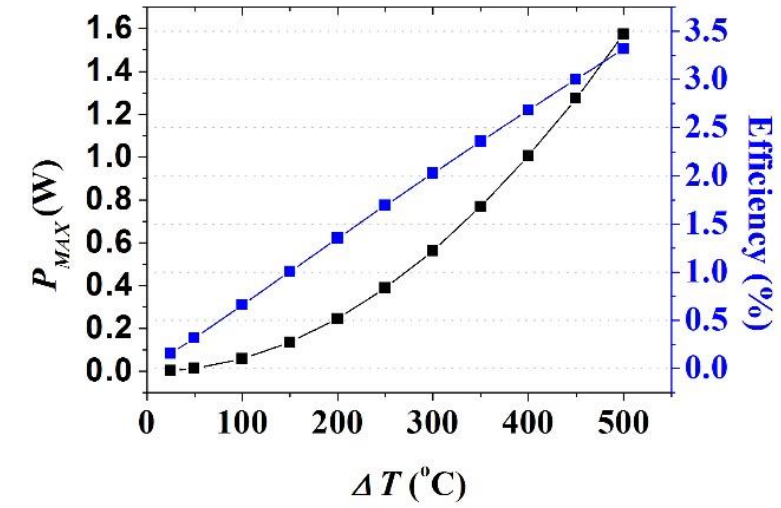

(a)

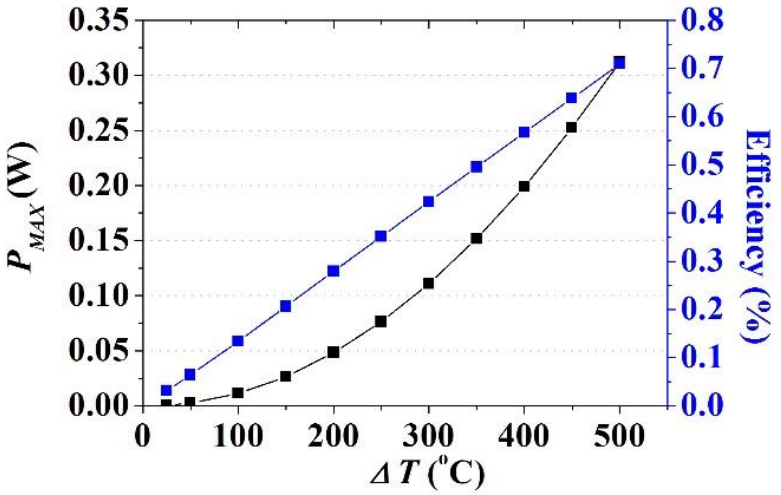

(b)

Figure 5.1-4: Simulated performance of 7 coupled thermoelectric module including maximum power output (P_{MAX}) and efficiency in **(a)** 'model 1' (prototypes with Ni (0.1 µm-thick) / Ni(P) (2 µm-thick) / Au (0.05 µm-thick) thermoelectrics' metallization and nano-Ag paste and Ag flakes bonding materials) and **(b)** 'model 2' (prototype with WSi_2 (1 µm-thick) / Au (0.05 µm-thick) metallization and Ag flakes-based bonding material).

Chapter 6

Thermoelectric Module Characterization

Three prototypes of the thermoelectric generator were build according to design and technique described in Chapter 3.5 using metallized $Mm_y(Fe,Co)_4Sb_{12}$ *p-type* and $(Ni,Co)Sb_3$ *n-type* skutterudites and tested at the high temperature rig and conditions described in Chapter 3.7. Results delivered from leg-to-leg joining experiments (Chapter 4.2), mainly electrical contact resistance (R_C) of thermoelectric – metal interconnect interface were used to assess and predict the performance and possible failure of the module at higher service temperatures. Two module prototypes – 'Module 1' and 'Module 2' consisted of *p-* and *n-type* thermoelectric materials metallized with Ni (0.1 μm-thick) / Ni(P) (2 μm-thick) / Au (0.05 μm-thick) layers were bonded to Ni(P)/Au plated DBC alumina substrates using Ag flake-based joining material (AREMCO Inc., US) and nano-Ag paste (NBE Technologies, LLC, US) respectively. The image of 'Module 1' can be found in Figure 6.1-1. The selection of Ni/Ni(P)/Au metallization along with Ag-based, low-temperature joining techniques was motivated by the acceptable *Rc* (< 25 $\mu\Omega cm^2$) measured at room temperature and good quality

contacts as revealed by SEM analysis (by meaning of continuous, crack and void free interfaces). Moreover, encouraged by the preliminary joining results, thermoelectric device with *p-* and *n-type* thermoelectric materials metallized with WSi_2 (1 µm-thick) / Au (0.05 µm-thick) metallization layers was assembled into module using Ag flake-based conductive adhesive (AREMCO Inc., US) referred as 'Module 3'. High-temperature performance of three thermoelectric prototypes developed at this research - 'Module 1', 'Module 2' and 'Module 3' measured in the open-air at different ΔT applied are summarized in Table 6.1-1.

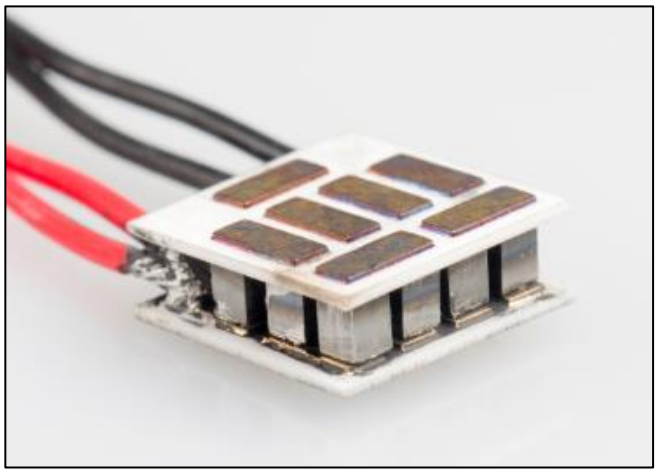

Figure 6.1-1: Photography of the 7-couple, thermoelectric prototype developed using Ni (0.1 µm-thick) / Ni(P) (2 µm-thick) / Au (0.05 µm-thick) plated $Mm_y(Fe,Co)_4Sb_{12}$ *p-type* and Ni,Co)Sb_3 *n-type* skutterudites bonded to Ni(P)/Au plated DBC alumina substrates using Ag flake material (AREMCO Inc., US) denoted as 'Module 1'.

Figure 6.1-2a present measured performance, i.e. power output (P_{OUT}) and output voltage (V) of Ni (0.1 µm-thick) / Ni(P) (2 µm-thick) / Au (0.05 µm-thick) metallized skutterudite measured as a function of current (I) and ΔT assembled using Ag-flakes adhesive (AREMCO Inc., US). Among three developed skutterudite-based thermoelectric modules, device fabricated using this technique

(device no. 'Module 1') had the highest measured P_{MAX} of 607.98 mW at ΔT = 450 °C, which transfers to power density of 695 mW/cm^2 per thermoelectric material area and 270.21 mW/cm^2 per module area. This is significantly lower than the performance of the best skutterudite-based thermoelectric modules reported in the literature (as summarized in Table 2.4-2) as off-the-shelf, low-performance Mm_y(Fe,Co)$_4$Sb$_{12}$ *p-type* and (Ni,Co)Sb$_3$ *n-type* thermoelectric materials were used in this study. Commercially available thermoelectric materials were used as they are available in high industrial volumes but their synthesis conditions were fully optimized, as both *n-* and *p-type* as-sintered materials had high fraction of secondary phases formed during the SPS process (Chapter 4.1) and presence of un-reacted antimony found within *p-type* material. An internal module resistance of $R_{TEG,E}$ ~ 37.76 mΩ measured at room temperature did not show significant changes at higher temperatures and increased only by 69.3% at ΔT = 450 °C ($R_{TEG,E}$ ~ 63.91 mΩ). This is consistent with simulation results as discussed later in Figure 6.1-3b. Moreover, as seen in Figure 6.1-2, the linear increase of measured P_{MAX} suggests that contacting interfaces of 'Module 1' were stable during the high temperature testing in the open air. In the similar design, Ni (0.1 µm-thick) / Ni(P) (2 µm-thick) / Au (0.05 µm-thick) metallized *p-* and *n-type* skutterudites were used to fabricate 'Module 2' using nano-Ag paste (NBE Technologies, LLC, US). As can be seen in Figure 6.1-2b, 'module 2' slightly outperformed 'Module 1' up to ΔT = 350 °C with P_{MAX} of 429.05 mW (measured at ΔT = 350 °C) which transfers to power density of 490.34 mW/cm^2 per thermoelectric material area and 190.68 mW/cm^2 per module area. The highest P_{MAX} measured at ΔT = 350 °C of the module joined with nano-Ag is 24.83% higher than corresponding module based on the Ag flake-based adhesive and failed at the module's T_H higher than 380 °C. The 'Module 2' failure is

presumably caused by the thermal instabilities at the contacting interfaces, specifically by the nano-Ag paste, as module internal resistance ($R_{TEG,E}$) increased up to 158.7% at ΔT = 450 ºC leading to the low P_{MAX} of 277.75 mW (Figure 6.1-3b).

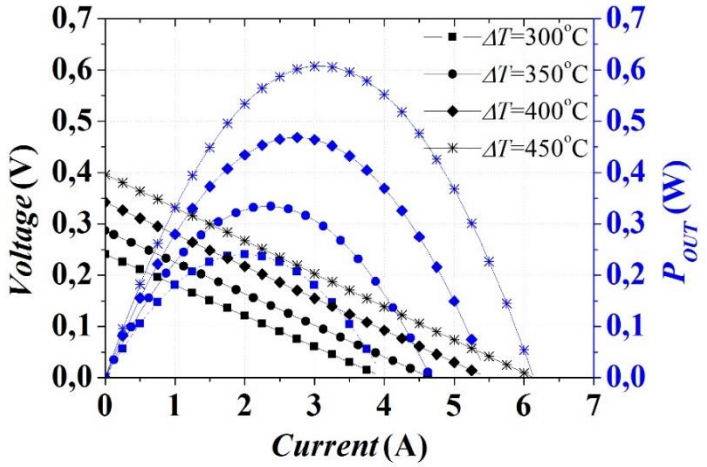

(a)

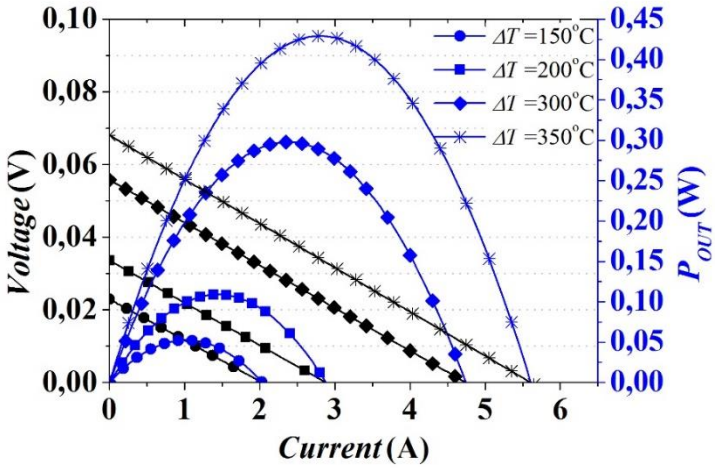

(b)

Figure 6.1-2: Performance of the thermoelectric prototype developed with Ni (0.1 µm-thick) / Ni(P) (2 µm-thick) / Au (0.05 µm-thick) plated *p*- and *n-type* skutterudite materials using **(a)** Ag flake-based conductive adhesive (AREMCO Inc., US) referred as 'Module 1'and **(b)** Ag-nano paste (NBE Technologies, LLC, US) referred as 'Module 2'.

In order to verify the validity of the numerical model and investigate possible drawbacks of the fabrication process both numerical and experimental results were compared and shown in Figure 6.1-3. As seen in a Figure 6.1-3a, measured maximum power output of the 'Module 1' was approx. 70.5% lower than the value obtained from the simulation. It is presumably caused by the underestimation of thermal contact resistance ($R_{C,T}$) in pellet to interconnect assumed in the simulations (of $1.5 \cdot 10^{-4}$ Km^2W^{-1}). Moreover, double-sided alumina substrate is expected to reduce area of contact by 39% and increasing thermal contact resistance ($R_{C,T}$) on ceramic to heat sink interface. It can be also confirmed by the deviations in the measured and simulated V_{OC} with approx. 50.1% difference between both as seen in equation (8). Interestingly, slightly lower than expected $R_{TEG,E}$ was measured for 'Module 1' and 'Module 2' at lower temperatures suggests either shunting of electrical circuit or better than modelled electrical performance of thermoelectric material and contacting interfaces.

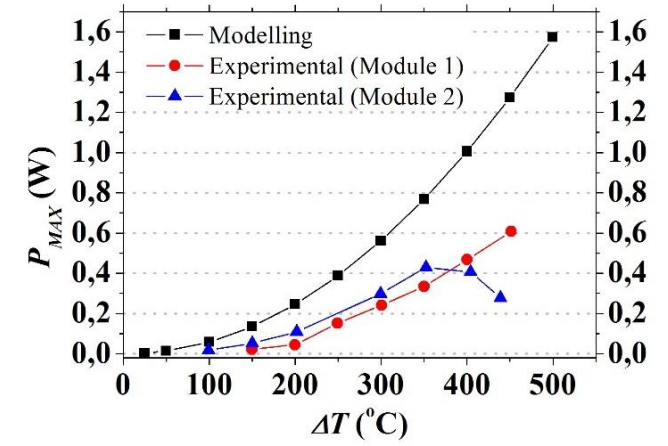

(a)

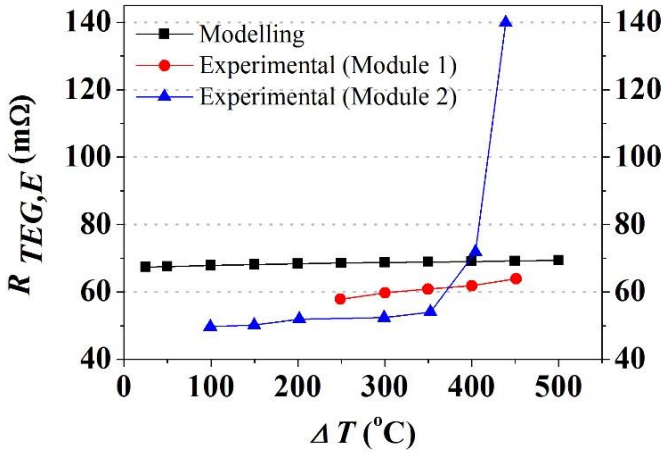

(b)

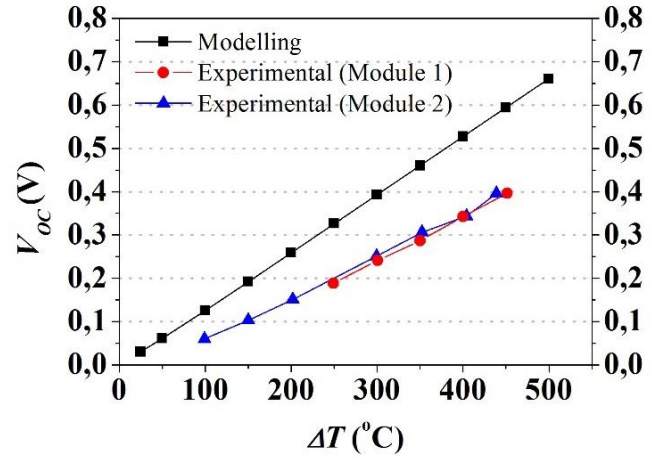

(c)

Figure 6.1-3: Modelled and measured performance of the 7-couple TE prototype with Ni (0.1 µm-thick) / Ni(P) (2 µm-thick) / Au (0.05 µm-thick) coated *p*- and *n-type* skutterudites developed using different bonding technique with **(a)** P_{MAX}, **(b)** $R_{TEG,E}$ and **(c)** V_{OC} as a function of ΔT applied across the module.

Thermoelectric module no. 'Module 3' developed with *p*- and *n-type* skutterudites and metallized with WSi_2 (1 µm-thick) / Au (0.05 µm-thick) layers had the lowest output power for a given ΔT of all measured modules, which is attributed to its higher internal electrical resistance as described by the Equation (10). Figure 6.1-4 shows the power output and voltage of the device as a function of the measured temperature difference across the module (ΔT). The maximum power output of 115.45 mW was measured at ΔT = 450 ºC which transfers to power density of 131.94 mW/cm^2 per thermoelectric material area and 51.31 mW/cm^2 per module area. This is approx. 74.4% lower than the P_{MAX} delivered from the modelling (Figure 6.1-5a) and is consistent with the difference between simulation and experiments observed in the 'Module 1' and 'Module 2'.

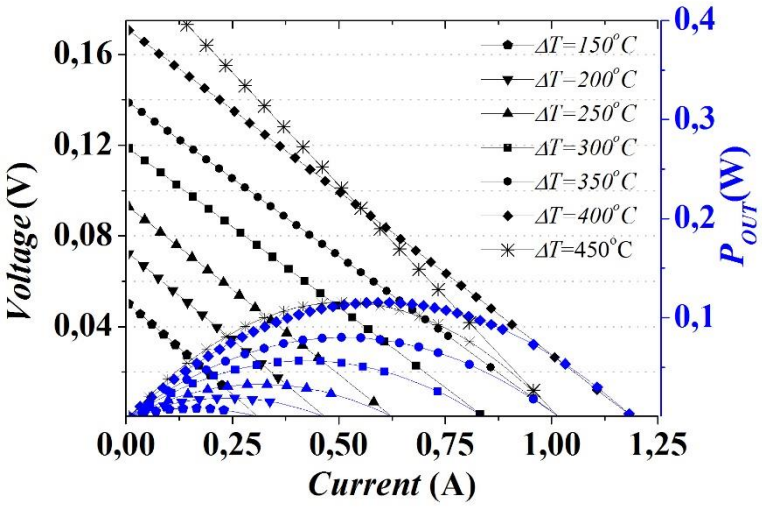

Figure 6.1-4: High-temperature performance of the thermoelectric prototype developed with WSi_2 (1 µm-thick) / Au (0.05 µm-thick) metallized *p*- and *n-type* skutterudites using Ag flake-based joining material (AREMCO Inc., US) referred as 'Module 3'.

By comparing the V_{OC} (Figure 6.1-5c) is clear that thermal contact resistance still might be an issue as both measured and simulated values differed of approx. 25.8%. As seen in Figure 6.1-5b, measured $R_{TEG,E}$ was significantly decreasing presumably due to partial annealing of amorphous WSi_2 metallization layer on the hot side of thermoelectric module. Initial annealing test shown in Appendix C (Figure C. 1) and reduction of WSi_2 sheet resistivity during the module testing suggest that pre-annealing would be beneficial for overall performance of thermoelectric module.

High-temperature stability of thermoelectric modules can be confirmed by changes in the internal module resistance ($R_{TEG,E}$) upon heating. As seen in Figure 6.1-3a, $R_{TEG,E}$ of the prototype developed using Ni (0.1 µm-thick) / Ni(P) (2 µm-thick) / Au (0.05 µm-thick) plated *p-* and *n-type* skutterudites and Ag-nano based joining material increased up to 140 mΩ measured at ΔT = 450 ºC in air ('module 2'). The failure analysis can be based on microstructural analysis of isothermally aged samples shown in Chapter 4.2.5 and assumption the *p-type* contacts did not survive high-temperature treatment (> 400 ºC) and were the reason behind increase of module internal resistance. Based on the $R_{TEG,E}$ of 'module 2' measured at ΔT = 450 ºC, Ag flake-based joining material was assumed to be more stable at higher service temperature as no changes of internal module resistivity was observed.

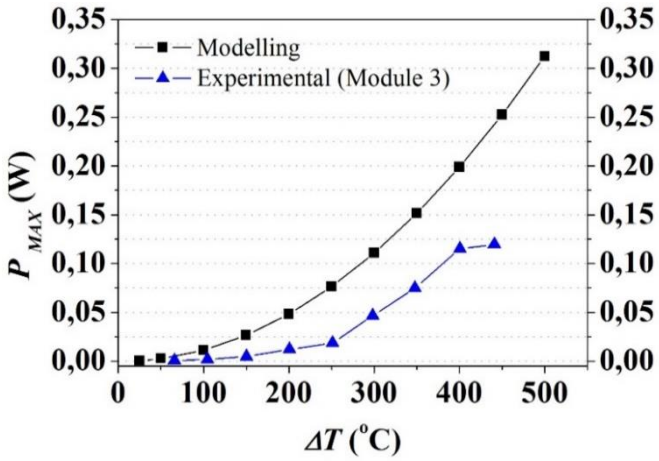

(a)

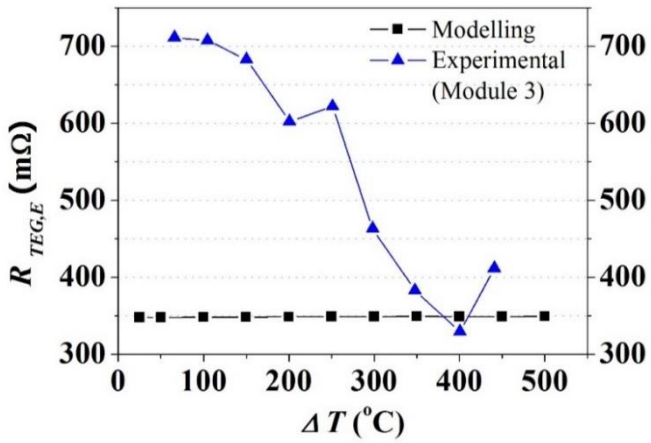

(b)

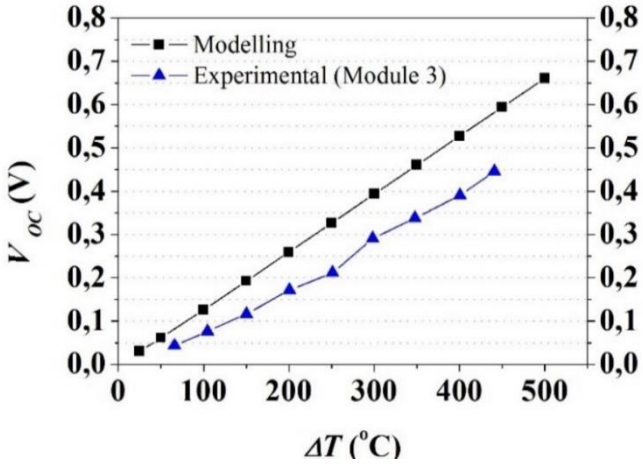

(c)

Figure 6.1-5: Simulated and measured performance of the 7 couple thermoelectric prototype with WSi_2 (1 µm-thick) / Au (0.05 µm-thick) metallized skutterudites assembled using Ag flakes (AREMCO Inc., US) and **(a)** maximum power output (P_{MAX}), **(b)** $R_{TEG,E}$ and **(c)** V_{OC} as a function of temperature difference (ΔT) applied across the module.

Table 6.1-1: Summary of high temperature performance measurements of skutterudite-based thermoelectric generators developed in this research. (V_{OC} is open circuit voltage, $R_{TEG,E}$ is internal module resistance and P_{MAX} is maximum power output).

TEG Properties		**Module 1**	**Module 2**	**Module 3**
Metallization (thickness [µm])		Ni/Ni(P)/Au (0.1/2/0.05 µm)	Ni/Ni(P)/Au (0.1/2/0.05 µm)	WSi_2/Au (1/0.05 µm)
Joining Material		Ag flake joining material (AREMCO Inc., US)	Nano-Ag paste (NBE Technologies, LLC, US)	Ag flake joining material (AREMCO Inc., US)
Module dimensions	**Base area [mm]**	15 × 15	15 × 15	15 × 15
	TE legs dimension [mm]	2.5 × 2.5 × 3	2.5 × 2.5 × 3	2.5 × 2.5 × 3
Following thermoelectric module performance was measured using high temperature testing rig and conditions described in Chapter 3.7				
ΔT = 150 °C	V_{OC} **(V)**	0.058	0.103	0.116
	$R_{TEG,E}$ **(mΩ)**	37.76	50.16	666.42
	P_{MAX} **(mW)**	22.31	52.45	4.85
ΔT = 200 °C	V_{OC} **(V)**	0.089	0.151	0.172
	$R_{TEG,E}$ **(mΩ)**	38.97	51.94	597.56
	P_{MAX} **(mW)**	51.13	100.89	12.23

ΔT = 250 ºC	V_{OC} (V)	0.188	-	0.212
	$R_{TEG,E}$ (mΩ)	57.86	-	594.15
	P_{MAX} (mW)	151.70	-	18.65
ΔT = 300 ºC	V_{OC} (V)	0.241	0.251	0.291
	$R_{TEG,E}$ (mΩ)	59.72	52.52	463.34
	P_{MAX} (mW)	240.62	297.78	46.50
ΔT = 350 ºC	V_{OC} (V)	0.287	0.306	0.338
	$R_{TEG,E}$ (mΩ)	60.88	54.05	383.14
	P_{MAX} (mW)	334.29	429.05	74.89
ΔT = 400 ºC	V_{OC} (V)	0.342	0.343	0.390
	$R_{TEG,E}$ (mΩ)	61.82	71.95	329.68
	P_{MAX} (mW)	468.42	405.13	115.31
ΔT = 450 ºC	V_{OC} (V)	0.396	0.396	0.458
	$R_{TEG,E}$ (mΩ)	63.91	139.84	452.05
	P_{MAX} (mW)	607.98	277.75	115.45

Chapter 7

Conclusions and Recommendations

The fabrication process of a thermoelectric generator working at medium-high temperature regime (up to 500 ^{o}C) is evaluated in this study. To accomplish this, a thermoelectric system utilising commercially available off-the-shelf skutterudite-based material is proposed. Several joining techniques and metallization configurations have been already reported and majority of them suffers from the lack of high-temperature stability at the module's service temperature or insufficient evidence of their electrical and mechanical performance. As such, novel fabrication techniques for cost-effective medium-high thermoelectric generator were explored.

At the first step, elemental powders of $Mm_y(Fe,Co)_4Sb_{12}$ *p-type* and $(Ni,Co)Sb_3$ *n-type* skutterudites have been *in-situ* synthesized using spark plasma sintering technique and their high-temperature thermoelectric performance has been measured. The average zT ($\overline{zT}$) of 0.12 and 0.27 has been measured for $Mm_y(Fe,Co)_4Sb_{12}$ *p-type* and $(Ni,Co)Sb_3$ *n-type* materials respectively, between 50 ^{o}C and 450 ^{o}C which is significantly lower in comparison to similar compositions previously reported. X-Ray and SEM EDS analysis have been performed on as-sintered thermoelectric material revealing successful formation of skutterudite

phase and presence of secondary phases within thermoelectric matrix. The regions of inhomogeneous (Co,Ni)Sb phase distribution have been found in the *n-type* material while the $FeSb_2$ phase and unreacted Sb have been present in the *p-type* thermoelectric matrix along with small grains of unreacted Fe. At the second stage, bonding trials have been performed in the leg-to-leg joining configurations with a nickel interconnect clamped between thermoelectric and bonding material to reproduce conditions usually found in the prototype module. Such specimens have been intensively investigated in terms of their mechanical and electrical performance by measuring the electrical contact resistance R_C and apparent shear strength (adapted to ASTM D905 standard [99]) along with EDS analysis to reveal contacts quality and formation of any undesirable phases at the contacting interfaces. Two conventional high-temperature joining techniques have been investigated and included furnace brazing (in argon) using commercial 56 at% Ag – 22 at% Cu – 17 at% Zn – 5 at% Sn braze (Silver-flo^{TM} 56, Johnson Matthey, UK) and Ag-paste (Q-INKS S.r.l, Italy). These joining materials are characterized with good wetting performance on both non-metallized and metallized skutterudite surfaces and melt in tolerable temperature range between 650 and 660 ^{o}C. The characteristic porous microstructure of the $Mm_y(Fe,Co)_4Sb_{12}$ *p-type* material has been found near the bonding interface and was proven to be antimony deficient region. The porous microstructure has been caused by the lack of thermal stability of the *p-type* thermoelectric utilized in this research as the bonding temperature exceeded materials' sintering temperature and sublimation of pure antimony that was originally residing at the grain boundaries. Moreover, significant amount of joining material was dissolved as the constituent elements of the braze were found inside the thermoelectric material. Interestingly, Ti (0.3 µm-thick) / Ni (1.2 µm-thick) and Ni (0.1 µm-thick) / Ni(P) (2 µm-thick)

metallization has also been dissolved during brazing tests and due to the lack of diffusion barrier at the interface, formation of Ni_5Sb_2 and (Ni,Co)Sb reaction layers has occurred in both $Mm_y(Fe,Co)_4Sb_{12}$ *p-type* and $(Ni,Co)Sb_3$ *n-type* materials. The growth of relatively brittle intermetallic compounds at contacting interfaces is presumably a reason behind the lack of contacts' high-temperature stability as specimens did not survive isothermal aging at 450 ^oC in flowing argon. This implies that the thermoelectric prototype module could potentially deteriorate at elevated temperatures due to the lack of high-temperature chemical stability between Ag-Cu based brazes and skutterudites. The Mo (0.3 μm-thick) / Ni (1.2 μm-thick) metallization has been proven to effectively block elemental interdiffusion and reaction layer formation within both *n-* and *p-type* contacts at high temperature but molybdenum layer delaminated due to the significant mismatch of thermal expansion coefficients with skutterudite materials.

Two alternative, low-temperature joining materials were realized in the high-temperature thermoelectric systems for the first time. The Ag-nano (NBE Technologies, LLC, US) and Ag flake-based (AREMCO Inc., US) joining materials were tested with three different metallization configuration which included W (1 μm-thick) / Au (0.05 μm-thick), WSi_2 (1 μm-thick) / Au (0.05 μm-thick) and Ni (0.1 μm-thick) / Ni(P) (2 μm-thick) / Au (0.05 μm-thick) PVD coated skutterudites. The low joining temperature (< 273 ^oC) helped with a formation of continuous bonding lines between thermoelectric and joining material without visible reaction layer formed, unchanged material microstructure and $Rc < 20$ $\mu\Omega cm^2$ when Ni/Ni(P)/Au metallization was used. Initial isothermal aging tests at 450 ^oC (in Argon) were proven to be destructive for skutterudites-based contacts and lack of metallization-skutterudite interface stability might influence the reliability of high-temperature modules but needs more quantifying.

It has also been shown that Solid-Liquid Interdiffusion (SLID) is a possible technique for bonding metallic interconnects with thermoelectric material using a novel, aluminium – nickel multi-layered system. Two different process conditions have been tested and included bonding at temperature below melting of aluminium (< 660 ^{o}C) and at its melting point (660 ^{o}C). The same bonding parameters have been found to create contacts with a final microstructure falling in the two-phase region comprised of Al_3Ni and Al_3Ni_2 intermetallic compounds with a different Al_3Ni/Al_3Ni_2 ratio depending on the joining conditions. High-temperature reliability and microstructural changes in the joining material have been evaluated in terms of isothermal ageing at 450 ^{o}C in flowing Ar, showing that the homogenisation process leads to the reduction of Al_3Ni phase in favour of growing Al_3Ni_2. In addition, it has been proven that avoiding residual aluminium in the joint by using a higher process temperature is advantageous for improved stability. The resulting electrical contact resistances and apparent shear strengths for components with residual aluminium have been measured to be (2.8 ± 0.4) x 10^{-5} Ω·cm^2 and 5.1 ± 0.5 MPa and with aluminium completely transformed into Al_3Ni and Al_3Ni_2 IMCs were (4.8 ± 0.3) x 10^{-5} Ω·cm^2 and 4.5 ± 0.5 MPa respectively. The contact specimens bonded with this technique were characterised with relatively poor mechanical performance and thermoelectric prototypes did not survived clamping with uniaxial pressure of 1 MPa needed for the high-temperature performance measurement. In-depth failure analysis performed on contacting interfaces suggests that Ni(P) layer, a source of nickel needed for the Al-Ni reaction to occur, is not stable at high-temperature applications and alternative pure nickel could be implemented. The high phosphorus contents within Ni(P) layer, as well as nickel significant depletion, led

to P-rich interfacial layer formation along with relative brittle Ni-P and Fe-P IMCs, being responsible for contacts poor mechanical stability.

The proposed fabrication techniques were characterised in terms of their practicability and based on their electrical, mechanical and microstructural performance the decision of prototype fabrication has been made. Three module prototypes based on various joining techniques and metallization configurations have been successfully fabricated. Two modules consisted of $Mm_y(Fe,Co)_4Sb_{12}$ *p-type* and $(Ni,Co)Sb_3$ *n-type* thermoelectric materials metallized with Ni (0.1 µm-thick) / Ni(P) (2 µm-thick) / Au (0.05 µm-thick) layers were bonded to Ni(P)/Au plated DBC alumina substrates using Ag flake-based joining material (AREMCO Inc., US) and Ag-nano paste (NBE Technologies, LLC, US) respectively. Additionally, prototype module made of WSi_2 (1 µm-thick) / Au (0.05 µm-thick) metallized *p-* and *n-type* skutterudites has also been presented. The high-temperature performance of prototype modules was measured using in-house developed testing rig in the air. The highest performing 7 couple thermoelectric module had P_{MAX} of 608 mW and power density of 695 mW/cm^2 measured at ΔT = 450 ºC in air. This module was developed using Ag flake-based joining material (AREMCO Inc., US) and skutterudite materials with metallized with Ni (0.1 µm-thick) / Ni(P) (2 µm-thick) / Au (0.05 µm-thick) thermoelectrics. It was assumed that relatively high-performance of developed prototypes was achieved thanks to the continuous, and crack-free contact interface formed by using low-temperature, Ag-based joining material. These interfaces were also characterized with low electrical contact resistance and reasonably good mechanical performance so that continuous electron and heat flow was allowed.

Results presented in this research have potential for further exploration in the high temperature thermoelectric systems, not only limited to Skutterudite-based ($CoSb_3$) materials.

- Co-sintering of metallization layers and thermoelectric powder by Spark Plasma Sintering (or hot pressing) has a great potential in reducing time-consuming module fabrication process. This can be further optimized for thermoelectric-metallization-interconnect joining at one-step assembly process. Initial tests revealed that metallization layer used to delaminate during cutting into thermoelectric legs (machining) when standard diamond cutting disc is used. It is believed that delamination can be avoided if thermoelements are individually co-sintered to desirable final shape.
- Low temperature joining techniques based on Ag material are proven to form high-performance electrical contacts in the prototype thermoelectric modules. These joining materials are fulfilling all requirements highlighted in Chapter 2.3, but more work is needed to confirm their reliability at higher service temperature. It is also recommended to control the thickness of joining material (< 30 μm), heating ramp and pressure applied during the joining process as they normally influence properties of sintered contacts.
- Solid-Liquid Interdiffusion (SLID) bonding technique using Al-Ni interlayers can be further implemented into other medium-high and high temperature regime thermoelectric systems. In the presented research Ni-P interlayer was used as a source of elemental nickel needed for the joining reaction to occur but its depletion led to a formation of brittle P-rich layer at the thermoelectric-Ni(P) interface and mechanical failure. Therefore, it is recommended to investigate other nickel-based interlayers that could be preferably phosphorous (and boron) free.

It is recognized that numerous long-term reliability issues remain and must be further investigated. Thermoelectric-to-interconnect contacts must be analysed in terms of their high-temperature stability and standard testing procedure should be conceptualized. Initial isothermal aging tests revealed lack of high-temperature mechanical stability so more work on the long-term reliability is needed such as thermal shock and cycling along with accelerated life testing. These tests should also be performed on the prototype module level. Effective diffusion barrier to supress Sb and Co diffusion must be demonstrated on skutterudite-based thermoelectric materials. Metallization layers must be produced with good diffusional phase stability and excellent electrical and thermal performance. It is desirable to further investigate alternative *n*- and *p-type* skutterudite material synthesis techniques so that higher than reported zT values can be achieved.

References

1. U.S. Energy Information Administration International Energy Outlook 2018 Executive Summary Available online: https://www.eia.gov/outlooks/ieo/ (accessed on Sep 27, 2018).

2. El, C.; Lamont, L.A.; El, Z. Review of photovoltaic technologies. *Renew. Sustain. Energy Rev.* 2011, *15*, 2165–2175.

3. Ferrari, C.; Melino, F.; Pinelli, M.; Spina, P.R.; Venturini, M. Overview and Status of Thermophotovoltaic Systems. *Energy Procedia* 2014, *45*, 160–169.

4. Steele, B.C.H. Fuel-cell technology: Running on natural gas. *Nature* 1999, *400*, 619–621.

5. European Commission 2030 Energy Strategy - A policy framework for climate and energy in the period from 2020 up to 2030 Available online: /energy/en/topics/energy-strategy-and-energy-union/2030-energy-strategy (accessed on Sep 27, 2018).

6. Chiwanga, S.; Tuley, R.; Placha, K.; Robbins, M.; Gilchrist, B.; Simpson, K. Automotive power harvesting/thermoelectric applications. *RSC Energy Environ. Ser.* 2017, *2017-January*, 230–251.

7. Bode, C.; Friedrichs, J.; Somdalen, R.; Kohler, J.; Buchter, K.-D. Advances in Aerospace Technology.; Arizona, USA; Vol. 1.

8. Bass, J.C.; Farley, R.L. Proceedings of the 16th International Conference on Thermoelectrics (ITC).; 1997; p. 547.

9. LeBlanc, S.; Yee, S.K.; Scullin, M.L.; Dames, C.; Goodson, K.E. Material and manufacturing cost considerations for thermoelectrics. *Renew. Sustain. Energy Rev.* 2014, *32*, 313–327.

10. Shi, X.; Bai, S.; Xi, L.; Yang, J.; Zhang, W.; Chen, L.; Yang, J. Realization of high thermoelectric performance in n-type partially filled skutterudites. *J.*

Mater. Res. 2011, *26*, 1745–1754.

11. Huang, L.; Zhang, Q.; Yuan, B.; Lai, X.; Yan, X.; Ren, Z. Recent progress in half-Heusler thermoelectric materials. *Mater. Res. Bull.* 2016, *76*, 107–112.

12. Srinivasan, B.; Gautier, R.; Gucci, F.; Fontaine, B.; Halet, J.-F.; Cheviré, F.; Boussard-Pledel, C.; Reece, M.J.; Bureau, B. Impact of Coinage Metal Insertion on the Thermoelectric Properties of GeTe Solid-State Solutions. *J. Phys. Chem. C* 2018, *122*, 227–235.

13. Nozariasbmarz, A.; Agarwal, A.; Coutant, Z.A.; Hall, M.J.; Liu, J.; Liu, R.; Malhotra, A.; Norouzzadeh, P.; Öztürk, M.C.; Ramesh, V.P.; et al. Thermoelectric silicides: A review. *Jpn. J. Appl. Phys.* 2017, *56*, 05DA04.

14. Holgate, T.C.; Bennett, R.; Hammel, T.; Caillat, T.; Keyser, S.; Sievers, B. Increasing the Efficiency of the Multi-mission Radioisotope Thermoelectric Generator. *J. Electron. Mater.* 2015, *44*, 1814–1821.

15. CoACH Project - Advanced glasses, Composites And Ceramics for High growth Industries Available online: http://www.europeanthermodynamics.com/research/therm-coach (accessed on May 3, 2018).

16. Snyder, G.J.; Toberer, E.S. Complex thermoelectric materials. *Nat. Mater.* 2008, *7*, 105–114.

17. LeBlanc, S. Thermoelectric generators: Linking material properties and systems engineering for waste heat recovery applications. *Sustain. Mater. Technol.* 2014, *1–2*, 26–35.

18. Tuley, R.; Simpson, K. ZT Optimization: An Application Focus. *Mater. Basel Switz.* 2017, *10*.

19. Fitriani; Ovik, R.; Long, B.D.; Barma, M.C.; Riaz, M.; Sabri, M.F.M.; Said, S.M.; Saidur, R. A review on nanostructures of high-temperature thermoelectric materials for waste heat recovery. *Renew. Sustain. Energy Rev.* 2016, *64*, 635–659.

20. Rogl, G.; Rogl, P. Skutterudites, a most promising group of thermoelectric materials. *Curr. Opin. Green Sustain. Chem.* 2017, *4*, 50–57.

21. Rull-Bravo, M.; Moure, A.; Fernández, J.F.; Martín-González, M.

Skutterudites as thermoelectric materials: revisited. *RSC Adv.* 2015, *5*, 41653–41667.

22. Fidrosy, S.A.; Paik, J.-A.; Smith, K.L.; Li, B.C.-Y.; Chi, S.C.; Yu, K.; Fleurial, J.-P.; Uhl, D.M.; Caillat, T.; Nakasukasa, G.H.; et al. Skutterudite thermoelectric materials and methods for making 2017.

23. Rogl, G.; Grytsiv, A.; Anbalagan, R.; Bursik, J.; Kerber, M.; Schafler, E.; Zehetbauer, M.; Bauer, E.; Rogl, P. Direct SPD-processing to achieve high-ZT skutterudites. *Acta Mater.* 2018, *159*, 352–363.

24. Skomedal, G.; Holmgren, L.; Middleton, H.; Eremin, I.S.; Isachenko, G.N.; Jaegle, M.; Tarantik, K.; Vlachos, N.; Manoli, M.; Kyratsi, T.; et al. Design, assembly and characterization of silicide-based thermoelectric modules. *Energy Convers. Manag.* 2016, *110*, 13–21.

25. Mo/Ti Diffusion Bonding for Making Thermoelectric Devices - Tech Briefs Available online: https://www.techbriefs.com/component/content/article/tb/techbriefs/electronics-and-computers/2014 (accessed on Jul 23, 2018).

26. Salvador, J.R.; Cho, J.Y.; Ye, Z.; Moczygemba, J.E.; Thompson, A.J.; Sharp, J.W.; Koenig, J.D.; Maloney, R.; Thompson, T.; Sakamoto, J.; et al. Conversion efficiency of skutterudite-based thermoelectric modules. *Phys. Chem. Chem. Phys.* 2014, *16*, 12510–12520.

27. Bjørk, R. The Universal Influence of Contact Resistance on the Efficiency of a Thermoelectric Generator. *J. Electron. Mater.* 2015, *44*, 2869–2876.

28. Wais, M.; Held, K.; Battiato, M. Importance of Schottky barriers for wide-bandgap thermoelectric devices. *Phys. Rev. Mater.* 2018, *2*, 045402.

29. Rowe, D.M.; Min, G. Evaluation of thermoelectric modules for power generation. *J. Power Sources* 1998, *73*, 193–198.

30. Prasad, R.P. Metallurgy of Soldering and Solderability. In *Surface Mount Technology*; Springer, Boston, MA, 1997; pp. 444–492 ISBN 978-0-412-12921-6.

31. Nascimento, R.M. do; Martinelli, A.E.; Buschinelli, A.J.A. Review Article: recent advances in metal-ceramic brazing. *Cerâmica* 2003, *49*, 178–198.

32. Siow, K.S. Are Sintered Silver Joints Ready for Use as Interconnect Material

in Microelectronic Packaging? *J. Electron. Mater.* 2014, *43*, 947–961.

33. Loto, C.A. Electroless Nickel Plating – A Review. *Silicon* 2016, *8*, 177–186.

34. Jacobson, D.M.; Humpston, G. *Principles of Brazing*; ASM International, 2005; ISBN 978-1-61503-104-7.

35. Caillat, T.; Fleurial, J.-P.; Snyder, G.J.; Zoltan, A.; Zoltan, D.; Borshchevsky, A. A New High Efficiency Segmented Thermoelectric Unicouple.; 1999.

36. Caillat, T.; Fleurial, J.-; Snyder, G.N.; Zoltan, A.; Zoltan, D.; Borshchevsky, A. Development of a high efficiency thermoelectric unicouple for power generation applications. In Proceedings of the Eighteenth International Conference on Thermoelectrics. Proceedings, ICT'99 (Cat. No.99TH8407); 1999; pp. 473–476.

37. Wojciechowski, K.T.; Zybala, R.; Mania, R. High temperature CoSb3-Cu junctions. *Microelectron. Reliab.* 2011, *51*, 1198–1202.

38. Zybala, R.; Wojciechowski, K.; Schmidt, M.; Mania, R. Junctions and diffusion barriers for high temperature thermoelectric modules.; 2009; Vol. 1, pp. 341–344.

39. Chen, S.; Chu, A.H.; Wong, D.S.-H. Interfacial reactions at the joints of CoSb3-based thermoelectric devices. *J. Alloys Compd.* 2017, *699*, 448–454.

40. Fleurial, J.-P.; Caillat, T.; Chi, S.C. Electrical contacts for skutterudite thermoelectric materials 2012.

41. Kaszyca, K.; Schmidt, M.; Chmielewski, M.; Pietrzak, K.; Zybala, R. Joining of thermoelectric material with metallic electrode using Spark Plasma Sintering (SPS) technique. *Mater. Today Proc.* 2018, *5*, 10277–10282.

42. Shi, L.; Huang, X.; Gu, M.; Chen, L. Interfacial structure and stability in Ni/SKD/Ti/Ni skutterudite thermoelements. *Surf. Coat. Technol.* 2016, *285*, 312–317.

43. Chen, W.; Chen, S.; Tseng, S.; Hsiao, H.; Chen, Y.; Snyder, G.J.; Tang, Y. Interfacial reactions in Ni/CoSb3 couples at 450°C. *J. Alloys Compd.* 2015, *632*, 500–504.

44. Zhao, D.; Li, X.; He, L.; Jiang, W.; Chen, L. High temperature reliability evaluation of CoSb3/electrode thermoelectric joints. *Intermetallics* 2009, *17*, 136–

141.

45. Zhao, D.; Geng, H.; Chen, L. Microstructure Contact Studies for Skutterudite Thermoelectric Devices. *Int. J. Appl. Ceram. Technol.* 2012, *9*, 733–741.

46. Zhao, D.; Li, X.; He, L.; Jiang, W.; Chen, L. Interfacial evolution behavior and reliability evaluation of CoSb3/Ti/Mo–Cu thermoelectric joints during accelerated thermal aging. *J. Alloys Compd.* 2009, *477*, 425–431.

47. Fan, J.; Chen, L.; Bai, S.; Shi, X. Joining of Mo to CoSb3 by spark plasma sintering by inserting a Ti interlayer. *Mater. Lett.* 2004, *58*, 3876–3878.

48. Fleurial, J.-P.; Borshchevsky, A.; Caillat, T. New thermoelectric materials and devices for terrestrial power generators.; ASCE, 1997; pp. 293–298.

49. Saber, H.H.; El-Genk, M.S.; Caillat, T. Tests results of skutterudite based thermoelectric unicouples. *Energy Convers. Manag.* 2007, *48*, 555–567.

50. García-Cañadas, J.; Powell, A.V.; Kaltzoglou, A.; Vaqueiro, P.; Min, G. Fabrication and Evaluation of a Skutterudite-Based Thermoelectric Module for High-Temperature Applications. *J. Electron. Mater.* 2013, *42*, 1369–1374.

51. Salvador, J.R.; Cho, J.Y.; Ye, Z.; Moczygemba, J.E.; Thompson, A.J.; Sharp, J.W.; König, J.D.; Maloney, R.; Thompson, T.; Sakamoto, J.; et al. Thermal to Electrical Energy Conversion of Skutterudite-Based Thermoelectric Modules. *J. Electron. Mater.* 2013, *42*, 1389–1399.

52. Stobart, R.K.; Yang, Z. The Development of Skutterudite-Based Thermoelectric Generators for Vehicles. *SAE Tech. Pap.* 2018, *2018-April*.

53. Yang, Z.; Pradogonjal, J.; Phillips, M.; Lan, S.; Powell, A.; Vaqueiro, P.; Gao, M.; Stobart, R.; Chen, R. Improved Thermoelectric Generator Performance Using High Temperature Thermoelectric Materials. *SAE Tech. Pap.* 2017, *2017-March*.

54. Song, B.; Lee, S.; Cho, S.; Song, M.-J.; Choi, S.-M.; Seo, W.-S.; Yoon, Y.; Lee, W. The effects of diffusion barrier layers on the microstructural and electrical properties in CoSb3 thermoelectric modules. *J. Alloys Compd.* 2014, *617*, 160–162.

55. ZHANG, Q.-H.; LIAO, J.-C.; TANG, Y.-S.; GU, M.; LIU, R.-H.; BAI, S.-Q.; CHEN, L.-D. Interface Stability of Skutterudite Thermoelectric

Materials/Ti88Al12. *J. Inorg. Mater.* 2018, *33*, 889–894.

56. Zhang, Q.; Liao, J.; Tang, Y.; Gu, M.; Ming, C.; Qiu, P.; Bai, S.; Shi, X.; Uher, C.; Chen, L. Realizing a thermoelectric conversion efficiency of 12% in bismuth telluride/skutterudite segmented modules through full-parameter optimization and energy-loss minimized integration. *Energy Environ. Sci.* 2017, *10*, 956–963.

57. TANG, Y.-S.; BAI, S.-Q.; REN, D.-D.; LIAO, J.-C.; ZHANG, L.-T.; CHEN, L.-D. Interface Structure and Electrical Property of Yb0.3Co4Sb12/Mo-Cu Element Prepared by Welding Using Ag-Cu-Zn Solder. *J. Inorg. Mater.* 2015, *30*, 256–260.

58. Zhao, D.; Geng, H.; Teng, X. Fabrication and reliability evaluation of CoSb3/W–Cu thermoelectric element. *J. Alloys Compd.* 2012, *517*, 198–203.

59. Fan, X.C.; Gu, M.; Shi, X.; Chen, L.D.; Bai, S.Q.; Nunna, R. Fabrication and reliability evaluation of Yb0.3Co4Sb12/Mo–Ti/Mo–Cu/Ni thermoelectric joints. *Ceram. Int.* 2015, *41*, 7590–7595.

60. Rao, A.; Bosak, G.; Joshi, B.; Keane, J.; Nally, L.; Peng, A.; Perera, S.; Waring, A.; Poudel, B. A TiAlCu Metallization for ‘n’ Type CoSb x Skutterudites with Improved Performance for High-Temperature Energy Harvesting Applications. *J. Electron. Mater.* 2017, *46*, 2419–2431.

61. JIE, Q.; Ren, Z.; Chen, G. Fabrication of stable electrode/diffusion barrier layers for thermoelectric filled skutterudite devices 2017.

62. Guo, J.Q.; Geng, H.Y.; Ochi, T.; Suzuki, S.; Kikuchi, M.; Yamaguchi, Y.; Ito, S. Development of Skutterudite Thermoelectric Materials and Modules. *J. Electron. Mater.* 2012, *41*, 1036–1042.

63. Ochi, T.; Nie, G.; Suzuki, S.; Kikuchi, M.; Ito, S.; Guo, J.Q. Power-Generation Performance and Durability of a Skutterudite Thermoelectric Generator. *J. Electron. Mater.* 2014, *43*, 2344–2347.

64. Park, S.H.; Jin, Y.; Cha, J.; Hong, K.; Kim, Y.; Yoon, H.; Yoo, C.-Y.; Chung, I. High-Power-Density Skutterudite-Based Thermoelectric Modules with Ultralow Contact Resistivity Using Fe–Ni Metallization Layers. *ACS Appl. Energy Mater.* 2018, *1*, 1603–1611.

65. Sang Hyun Park; Yoo, C.-Y.; Jin, Y.H.; Hana, Y.; Byung Jin, C. Fe-Ni/Ti Metalized skutterudite thermoelectric material and method of manufacturing the same.

66. Lee, Y.S.; Kim, S.J.; Kim, B.G.; Lee, S.; Seo, W.-S.; Kim, I.-H.; Choi, S.-M. Research for Brazing Materials of High-Temperature Thermoelectric Modules with CoSb3 Thermoelectric Materials. *J. Electron. Mater.* 2017, *46*, 3083–3088.

67. Seo, S.-H.; Kim, S.J.; Lee, S.; Seo, W.-S.; Kim, I.-H.; Choi, S.-M. Fabrication of Metallic Glass Powder for Brazing Paste for High-Temperature Thermoelectric Modules. *J. Electron. Mater.* 2018, *47*, 3159–3163.

68. Luo, H.-T.; Chen, S.-W. Phase equilibria of the ternary Ag-Cu-Ni system and the interfacial reactions in the Ag-Cu/Ni couples. *J. Mater. Sci.* 1996, *31*, 5059–5067.

69. Lin, T.Y.; Liao, C.N.; Wu, A.T. Evaluation of diffusion barrier between lead-free solder systems and thermoelectric materials. *J. Electron. Mater.* 2012, *41*, 153–158.

70. de Boor, J.; Gloanec, C.; Kolb, H.; Sottong, R.; Ziolkowski, P.; Müller, E. Fabrication and characterization of nickel contacts for magnesium silicide based thermoelectric generators. *J. Alloys Compd.* 2015, *632*, 348–353.

71. Zhang, B.; Zheng, T.; Wang, Q.; Zhu, Y.; Alshareef, H.N.; Kim, M.J.; Gnade, B.E. Contact resistance and stability study for Au, Ti, Hf and Ni contacts on thin-film Mg2Si. *J. Alloys Compd.* 2017, *699*, 1134–1139.

72. Iguchi, Y.; Katona, G.L.; Cserháti, C.; Langer, G.A.; Erdélyi, Z. On the miscibility gap of Cu-Ni system. *Acta Mater.* 2018, *148*, 49–54.

73. Zhao, D.; Tian, C.; Tang, S.; Liu, Y.; Jiang, L.; Chen, L. Fabrication of a CoSb3-based thermoelectric module. *Mater. Sci. Semicond. Process.* 2010, *13*, 221–224.

74. Tavassoli, A.; Grytsiv, A.; Failamani, F.; Rogl, G.; Puchegger, S.; Müller, H.; Broz, P.; Zelenka, F.; Macciò, D.; Saccone, A.; et al. Constitution of the binary M-Sb systems (M = Ti, Zr, Hf) and physical properties of MSb2. *Intermetallics* 2018, *94*, 119–132.

75. Lin, T.Y.; Liao, C.N.; Wu, A.T. Evaluation of Diffusion Barrier Between

Lead-Free Solder Systems and Thermoelectric Materials. *J. Electron. Mater.* 2012, *41*, 153–158.

76. Leszczynski, J.; Wojciechowski, K.T.; Malecki, A.L. Studies on thermal decomposition and oxidation of CoSb3. *J. Therm. Anal. Calorim.* 2011, *105*, 211.

77. Stephens, J.J. *Elevated temperature creep properties for selected active metal braze alloys*; University of North Texas Libraries: Albuquerque, New Mexico, 1997;

78. Hari Kumar, K.C.; Wollants, P.; Delacy, L. Thermodynamic assessment of the Ti-Zr system and calculation of the Nb-Ti-Zr phase diagram. *J. Alloys Compd.* 1994, *206*, 121–127.

79. Group, T.M. Expansion Compression Contacts for Thermoelectric Legs Available online: https://www.techbriefs.com/component/content/article/tb/techbriefs/physical-sciences/5190 (accessed on Nov 18, 2018).

80. Nickel-Graphite Composite Compliant Interface and/or Hot Shoe Material - Tech Briefs Available online: https://www.techbriefs.com/component/content/article/tb/techbriefs/materials/17192 (accessed on Nov 18, 2018).

81. Techbriefs Media Expansion Compression Contacts for Thermoelectric Legs Available online: https://www.techbriefs.com/component/content/article/tb/techbriefs/physical-sciences/5190 (accessed on Nov 17, 2018).

82. Saber, H.H.; El-Genk, M.S. Effects of metallic coatings on the performance of skutterudite-based segmented unicouples. *Energy Convers. Manag.* 2007, *48*, 1383–1400.

83. Sakamoto, J.; Caillat, T.; Fleurial, J.-P.; Jones, S.; Paik, J.-A.; Dong, W. Improving Thermoelectric Device Performance and Durability through the Integration of Advanced, Aerogel-Based Ceramics. In *Electroceramic Materials and Applications*; Wiley-Blackwell, 2011; pp. 275–290 ISBN 978-1-118-14412-1.

84. Konig, J. Skutterudite Modules - Thermoelectric High Temperature Modules Based On Skutterudites Available online: https://www.ipm.fraunhofer.de/content/dam/ipm/en/PDFs/product-

information/TE/KUT/Skutterudite-thermoelectric-modules-high-temperature.pdf.

85. Konig, J.D. Thermoelectrics: History, recent progress and future aspects 2014.

86. Sharp, J. Thermoelectric modules for a prototype waste heat recovery system 2014.

87. Felten, F. Thermoelectric generator for automotive application 2014.

88. Nie, G.; Suzuki, S.; Tomida, T.; Sumiyoshi, A.; Ochi, T.; Mukaiyama, K.; Kikuchi, M.; Guo, J.Q.; Yamamoto, A.; Obara, H. Performance of Skutterudite-Based Modules. *J. Electron. Mater.* 2017, *46*, 2640–2644.

89. Smith, K.L.; Li, B.C.; Firdosy, S.; Sujittosakul, S.; Errico, M.; Nakatsukasa, G.; Fleurial, J.-P.; Ewell, R. Development of Filled-Skutterudite Based Thermopile for High Temperature Sensors for Space and Terrestrial Applications. In *14th International Energy Conversion Engineering Conference*; AIAA Propulsion and Energy Forum; American Institute of Aeronautics and Astronautics, 2016.

90. Zong, P.; Hanus, R.; Dylla, M.; Tang, Y.; Liao, J.; Zhang, Q.; Snyder, G.J.; Chen, L. Skutterudite with graphene-modified grain-boundary complexion enhances zT enabling high-efficiency thermoelectric device. *Energy Environ. Sci.* 2017, *10*, 183–191.

91. Prado-Gonjal, J.; Phillips, M.; Vaqueiro, P.; Min, G.; Powell, A.V. Skutterudite Thermoelectric Modules with High Volume-Power-Density: Scalability and Reproducibility. *ACS Appl. Energy Mater.* 2018.

92. A multi-mission radioisotope thermoelectric generator (MMRTG) for Mars 2020 - IEEE Conference Publication Available online: https://ieeexplore-ieee-org.ezproxy.biblio.polito.it/document/7943688/ (accessed on Jul 23, 2018).

93. Schock, A.; Sookiazian, H. Design Optimization of RTG for Solar-Polar Mission. *Proc. Intersoc. Energy Convers. Eng. Conf.* 2017, *2*, 1444–1454.

94. Advanced Thermoelectric Technology: Powering Spacecraft and Instruments to Explore the Solar System | Science Mission Directorate Available online: https://science.nasa.gov/technology/technology-stories/advanced-thermoelectric-technology (accessed on Jan 18, 2019).

95. B08 Committee *Specification for Electroplated Engineering Nickel Coatings*; ASTM International;

96. B08 Committee *Specification for Autocatalytic (Electroless) Nickel-Phosphorus Coatings on Metal*; ASTM International;

97. ASTM D3359-17, Standard Test Methods for Rating Adhesion by Tape Test ASTM International, West Conshohocken, PA 2017.

98. Ravi, V.; Firdosy, S.; Caillat, T.; Brandon, E.; Van, D.W.; Maricic, L.; Sayir, A. Thermal expansion studies of selected high-temperature thermoelectric materials. *J. Electron. Mater.* 2009, *38*, 1433–1442.

99. ASTM D905-08(2013) Standard Test Method for Strength Properties of Adhesive Bonds in Shear by Compression Loading, ASTM International, West Conshohocken, PA, 2013,.

100. Katsuyama, S.; Kanayama, Y.; Ito, M.; Majima, K.; Nagai, H. Thermoelectric properties of CoSb3 with dispersed FeSb2 particles. *J. Appl. Phys.* 2000, *88*, 3484–3489.

101. Zhang, L.; Sakamoto, J. The microstructural stability and thermoelectric properties of Mm 0.9Fe3.5Co0.5Sb12-based skutterudites. *Mater. Chem. Phys.* 2013, *138*, 601–607.

102. Antimony (Sb) Debye temperature, heat capacity, density, melting point. In *Non-Tetrahedrally Bonded Elements and Binary Compounds I*; Madelung, O., Rössler, U., Schulz, M., Eds.; Landolt-Börnstein - Group III Condensed Matter; Springer Berlin Heidelberg: Berlin, Heidelberg, 1998; pp. 1–4 ISBN 978-3-540-31360-1.

103. Zhang, L.; Grytsiv, A.; Kerber, M.; Rogl, P.; Bauer, E.; Zehetbauer, M. Thermoelectric performance of mischmetal skutterudites MmyFe4-xCoxSb12 at elevated temperatures. *J. Alloys Compd.* 2010, *490*, 19–25.

104. He, Q.; Hu, S.; Tang, X.; Lan, Y.; Yang, J.; Wang, X.; Ren, Z.; Hao, Q.; Chen, G. The great improvement effect of pores on ZT in Co1-x Nix Sb3 system. *Appl. Phys. Lett.* 2008, *93*, 042108.

105. Kim, J.; Ohishi, Y.; Muta, H.; Kurosaki, K. Enhancement of thermoelectric properties of p-type single-filled skutterudites CexFeyCo4-ySb12 by tuning the

Ce and Fe content. *AIP Adv.* 2018, *8*, 105104.

106. Dahal, T.; Gahlawat, S.; Jie, Q.; Dahal, K.; Lan, Y.; White, K.; Ren, Z. Thermoelectric and mechanical properties on misch metal filled p-type skutterudites Mm0.9Fe4−xCoxSb12. *J. Appl. Phys.* 2015, *117*, 055101.

107. Sales, B.C.; Mandrus, D.; Williams, R.K. Filled Skutterudite Antimonides: A New Class of Thermoelectric Materials. *Science* 1996, *272*, 1325–1328.

108. Gucci, F.; Saunders, T.G.; Reece, M.J. In-situ synthesis of n-type unfilled skutterudite with reduced thermal conductivity by hybrid flash-spark plasma sintering. *Scr. Mater.* 2018, *157*, 58–61.

109. Kim, I.-H.; Ur, S.-C. Electronic transport properties of Ni-doped CoSb3 prepared by encapsulated induction melting. *Met. Mater. Int.* 2007, *13*, 53–58.

110. F01 Committee *Specification for Metallized Surfaces on Ceramic*; ASTM International;

111. Gu, M.; Bai, S.; Xia, X.; Huang, X.; Li, X.; Shi, X.; Chen, L. Study on the High Temperature Interfacial Stability of Ti/Mo/Yb0.3Co4Sb12 Thermoelectric Joints. *Appl. Sci.* 2017, *7*, 952.

112. A thermodynamic study on the Ag-Sb-Sn system. *J. Alloys Compd.* 1996, *238*, 155–166.

113. Varahramyan, K.; Verret, E.J. A model for specific contact resistance applicable for titanium silicide-silicon contacts. *Solid-State Electron.* 1996, *39*, 1601–1607.

114. Ward, A.; Henning, J.; Hagleitner, H.; Wieber, K. Silicon-rich nickel-silicide ohmic contacts for SiC semiconductor devices 2006.

115. Hara, T.; Hayashida, H.; Takahashi, S.; Yamanoue, A. Tungsten silicide barrier layers in aluminium ohmic contact systems. *Thin Solid Films* 1989, *177*, 9–16.

116. Peng, P.; Hu, A.; Gerlich, A.P.; Zou, G.; Liu, L.; Zhou, Y.N. Joining of silver nanomaterials at low temperatures: processes, properties and applications. *ACS Appl. Mater. Interfaces* 2015, *7*, 12597–12618.

117. Mallory, G.O.; Hajdu, J.B. *Electroless Plating: Fundamentals and Applications*; William Andrew, 1990; ISBN 978-0-936569-07-9.

118. Hara, T.; Enomoto, S.; Ohtsuka, N.; Shima, S. Barrier Effects of Tungsten Infer-Layer for Aluminum Diffusion in Aluminum/Silicon Ohmic-Contact System. *Jpn. J. Appl. Phys.* 1985, *24*, 828.

119. Bernstein, L. Semiconductor Joining by the Solid-Liquid-Interdiffusion (SLID) Process: I. The Systems Ag-In, Au-In, and Cu-In. *J. Electrochem. Soc.* 1966, *113*, 1282–1288.

120. Made, R.I.; Gan, C.L.; Yan, L.L.; Yu, A.; Yoon, S.W.; Lau, J.H.; Lee, C. Study of Low-Temperature Thermocompression Bonding in Ag-In Solder for Packaging Applications. *J. Electron. Mater.* 2009, *38*, 365.

121. Fukumoto, S.; Miyake, K.; Tatara, S.; Matsushima, M.; Fujimoto, K. Solid-Liquid Interdiffusion Bonding of Copper Using Ag-Sn Layered Films. *Mater. Trans.* 2015, *56*, 1019–1024.

122. Deillon, L.; Hessler-Wyser, A.; Hessler, T.; Rappaz, M. Solid-liquid interdiffusion (SLID) bonding in the Au-In system: Experimental study and 1D modelling. *J. Micromechanics Microengineering* 2015, *25*.

123. Tollefsen, T.A.; Larsson, A.; Løvvik, O.M.; Aasmundtveit, K. Au-Sn SLID Bonding—Properties and Possibilities. *Metall. Mater. Trans. B* 2012, *43*, 397–405.

124. Larsson, A.; Tollefsen, T.A.; L⊘vvik, O.M.; Aasmundtveit, K.E. Ni-Sn solid-liquid interdiffusion (SLID) bonding for thermo-electric elements in extreme environments #x2014; FEA of the joint stress. In Proceedings of the 2015 European Microelectronics Packaging Conference (EMPC); 2015; pp. 1–6.

125. Huang, T.-C.; Smet, V.; Kawamoto, S.; Pulugurtha, M.R.; Tummala, R.R. Accelerated Metastable Solid–liquid Interdiffusion Bonding with High Thermal Stability and Power Handling. *J. Electron. Mater.* 2018, *47*, 368–377.

126. Kumar, K.G. A Novel Intermetallic Nickel Aluminide (Ni3Al) as an Alternative Automotive Body Material. *Int. J. Eng.* 2011, *11*, 8.

127. Kanetsuki, S.; Kuwahara, K.; Egawa, S.; Miyake, S.; Namazu, T. Effect of thickening outermost layers in Al/Ni multilayer film on thermal resistance of reactively bonded solder joints. *Jpn. J. Appl. Phys.* 2017, *56*, 06GN16.

128. Kun, Y.; Hanqing, X.; Yilong, D.; Fei, T.; Sufeng, F.; Xueyan, Q.; Li, W.

Bonding Process and Application Properties of an Al-Ni Layer Composite Sheet for Lithium-ion Battery Packaging. *Rare Met. Mater. Eng.* 2016, *45*, 1100–1105.

129. Chuang, T.H.; Lin, H.J.; Chuang, C.H.; Yeh, W.T.; Hwang, J.D.; Chu, H.S. Solid Liquid Interdiffusion Bonding of (Pb, Sn)Te Thermoelectric Modules with Cu Electrodes Using a Thin-Film Sn Interlayer. *J. Electron. Mater.* 2014, *43*, 4610–4618.

130. Lin, Y.C.; Lee, K.T.; Hwang, J.D.; Chu, H.S.; Hsu, C.C.; Chen, S.C.; Chuang, T.H. Solid Liquid Interdiffusion Bonding of Zn4Sb3 Thermoelectric Material with Cu Electrode. *J. Electron. Mater.* 2016, *45*, 4935–4942.

131. Sha, W.; Wu, X.; Keong, K.G. 10 - Crystallisation of nickel–phosphorus (Ni–P) deposits with high phosphorus content. In *Electroless Copper and Nickel–Phosphorus Plating*; Sha, W., Wu, X., Keong, K.G., Eds.; Woodhead Publishing Series in Metals and Surface Engineering; Woodhead Publishing, 2011; pp. 141–162 ISBN 978-1-84569-808-9.

132. Okamoto, H. Al-Ni (aluminum-nickel). *J. Phase Equilibria* 1993, *14*, 257–259.

133. Ding, Z.; Hu, Q.; Lu, W.; Sun, S.; Xia, M.; Li, J. In situ observation on the formation of intermetallics compounds at the interface of liquid Al/solid Ni. *Scr. Mater.* 2017, *130*, 214–218.

134. Edelstein, A.S.; Everett, R.K.; Richardson, G.R.; Qadri, S.B.; Foley, J.C.; Perepezko, J.H. Reaction kinetics and biasing in Al/Ni multilayers. *Mater. Sci. Eng. A* 1995, *195*, 13–19.

135. Dhakal, R.; Huh, Y.; Galipeau, D.; Y, X. AlSb Compound Semiconductor as Absorber Layer in Thin Film Solar Cells. In *Solar Cells - New Aspects and Solutions*; Kosyachenko, L.A., Ed.; InTech, 2011 ISBN 978-953-307-761-1.

136. Seith, W.; Heumann, T. *Diffusion of metals : exchange reactions*; Springer Press: Berlin, 1955;

137. Wołczyński, W.; Okane, T.; Senderowski, C.; Kania, B.; Zasada, D.; Janczak-Rusch, J. Meta-Stable Conditions of Diffusion Brazing. *Arch. Metall. Mater.* 2011, *56*, 311–323.

138. Tumminello, S.; Sommadossi, S. Growth kinetics of intermetallic phases in

transient liquid phase bonding process (TLPB) in Al/Ni system. *Defect Diffus. Forum* 2012, *323–325*, 465–470.

139. MacDonald, W.D.; Eagar, T.W. Isothermal solidification kinetics of diffusion brazing. *Metall. Mater. Trans. Phys. Metall. Mater. Sci.* 1998, *29*, 315–325.

140. Eremenko, V.N.; Natanzon, Y.V.; Titov, V.P. Dissolution kinetics and diffusion coefficients of iron, cobalt, and nickel in molten aluminum. *Sov. Mater. Sci. Transl Fiz.-Khimicheskaya Mekhanika Mater. Acad. Sci. Ukr. SSR* 1978, *14*, 579–584.

141. Liu, X.J.; Gao, F.; Wang, C.P.; Ishida, K. Thermodynamic assessments of the Ag-Ni binary and Ag-Cu-Ni ternary systems. *J. Electron. Mater.* 2008, *37*, 210–217.

142. Chuang, T.-H.; Yeh, W.-T.; Chuang, C.-H.; Hwang, J.-D. Improvement of bonding strength of a (Pb, Sn)Te-Cu contact manufactured in a low temperature SLID-bonding process. *J. Alloys Compd.* 2014, *613*, 46–54.

143. Ferreres, X.R.; Aminorroaya Yamini, S.; Nancarrow, M.; Zhang, C. One-step bonding of Ni electrode to n-type PbTe — A step towards fabrication of thermoelectric generators. *Mater. Des.* 2016, *107*, 90–97.

144. US Patent Application for ELECTRICAL CONTACTS FOR SKUTTERUDITE THERMOELECTRIC MATERIALS Patent Application (Application #20120006376 issued January 12, 2012) - Justia Patents Search Available online: https://patents.justia.com/patent/20120006376 (accessed on Apr 13, 2019).

145. Okamoto, H. Mo-ni (molybdenum-nickel). *J. Phase Equilibria* 1991, *12*, 703–703.

146. Murray, J.L. The Ti−Zr (Titanium-Zirconium) system. *Bull. Alloy Phase Diagr.* 1981, *2*, 197–201.

Appendix A: EDS analysis

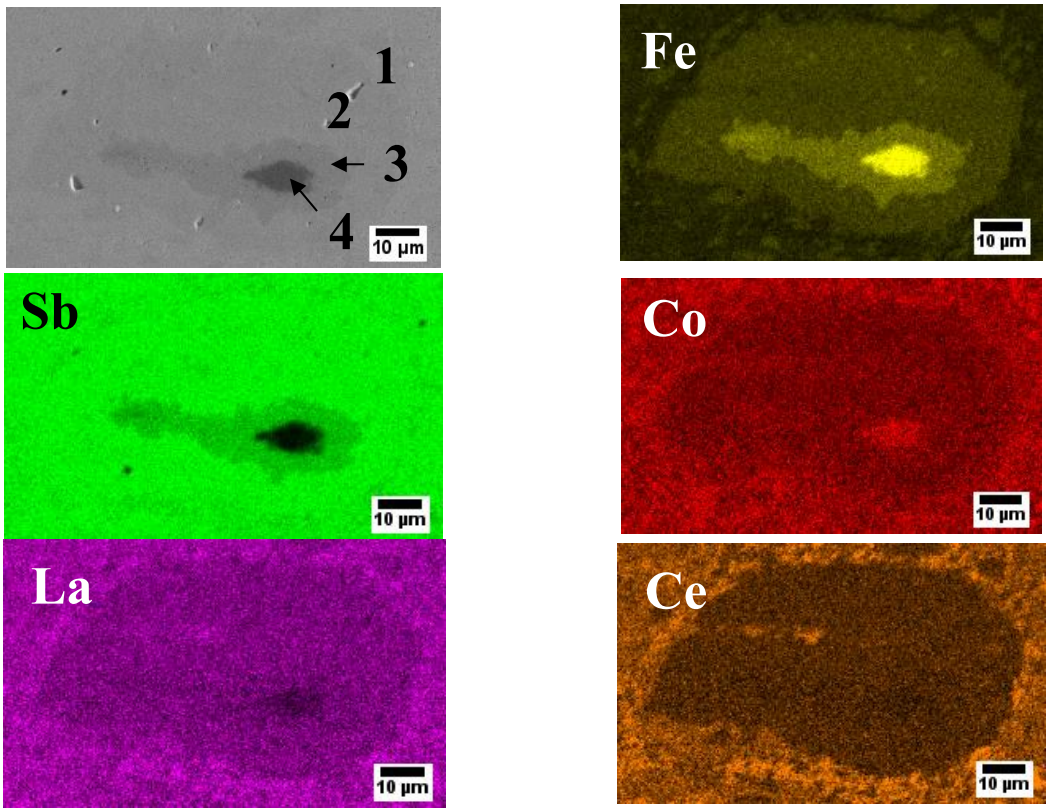

Figure A. 1: EDS analysis of the $Mm_yFe_{4-x}Co_xSb_{12}$ *p-type* thermoelectric material (*Mm*-mischmetal) after consolidation at 600 °C for 5 min using SPS revealing the formation of (1) $Mm_y(Co,Fe)_4Sb_{12}$ (3.49 at% Ce – 1.33 at% La – 4 at% Co – 18 at% Fe – 73 at% Sb), (2) $FeSb_2$ (28 at.% Fe—72 at.% Sb), (3) Fe-rich $FeSb_2$ (50 at.% Fe—50 at.% Sb) and (4) pure Fe (100 at% Fe) phases with elemental mapping of Fe, Sb, Co, La and Ce.

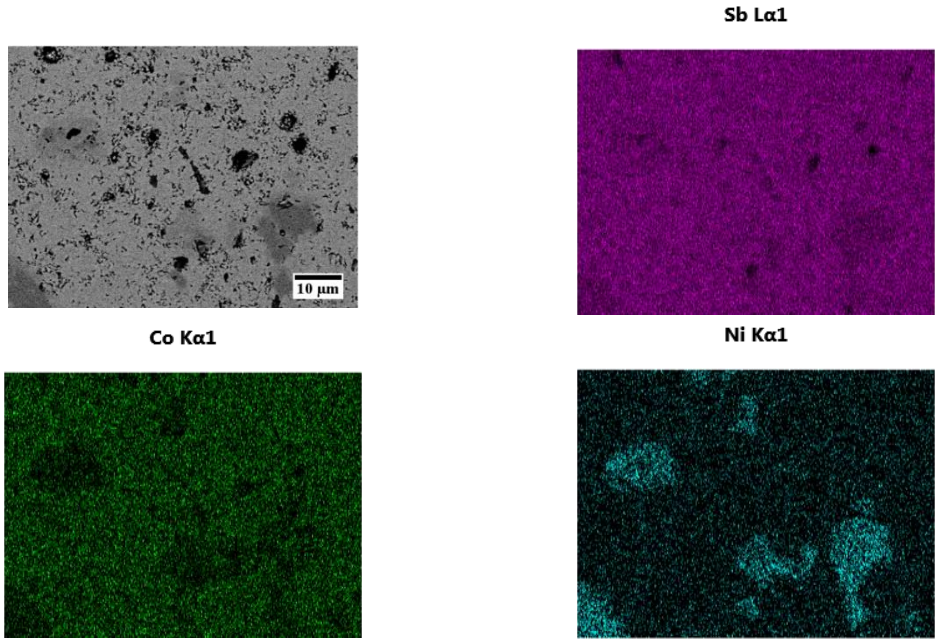

Figure A. 2: EDS analysis of $(Ni,Co)_1Sb_3$ *n-type* thermoelectric material after consolidation at 750 °C for 5 min using SPS with elemental mapping of Sb, Co and Ni.

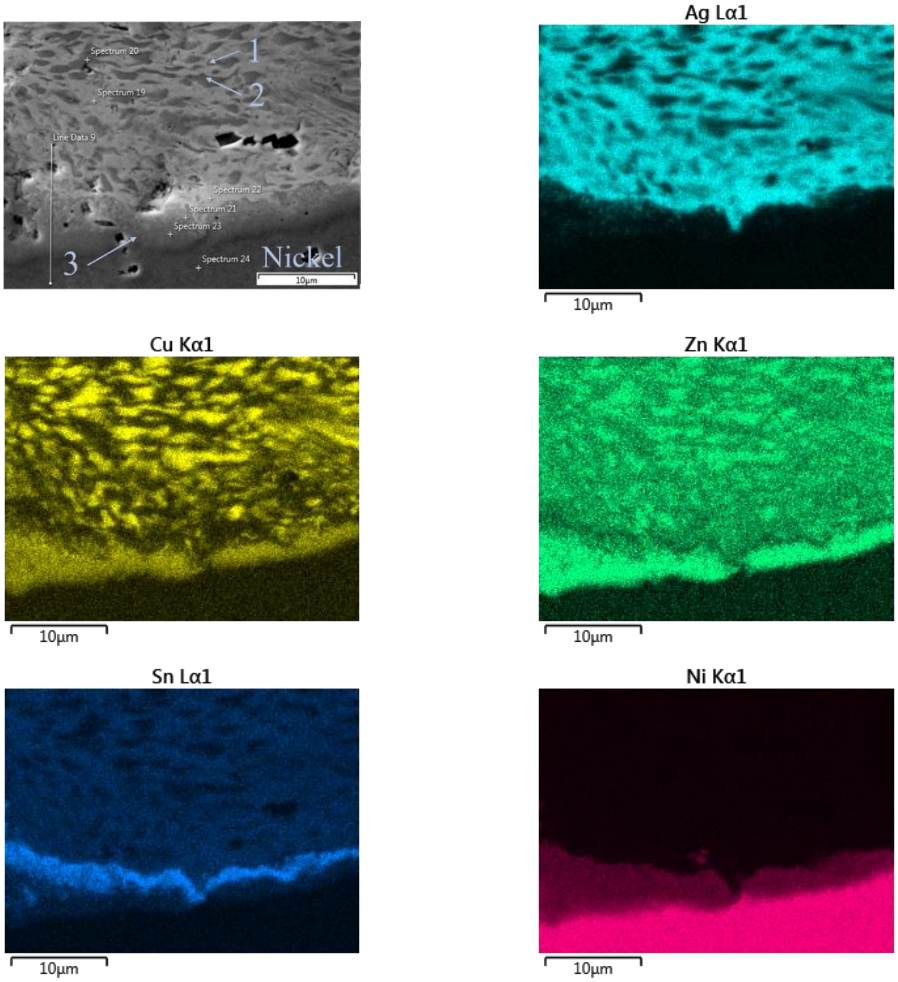

Figure A. 3: EDS elemental mapping of the nickel (Ni) – silver-flo^{TM} 56 braze (Ag 56 at% - Cu 22 at% - Zn 17 at% - Sn 5 at%, Johnson Matthey, UK) interface after brazing at 655 ^{o}C for 5 minutes in Ar. Chemical composition of phases: (1). Ag 76 at% - Zn 13 at% - Cu 9 at% - Sn 2 at% - Ni 1 at%; (2). Cu 67 at% - Zn 23 at% - Ag 8 at%, Zn 1 at% - Sn 1 at%; (3). Ni 36 at% - Cu 32 at% - Zn 24 at% - Ag 2.5 at% - Sn 4 at%. Elemental mappings of silver (Ag), copper (Cu), zinc (Zn), tin (Sn) and nickel (Ni) are also included.

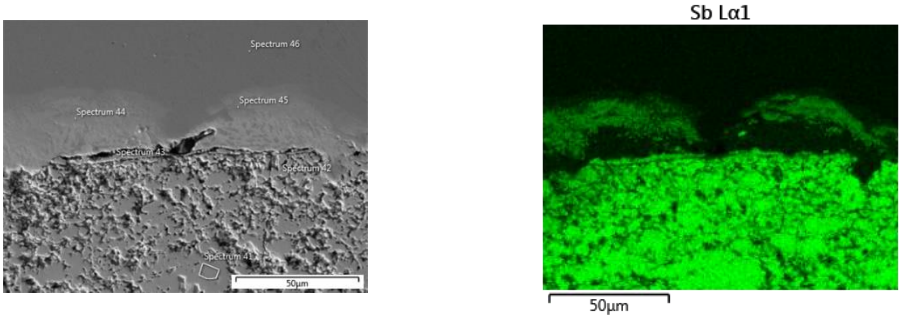

Figure A. 4: EDS EDS analysis of the Ti (0.3 µm-thick) / Ni (1.2 µm-thick) metallized $Mm_yFe_{4-x}Co_xSb_{12}$ *p-type* thermoelectric material after furnace brazing at 655 ^{o}C for 5 min using Ag56-Cu-Zn-Sn braze (Johnson Matthey, UK) with elemental mapping of antimony (Sb), iron (Fe), cerium (Ce), lanthanum (La), cobalt (Co), nickel (Ni), silver (Ag), zinc (Zn), copper (Cu), tin (Sn) and titanium (Ti).

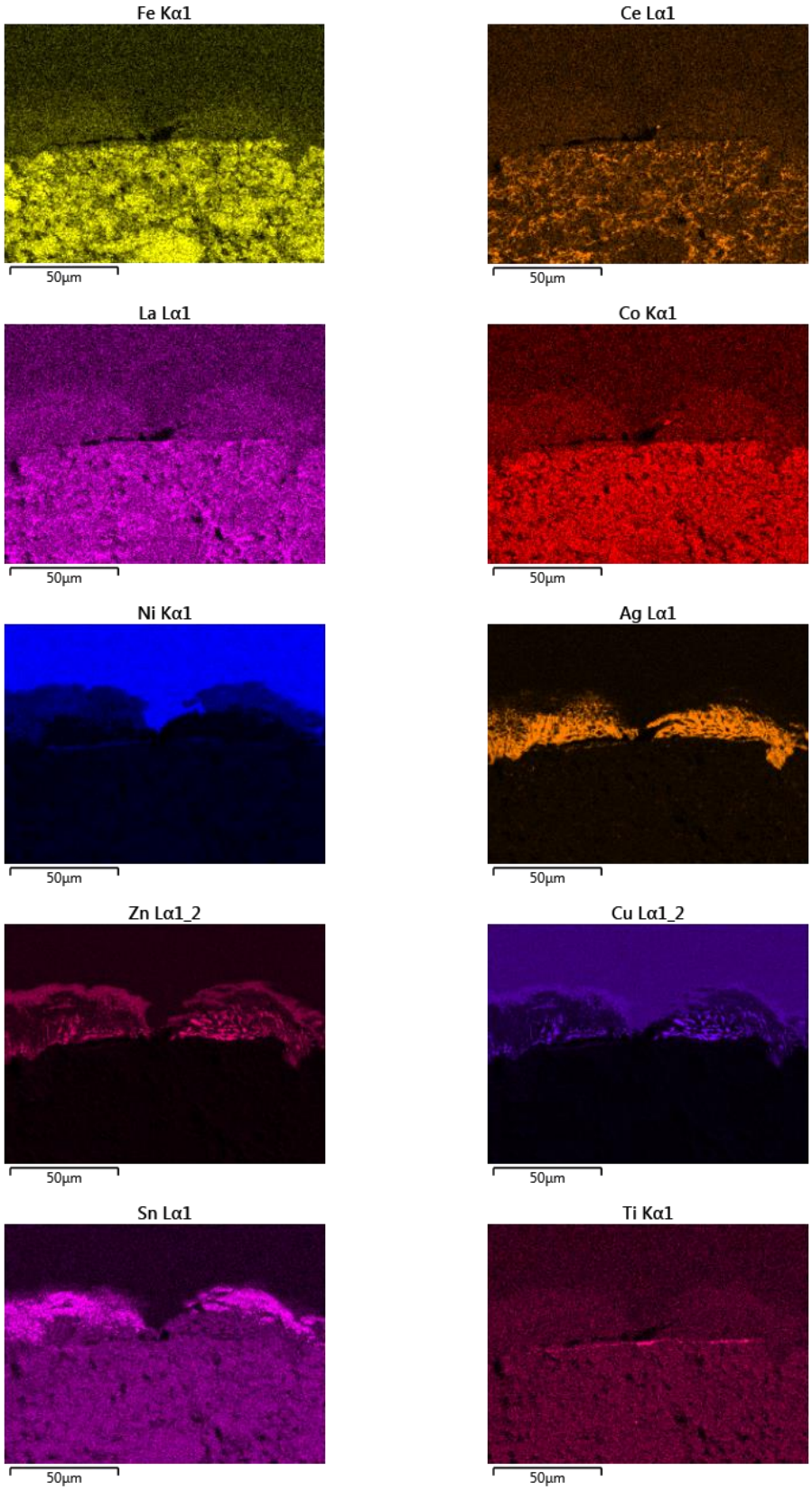

Figure A. 4 (Continued)

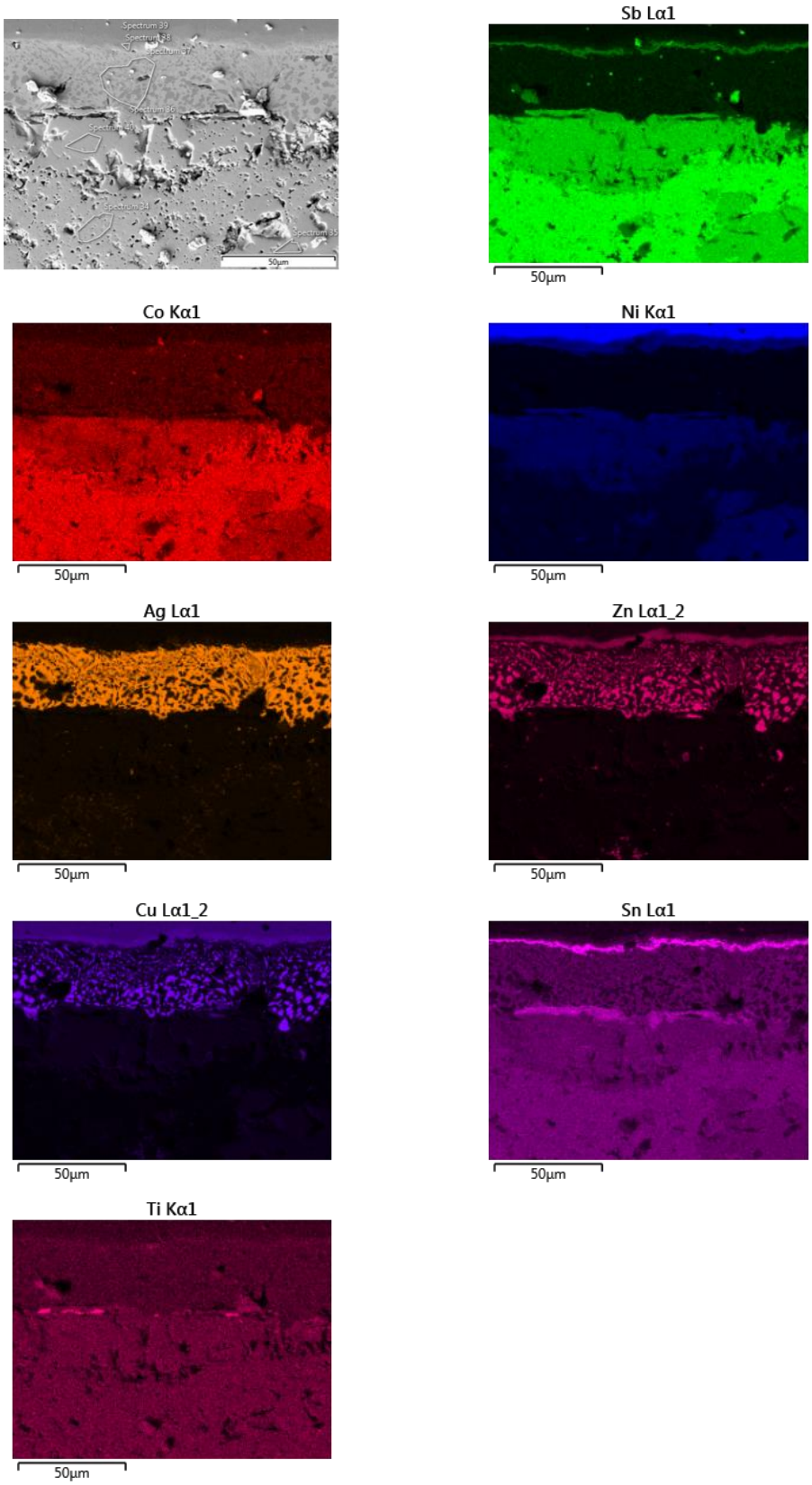

Figure A. 5: EDS analysis of Ti (0.3 µm-thick) / Ni (1.2 µm-thick) metallized $(Ni,Co)_1Sb_3$ *n-type* thermoelectric material after furnace brazing at 655 ºC for 5 min using Ag56-Cu-Zn-Sn braze (Johnson Matthey, UK) with elemental mapping of antimony (Sb), cobalt (Co), nickel (Ni), silver (Ag), zinc (Zn), copper (Cu), tin (Sn) and titanium (Ti).

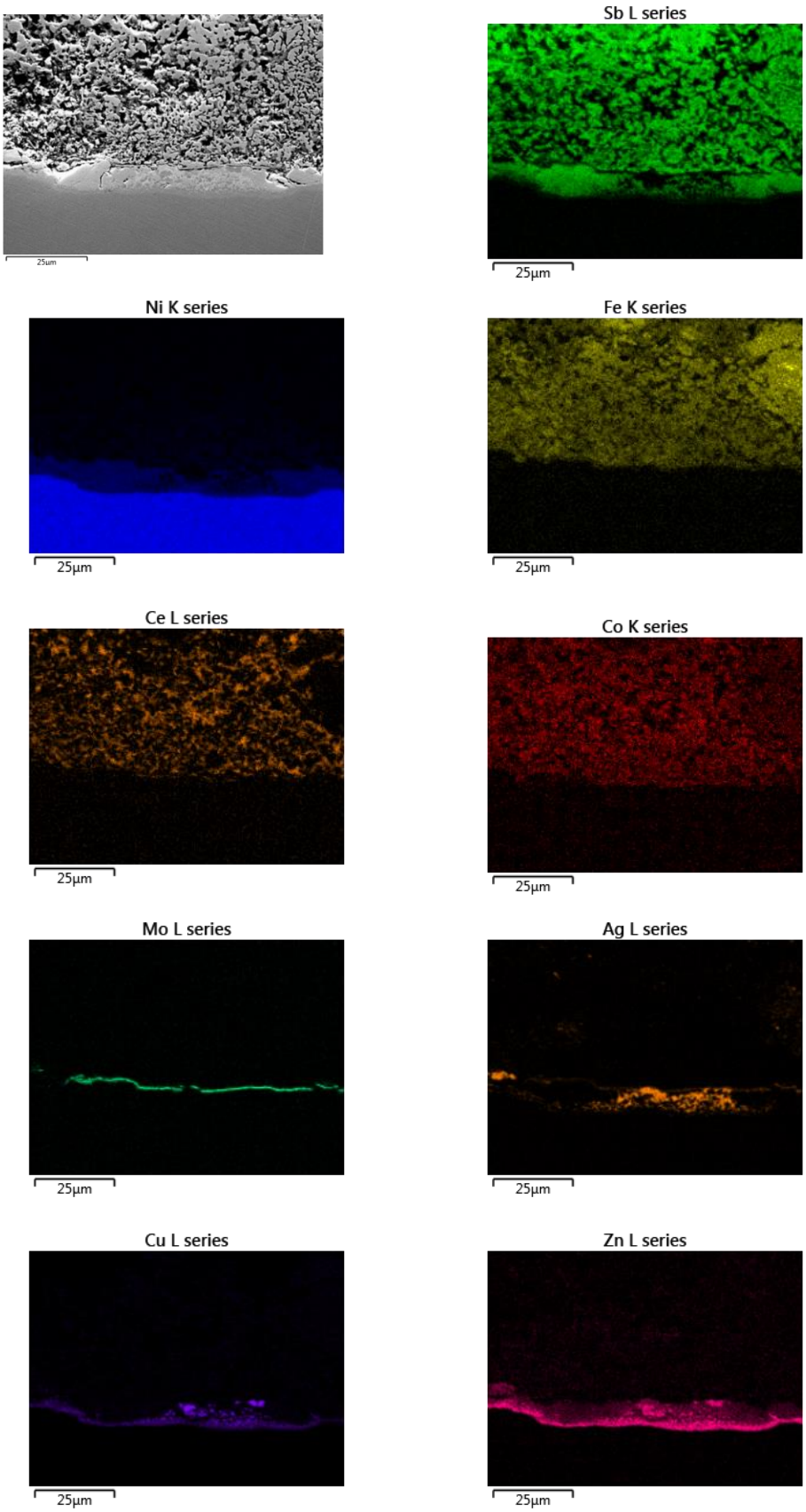

Figure A. 6: EDS EDS analysis of Mo (0.3 µm-thick) / Ni (1.2 µm-thick) metallized $Mm_yFe_{4-x}Co_xSb_{12}$ *p-type* thermoelectric material after furnace brazing at 655 °C for 5 min using Ag56-Cu-Zn-Sn braze (Johnson Matthey, UK) with elemental mapping of Sb, Ni, Fe, Ce, Co, Mo, Ag, Cu, Zn, Sn and O_2.

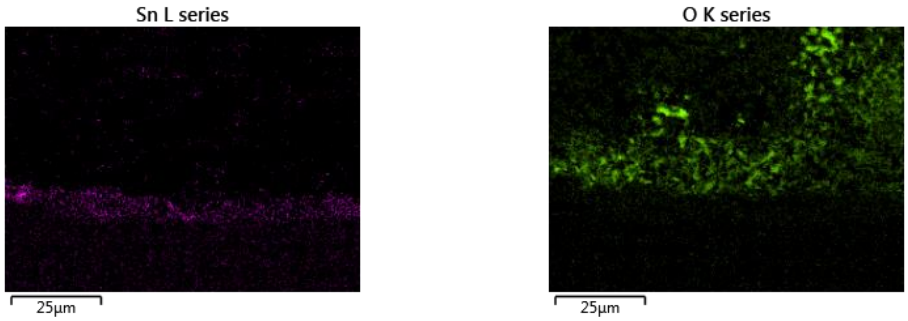

Figure A. 6 (Continued)

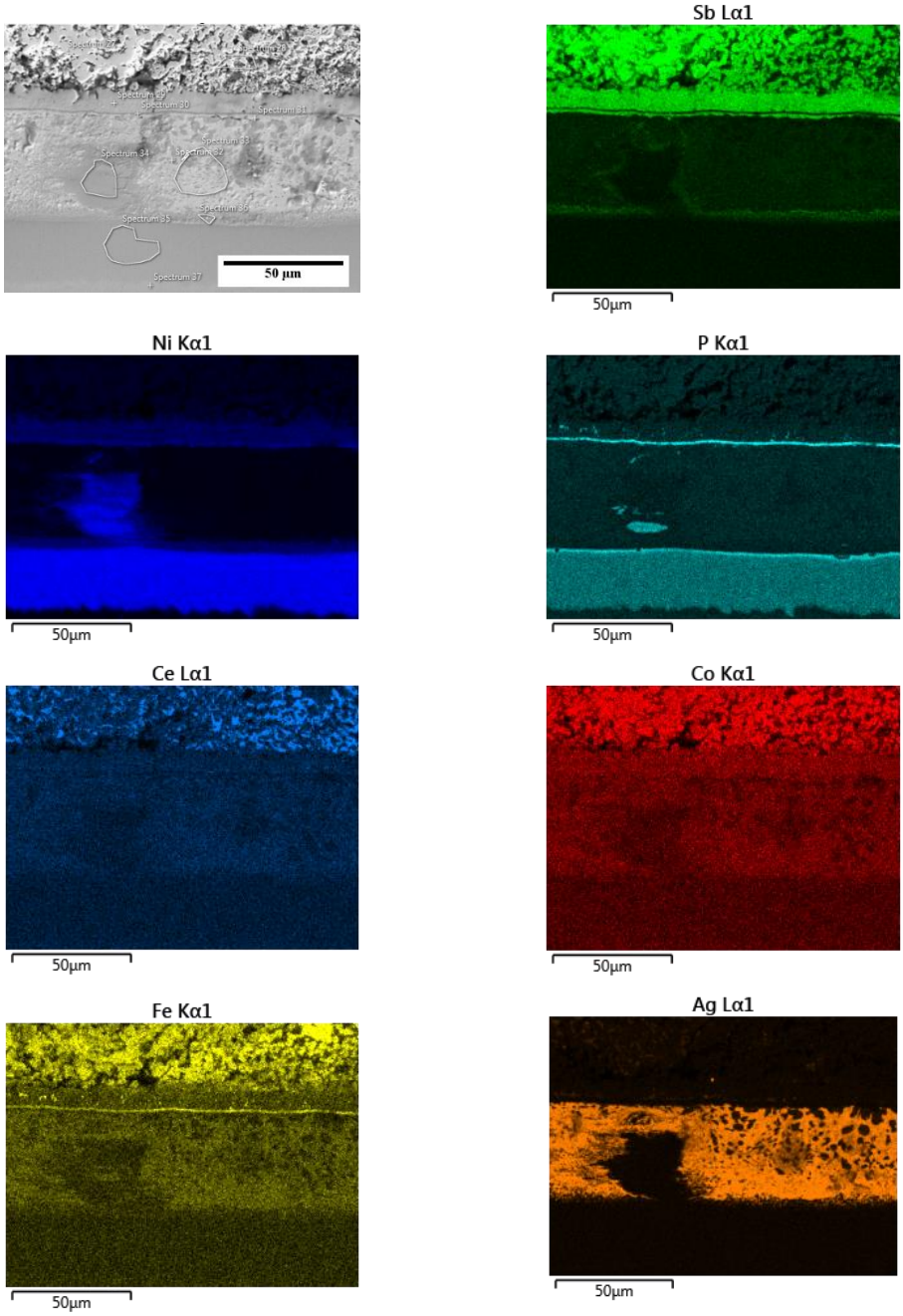

Figure A. 7: EDS analysis of Ni/Ni(P) coated $Mm_yFe_{4-x}Co_xSb_{12}$ *p-type* thermoelectric after joining to Ni(P) coated Cu at 655 ºC for 5 min using Ag56-Cu-Zn-Sn (Johnson Matthey, UK) braze with elemental mapping of Sb, Ni, P, Ce, Co, Fe, Ag, Cu, Zn, Sn and La.

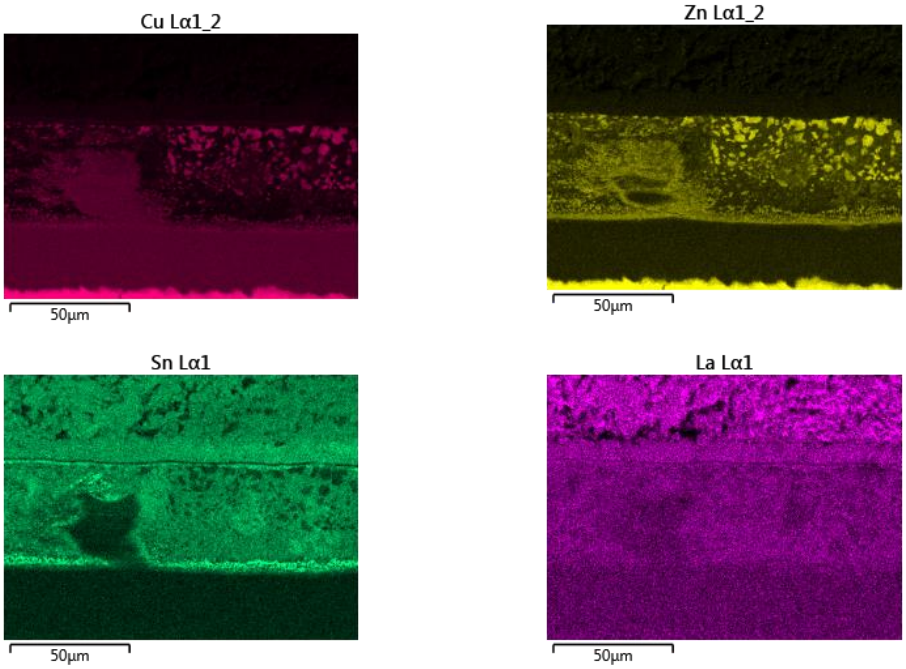

Figure A. 7 (Continued)

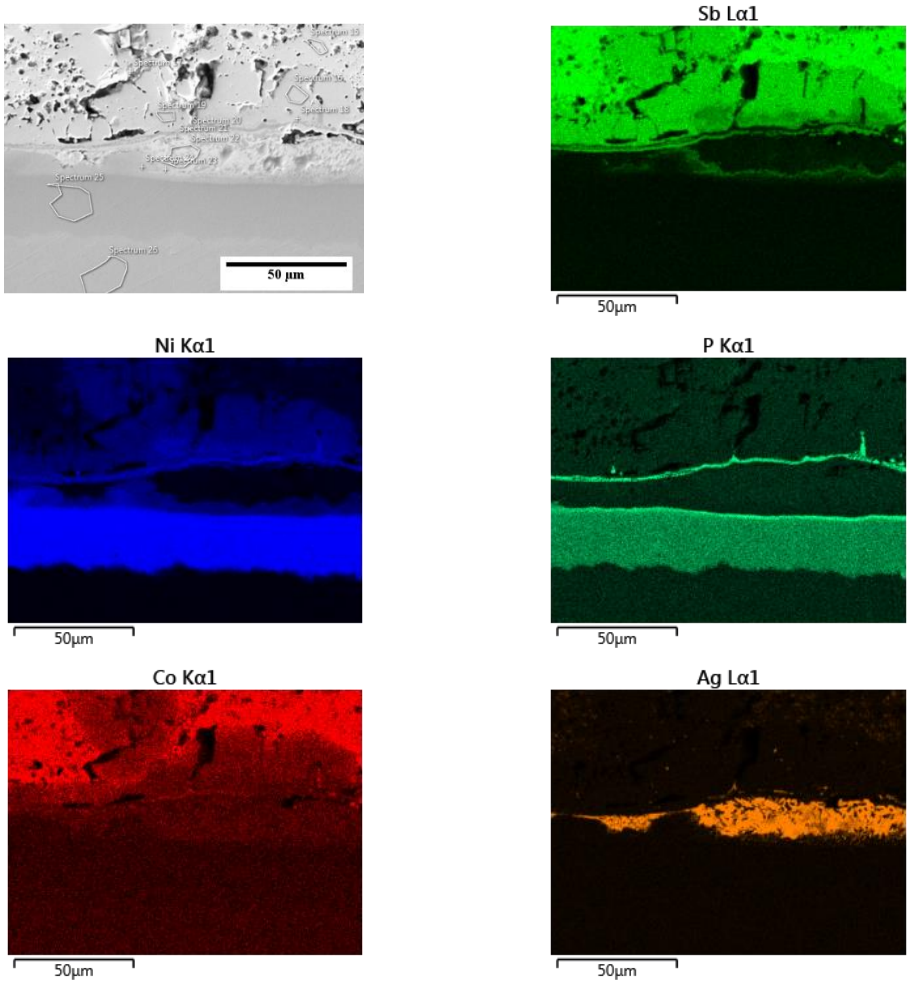

Figure A. 8: EDS analysis of Ni/Ni(P) coated $(Ni,Co)_1Sb_3$ *n-type* thermoelectric after joining to Ni(P) coated Cu at 655 ºC for 5 min using Ag56-Cu-Zn-Sn (Johnson Matthey, UK) braze with elemental mapping of Sb, Ni, P, Co, Ag, Cu, Zn and Sn.

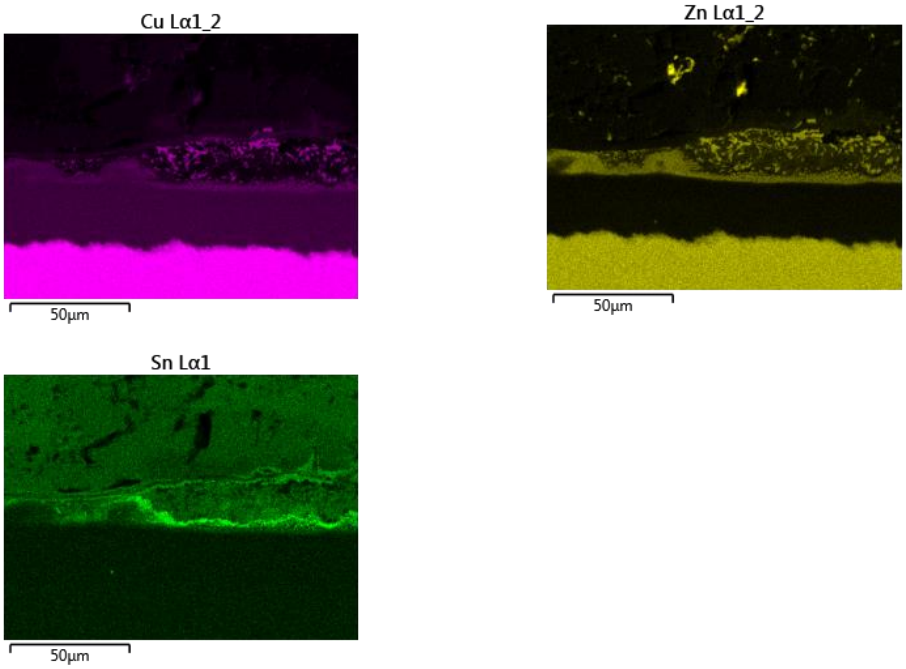

Figure A. 8 (Continued)

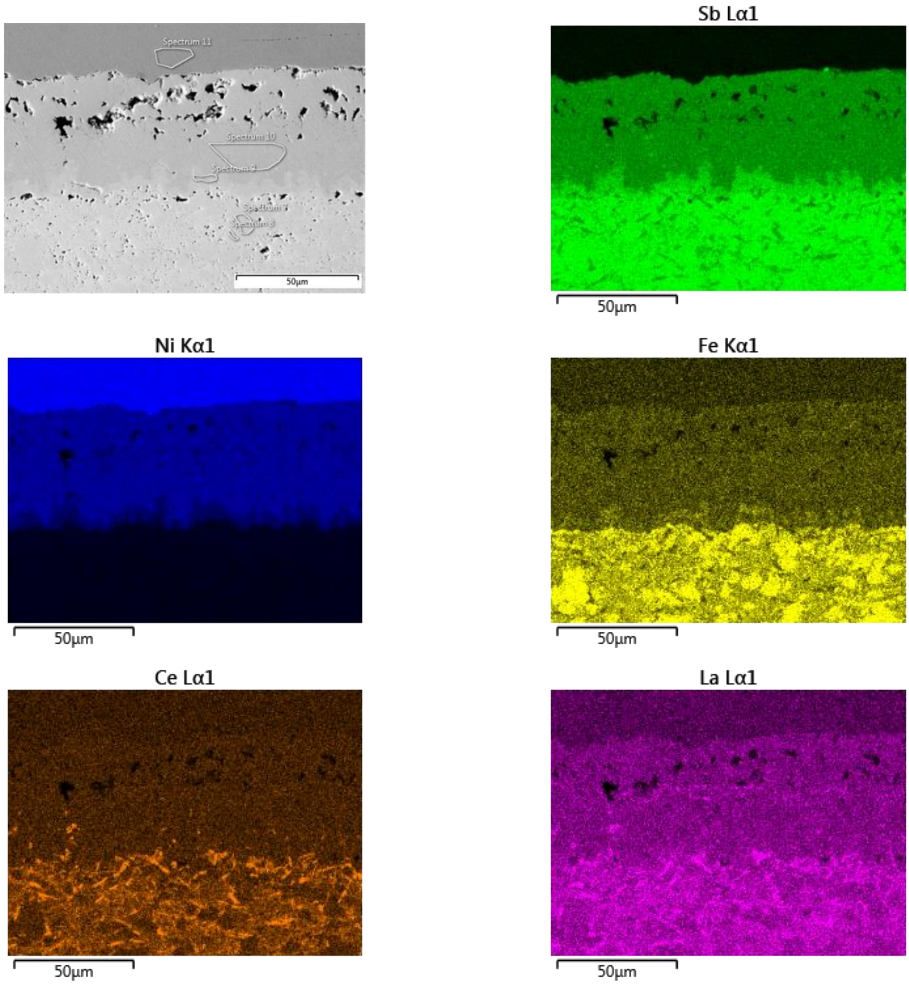

Figure A. 9: EDS analysis of Ti (0.3 µm-thick) / Ni (1.2 µm-thick) metallized $Mm_yFe_{4-x}Co_xSb_{12}$ *p-type* thermoelectric bonded to nickel using silver paste at 652 ºC in Ar with elemental mapping of Sb, Ni, Fe, Ce, La, Co, Ag and Ti.

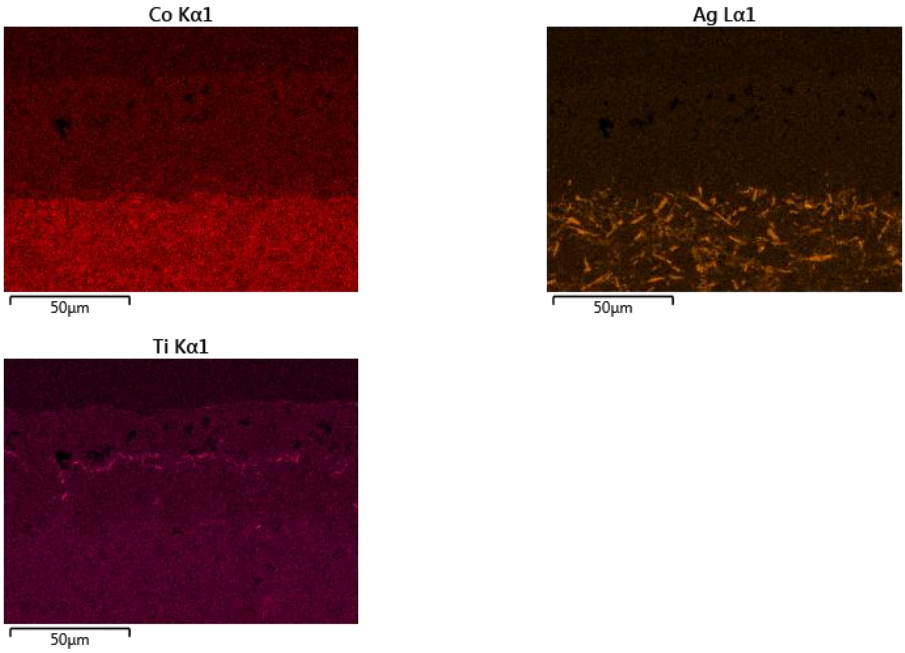

Figure A. 9 (Continued)

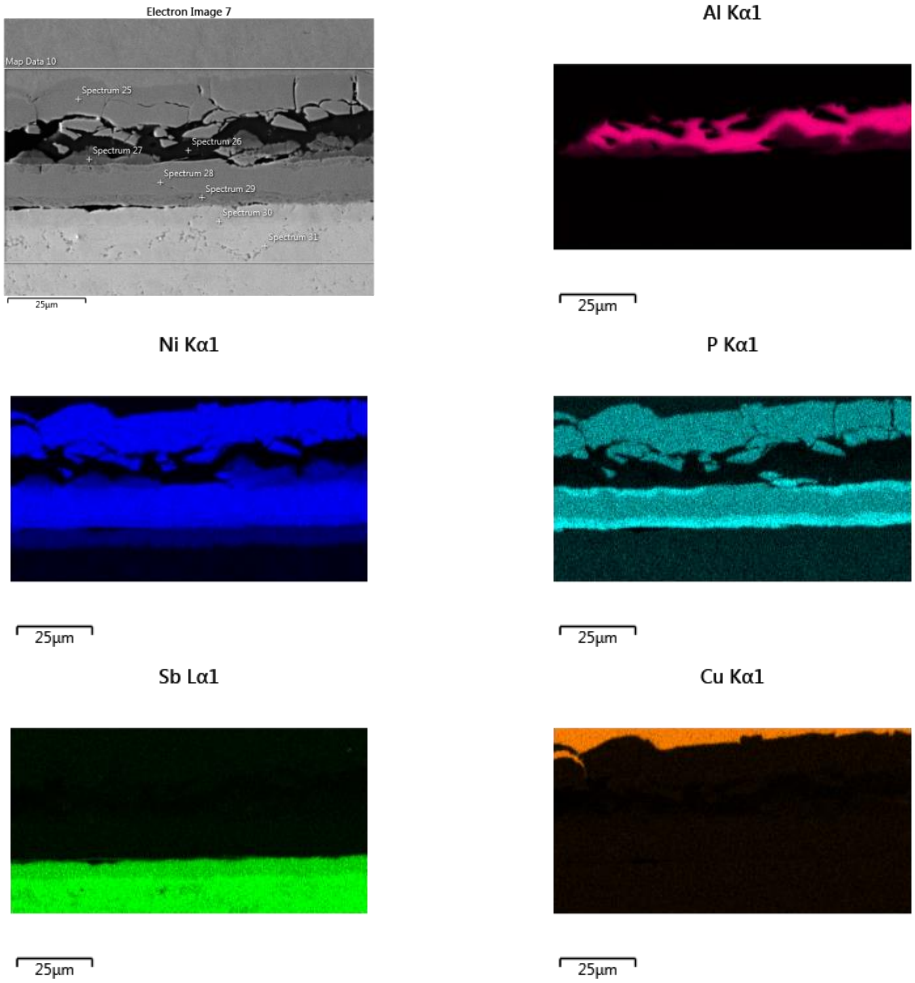

Figure A. 10: EDS analysis of $Mm_yFe_{4-x}Co_xSb_{12}$ *p-type* interfaces bonded to Ni(P) coated Cu interconnect using Al-Ni SLID technique (at 585 ºC for 15 minutes in Ar) with elemental mapping of Al, Ni, P, Sb, Cu, Fe, Co, La and Ce.

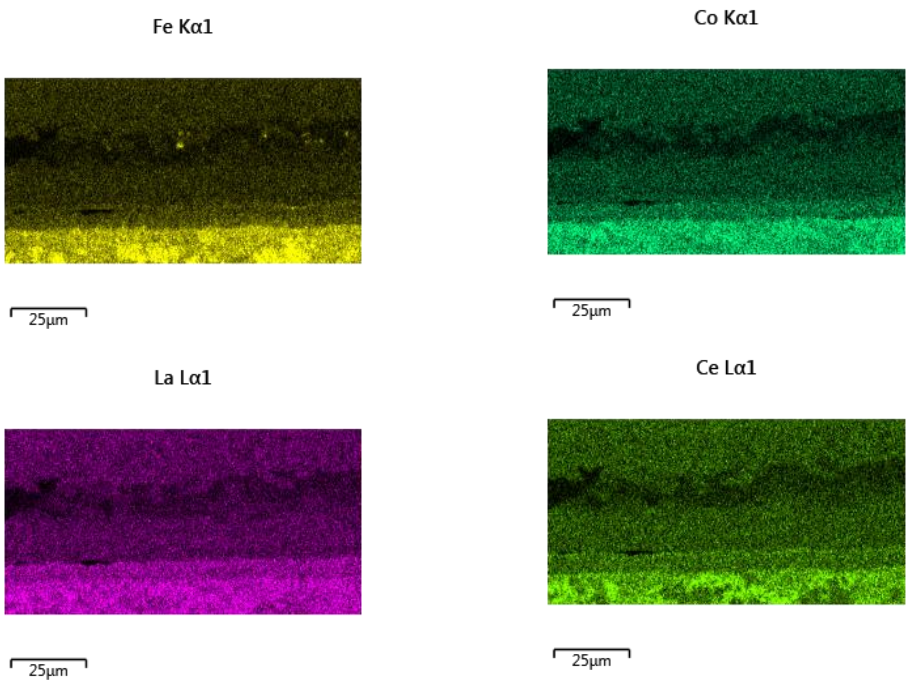

Figure A. 10 (Continued)

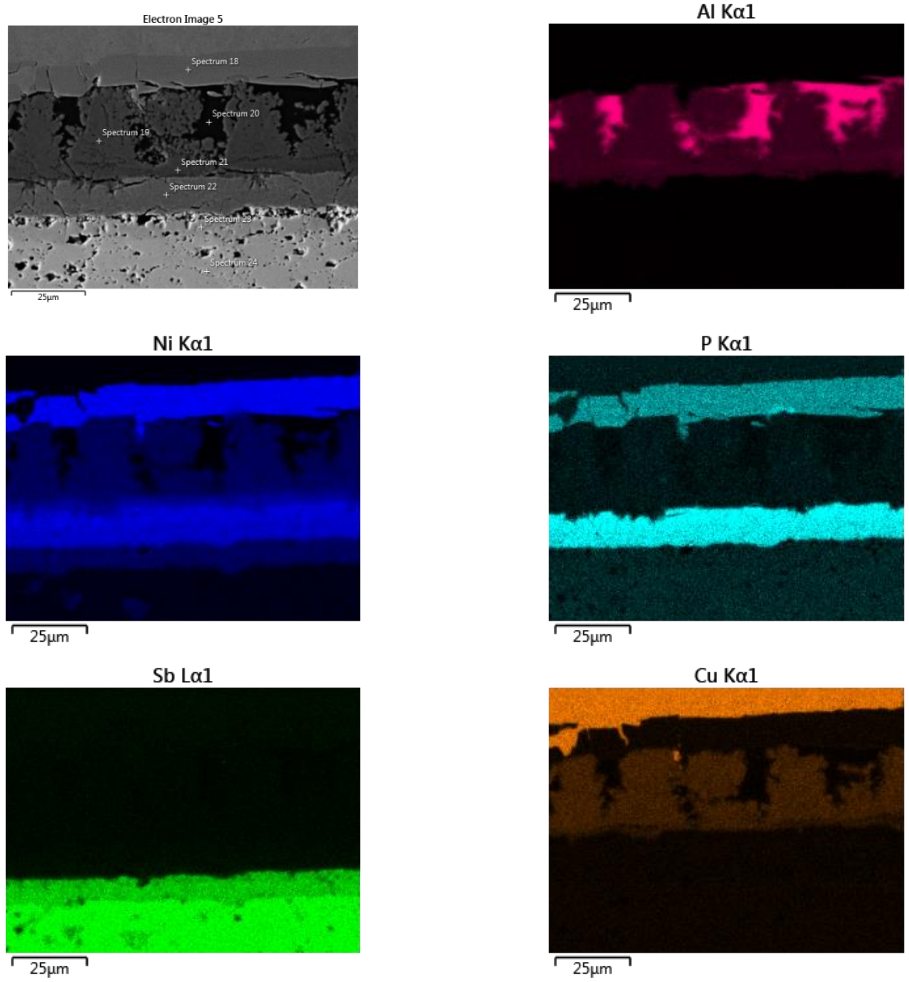

Figure A. 11: EDS analysis of $(Ni,Co)_1Sb_3$ *n-type* interfaces bonded to Ni(P) coated Cu interconnect using Al-Ni SLID technique (at 585 ºC for 15 minutes in Ar) with elemental mapping of Al, Ni, P, Sb, Cu and Co.

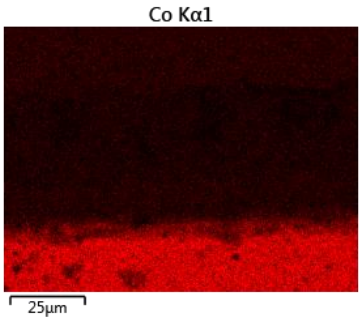

Figure A. 11 (Continued)

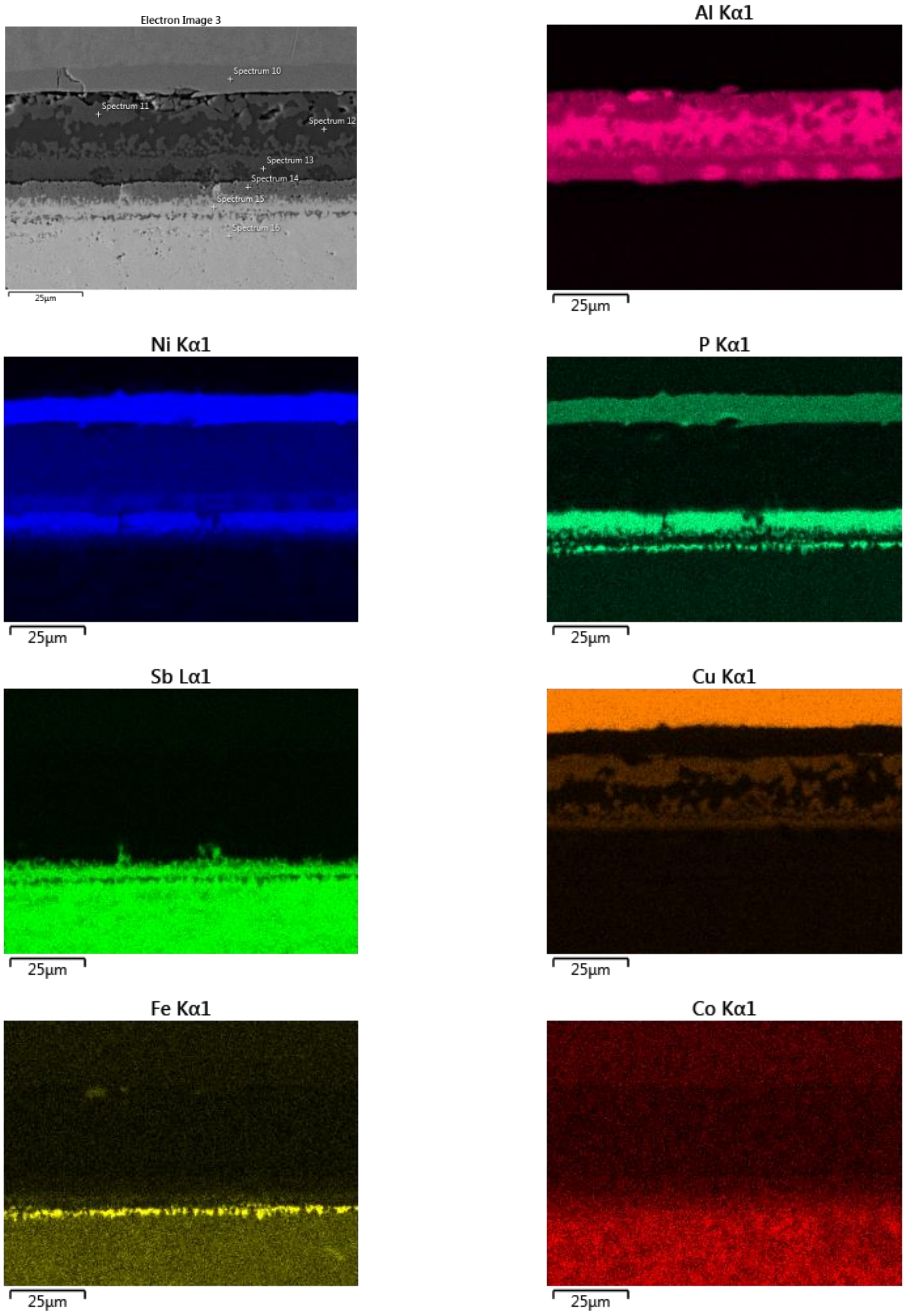

Figure A. 12: EDS analysis of $Mm_yFe_{4-x}Co_xSb_{12}$ *p-type* interfaces bonded to Ni(P) coated Cu interconnect using Al-Ni SLID technique (at 660 ºC for 4.6 min in Ar) with elemental mapping of Al, Ni, P, Sb, Cu, Fe, Co, La, Ce.

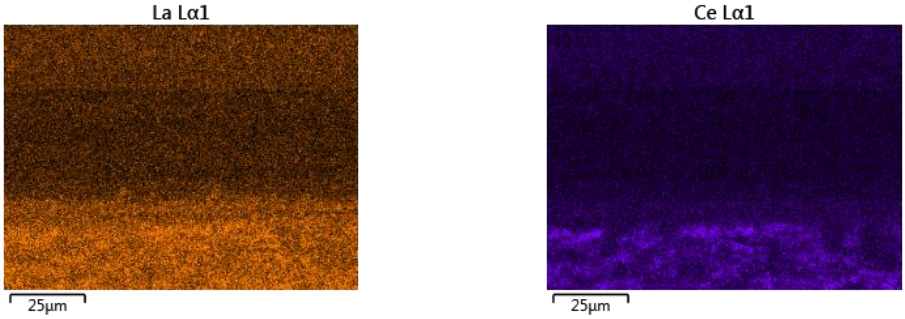

Figure A. 12 (Continued)

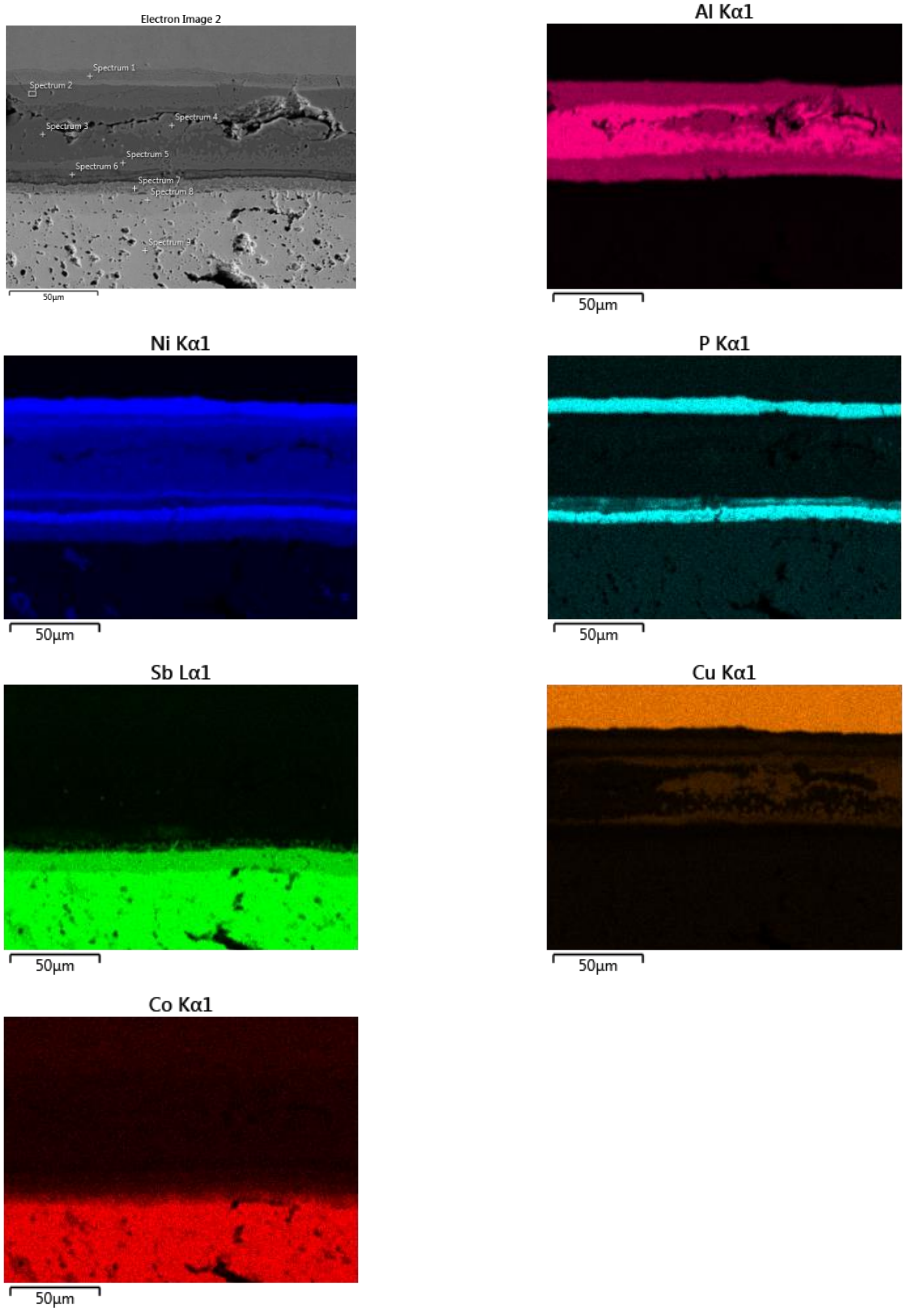

Figure A. 13: EDS analysis of $(Ni,Co)_1Sb_3$ *n-type* interfaces bonded to Ni(P) coated Cu interconnect using Al-Ni SLID technique (at 660 ºC for 4.6 min in Ar) with elemental mapping of Al, Ni, P, Sb, Cu and Co.

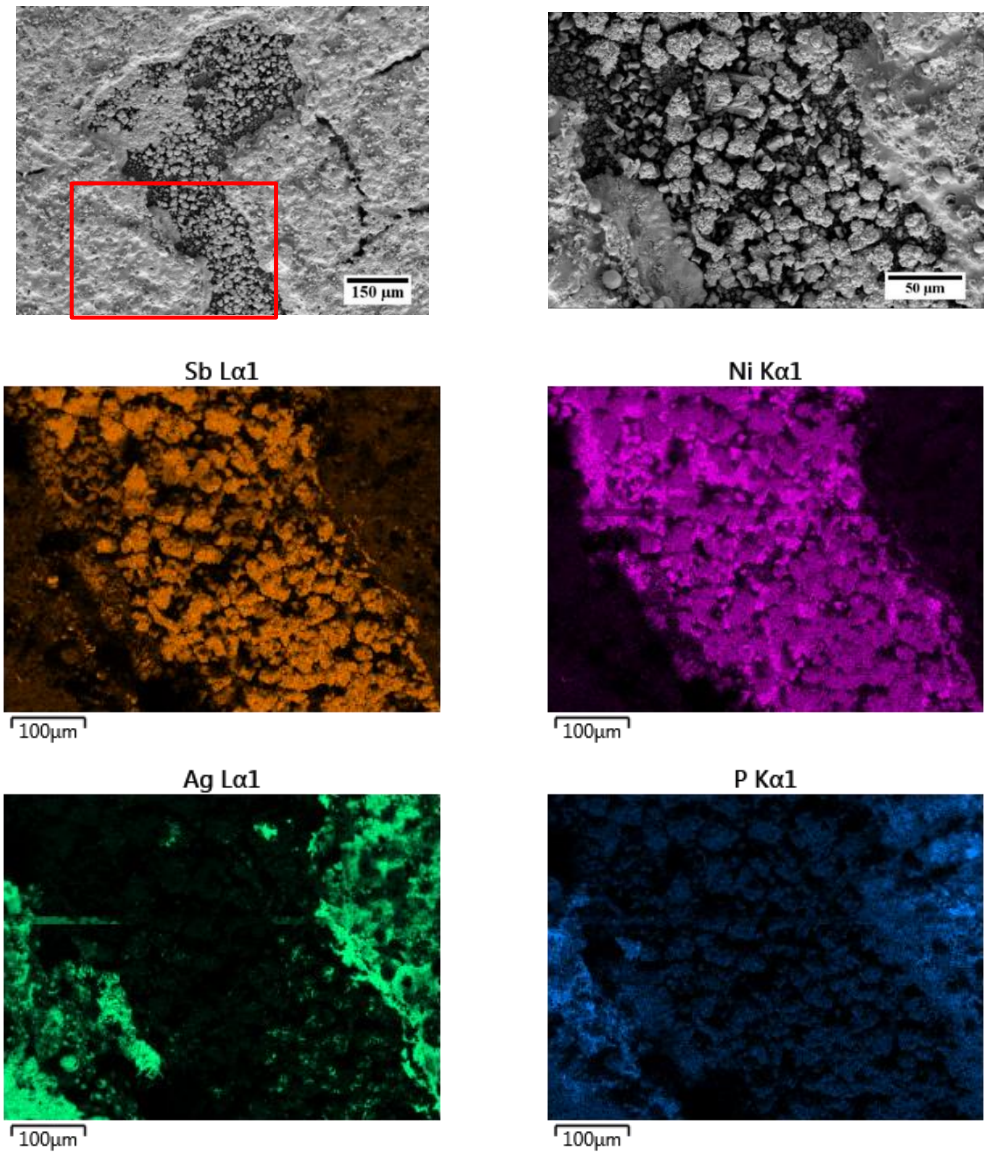

Figure A. 14: Top-view of fractured Ni/Ni(P) plated $Mm_yFe_{4-x}Co_xSb_{12}$ *p-type* surface which was joined to nickel interconnect using Ag paste (Q-INKS S.r.l, Italy) after shear strength testing - red square presents enlarged area shown in the next image along with elemental mapping of Sb, Ni, Ag and P obtained by EDS analysis.

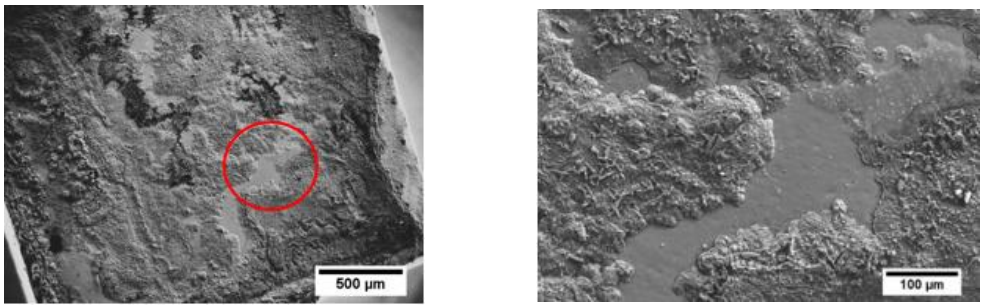

Figure A. 15: Top-view of fractured Ni/Ni(P) plated $Mm_yFe_{4-x}Co_xSb_{12}$ *p-type* interfaces bonded to Ni(P) coated Cu interconnect using Al-Ni SLID technique (at 660 ºC for 4.6 min in Ar) after shear strength testing. Red square presents enlarged area shown in the next image along with elemental mapping of Al, P and Ni.

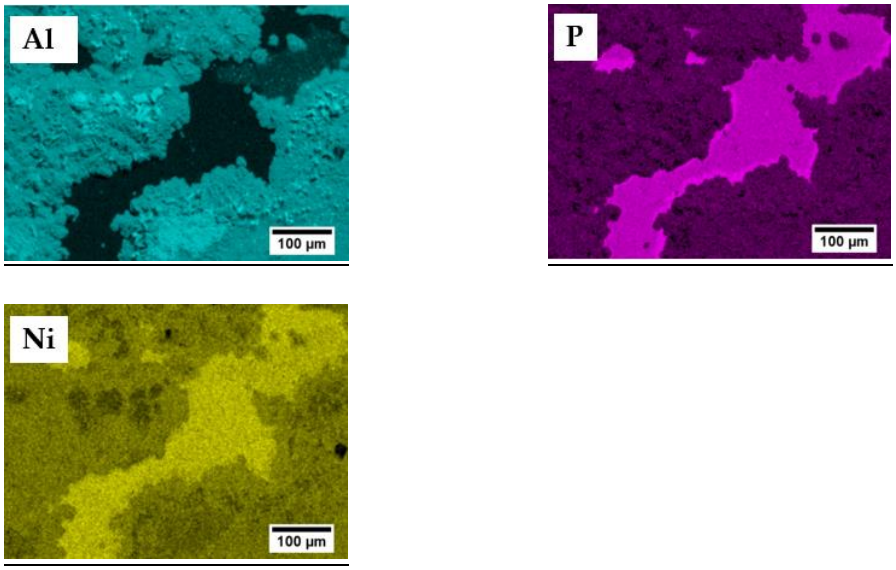

Figure A. 15 (Continued)

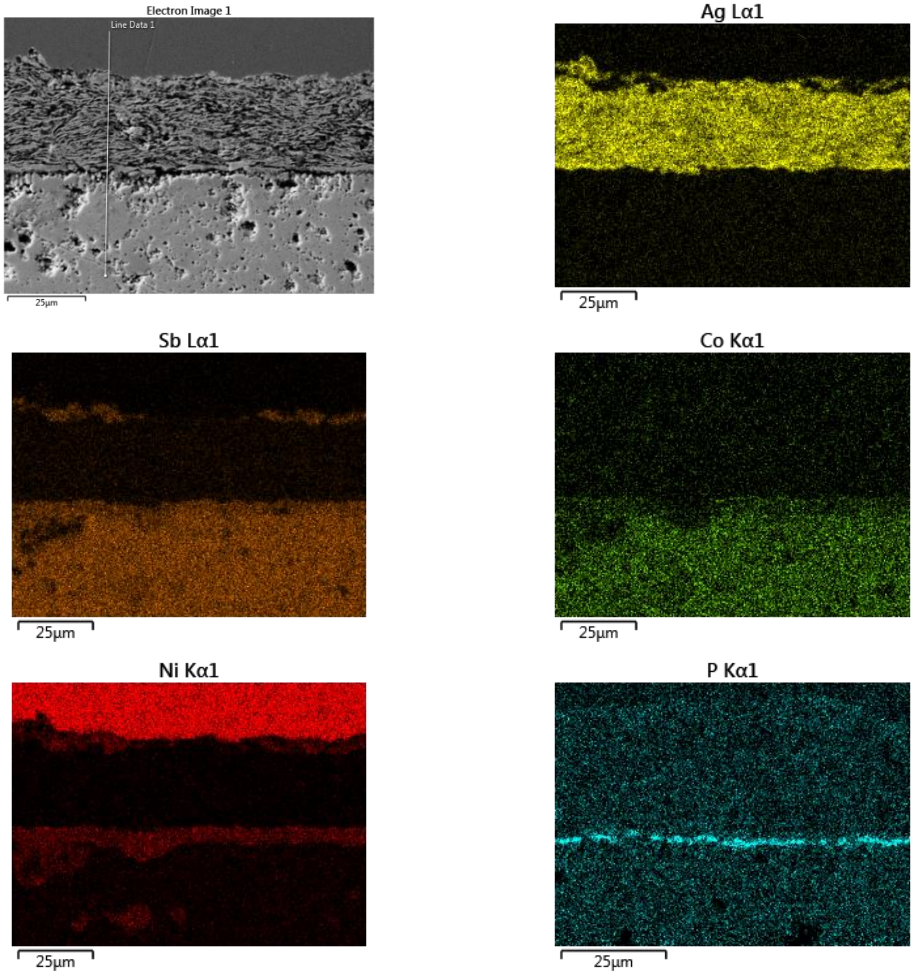

Figure A. 16: EDS analysis of Ni/Ni(P)/Au plated $(Ni,Co)_1Sb_3$ *n-type* interfaces bonded to Au coated Ni interconnect using Ag flake joining material (AREMCO Inc.) at 110 ºC in the air and isothermally aged at 450 ºC for 48h in Ar with elemental mapping of Ag, Sb, Co, Ni, P.

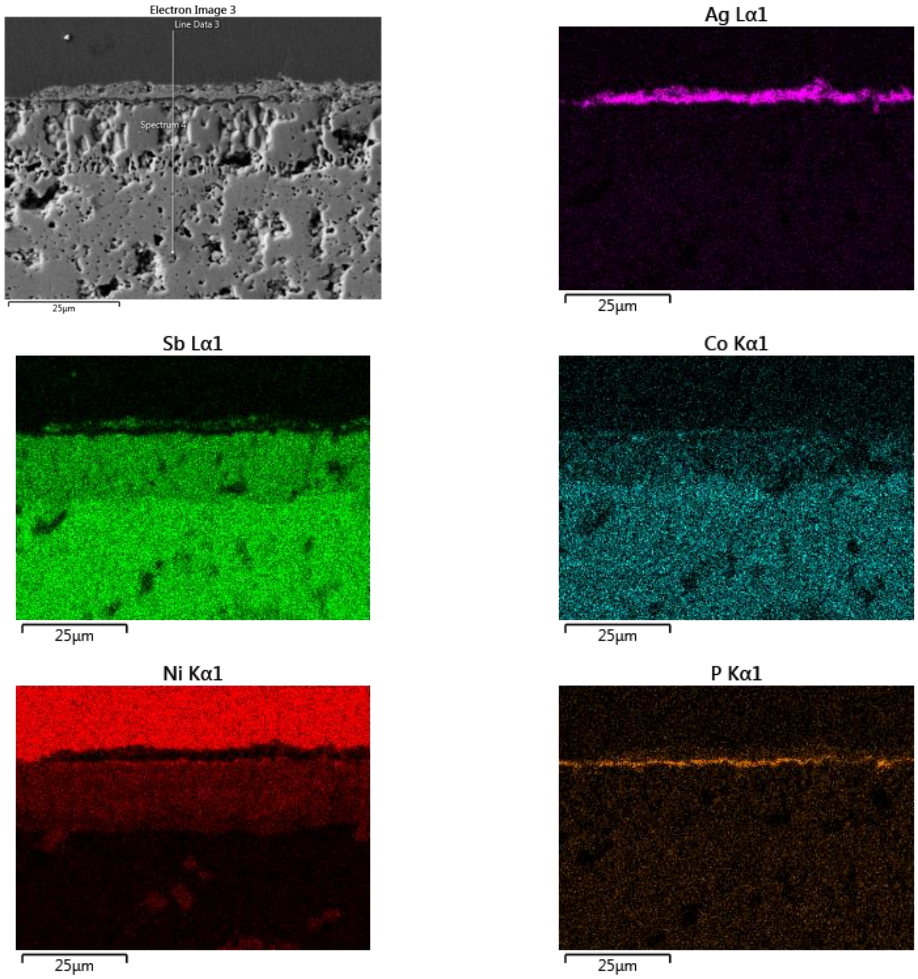

Figure A. 17: EDS analysis of Ni/Ni(P)/Au plated $(Ni,Co)_1Sb_3$ *n-type* interfaces bonded to Au coated Ni interconnect using Ag-nano joining material (NBE Technologies, LLC, US) at 273 °C in open air and isothermally aged at 450 °C for 48 hours in flowing Ar. Elemental mapping of Ag, Sb, Co, Ni, P are also presented.

Appendix B Simulated performance of TE devices

Table B. 1: Simulated performance of skutterudite module with Ni (0.1 µm-thick) / Ni(P) (2 µm-thick) / Au (0.05 µm-thick) metallization ('Model 1') and WSi_2 (1 µm-thick) / Au (0.05 µm-thick) metallization ('Model 2') optimized to 7 couple TE device.

ΔT (°C)	Voltage (V)	Current (A)[14]		P_{MAX} (mW)		Efficiency (%)		R_{LOAD} (mΩ)		V_{OC} (mV)
	Model 1 / Model 2	Model 1	Model 2	Model 1	Model 2	Model 1	Model 2	Model 1	Model 2	Model 1 / Model 2
25	0.015	-0.22	-0.04	3.401	0.66	0.156	0.031	67.39	347.75	30.27
50	0.031	-0.45	-0.08	13.92	2.70	0.319	0.064	67.55	347.90	61.33
100	0.062	-0.92	-0.18	58.06	11.32	0.657	0.133	67.86	348.24	125.54
150	0.096	-1.40	-0.28	135.44	26.50	1.007	0.206	68.13	348.52	192.13
200	0.129	-1.89	-0.37	245.59	48.19	1.352	0.279	68.37	348.76	259.16
250	0.163	-2.37	-0.47	387.94	76.3	1.691	0.351	68.56	348.95	326.2
300	0.196	-2.85	-0.56	562.21	110.78	2.025	0.423	68.74	349.12	393.17
350	0.230	-3.33	-0.66	768.18	151.65	2.355	0.495	68.90	349.28	460.12
400	0.263	-3.81	-0.75	1005.6	198.87	2.68	0.566	69.05	349.01	527.03
450	0.296	-4.29	-0.85	1274.2	252.43	3	0.638	69.2	349.15	593.89
500	0.330	-4.76	-0.95	1573.9	312.30	3.3154	0.709	69.35	349.29	660.71

[14] The electric current was simulated to be out of positive lead, giving a negative current value

Appendix C XRD analysis

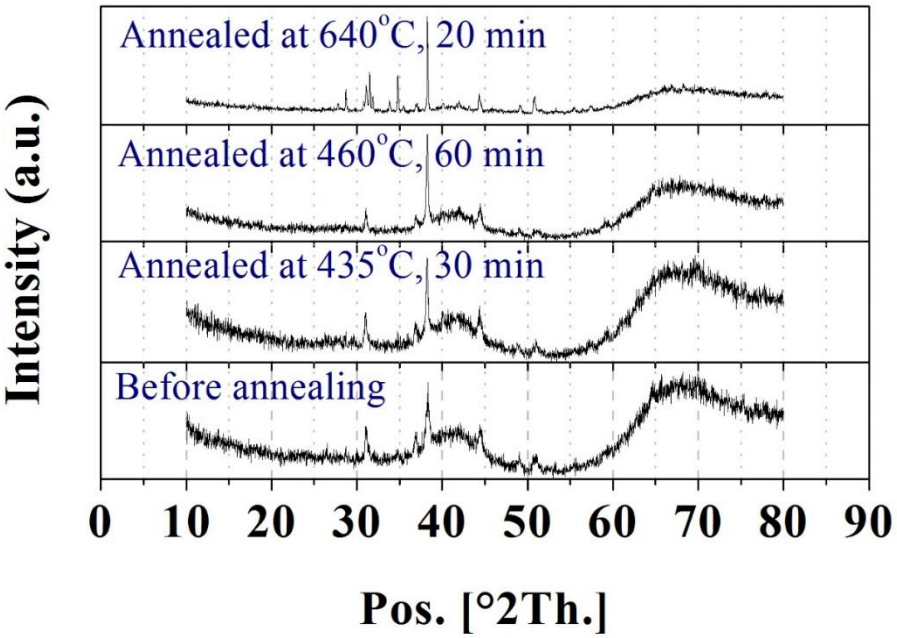

Figure C. 1: XRD patterns of $Mm_yFe_{4-x}Co_xSb_{12}$ *p-type* material metallized with WSi_2 (1 µm-thick) / Au (0.05 µm-thick) layers before and after annealing at 435 ºC for 30 minutes, 460 ºC for 60 min and 640 ºC for 20 in flowing argon.

Appendix D Numerical modelling

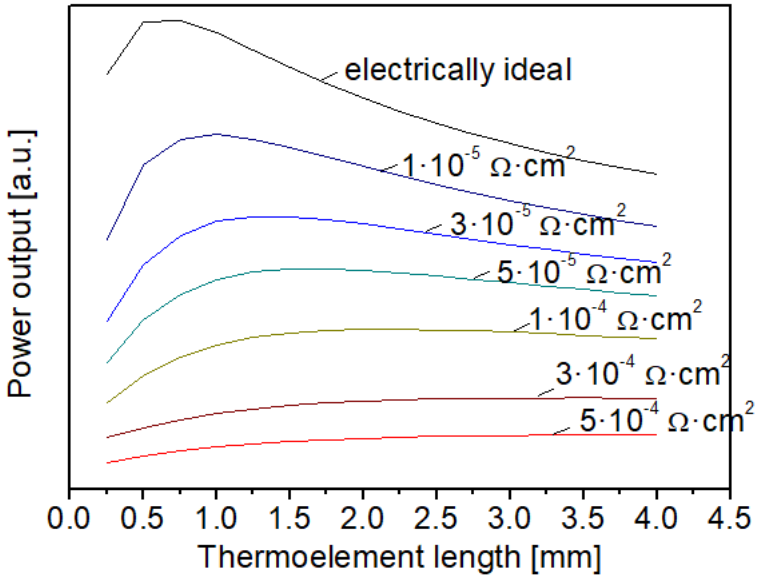

(a)

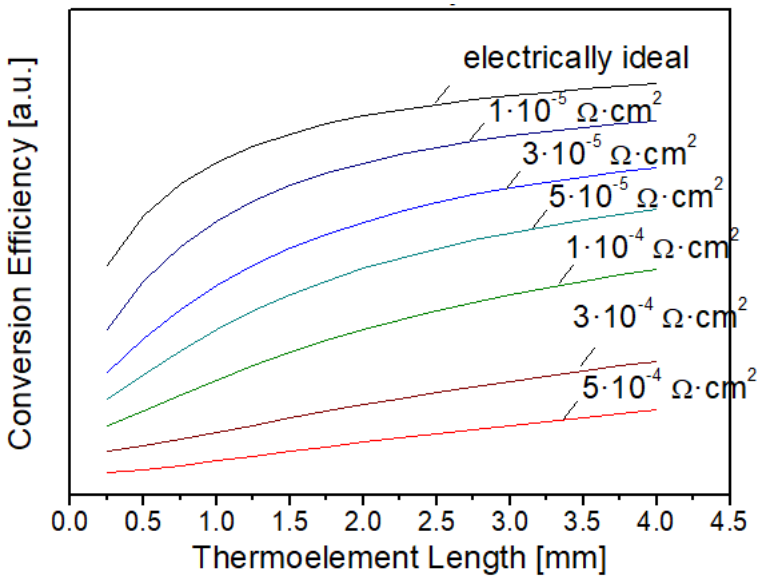

(b)

Figure D. 1: Simulated influence of electrical contact resistance *Rc* and thermoelement length on the **(a)** power output and **(b)** conversion efficiency of thermoelectric material.